

Understanding the Photogeneration Process in Organic Photovoltaics: From the Bulk to the Edges

by

Kan Ding

A dissertation submitted in partial fulfillment
of the requirements for the degree of
Doctor of Philosophy
(Physics)
in the University of Michigan
2021

Doctoral Committee:

Professor Stephen Forrest, Chair
Professor Hui Deng
Professor Jennifer Ogilvie
Professor Max Shtein

Kan Ding

dingkan@umich.edu

ORCID iD: 0000-0002-7119-1487

© Kan Ding 2021

To my parents

To Shida

Acknowledgements

Along the long journey to this dissertation, I have received help from so many people. This dissertation could not have been finished without them. First, I would like to thank my advisor, Professor Stephen Forrest. One of the luckiest things that have happened to me in my life is joining his group. I thank him for his patience during my early years when I was running around like a headless chicken; I thank him for the freedom he granted me to explore what I feel interested. I thank him for the guidance whenever I got lost. And I also thank him for his skepticism when I was overexcited or overconfident. His passion toward research and science deeply inspires me and his seemingly endless energy often makes me jealous. He makes a great example for me about how a successful researcher thinks about a problem, a project, and about the world.

Next, I want to thank some of the senior group mates that offered great help to me, Anurag Panda, Xiao Liu, Quinn Burlingame, Yongxi Li, Shaocong Hou and Yue Qu. Panda was my student mentor when I joined the group. He taught me all the experimental skills from material preparation to equipment operation, and so many things about the graduate life. Xiao Liu is my big-time collaborator. We collaborated on almost every project during our overlapping years. He is an electrical engineer but thinks like a scientist. I benefit so much from our collaboration. Quinn Burlingame is a skeptical thinker. Although we are good friends, we spent hours and hours debating on all kinds of topics. After every debate, I always find my understanding about a topic got much deepened, no matter I won or lost. I truly enjoyed those debates. Yongxi is the best

chemist I have met. He has been my main source of chemical wisdom in the later years of my PhD career and provided great help to my research. Shaocong is a true master of optics. He also gave me many great advises both in research and in life. Yue is one of the smartest people I have ever met. His sharp thoughts gave me a lot of inspirations.

I want to also thank all other OCMers I have met in the group, Xiaozhou Che, Caleb Coburn, Dejiu Fan, Jongchan Kim, Byungjun Lee, Kyusang Lee, Jaesang Lee, Xin Xiao, Xiaheng Huang, Xinjing Huang, Boning Qu, Claire Arneson, Hafiz Sheriff, Jeffery Horowitz, Haonan Zhao and Bin Liu. The OCM group has such a robust mix of excellent researchers from various background. Discussing with them was always helpful and intriguing. I am also grateful to Eva Ruff, our administrative staff. She has provided tremendous help for me on various otherwise time-consuming issues. I also owe thanks to the staff members at Michigan Center for Materials Characterization, Kai Sun, Haiping Sun, Allen Hunter and Tao Ma, who have offered me great help with the great instruments there.

Finally, I would like to thank my parents and my girlfriend, Shida Duan. Although for most of the time, they are on the other end of the planet, their love, understanding and support have been my fuel to move on. I would not have reached this point without them.

Kan Ding
Ann Arbor, Michigan
August 2021

Table of Contents

Dedication.....	ii
Acknowledgements.....	iii
List of Tables	x
List of Figures.....	xi
List of Appendices	xxi
List of Abbreviations	xxii
Abstract.....	xxv
Chapter 1 Introduction	1
1.1 Overview	1
1.2 Properties of Organic Semiconductors.....	3
1.2.1 Organic molecules	4
1.2.2 Organic films	7
1.2.3 Optical properties	8
1.2.4 Exciton transfer	11
1.2.5 Electronic properties.....	13
1.3 Fundamentals of Organic Photovoltaics	14
1.3.1 Charge transfer states	14
1.3.2 Organic bulk heterojunctions	15
1.3.3 Device architectures	16

1.3.4 Performance characterization	19
1.3.5 Device fabrication	23
1.4 Organization of the Thesis	27
Chapter 2 Charge Transfer States in Organic Bulk Heterojunctions	29
2.1 Charge Transfer States in DBP/C ₇₀ Bulk Heterojunctions.....	29
2.1.1 CT state energy spectrum in DBP/C ₇₀ bulk heterojunctions	31
2.1.2 Morphology study of DBP/C ₇₀ bulk heterojunctions	34
2.1.3 Time-resolved PL	35
2.1.4 Reverse-biased EQE and IQE	36
2.1.5 TDDFT calculation.....	38
2.1.6 Confined Schrödinger equation calculation	40
2.2 Charge Transfer States in DBP/C ₇₀ Alternating-layer Structures	44
2.2.1 Samples of alternating DBP and C ₇₀ layers.....	45
2.2.2 CT state energy spectrum in DBP/C ₇₀ alternating layer structures	47
2.2.3 Nanomorphology of DBP/C ₇₀ alternating layer structures.....	48
2.2.4 Kinetic Monte Carlo simulation of DBP/C ₇₀ blend.....	50
2.3 Charge Transfer States in Nonfullerene Acceptor-Based OPVs.....	56
2.3.1 Energy loss in nonfullerene acceptor-based OPVs	57
2.3.2 Semiclassical Marcus charge transfer theory	58
2.3.3 Exciton binding energy vs. molecular size.....	63
2.3.4 EL and EQE spectra of OPVs with various BHJs.....	69
2.3.5 Strategies to design molecules with low energy losses	71
2.4 Conclusions	75
Chapter 3 Interfacial Energy Loss in Organic Photovoltaics.....	77
3.1 Introduction	77

3.2 Identifying the Interfacial Energy Loss.....	78
3.2.1 Theoretical derivations	78
3.2.2 Impact of interfacial energy loss on J-V characteristics.....	81
3.2.3 Interfacial dipoles on BHJ/MoO _x interface	84
3.3 Reducing the Interfacial Energy Loss with an Acceptor Anode Interface Layer	90
3.3.1 Interfacial voltage loss and interfacial D/A ratio	90
3.3.2 Hole transporting mechanism of the acceptor interface layer	91
3.3.3 Anode interface layer with other active layers	92
3.4 Conclusions	93
Chapter 4 Bulk Quantum Efficiency of Organic Photovoltaics.....	94
4.1 Theory	94
4.2 Experimental Verification	99
4.2.1 BQE of DBP:C ₇₀ OPVs with various ABLs.....	99
4.2.2 BQE of DTDCPB:C ₇₀ OPVs with various AILs.....	101
4.2.3 BQE of OPVs with gradient D/A ratios	103
4.2.4 BQE of solution-processed NFA-based OPVs.....	104
4.3 Details of BQE analysis	106
4.3.1 Determination of the saturation current.....	107
4.3.2 The intensity dependence of BQE.....	108
4.3.3 Correction to BQE due to poor contact	109
4.3.4 Step-to-step guidance of BQE calculation	110
4.3.5 OPVs with Energy Barriers	111
4.4 Conclusions	112
Chapter 5 Photodegradation of Organic Photovoltaics.....	113
5.1 Photo-stability of DBP:C ₇₀ OPVs	113

5.1.1 BQE analysis for DBP:C ₇₀ OPVs.....	115
5.1.2 BQE degradation equation due to a low concentration of traps.....	116
5.1.3 Partially aged device.....	118
5.2 Photo-stability of NFA-based OPVs.....	120
5.2.1 BQE analysis for PCE-10:BT-CIC OPVs.....	121
5.2.2 Photocatalytic reaction between NFA and ZnO.....	122
5.2.3 IC-SAM protection layer.....	123
5.2.4 GIWAXS and TEM study.....	125
5.2.5 UV induced degradation.....	127
5.2.6 Light intensity dependence of OPV photostability.....	129
5.3 Conclusions.....	132
Chapter 6 Thermal Stability of Organic Photovoltaics.....	133
6.1 Thermal Degradation of inverted NFA-based OPVs.....	133
6.1.1 J-V characteristics and EQE.....	133
6.1.2 C ₇₀ anode interlayer.....	136
6.1.3 BQE analysis.....	139
6.1.4 STEM and EDS mapping.....	141
6.1.5 XPS study of BHJ/MoO _x interface.....	143
6.2 Thermal Degradation of conventional structured NFA-based OPVs.....	145
6.2.1 J-V characteristics.....	145
6.2.2 BQE analysis.....	147
6.3 Thermal Degradation vs. Photodegradation.....	147
6.4 Conclusions.....	150
Chapter 7 Outlook.....	152
7.1 Unanswered Questions.....	152

7.1.1 Channeling photocurrent outside the device area.....	152
7.1.2 J-V characteristics and BQE at low temperatures	155
7.2 Proposed Future Work	157
7.2.1 Physical meaning of BQE- V_{bulk} characteristics.....	157
7.2.2 Understanding OPV edges	158
7.2.3 Understanding the photodegradation mechanisms.....	158
7.3 Outlook for Organic Solar Cells.....	159
Appendices.....	161
Bibliography	177

List of Tables

Table 1.1 Comparison of properties of organic and inorganic semiconductors. ⁴¹	3
Table 2.1 The calculated polarizability (Unit: nm ³) tensor of fullerenes and NFAs.	66
Table 2.2 The intramolecular reorganization energy upon electron transfer λI – of archetypical fullerenes and NFAs.	67
Table 3.1 Device performance using various active layers with and without an acceptor anode interface layer (AIL).	92
Table 4.1 Device characteristics of OPVs with a DBP:C ₇₀ BHJ and various anode buffer layer (ABL) materials.	102
Table 4.2 Device characteristics of OPVs with a DTDCPB:C ₇₀ BHJ and various anode interface layer (AIL) materials.	103
Table 4.3 Device characteristics of OPVs with gradient mixed DTDCPB:C ₇₀ BHJs and various anode buffer layers (ABL). The C ₇₀ concentrations are referenced from the anode to the cathode side.	104
Table 4.4 Device characteristics of inverted OPVs with a PCE-10:BT-CIC BHJ and various cathode buffer layer (CBL) and AIL compositions.	106
Table 5.1 Device characteristics of DBP:C ₇₀ OPVs with various aging procedures.	119
Table 6.1 Effects of various photo and thermal degradation mechanism and methods to suppress them.	148
Table A.0.1 Chemical structures and short names of molecules	162

List of Figures

Figure 1.1 (a) A flexible OLED screen developed by LG Display. (b) Transparent OLED display at a hotel front desk allows agents to provide helpful information while maintaining in-person contact with guests. Images are from internet.	2
Figure 1.2 (a) A flexible OPV module developed by Toyobo Co., Ltd. (b) View through a color-neutral semi-transparent OPV developed by OCM group at University of Michigan. ⁴⁰	3
Figure 1.3 (a) Chemical structure of a small molecule, C ₇₀ . (b) Chemical structure of a polymer, PCE-10.....	5
Figure 1.4 Electron density distribution of the (a) HOMO and (b) LUMO of a DBP molecule calculated by density functional theory (DFT). ⁴⁴	6
Figure 1.5 (a) Solutions (b) molecular structures and (c) normalized absorption spectrum of molecules with various colors. ⁴⁷	7
Figure 1.6 (a) Unit cell of C ₇₀ crystal. (b) TEM image of C ₇₀ crystal. ⁴⁹	8
Figure 1.7 Three types of excitons and their different properties.....	9
Figure 1.8 (a) Energy levels of orbitals in the ground state and exciton state with the electron occupation denoted by arrows pointing up (spin up) or down (spin down). (b) Ground and exciton state potentials vs. the configuration coordinate. Each vibronic level is labeled by its quantum number. Absorption and emission spectra of DBP are indicated on the left. ⁴¹	11
Figure 1.9 Three types of exciton transfer.....	12
Figure 1.10 Schematic diagram of an electron placed in a polarized molecular crystal. Due to the electric field from the electron, the dipoles of the molecules are oriented to screen the electron. ⁶⁴	13
Figure 1.11 Schematics of successive steps of the photogeneration process in OPVs.....	15
Figure 1.12 Schematics of a planar HJ and a BHJ.....	16

Figure 1.13 (a) Typical structure of an OPV. (b) Energy diagram of the OPV in (a).	17
Figure 1.14 Working principle of a tandem OPV with two subcells connected in series. ⁸¹	18
Figure 1.15 J - V characteristics of a tandem OPV device and its two single-junction subcells. ⁴³	18
Figure 1.16 (a) Dark and illuminated (green) J - V characteristics of an OPV device and the photocurrent, J_{ph} (red), which is calculated as the difference between the dark current J_d (purple) and illuminated current J (green). (b) Dark and illuminated J - V characteristics of a silicon solar cell.....	20
Figure 1.17 J - V characteristics of an OPV with various series resistances.	21
Figure 1.18 Experimental setup to measure the EQE.	22
Figure 1.19 EQE spectra of DBP:C ₇₀ OPVs with various DBP concentrations (left axis). Also plotted are the absorption spectra of DBP and C ₇₀ (right axis).....	23
Figure 1.20 Schematic of a typical VTE system.....	24
Figure 1.21 Illustration of steps of spin coating.	25
Figure 1.22 Schematic diagram of an OVPD chamber. The source material in the source cell is heated and evaporate into the inert carrier gas stream. The source molecules are carried in a hot-walled chamber by the carrier gas to a cooled substrate where they are physisorbed. ⁹¹	25
Figure 1.23 Scanning electron microscope (SEM) images of CuPc film surface morphology deposited by OPVD with various parameters. ⁹²	26
Figure 1.24 An illustration of roll-to-roll deposition and patterning of organic devices. ⁹⁶	27
Figure 2.1 (a) Electroluminescence (EL) spectra from OPVs with different C ₇₀ concentrations in blends with DBP under +3V forward bias. The spectra above and below 1.22 eV are detected by a Si CCD and a InGaAs photoreceiver, respectively. The spectra are offset for clarity. Two charge transfer excitons are labelled CT ₁ and CT ₂ . The spectra from neat DBP and C ₇₀ are shown for comparison. (b) Voltage dependence of EL with 90% and 50% C ₇₀ concentrations in DBP. 32	
Figure 2.2 (a) Steady-state photoluminescence spectra from DBP/C ₇₀ blends excited by a $\lambda = 442$ nm wavelength laser at 20 K. Both CT and monomer singlet emission spectra are noted. The spectra are offset for clarity. (b) CT exciton energies vs C ₇₀ concentration. The curves are a guide for the eye.	33
Figure 2.3 (a) Intensity of the (111) C ₇₀ X-ray diffraction peak of several DBP/C ₇₀ blends whose C ₇₀ concentrations are provided in the legend. (b) Transmission electron microscope images of blends with different C ₇₀ concentrations. Crystalline C ₇₀ domain boundaries are outlined in white. Scale bars in the lower left of each micrograph are 20 nm.....	35

Figure 2.4 (a) Time-resolved PL for a DBP/C ₇₀ blend with 90% C ₇₀ at 295 K and 20 K. (b) CT state lifetime vs C ₇₀ concentration at 295 and 20K. The error bars are the 95% confidence intervals. The data points are connected by curves to guide the eye.	36
Figure 2.5 External quantum efficiency at 0 and -5 V reverse bias for OPVs with (a) 90% C ₇₀ concentration in DBP, neat C ₇₀ , and neat DBP; (b) 50% C ₇₀ concentration in DBP. The EQE at -5 V is equal to ηA. The internal quantum efficiency spectra for two blends are shown with blue lines.	37
Figure 2.6 (a) Calculated singlet energies of different monomer, dimer, trimer, and tetramer combinations of DBP and C ₇₀ using TDDFT. On the abscissa, DBP is abbreviated as D. (b) Visualized charge density difference analysis of the first four CT states of the DBP-C ₇₀ dimer (left) and trimer (right) complexes. The electron (purple) and the hole (yellow) density distributions are located on the C ₇₀ and DBP molecules, respectively.	39
Figure 2.7 Schematics of CT delocalization in various nano morphological environments.	41
Figure 2.8 (a) Measured peak energies of CT ₂ states (data points) and calculated CT binding energies (red line) as functions of C ₇₀ domain radius, ⟨r ₀ ⟩. Inset: Calculated electron density distribution for a domain with ⟨r ₀ ⟩ = 2 nm. (b) (Top) Calculated probability density overlap J vs ⟨r ₀ ⟩. (Bottom) Measured recombination rate k _d for CT ₂ vs ⟨r ₀ ⟩.	43
Figure 2.9 (a) Bright field (BF) cross-sectional scanning transmission electron microscopic image of 5 pairs of 2 nm thick alternating layers capped by a 20 nm thick C ₇₀ layer and a 150 nm thick Ag protection layer. The dark spots are due to Ag diffusion from the contact. (b) Image of 5 pairs of 5 nm thick alternating layers capped by a 20 nm thick C ₇₀ layer and a 50 nm thick Ag layer.	46
Figure 2.10 (a) Room temperature photoluminescence (PL) spectra of multilayer stacks consisting of alternating layers of DBP and C ₇₀ and a 1:1 mixed sample. To achieve a total thickness of 40 nm, the multilayer stacks with alternating layer thicknesses of 1, 2, 3, and 5 nm contain 20, 10, 7, and 4 pairs of DBP and C ₇₀ layers, respectively. The spectra are normalized to the same integrated intensity, and are offset for clarity. (b) Photoluminescence peak energies of CT ₂ states, E ₂ , and calculated Coulombic binding energies vs layer thickness.	48
Figure 2.11 (a) Average C ₇₀ cluster radius ⟨r⟩ vs DBP concentration in DBP:C ₇₀ blends. The radii obtained from X-ray diffraction and KMC simulations (circles) are indicated. Error bars for the X-ray diffraction data arise from uncertainties in line widths at half maxima. Error bars are standard deviations of the simulated cluster size distributions. (b) Measured (squares) and calculated (circles) E ₂ based on the simulated nanocrystallite radius, ⟨r⟩, vs DBP concentration. The error bars for the PL data arise from Gaussian fits to the CT ₂ peak while the error bars for the simulated results are standard deviations of the cluster size distributions.	49
Figure 2.12 (a) Atomic force microscopic (AFM) image of the top surface of a neat C ₇₀ film. (b) Top surface of a simulated C ₇₀ film. (c) Histogram of surface roughness of the film in (a). (d) Histogram of surface roughness of the simulated film in (d).	52

Figure 2.13 Measured and simulated average C_{70} domain sizes and CT_2 peak energies vs. DBP concentration..... 53

Figure 2.14 (a) Three-dimensional simulation of a 10 nm deep by 80 nm thick slice of a 1:8 DBP: C_{70} blended HJ. Growth is simulated by molecules arriving at top of the surface starting at the anode lying at the bottom. Blue areas are C_{70} molecules. Green (red) areas are DBP molecules that form (do not form) percolating paths to the anode. Note the voids in the thin film. The simulation comprises 600, 000 molecules. (b) Three-dimensional simulation of the DBP percolating paths of a 50 nm deep and 80 nm thick vertical slice of a blend with 10 mol % DBP in C_{70} . The C_{70} molecules are not shown. Percolating paths are identified by connecting adjacent DBP molecules with green lines. 54

Figure 2.15 Two-dimensional density of DBP percolating paths, ρ , in the substrate plane as a function of distance from the anode, z (triangles). An exponential fit to the data is shown by the line..... 55

Figure 2.16 Energy diagrams of (a) charge transfer from the acceptor exciton (A^*) to the charge transfer (CT) state (A^-/D^+), and (b) nonradiative recombination from the CT state (A^-/D^+) to the ground state (A/D). The Gibbs free energies are ΔE_{CT} in (a) and E_{CT} in (b). Symmetric parabolic potentials are assumed for the initial and final states. The vibrational levels (n, n' , and $n'' = [0, 1, 2, \dots]$) are equally spaced. Equilibrium configurations of A^*/D , A^-/D^+ , and A/D manifolds are indicated by Q_1, Q_2 and Q_3 , respectively. 60

Figure 2.17 Charge transfer rate, k_{CT} , vs the energy loss on CT state formation, ΔE_{CT} , as functions of (a) the intermolecular reorganization energy, λ_0 , and (b) intramolecular coupling strength, S . (c) Nonradiative recombination rate k_{nr} vs E_{CT} as functions of λ_0 and (d) S 63

Figure 2.18 (a) The molecular structure of BT-C1C. The red bold line traces the electron-conjugation path comprising alternating C-C single and double bonds. Blue dashed circles indicate the electron-rich (i.e., oxy-) and deficient (i.e., chloro- and cyano-) moieties that affect the electron distributions in the molecules. (b) The electron and hole density distributions along the molecular length of BT-C1C calculated using DFT. (c) The molecular structural formulas of IDT-IC and IDTIDT-IC that have different lengths of the electron-donating cores as indicated in the shaded regions. 65

Figure 2.19 Exciton binding energy, E_B , found via DFT vs effective molecular volume for several acceptor molecules indicated in legend whose molecular formulas are in Appendix A. The red solid line is a fit assuming electron confinement within the effective molecular volume for each molecule. The calculation assumes a dielectric parameter, $f = 5.4$. The shaded area is the 95% confidence band. The blue dashed line assumes f depends on molecular polarizability from (b). The confidence limits of the calculations are shown by dotted lines. (b) The calculated molecular polarizability along the molecular longitudinal axis, a_{xx} , vs the effective molecular length l . The dashed line is the fit using an empirical power law described in text. 66

Figure 2.20 Measured k_{CT} vs ΔE_{CT} for HJs comprising (a) 1. BT-IC/PBDBT, 2. BT-IC/J61, 3. BT-IC/P3HT, 4. BT-C1C/PCDTBT, 5. BT-C1C/PBDBT, 6. BT-C1C/J61, (b) 1. IT-IC/PCDTBT, 2. IT-IC/PBDBT, 3. IT-IC/J61, 4. IT-IC/P3HT, and (c) 1. PC₇₁BM/F8T2, 2. PC₇₁BM/F8, 3.

PC₇₁BM/F8BT, 4. ICBA/F8T2, 5. PC₆₁BM/F8T2, 6. PC₆₁BM/F8, 7. PC₆₁BM/F8BT, 8. C₇₀/CBP, 9. C₇₀/TCTA, 10. C₇₀/NPD, and 11. C₇₀/TPTPA. The dashed lines in (a) and (b) are the fits using semi-classical Marcus theory [Eq. (2.3.4) in text]. The blue dashed line in (c) is a guide to the eye. Nonshaded sections are the Marcus normal regions, and shaded sections are the inverted regions. All molecular structural formulas are found in Appendix A. 68

Figure 2.21 Measured k_{CT} vs temperature, T , for (a) BT-IC/PBDBT and (b) IT-IC/PBDBT HJs. The dashed lines are the fits assuming thermal activation..... 69

Figure 2.22 Electroluminescence (EL) and external quantum efficiency (EQE) spectra of OPVs based on (a) neat IT-IC, PBDBT, and their blended heterojunction. (b) Neat PC₇₁BM, PBDBT, and their blended heterojunction. The CT state emission at low energy is extracted from the EL spectra by subtracting the spectra from the neat layers. The CT state absorption spectra are extracted by a Gaussian fit of the EQE spectra along the low energy shoulders. The arrows between the short lines indicate the Franck-Condon shift, E_{FC} , of the CT spectra. 70

Figure 3.1 (a) OPV structure with the active region divided into the interface and the bulk regions with C₇₀ concentrations of x and y , respectively. (b) Energy level diagram of a DBP/C₇₀ OPV at open circuit. The blurred red/blue lines represent the DBP/C₇₀ HOMOs with a finite width of the density of states. 79

Figure 3.2 (a) Energy level diagram near the interface between a DBP/C₇₀ mixed layer and MoO_x at open circuit. The blue and yellow arrows represent the flow of electrons and holes, respectively. (b) Energy level diagram near the interface between a DBP/C₇₀ mixed layer and MoO_x at open circuit when a 2-nm-thick neat C₇₀ anode interface layer (AIL) is inserted between the bulk layer and the MoO_x. 80

Figure 3.3 (a) Current density-voltage (J - V) characteristics under one sun simulated AM1.5G illumination of OPVs with identical C₇₀ concentrations in the bulk of $y = 90\%$, and various C₇₀ concentrations, x , in AIL. (b) Open circuit voltage, V_{oc} (red squares) and simulated interfacial potential drop, V_{int} (black diamonds) vs. x . (c) J - V characteristics of OPVs with $x = 100\%$, and various y . (d) Device V_{oc} (red squares) and charge transfer state energy measured from photoluminescence spectra (black diamonds) vs. y 82

Figure 3.4 (a) J - V characteristics for the dark current density J_D (dotted), photocurrent density J_{ph} (dash) and total current density J (solid) of devices with a C₇₀ (red), and a DBP AIL (black). (b) The same J - V characteristics as in (a) replotted with reference to voltage across the active layer, V_{bulk} . The vertical dashed line corresponds to V_{oc} 83

Figure 3.5 J - V characteristics of OPVs with a neat C₇₀ AIL of various thicknesses. The bulk layer of all devices consists of DBP as donor and C₇₀ as acceptor with $y = 80\%$ 84

Figure 3.6 (a) J - V characteristics of OPVs with $x = 100\%$ (solid line) and $x = 0\%$ (dash line) when $y = 90\%$ (red), 50% (blue) and 30% (black), respectively. (b) Simulated hole density ρ_h (histogram) and electric potential shift from the bulk $\Delta\phi$ (lines) near the active region/anode buffer layer (ABL) interface for devices with a C₇₀ or a DBP AIL with $y = 90\%$. (c) Simulated ρ_h (histogram) and $\Delta\phi$ (lines) near the active region/ABL interface for devices with a C₇₀ IL or a DBP IL with $y = 50\%$ 88

Figure 3.7 (a) J - V characteristics of OPVs with PEDOT:PSS as the anode buffer layer (ABL), with a C₇₀ AIL (black) and a DBP AIL (red) when $y = 90\%$. (b) J - V characteristics of OPVs with HAT-CN as the ABL, with a C₇₀ (black) and a DBP AIL (red) when $y = 90\%$ 89

Figure 3.8 Highest occupied molecular orbital (HOMO) energy bending (relative to the bulk) vs. distance from the ABL interface for C₇₀/MoOx interface (black), DBP/MoOx interface (red), C₇₀/PEDOT:PSS interface (blue) and C₇₀/HAT-CN interface (pink) measured by ultraviolet photoelectron spectroscopy. The vertical error bars represent the energy resolution of the measurement and the horizontal error bars represent the uncertainty of the organic layer thickness..... 90

Figure 4.1 Energy level diagram of an OPV under forward bias that is smaller than the open-circuit voltage. The hole quasi-Fermi energy, E_{Fh} , is pinned at δ_1 above the donor HOMO level on the anode side while the electron quasi-Fermi energy, E_{Fe} , is at δ_2 below the acceptor LUMO level on the cathode side. The schematic indicates the flow directions of the photogenerated charges from an exciton. 96

Figure 4.2 (a) Energy level diagram of an “ideal OPV” of which all contacts are ohmic under reverse bias. (b) Energy level diagram of an ideal OPV at short-circuit. (c) Energy level diagram of an ideal OPV under solar cell working condition. (d) Energy level diagram of an ideal OPV when there is no electric field in the BHJ. 98

Figure 4.3 (a) BQE- V_{bulk} characteristics of OPVs with identical bulk heterojunction (BHJ) layers of DBP as the donor and C₇₀ as the acceptor (1:8 by volume, 54 nm), and various anode buffer layers (ABLs). Inset: Device structure. (b) Current density-voltage (J - V) characteristics of devices in (a). 101

Figure 4.4 (a) BQE- V_{bulk} characteristics of OPVs with identical BHJs of DTDCPB as the donor and C₇₀ as the acceptor (1:2 by volume, 80 nm) and various anode interface layers (AILs). Inset: Device structure. (b) J - V characteristics of devices in (a). 102

Figure 4.5 (a) BQE- V_{bulk} characteristics of DTDCPB:C₇₀ OPVs with gradient C₇₀ concentrations from the anode to the cathode side (80 nm), and various anode buffer layers (ABLs). Inset: Device structure. (b) Current density-voltage (J - V) characteristics of devices in (a)..... 104

Figure 4.6 (a) BQE- V_{bulk} characteristics of OPVs with identical BHJs of PCE-10 as the donor and BT-CIC as the acceptor (1:1.5 by weight, 80 nm) and various cathode buffer layer (CBL)/AIL compositions. Inset: Device structure. (b) J - V characteristics of devices in (a). 105

Figure 4.7 (a) BQE- V_{bulk} characteristics of a PCE-10:BT-CIC OPV aged for 46 days using $J_{sat} = J(-1V)$ and $J_{sat} = J(-5V)$. (b) BQE- V_{bulk} characteristics in (a) plotted on different vertical scales. 107

Figure 4.8 (a) Normalized photocurrent J_{ph} vs. voltage characteristics of a DBP:C₇₀ OPV under various illumination intensities, and the increase in injection current, ΔJ_{inj} . (b) The responsivity vs. light intensity..... 109

Figure 4.9 (a) J_{ph} - V characteristics of four identical PCE-10:BT-CIC OPVs on the same substrate with various contact conditions. (b) Corrected BQE- V_{bulk} characteristics of devices in (a). 110

Figure 4.10 (a) J_{ph} - V characteristics of a PCE-10:BT-CIC OPV with solid and poor contact. (b) As-calculated BQE- V_{bulk} characteristics for solid and poor contact devices and corrected BQE- V_{bulk} characteristics for the poor contact device. 111

Figure 4.11 (a) J - V characteristics of DBP:C₇₀ OPVs with various mixing ratios and C₇₀ AILs of various thicknesses. (b) As-calculated BQE- V_{bulk} characteristics for OPVs in (a). 112

Figure 5.1 (a) Normalized PCE plotted against ageing time under illumination equivalent to 9.5 ± 1.4 , 20 ± 3 and 37 ± 5.5 Suns. Stretched exponential fits to each PCE against time dataset are shown by dashed lines. The inset shows PCE plotted against time for an OPV aged under ultraviolet illumination equivalent to 20 Suns. (b) Normalized J_{sc} , V_{oc} and FF plotted against ageing time under illumination equivalent to 9.5 ± 1.4 , 20 ± 3 and 37 ± 5.5 Suns. 115

Figure 5.2 (a) BQE- V_{bulk} characteristics of a DBP:C₇₀ OPV aged under white light with an intensity equivalent to 27 suns. Inset: V_{80} vs. aging time. (b) V_{off} and J_{sat} vs. aging time. 116

Figure 5.3 (a) Experimental (symbols) and fitted (lines) values of the decrease in BQE relative to the as-grown device (Δ BQE) vs. V_{bulk} at various aging times. (b) Maximum values of Δ BQE vs. aging time. 118

Figure 5.4 (a) Structure of the partly aged and fully aged OPVs. The ITO layer, MoO_x layer and bottom 10 nm of the BHJ were aged under white light with an intensity equivalent to 27 suns for 17 days in the partly aged device. (b) BQE- V_{bulk} characteristics of the partly aged device, the as-grown device, and the fully aged device. 119

Figure 5.5 (a) BQE- V_{bulk} characteristics of an inverted OPV with a PCE-10:BT-CIC BHJ and a ZnO CBL aged under simulated AM 1.5G illumination. Inset: V_{80} vs. aging time. (b) V_{off} and J_{sat} vs. aging time. (c) Experimental (symbols) and fitted (lines) decrease in BQE (Δ BQE) vs. V_{bulk} vs. aging time. (d) The maximum values of Δ BQE vs. aging time. 122

Figure 5.6 UV-Vis absorption spectra plotted vs. aging time under ultraviolet illumination with intensity equivalent to 60 suns of thin film of (a) PCE-10 on ZnO, (b) BT-CIC on ZnO. 123

Figure 5.7 UV-Vis absorption spectra plotted vs. aging time under ultraviolet illumination with intensity equivalent to 60 suns of thin film of (a) BT-CIC/IC-SAM/ZnO, (b) PCE-10:BT-CIC/IC-SAM/ZnO. 124

Figure 5.8 (a) Time evolution of BQE- V_{bulk} characteristics of a PCE-10:BT-CIC control OPV under simulated AM 1.5G illumination. Inset: V_{off} vs. aging time. (b) Time evolution of BQE- V_{bulk} characteristics of a PCE-10:BT-CIC OPV with an IC-SAM inserted between the BHJ and the ZnO layer under simulated AM 1.5G illumination. Inset: V_{off} vs. aging time. 125

Figure 5.9 (a) In-plane (dotted line) and out-of-plane (solid line) sector-averaged profiles extracted from grazing incidence wide-angle x-ray scattering (GIWAXS) patterns, q is the scattering vector. (b) TEM image of cross-sectional slices of a fresh PCE-10:BT-CIC device

without an interface buffer layer. (c) Fresh PCE-10:BT-CIC device with an IC-SAM layer inserted at the ZnO/BHJ interface. (d) Aged PCE-10:BT-CIC device with an IC-SAM layer inserted at the ZnO/BHJ interface under 27 ± 3.8 suns illumination for 870 h. 127

Figure 5.10 Time evolution of BQE- V_{bulk} characteristics of a PCE-10:BT-CIC OPV with an IC-SAM inserted between BHJ and ZnO and a UV filter (cutoff at 400 nm) under simulated AM 1.5G illumination. Inset: V_{off} vs. aging time. 128

Figure 5.11 Transmittance spectra of the glass substrate with and without the ZnO coating with various aging periods. 129

Figure 5.12 (a), (b), (c) Change of BQE over time of BT-CIC:PCE-10 OPVs under white light illumination equivalent to 10, 20 and 27 Suns. (d), (e), (f) Change of the V_{off} over time under white light illumination equivalent to 10, 20 and 27 Suns. 130

Figure 5.13 Maximum values of BQE decrease, ΔBQE_{max} , vs. squared aging time, t_{square} , of BT-CIC:PCE-10 OPVs under various white light intensities. 131

Figure 6.1 Time evolution of $J-V$ characteristics of a PCE-10:BT-CIC device when heated under 50 °C in the dark. Inset: Device structure. 135

Figure 6.2 (a) $J-V$ characteristics of a PCE-10:BT-CIC control device when heated under 80 °C after various aging periods. (b) External quantum efficiency (EQE) spectra of the control device when heated under 80 °C after various aging periods. 136

Figure 6.3 Time evolution of $J-V$ characteristics of a PCE-10:BT-CIC device with a 2 nm thick C_{70} layer inserted between the MoO_x and BHJs when heated under 50 °C in the dark. Inset: Device structure. 137

Figure 6.4 Time evolution of PCEs of control devices (solid lines) and devices with the C_{70} protection layer (dash lines) heated under various temperatures. The errors of the PCEs are ± 0.2 % but not plotted for clarity. 138

Figure 6.5 PCE time evolution of PM6:Y6 OPVs with donor/acceptor ratios of 1:2 (black) and 1:1 (red) without (solid lines) and with (dash lines) the C_{70} protection layer. 139

Figure 6.6 (a) Time evolution of BQE- V_{bulk} characteristics of a control device at 80°C. Inset: time evolution of the V_{80} . (b) Time evolution of BQE- V_{bulk} characteristics of a buffered device at 80°C. Inset: time evolution of time evolution of the V_{80} . (c) Time evolution of V_{off} of control devices at various temperatures. (d) Time evolution of V_{off} of buffered devices at various temperatures. 141

Figure 6.7 (a) STEM image collected by a bright-field (BF) detector of a control device heated in the dark for 700 h at 80°C. (b) Zoomed in STEM image of the BHJ/ MoO_x interface collected by a low-angle annular dark field (LAADF) detector. (c) The EDS Cl weight concentration distributions of the as-cast device with a C_{70} layer, thermally aged device with a C_{70} layer and the thermally aged control device with the horizontal axis aligned to that in (a). (d) The Cl weight

concentration map near the BHJ/MoO _x interface with the horizontal axis aligned to that in (b).	143
Figure 6.8 X-ray photoelectron spectra (XPS) of the Mo 3d signal of MoO _x layers fabricated with a (a) PCE-10:BT-CIC 1:2 blend layer, held at room temperature (RT), (b) PCE-10:BT-CIC 1:2 blend layer, held at 90°C, (c) neat BT-CIC layer, held at RT, and (d) neat BT-CIC layer, held at 90°C for 100 h. XPS spectra of Cl 2p of MoO _x layers fabricated with a (e) PCE-10:BT-CIC 1:2 blend layer, held at RT, (f) PCE-10:BT-CIC 1:2 blend layer, held at 90°C, (g) neat BT-CIC layer, held at RT, and (h) neat BT-CIC layer, held at 90°C for 100 h.	144
Figure 6.9 Time evolution of J - V characteristics at 80°C of OPVs with ABL/CBL combinations of (a) PEDOT:PSS/TmPyPB, (b) MoO _x /BPhen, (c) PEDOT:PSS/PDINO.....	146
Figure 6.10 PCE time evolution under 80 °C of conventional structured OPVs with various ABL/CBL combinations.	146
Figure 6.11 Time evolution of BQE- V_{bulk} characteristics under 80 °C of the MoO _x _BPhen device. Inset: Time evolution of V_{off}	147
Figure 6.12 Schematic of the photo- and thermal degradation mechanisms related to the anode and cathode edges and interlayers to suppress them.....	149
Figure 6.13 (a) Time evolution of BQE- V_{bulk} characteristics under 80 °C of inverted PCE-10:BT-CIC device with the C ₇₀ anode protection layer and the IC-SAM cathode protection layer. Inset: Time evolution of V_{off} . (b) Time evolution of BQE- V_{bulk} characteristics of the same device under illumination of white light that is equivalent to 20 Suns. Inset: Time evolution of V_{off}	150
Figure 7.1 (a) Schematic of photocurrent mapping system. (b) Photocurrent distribution near the edge of a PCE-10:BT-CIC OPV device. (b) Photocurrent distribution along the Y axis for OPVs with and without a 2 nm C ₇₀ anode interlayer.	153
Figure 7.2 (a) Optical microscope image near the device edge where the MoO _x only extend out from the device area by 300 μm. (b) Photocurrent distribution of devices that: has full coverage of MoO _x along the Y direction (black), has partial coverage of MoO _x along the Y direction (red) and has no MoO _x coverage beyond the device area (blue), respectively.....	154
Figure 7.3 Photocurrent distribution near the device edge for (a) the as-cast device, (b) the device aged at 80°C for 44 h.	155
Figure 7.4 The J - V characteristics at various temperatures of (a) a control OPV device, (b) an OPV device with a IC-SAM between the BHJ and ZnO.....	156
Figure 7.5 (a) BQE- V_{bulk} characteristics of the device with IC-SAM at various temperatures. (b) The V_{off} and J_{sat} of the device with IC-SAM at various temperatures.....	157
Figure 7.6 A semi-transparent OPV module developed by the OCM group at University of Michigan, Ann Arbor. ²³⁸	159

Figure 7.7 Schematics of the ultraflexible, self-powered photoplethysmogram (PPG) sensor a human hand.²⁴⁷ 160

List of Appendices

Appendix A: Chemical Structures and Full Chemical Names of Molecules.....	161
Appendix B: Ultralong-Range Energy Transport in Disordered Organic Semiconductors at Room Temperature via Coherent Exciton-Polariton Propagation.....	170

List of Abbreviations

Acronyms

ABL	anode buffer layer
AFM	atomic force microscopy
AIL	anode interlayer
BF	bright field
BHJ	bulk heterojunction
BQE	bulk quantum efficiency
CB	conduction band
CBL	cathode buffer layer
CIL	cathode interlayer
CT	charge transfer
DFT	density functional theory
EDS	energy dispersive spectroscopy
EL	electroluminescence
EQE	external quantum efficiency
ETL	electron transporting layer

FC	Franck-Condon
FCC	face-centered cubic
FF	fill factor
FIB	focused ion beam
FRET	Förster resonant energy transfer
GIWAXS	grazing incidence wide-angle x-ray scattering
HJ	heterojunction
HOMO	highest occupied molecular orbital
HTL	hole transporting layer
IQE	internal quantum efficiency
ITO	indium tin oxide
J_{sat}	saturated photocurrent
J_{sc}	short-circuit current
J-V	current density-voltage
KMC	kinetic Monte Carlo
LUMO	lowest unoccupied molecular orbital
MPP	maximum power point
NFA	Non-fullerene acceptor
NIR	near infrared
OLED	organic light emitting diode
OPV	organic photovoltaic
OVPD	organic vapor phase deposition
PCE	power conversion efficiency

PL	photoluminescence
R2R	roll-to-roll
RT	room temperature
SEM	scanning electron microscopy
STEM	scanning transmission electron microscope
TDDFT	time dependent density functional theory
TEM	transmission electron microscope
UPS	ultraviolet photoelectron spectroscopy
UV	ultraviolet
VB	valence band
V_{oc}	open-circuit voltage
V_{off}	offset voltage
VTE	vacuum thermal evaporation
XPS	x-ray photoelectron spectroscopy
XRD	x-ray diffraction

Abstract

The field of organic semiconductors, with a history of over 70 years, has long been overshadowed by the mass industrial applications of inorganic semiconductors until the past decade, when high efficiency organic light emitting diodes (OLEDs) quickly grew in to a huge market with a \$40 billion annual revenue. The success of OLEDs has brought great attention from both the academia and the public to this group of materials. However, the performance of the organic photovoltaics (OPVs) has yet to meet the criteria as a player in the solar industry, popping a big question: what is missing for OPVs? In this thesis, the whole photogeneration process of OPVs is reviewed from nanoscopic mechanisms to macroscopic device performance, in a hope to provide guidelines towards high performance OPVs that can be commercially adopted.

The first part of this thesis is focused on the charge transfer (CT) states in organic bulk heterojunctions (BHJs). We use a combination of experimental, theoretical and computational methods to explore the optical and electrical properties of CT states and their relationship to molecular and morphological structures.

In the second part, we move from the BHJ to the edges of the OPV device and study the interfacial energy loss between the BHJ and peripheral layers. By studying the energy landscape near the interface, the interfacial energy losses are quantitatively characterized. A counterintuitive way to reduce the interfacial energy loss by up to 30% and improve the device open-circuit voltage is provided by growing a thin layer of acceptors on the anode side of the BHJ. With the

understanding of the interfacial voltage losses, we proceed to study the internal distribution of voltages on various layers of the OPV, which leads to the development of an analysis method that can separate the properties of the BHJ of and OPV from the peripheral structures by calculating its “bulk quantum efficiency” (BQE).

The third part of this thesis presents studies of the photo- and thermal stability of OPVs. A major part of the effort is focused on non-fullerene acceptor (NFA) based OPVs which currently provide the highest efficiencies. With the help of various experimental tools and the BQE analysis, we characterize various degrading mechanisms that limit NFA-based OPV stabilities. In Chapter 5, we show that photocatalytic reaction between BHJ and ZnO is a major cause to device photodegradation. A self-assembled monolayer between the BHJ and ZnO can effectively suppress this reaction. We also show that UV-induced damage to the BHJ is another source of photodegradation and a low-cost UV-absorbing coating is proposed to suppress it. As a result, a projected operational lifetime over 30 years is achieved. In Chapter 6, we show that thermally activated Cl redistribution in BHJ driven by a redox reaction at the BHJ/MoO_x interface leads to a check-mark shaped thermal degradation pattern. A thin layer of C₇₀ inserted between BHJ and MoO_x can effectively suppress this mechanism, significantly improving the device T₈₀ lifetime at 80°C from 20 min to 800 h. With these results, we achieve an OPV structure with excellent photo- and thermal stability, making one big step toward the commercial adoption of OPV.

In the last part, several unanswered questions are introduced with preliminary experimental results and proposals are made for future studies around understanding and improving OPV performance. In the end, an outlook for OPV devices is presented.

Chapter 1

Introduction

1.1 Overview

It has been over 70 years since the field of organic semiconductors was founded,¹⁻⁵ and over 30 years since the first organic optoelectronic devices were fabricated.⁶⁻⁷ However, organic optoelectronics only started to draw heavy public attention over the past decade due to the vast success of organic light-emitting diodes (OLEDs).⁷⁻¹⁵ After dominating the whole mobile phone screen market, OLEDs continue to expand their applications in the illumination and display industries. The unique properties of organic semiconductors grant many advantages to OLEDs, including high efficiency, high resolution, wider color range, flexibility, and transparency.¹⁶⁻²⁴ Figure 1.1 (a) and (b) show two examples of unique applications of OLEDs.

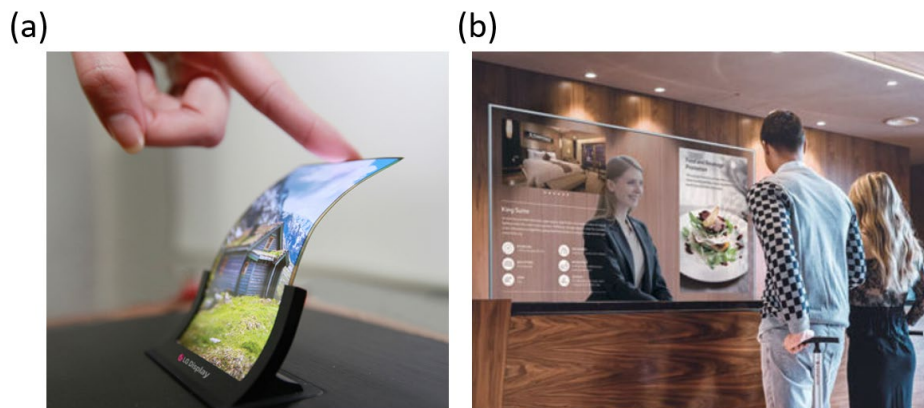
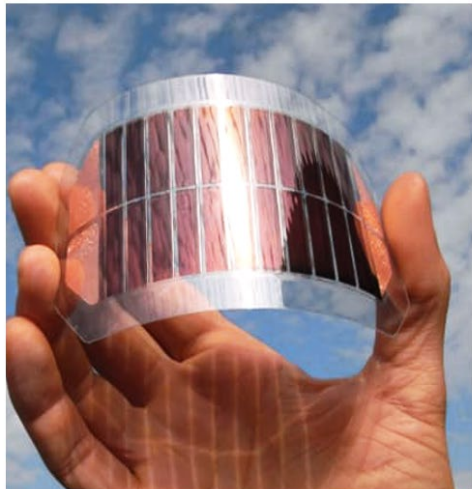


Figure 1.1 (a) A flexible OLED screen developed by LG Display. (b) Transparent OLED display at a hotel front desk allows agents to provide helpful information while maintaining in-person contact with guests. Images are from internet.

The success of OLEDs also draws attention from the fundamental science community to this unique group of materials. As theoretical and experimental methodologies are developed, the quantum mechanical understanding of organic semiconductors is rapidly advanced.²⁵⁻²⁸

Another member of the organic optoelectronic family, organic photovoltaic (OPV) cells, shares many of the advantages of OLEDs.²⁹⁻³³ Figure 1.2 (a) and (b) shows examples of flexible and semi-transparent OPVs, respectively. These advantages grant OPV the potential to have a share in the rapidly growing solar market. However, the biggest obstacle between OPVs and commercial applications, is their relatively low power conversion efficiency (PCE) and stability compared to solar cells based on traditional semiconductors. Although the OPV PCE has increased dramatically from a few percent to over 18% in recent years,³⁴⁻³⁶ it is still lower than solar cells based on perovskite (>22%)³⁷⁻³⁸ and inorganic semiconductors (>25%),³⁹⁻⁴⁰ In this chapter, we review the fundamentals of organic semiconductors and OPVs that are required for following chapters.

(a)



(b)



Figure 1.2 (a) A flexible OPV module developed by Toyobo Co., Ltd. (b) View through a color-neutral semi-transparent OPV developed by OCM group at University of Michigan.⁴¹

1.2 Properties of Organic Semiconductors

Although sharing the name of “semiconductor”, organic semiconductors share few similarities with traditional inorganic semiconductors. Table 1.2.1 compares some of the properties of organic and inorganic semiconductors. Their vastly different properties arise from the difference in fundamental structures of the materials. In this section, we review the unique properties of organic semiconductors and their physical and chemical origins, which are important for understanding the working principles of OPVs.

Table 1.1 Comparison of properties of organic and inorganic semiconductors.⁴²

Property	Organics	Inorganics
Bonding	van der Waals	Covalent/Ionic
Charge Transport	Polaron Hopping	Band Transport
Mobility	<0.1 cm ² /V·s	~1000 cm ² /V·s
Absorption	10 ⁵ -10 ⁶ cm ⁻¹	10 ⁴ -10 ⁵ cm ⁻¹
Excitons	Frenkel	Wannier-Mott
Binding Energy	~500-800 meV	~10-100 meV
Exciton Radius	~10 Å	~100 Å

1.2.1 Organic molecules

Organic semiconductors are ensembles of organic molecules, which are based mainly on carbon and hydrogen atoms, with a few atoms of other elements. The molecular structures are the dominating factors for interaction with the optical field, thus crucial for optoelectronic applications. The organic molecules used in organic optoelectronic devices are generally classified into two types: small molecules and polymers. Small molecules are isolated molecules with relatively small molecular weights (usually < 1,000 u). Figure 1.3(a) shows an example of the fullerene small molecule C₇₀, which is commonly used as an acceptor in vacuum deposited OPVs. Although strictly speaking, fullerenes like C₆₀ and C₇₀ are not organic molecules since they do not contain hydrogen, they are often considered organic due to similar properties. Polymers consist of chains of repeating units. The molecular weights of polymers are usually very large and uncertain. Figure 1.3 (b) shows an example of a polymer, PCE-10, which is commonly used as a donor in solution processed OPVs.⁴³⁻⁴⁴

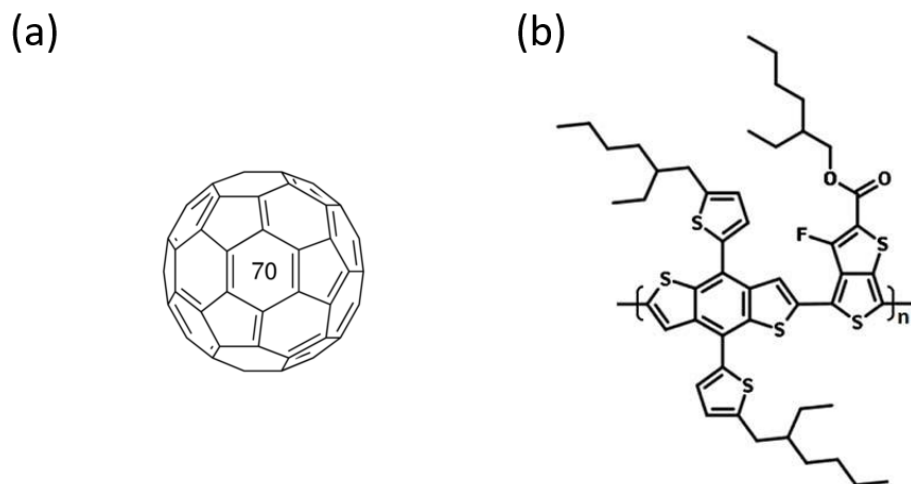


Figure 1.3 (a) Chemical structure of a small molecule, C₇₀. (b) Chemical structure of a polymer, PCE-10.

In contrast to inorganic semiconductors, where frontier electrons occupy periodic band states, frontier electrons in organic semiconductors occupy localized “orbitals”. Two especially important orbitals are the highest occupied molecular orbital (HOMO) and the lowest unoccupied molecular orbital (LUMO). The HOMO is analogous to the valence band in inorganic semiconductors, usually the ground state. The LUMO is analogous to the conduction band in inorganic semiconductors, usually the excited state for optical transitions. Figure 1.4(a) and (b) shows the electron density distributions of the HOMO and LUMO of DBP, a small molecule used as a donor in vacuum deposited OPVs. The calculation is done by density functional theory (DFT), which is an approximation for the multibody Schrödinger equation. Although the electron density distribution of the LUMO is different from that of the HOMO, it is still closely confined to the molecular skeleton, causing an excited electron to be closely bonded to the original molecule.

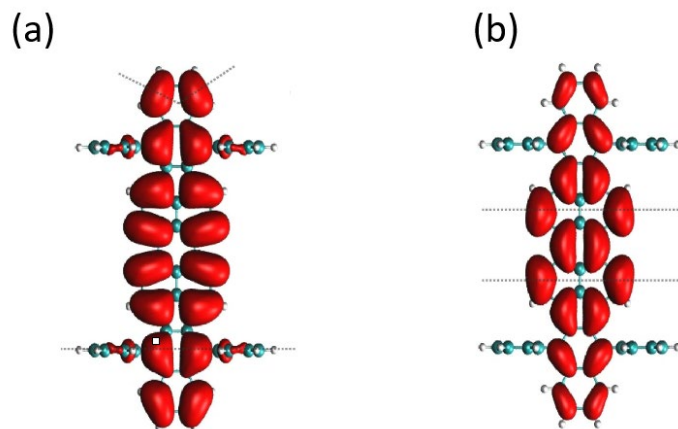


Figure 1.4 Electron density distribution of the (a) HOMO and (b) LUMO of a DBP molecule calculated by density functional theory (DFT).⁴⁵

One advantage brought by the confined electron states, is the high color tunability.⁴⁶⁻⁴⁷ The excitation energies of organic molecules are highly sensitive to the molecular structure, making it possible to cover targeted section of the solar spectrum. Figure 1.5 (a) shows the solutions of molecules with various colors. Molecular structures of several of them are shown in Fig. 1.5 (b). The normalized absorption spectra are shown in Fig. 1.5 (c).

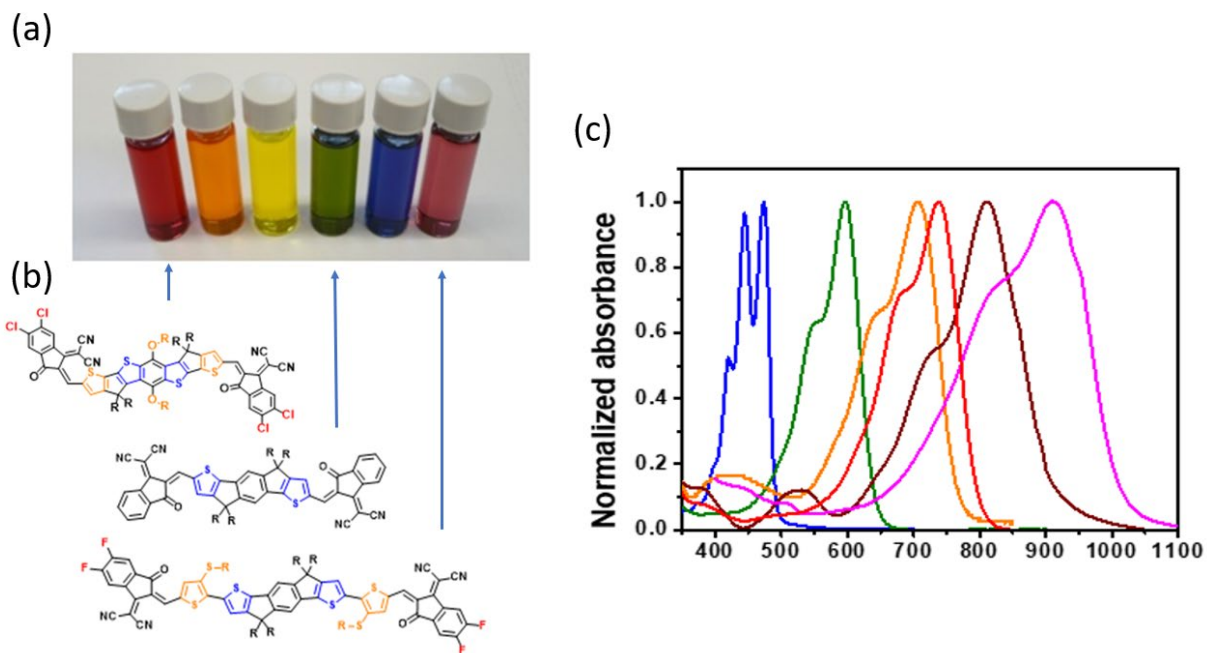


Figure 1.5 (a) Solutions (b) molecular structures and (c) normalized absorption spectrum of molecules with various colors.⁴⁸

1.2.2 Organic films

In organic semiconductors, the organic molecules are bonded together by van der Waals forces. Although much weaker than the covalent bonds in inorganic semiconductors, van der Waals force is the reason that organic semiconductors exist as solids at room temperatures. Some molecules can even form molecular crystals via the van der Waals force.⁴⁹ Figure 1.6 (a) shows the unit cell of a face-centered cubic (FCC) crystal of C_{70} . A transmission electron microscopic (TEM) image of a C_{70} crystal is shown in Fig. 1.6 (b).⁵⁰

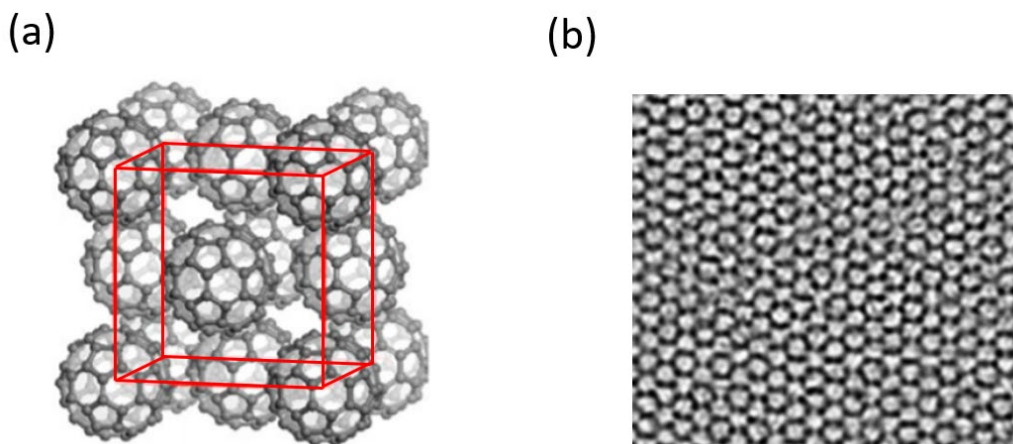


Figure 1.6 (a) Unit cell of C_{70} crystal. (b) TEM image of C_{70} crystal.⁵⁰

The intermolecular van der Waals force defines the thermal and mechanical properties of organic semiconductors, making them flexible, stretchable and compatible with vapor-phase fabrication.⁵¹

1.2.3 Optical properties

For optoelectronic applications, the most important property of organic semiconductors is their optical characteristics. As introduced in Section 1.2.1, the HOMO and LUMO are the ground and excited states for the optical excitation of the lowest energy. The energy difference between the HOMO and LUMO is the energy gap of organic semiconductors, analogous to the band gap of inorganic semiconductors. The HOMO-LUMO energy gap is only the smallest energy for optical excitation (light absorption), while the emission energy can be lower than the energy gap, as will be discussed below.⁵²⁻⁵⁴

Once excited, the atomic skeleton of the molecule will experience reconfiguration, also known as relaxation, due to changes in the electron orbitals. As a result, the energies of all orbitals are changed too. After the relaxation, the excited state is called the exciton state. Because the

excitons can be transferred among molecules, they are often regarded as pseudo particles. Depending on the magnitude of binding energy and charge distribution, there are three types of excitons, as shown in Fig. 1.7. The most common type is Frenkel excitons in organic materials.⁵⁵ Frenkel excitons have the highest binding energy (>200 meV) and the most localized wavefunction (usually confined to one or a few molecules).⁵⁶ Charge transfer (CT) excitons or CT states are shared between molecules with an energy level difference where the electron and hole are spatially separated.⁵⁷ CT states will be further discussed in Section 1.3.1. The Wannier-Mott excitons are delocalized state with small binding energies ($\ll 100$ meV).⁵⁸ They are usually observed in inorganic crystals at low temperatures. Here we focus on the Frenkel excitons, which are the direct products from light absorption in organic semiconductors.

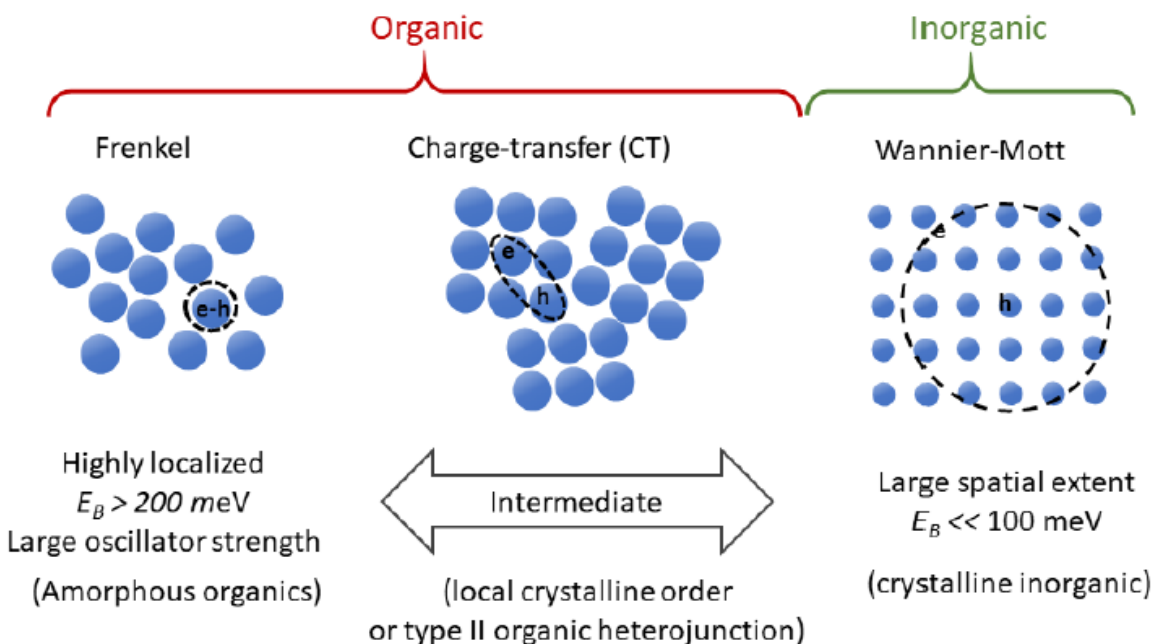


Figure 1.7 Three types of excitons and their different properties.

Because of relaxation, the emission energies of the exciton states are smaller than the optical gap, causing a red shift of the emission spectrum compared with the absorption spectrum.

This red shift is as known as the Franck-Condon shift or Stokes shift.⁵⁹ Figure 1.8 (a) shows the energy levels of molecular orbitals in the ground and excited state. In an exciton directly excited upon light absorption, the excited electron in the LUMO and the remaining electron in the HOMO have opposite spins. This is determined by the selection rules of optical transition. These excitons are singlets. However, it is possible for the two electrons to have the same spin, making the exciton a “dark state” for the optical transition. These excitons are triplets. Triplet excitons have lower energies than singlet excitons and play an important role in OLEDs.⁶⁰⁻⁶¹ However, for OPV applications, we focus on singlet excitons which interact with the optical field.

Another important feature of the absorption and emission spectra of organic molecules is the vibronic states. Although the dominating factor of the electron energy is the orbital it occupies, there are additional levels in the ground and excited state manifolds due to the vibration of the molecular structure. The energy separations between vibronic states are determined by the covalent bonding strengths in the molecule. These states are often described by an analogous harmonic oscillator in a pseudo space determined by the configuration coordinate, Q , which represents the atomic configuration of the entire molecule. Figure 1.7(b) shows the ground and excited manifolds vs. the configuration coordinate. Each vibronic level is labeled by its quantum number. Absorption and emission spectra of DBP are indicated on the left. The difference between the 0→0 peaks of the absorption and emission spectra is the Stokes shift.

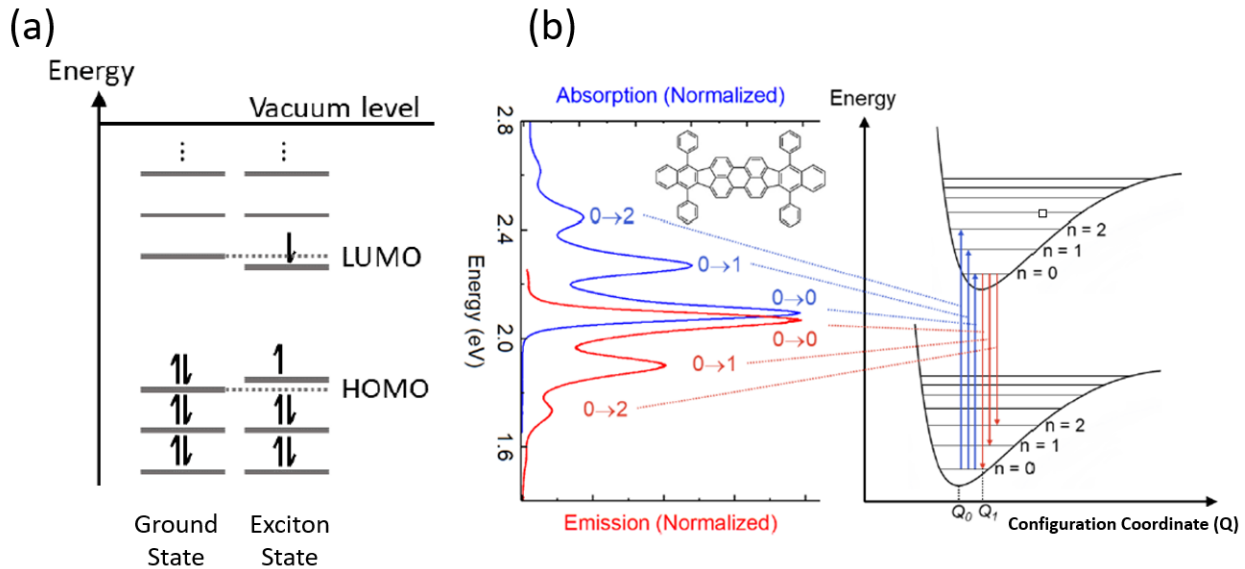


Figure 1.8 (a) Energy levels of orbitals in the ground state and exciton state with the electron occupation denoted by arrows pointing up (spin up) or down (spin down). (b) Ground and exciton state potentials vs. the configuration coordinate. Each vibronic level is labeled by its quantum number. Absorption and emission spectra of DBP are indicated on the left.⁴²

Due to the large overlap between the ground and excited state electron wavefunctions, the optical transition dipole moment is much larger compared with inorganic semiconductors. This leads to strong absorption, making it possible to fabricate OPV devices with active layers only tens of nanometers thick that can absorb most of incident light.³¹

1.2.4 Exciton transfer

As mentioned before, excitons are pseudo particles that can transport energy among molecules. There are three types of exciton transfers: Dexter transfer,⁴ Förster resonant energy transfer (FRET),³ and radiative transfer, as shown in Fig. 1.9.

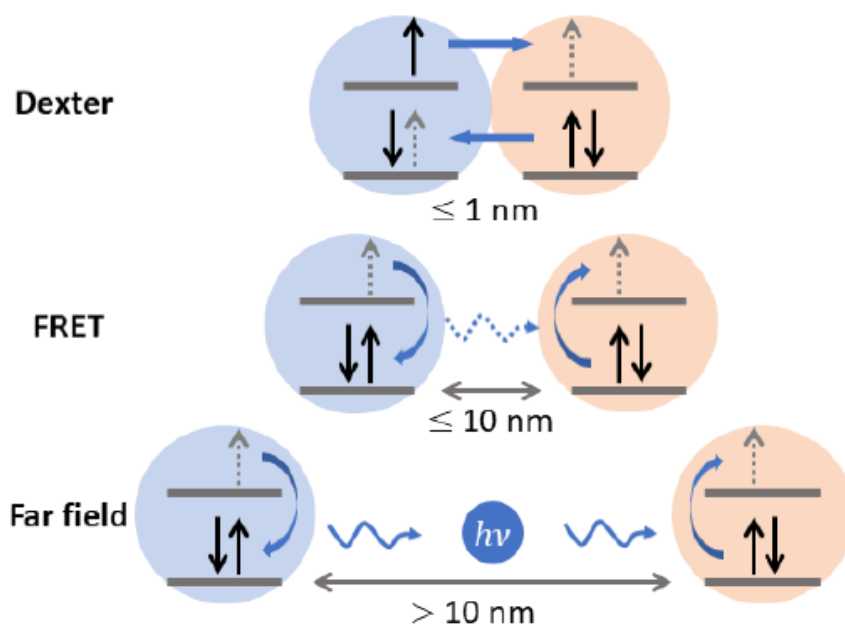


Figure 1.9 Three types of exciton transfer.

Dexter transfer is near field transfer and usually happen between adjacent molecules whose molecular orbitals overlap. Since Dexter transfer is an electronic interaction, it is not restricted by the selection rule of optical transitions, allowing either the same or different spin multiplicities of initial and final states, while the total spin is conserved. The transfer rate is directly proportional to the overlap integral between the initial and final states. The typical range for Dexter transfer is at the order of 1 nm.

FRET transfer originates from non-radiative resonant dipole-dipole coupling. It is often understood as the emission and absorption of a “virtual photon”. Although there is no coupling to the optical field, FRET transfer obeys the same selection rule of the optical transition and can only happen for singlet excitons. The range of FRET is longer than Dexter transfer but is still considered a near-field interaction (<10 nm).

Radiative transfer is essentially the emission and re-absorption of a photon. It happens at a much longer distance (>50 nm).

1.2.5 Electronic properties

As mentioned before, in contrast to the periodic band states in inorganic semiconductors, electrons in organic semiconductors occupy localized orbitals. The lack of a broad conduction band results in a charge mobility 4 orders of magnitude lower than inorganic semiconductors.^{42, 62} With that said, current flow is still possible through hopping and tunneling.⁶³

The first concept to learn about charge transport in organic semiconductors, is the polaron.⁶⁴⁻⁶⁵ Similar to the case in an exciton where an excited electron causes a relaxation of the molecular configuration, a net charge in organic semiconductors also causes the reconfiguration of the surrounding molecules. Figure 1.10 shows a schematic diagram of an electron placed in a polarized molecular crystal. The dipoles of surrounding molecules are oriented according to the electric field of the electron, to effectively screen out its electric field. Compared with free charge carriers in energy bands, polarons have much lower mobilities and much larger effective masses.⁶⁶

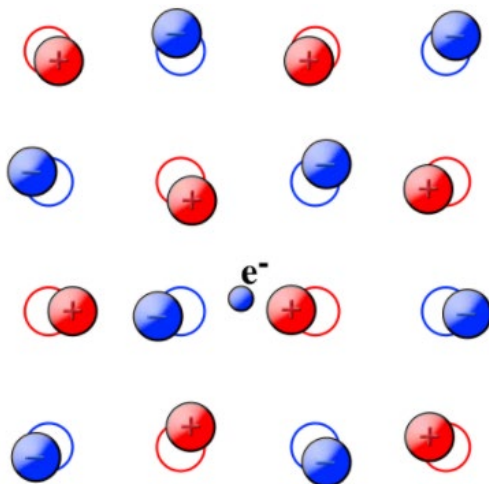


Figure 1.10 Schematic diagram of an electron placed in a polarized molecular crystal. Due to the electric field from the electron, the dipoles of the molecules are oriented to screen the electron.⁶⁷

Polarons do not occupy isolated molecular orbitals, but usually a superposition of several orbitals of neighboring molecules, allowing them to transport between molecules.⁶⁸ The polaron transport is enhanced along the chains of polymers.⁶⁹⁻⁷² The energy of a polaron is broadened by its disordered environment (~ 100 meV)⁷³⁻⁷⁴, which complicates the interfacial charge transfer process between layers, as will be discussed in Chapter 3.

1.3 Fundamentals of Organic Photovoltaics

As the “reverse” device of an OLED, an OPV converts light to electrical power. With the success of OLEDs, people naturally believe that OPV will be the next to be commercially adopted. However, it has not been the case up until now. The commercial application of OPVs is limited when their PCEs in laboratory conditions struggle to break 20%. Here we review the fundamental concepts of OPVs from photogeneration to device design and fabrication, in hopes to understand the potential and limits of OPVs.

1.3.1 Charge transfer states

Light absorption in organic semiconductors generates excitons instead of free charge carriers. The large binding energy of Frenkel excitons (~ 0.1 eV) prevents the electron and hole polarons to separate to generate photocurrent. Therefore, the active layers of OPVs usually consist of two molecules with different HOMO and LUMO energies, the acceptor and the donor. When an exciton diffuses to the donor/acceptor (D/A) interface, due to the energy level difference, the electron tends to occupy the LUMO of the acceptor while the hole occupies the HOMO of the donor.⁷⁵ The exciton is thus dissociated. However, due to the localized property of polarons, the spatially separated electron and hole can still be bond through Coulombic force across the

interface. This bonded pair of electron and hole polarons is the CT state. The CT states can also be directly excited by the optical field.⁷⁶ The CT excitation can either separate into polarons and contribute to the photocurrent, or recombine, emitting a photon with an energy smaller than the exciton. The CT state is closely related to device open-circuit voltage and has been one of the major focus of organic optoelectronic research.⁷⁶⁻⁷⁸ Figure 1.11 shows the successive steps of the photogeneration process. Every step has a possibility to lose the energy of the initial absorbed photon.

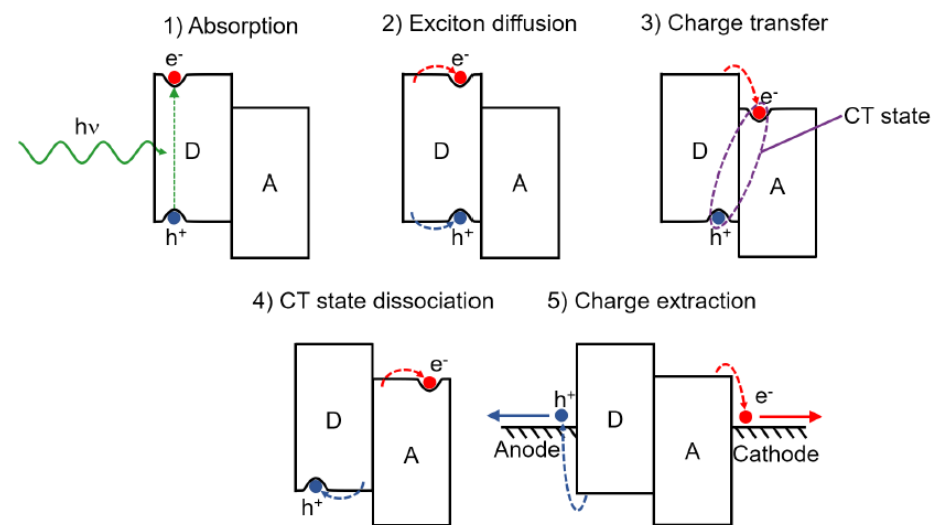


Figure 1.11 Schematics of successive steps of the photogeneration process in OPVs.

1.3.2 Organic bulk heterojunctions

One of the problems faced by OPVs in the early years, is the short diffusion length of excitons.⁷⁹⁻⁸⁰ As mentioned in Section 1.3.1, for an exciton to dissociate into a CT state, it must first diffuse to a D/A interface before recombination. This limits the active thickness to the same order of magnitude as the exciton diffusion length (~ 10 nm)⁸¹ for conventional planar heterojunctions. However, although organic semiconductors have strong absorption, the typical

absorption depth (~ 100 nm) is one order of magnitude larger than the exciton diffusion length. This fundamental tradeoff between absorption and diffusion significantly limited the OPVs performance until bulk heterojunctions (BHJs) were introduced,⁸²⁻⁸³ in which donor and acceptor molecules are mixed, as shown in Fig. 1.12. In organic BHJs, the distance an exciton needs to travel to find a D/A interface is significantly reduced, allowing exciton diffusion efficiency to approach unity even in thick active layers. This structure, however, results in significant recombination losses inside the BHJs, which will be discussed in Chapter 4.

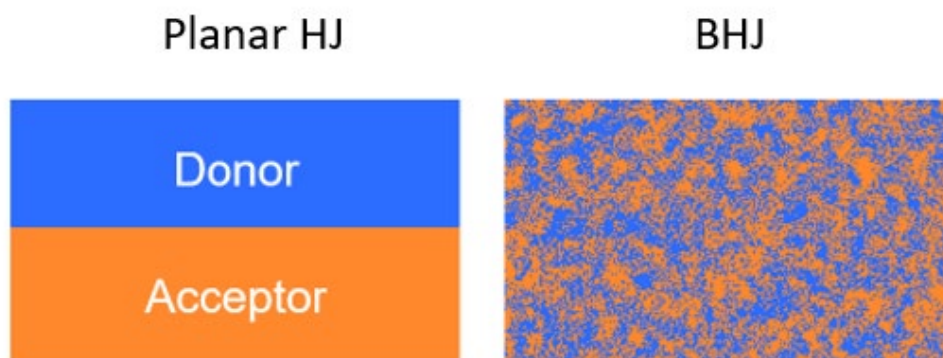


Figure 1.12 Schematics of a planar HJ and a BHJ.

1.3.3 Device architectures

Since the BHJ is a mixture of donor and acceptor molecules, there is no macroscopic orientation between them. The rectification of OPVs is due to carrier selective buffer layers. As shown in Fig. 1.13 (a), a typical OPV has the BHJ sandwiched between two buffer layers, an electron transporting layer (ETL) on the cathode side and a hole transporting layer (HTL) on the anode side. Usually, one of the electrodes is transparent, allowing incident light to reach the BHJ. The ETL usually has a HOMO or valence band below the donor HOMO, rejecting the holes in the BHJ. The HTL usually has a LUMO or conduction band above the acceptor LUMO, rejecting the

electrons in the BHJ. However, this is not always the case as will be discussed in Chapter 4. Figure 1.11(b) shows the energy diagram of a typical OPV. Due to the buffer layers, the photogenerated electrons can only be collected at the cathode while the photogenerated holes can only be collected at the anode.

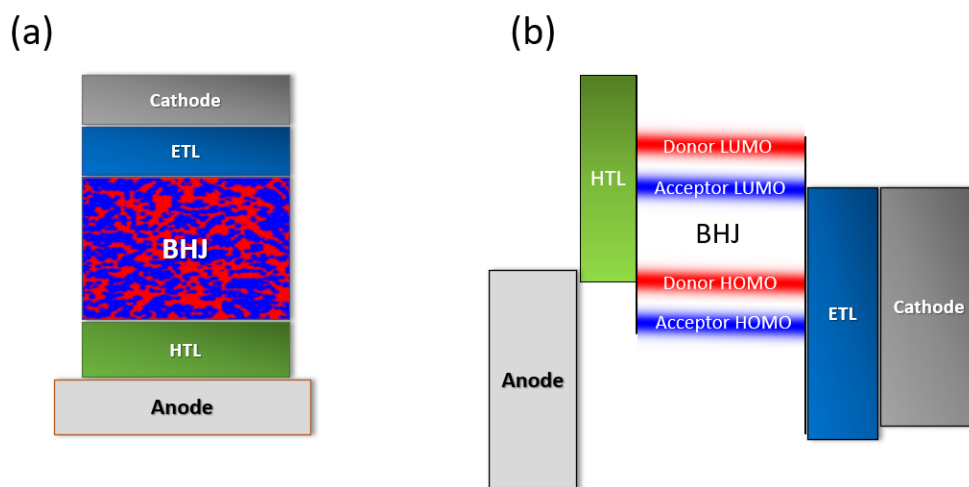


Figure 1.13 (a) Typical structure of an OPV. (b) Energy diagram of the OPV in (a).

A single cell structure in Figure 1.13 faces a fundamental tradeoff between the energy gap and the device voltage. Since the BHJ can only absorb photons with energy higher than the energy gap, a smaller gap would benefit the absorption. However, the device output voltage is limited by the HOMO-LUMO offset of the BHJ, which is in turn limited by the energy gap. A smaller energy gap would result in larger voltage loss. Therefore, a single cell works best for light with photon energies close to the energy gap. However, OPVs absorb the entire solar spectrum, significantly limiting single cell OPV efficiency.

To overcome this tradeoff between absorption and voltage, tandem OPVs are employed. As shown in Fig. 1.14, a tandem OPV contains two or more subcells connected in series. Each subcell has the energy gap designed to absorb a certain part of incident light. The different types

of charge carriers from neighboring subcells recombine in the charge recombination zone that balances the current in the tandem OPV.

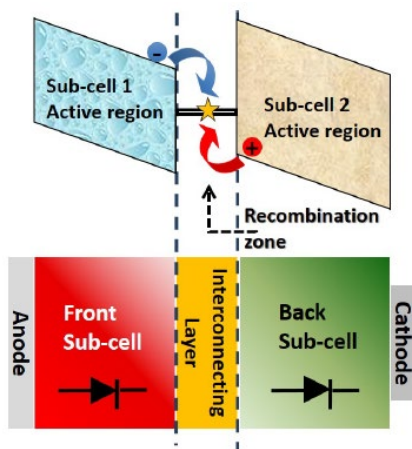


Figure 1.14 Working principle of a tandem OPV with two subcells connected in series.⁸⁴

Figure 1.15 shows the $J-V$ characteristics of a tandem OPV and its two subcells. The voltage of the OPV is the sum of the voltages of all subcells while the current is limited by the subcell with the lowest current. Therefore, balancing the currents of subcells is essential for achieving high tandem OPV efficiency. This design allows a tandem cell to have a broad absorption spectrum without suffering from significant voltage loss.

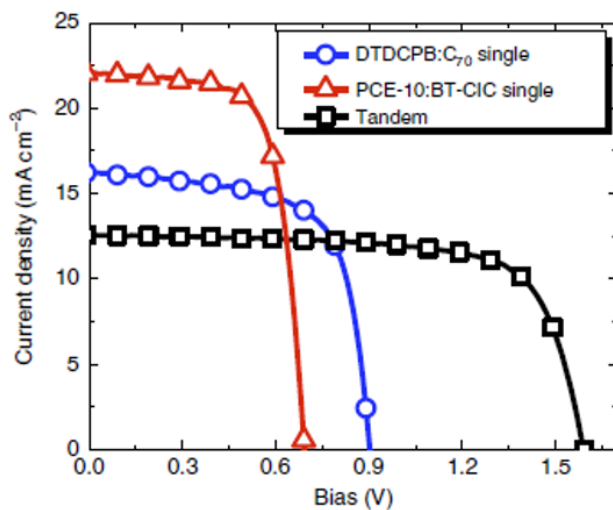


Figure 1.15 $J-V$ characteristics of a tandem OPV device and its two single-junction subcells.⁴⁴

1.3.4 Performance characterization

The current density-voltage (J - V) characteristic is the most important feature of an OPV since it determines the PCE. Figure 1.16(a) shows the dark and illuminated J - V characteristics of an OPV. The photocurrent, J_{ph} , is calculated as the difference between the dark current, J_d , and the illuminated, or total current, J . The maximum power point (MPP) is determined by maximizing the area of the grey square. The fill factor (FF) is calculated as:

$$FF = \frac{V_{MPP} \times J_{MPP}}{V_{oc} \times J_{sc}}, \quad (1.3.1)$$

where V_{MPP} and J_{MPP} are the voltage and current density at the MPP, V_{oc} is the open-circuit voltage, and J_{sc} is the short-circuit current density. The FF, V_{oc} and J_{sc} are the three commonly used metrics to characterize solar cell performance.

For comparison, the dark and illuminated J - V characteristics of a silicon solar cell are shown in Fig. 1.16(b). The J_d of silicon solar cells follow the famous Shockley diode equation:⁸⁵

$$J_d(V) = J_s \left[\exp\left(\frac{qV}{nkT}\right) - 1 \right], \quad (1.3.2)$$

where J_s is the reverse bias saturation current, n is the ideality factor, k is the Boltzmann constant, T is the temperature. The J_{ph} of the silicon cell is almost a constant due to the efficiency charge collection via band transport. As a result, the illuminated J - V characteristic have the exact shape as the J_d - V characteristic except for a constant offset. This makes the dark current J_d and the related quantity, ideality factor n , closely relevant to the PCE of inorganic solar cells.

For OPVs, the J_d - V characteristics are found to fit Eq. (1.3.2) too.⁸⁶⁻⁸⁷ However, as seen in Fig. 1.16(a), due to recombination loss inside the BHJ, the J_{ph} show a strong voltage dependence.

The MPP is almost entirely determined by the shape of the $J_{ph} - V$ characteristic. This point will be further discussed in Chapter 4.

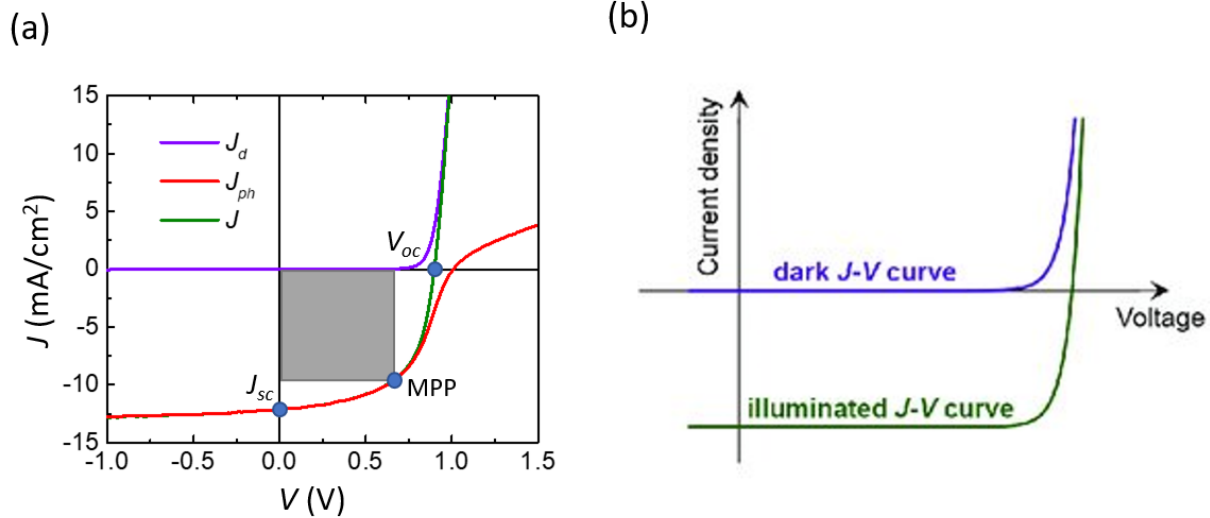


Figure 1.16 (a) Dark and illuminated (green) J - V characteristics of an OPV device and the photocurrent, J_{ph} (red), which is calculated as the difference between the dark current J_d (purple) and illuminated current J (green). (b) Dark and illuminated J - V characteristics of a silicon solar cell.

When the buffer layers or electrodes have poor conductivity, solar cells can suffer from series resistance.⁸⁸ Figure 1.17 shows the J - V characteristics of OPVs with various series resistance. When the series resistance increases, both J_{sc} and FF decrease, while V_{oc} remains the same.

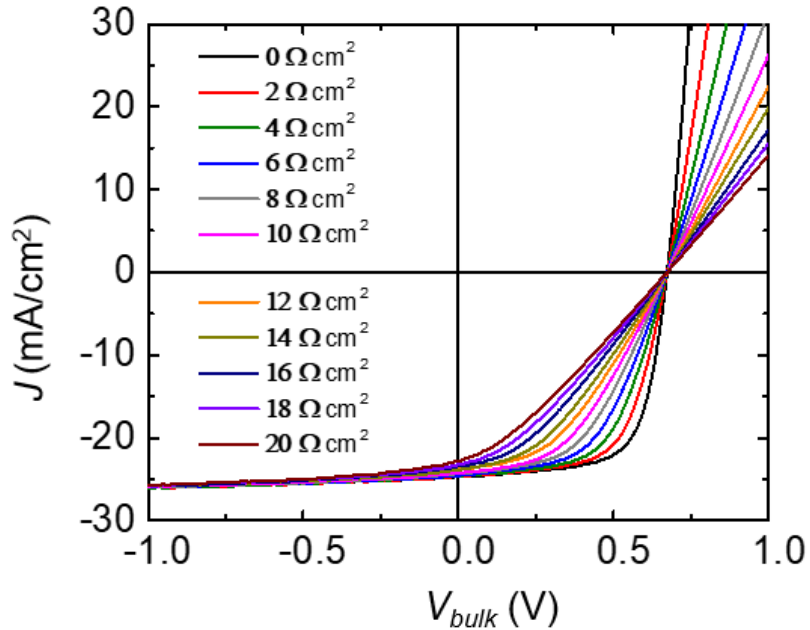


Figure 1.17 J - V characteristics of an OPV with various series resistances.

Although the J - V characteristic determines the PCE of an OPV, it provides limited information about the wavelength dependent OPV performance, which is important for designing and optimizing the active layer materials. For this purpose, the external quantum efficiency (EQE) is introduced. EQE measures the efficiency to extract a pair of photogenerated charges per incident photon of a certain wavelength. EQE is wavelength dependent. Figure 1.18 shows an EQE measurement setup. A white light source is monochromated and modulated by a chopper. The light is then focused onto the OPV via an optical fiber. A lock-in current amplifier is then used to measure the photocurrent from the device.

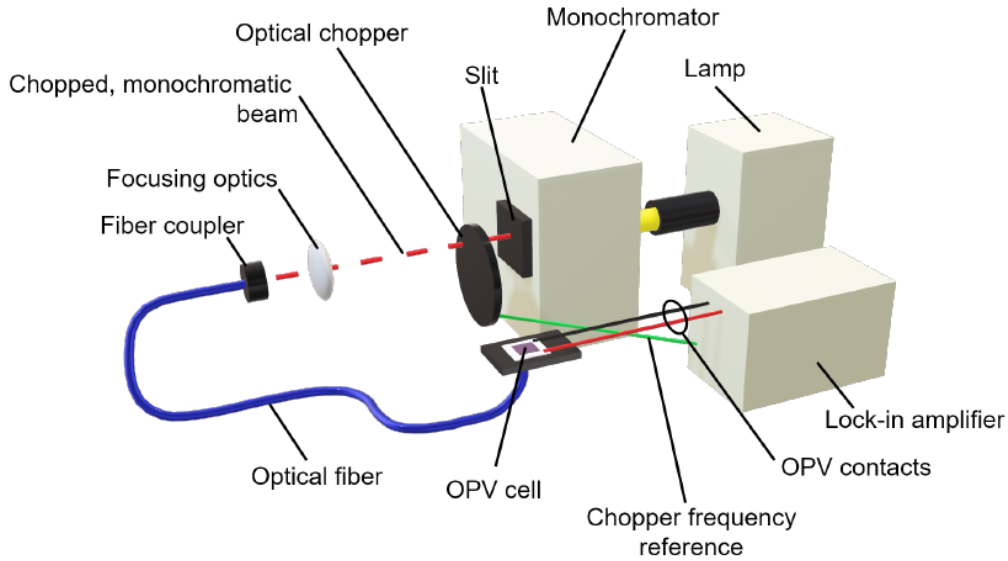


Figure 1.18 Experimental setup to measure the EQE.

Physically, the EQE accounts for losses in all the steps in the photogeneration process in Fig. 1.11. It is often expressed as:

$$EQE = \eta_A \times \eta_{diff} \times \eta_{diss} \times \eta_{cc}, \quad (1.3.3)$$

where η_A is the absorption efficiency, η_{diff} is the diffusion efficiency, η_{diss} is the dissociation efficiency, η_{cc} is the charge collection efficiency. For OPVs with BHJs, the η_{diff} is close to unity. The voltage dependence of the photocurrent is mainly caused by η_{diss} and η_{cc} as will be discussed in Chapter 4.

Figure 1.19 shows the EQE spectra of OPV devices with DBP as the donor and C_{70} as the acceptor with various DBP concentrations. The absorption spectra of DBP and C_{70} are also plotted. The shape of EQE is closely related to the absorption of the donor and the acceptor as the DBP absorption peaks show in the devices with high DBP concentrations.

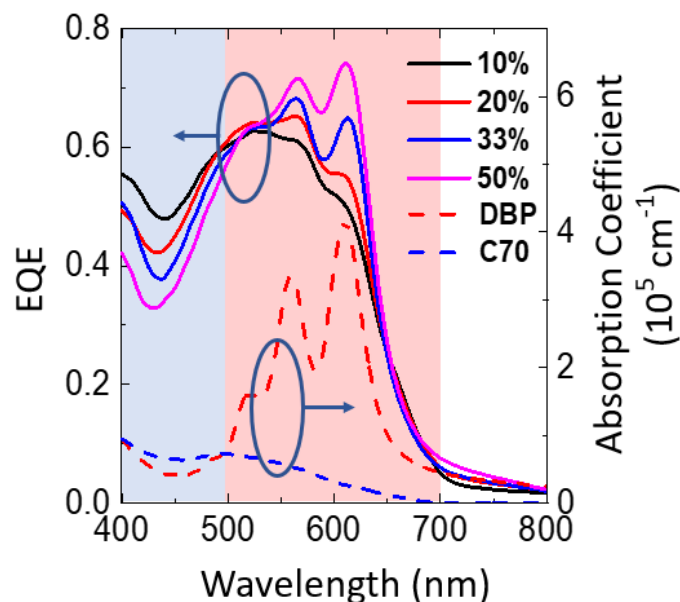


Figure 1.19 EQE spectra of DBP:C₇₀ OPVs with various DBP concentrations (left axis). Also plotted are the absorption spectra of DBP and C₇₀ (right axis).

The current of a tandem OPV, as mentioned in Section 1.3.3, is limited by the subcell with the smallest current. However, in EQE measurement, monochromatic illumination which is only absorbed in one of the subcells. Therefore, traditional EQE measurements are not applicable to tandem OPVs. In this case, a bias light source is required to achieve current balance in the tandem OPV.⁸⁹

1.3.5 Device fabrication

Due to the weak van der Waals bonds between molecules, many small molecule organic semiconductors have lower sublimation temperatures than their chemical decomposition temperatures, allowing them to be deposited by vacuum thermal evaporation (VTE), where organic materials are heated in a vacuum chamber into vapor phase and deposited onto the substrate. Figure 1.20 shows a schematic of a VTE deposition system. The thickness of the deposited film can be

monitored in-situ by quartz crystal monitors, allowing fine control of film thickness. VTE provides high material purity and allows the fabrication of complex structures, such as BHJs with gradient D/A ratios or alternating quantum wells.⁹⁰⁻⁹¹

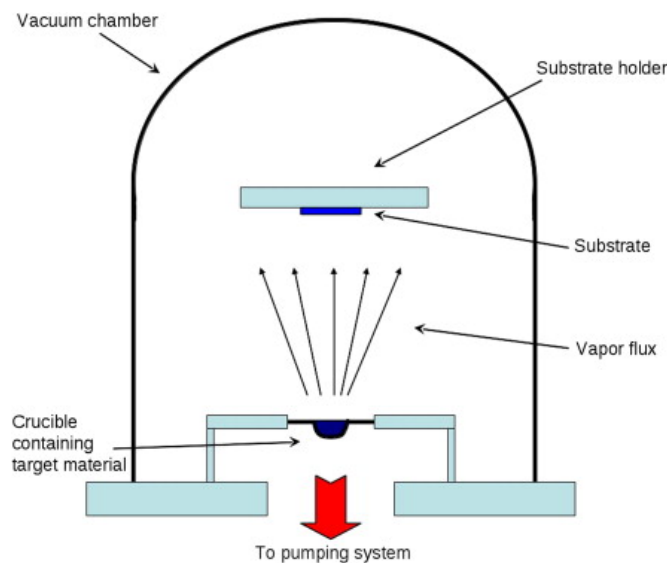


Figure 1.20 Schematic of a typical VTE system.

However, not all organic materials can be fabricated using VTE. For polymers and molecules with large molecular weight or low decomposition temperatures, spin coating is required. In this method, organic materials are dissolved in a solvent and then applied onto the substrate which is fixed on a spin stage. The spin stage rotates at a high speed, causing the solution to spread into a uniform film while the solvent evaporates. Figure 1.21 shows the steps of spin coating. While this method is convenient and inexpensive, the purity of fabricated film is lower compared to VTE since the process is not performed in vacuum. This method also suffers from the weak control of film thickness.

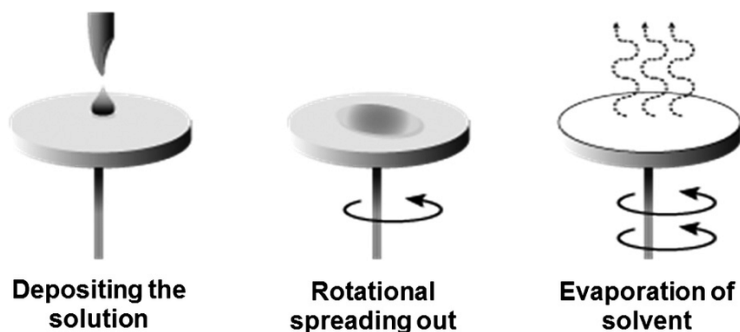


Figure 1.21 Illustration of steps of spin coating.

Another fabrication method for organic semiconductors is organic vapor phase deposition (OVPD).⁹²⁻⁹⁴ It differs from VTE in that the target molecules are evaporated into a hot inert carrier gas instead of vacuum. Figure 1.22 shows an illustration of a OVPD chamber. OVPD brings more control over the morphology of the deposited film by controlling the pressure, flow rate of the carrier gas and temperatures of the source cell and the substrate. Figure 1.23 shows the various surface morphologies achieved by OPVD at various source cell temperature/substrate temperature combinations.

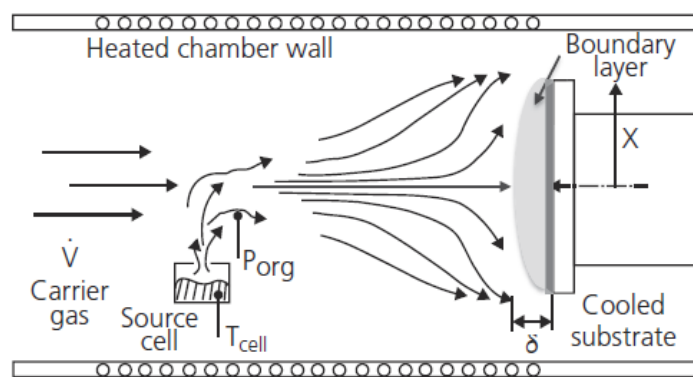


Figure 1.22 Schematic diagram of an OVPD chamber. The source material in the source cell is heated and evaporate into the inert carrier gas stream. The source molecules are carried in a hot-walled chamber by the carrier gas to a cooled substrate where they are physisorbed.⁹⁵

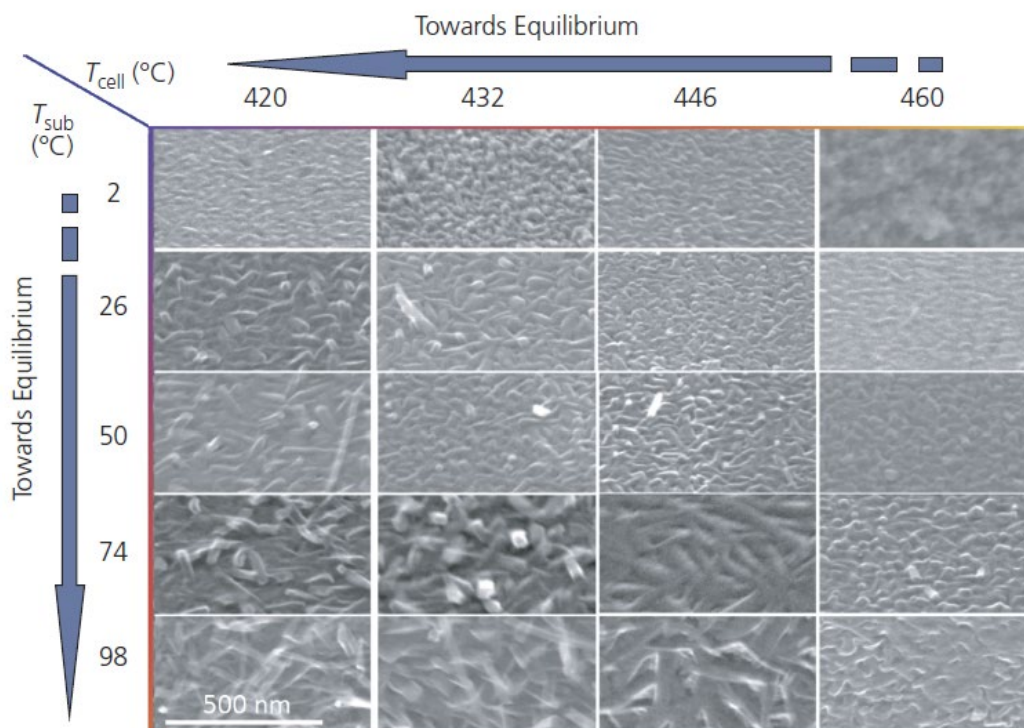


Figure 1.23 Scanning electron microscope (SEM) images of CuPc film surface morphology deposited by OPVD with various parameters.⁹⁶

The most promising technique to fabricate organic electronic devices, is roll-to-roll (R2R) fabrication, where circuits and electronic devices are rapidly “printed by the meter”.⁹⁷⁻⁹⁹ This technique fully utilizes the flexible properties of organic semiconductors and promises low-cost for their mass adoption. Figure 1.24 shows a schematic of R2R fabrication of organic devices.¹⁰⁰ However, a major challenge faced by R2R technique is the low manufacturing yield. To improve this, precise patterning techniques must be improved.

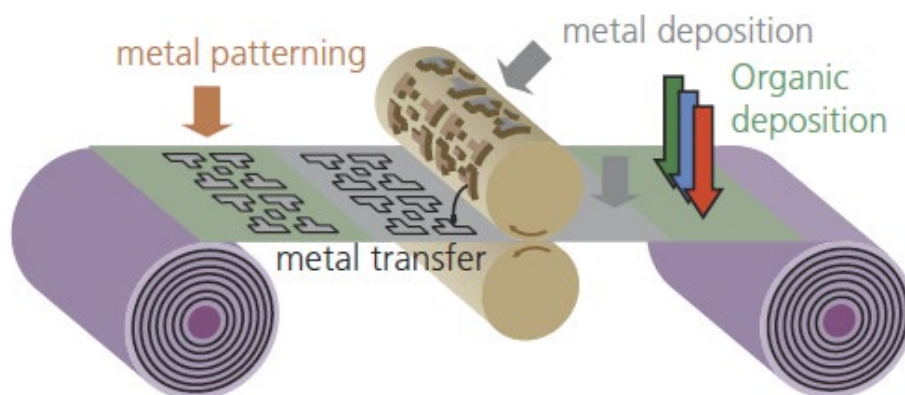


Figure 1.24 An illustration of roll-to-roll deposition and patterning of organic devices.¹⁰⁰

1.4 Organization of the Thesis

This thesis covers important microscopic and macroscopic mechanisms that are related to OPV efficiency and stability. Chapter 2 focuses on the CT states in the BHJs in various material systems and structures. The energies and properties of CT states are studied at the quantum mechanical level with quantitative models proposed. Chapter 3 moves to the BHJ/buffer layer interfaces where the electric field and charge distributions are studied. The interfacial voltage loss is understood and a method to reduce it is presented. Starting from this chapter, the theory and simulation results are directly connected to device J - V characteristics. In Chapter 4, an analyzing method is derived by calculating the “bulk quantum efficiency” (BQE) of an OPV device. This method can separate the properties of the BHJ from the peripheral layers (buffer layers and electrodes) and provides important insights for understanding the photogeneration process in OPVs. Chapter 5 and 6 study the photo- and thermal stabilities of OPVs, respectively. With the help of various experimental tools and the BQE analysis, several degradation mechanisms are identified. For each mechanism, we provide a method to suppress it. As a result, an OPV structure

with excellent photo- and thermal stabilities is demonstrated. In Chapter 7, results from several unfinished projects are presented with further experiments proposed. Also presented is an outlook for the future of OPV devices. The chemical structures and full chemical names of molecules used are provided in Appendix A. In Appendix B, a study of coherent exciton-polariton propagation in organic semiconductors via ultra-strong coupling to a Bloch surface wave photon is presented.

Chapter 2

Charge Transfer States in Organic Bulk Heterojunctions

OPV devices commonly employ “type II” HJs, where both the electron affinity and ionization potential of the donor are higher than that of the acceptor. Exciton dissociation at the donor-acceptor interface gives rise to the formation of a CT state that plays a crucial role in photogeneration of charges, and thus determines the OPV open circuit voltage and short circuit current.¹⁰¹⁻¹⁰² A considerable body of research has developed to study these interfacial CT states whose existence has been confirmed by the observation of their distinct absorption or luminescence features. Photoluminescence peaks with energy less than the lowest Frenkel exciton energy in the comprising materials have been attributed to the radiative recombination of CT complexes.^{87, 103-104} Other methods, including transient absorption,¹⁰⁵ time resolved photoluminescence (PL),¹⁰⁶ electro-absorption,^{104, 107} time-resolved two-photon photoemission,^{28, 78, 108-111} time-resolved second harmonic generation¹¹² and theoretical quantum chemical calculations^{78, 113} have been applied to understand the character of CT states.

2.1 Charge Transfer States in DBP/C₇₀ Bulk Heterojunctions

Vacuum deposited small molecular OPVs based on fullerene acceptors have been a significant focus of the OPV community¹¹⁴ until recently after solution processed OPVs based on

NFAs were introduced. A key to improving fullerene-based OPV performance is to optimize the donor-acceptor blend ratio in the photoactive HJs. While dilute-donor and fullerene acceptor blends are commonly used, the fundamental properties of CT states such as their energy levels and dynamics have yet to be fully clarified. Bernardo, *et al.* explored CT states at NPD/C₆₀ HJs with varying fullerene fraction and found that the dependence of CT state energy on dielectric constant is affected by the crystallinity of C₆₀ in the blend. But their luminescence spectra failed to cover energies < 1.2 eV, giving incomplete data of the important CT spectral features at long wavelengths.¹⁰⁴ Arndt, *et al.* studied the time-resolved and temperature-dependent PL of CT states in poly(3-hexyl thiophene) (P3HT)/[6,6]-phenyl-C61-butyric acid methyl ester (PCBM) blends. They showed that an excess amount of fullerene led to an increased probability of CT state formation, although the disruption of the polymer packing at high fullerene concentrations negatively influences charge separation.¹⁰⁶ Piersimoni, *et al.* discussed the change of film morphology and energies of CT states in the blends consisting of poly[2-methoxy-5-(30,70-dimethyloctyloxy)-1,4-phenylene vinylene] (MDMO-PPV) as donor and fullerene molecules with different side chains as acceptors, where the CT energy decreases as fullerene concentration increases.¹¹⁵

In this subchapter, we focus on small molecule blend HJs comprising the donor tetraphenyldibenzoperiflanthen (DBP) and the acceptor, C₇₀. When used in an OPV structure, the device performance is optimized at a surprisingly dilute donor volume ratio of 1:8 DBP:C₇₀ (~90% C₇₀).¹¹⁶ Charge transfer state properties at various blend ratios are studied by means of both steady-state and time-resolved PL, electroluminescence (EL), and reverse-biased OPV external quantum efficiency (*EQE*) and analyzed based on density functional theory. We identify two CT states in blends where the amorphous DBP:C₇₀ mixed and nanocrystalline C₇₀ phases co-exist; a localized,

high binding energy CT₁ state, and a delocalized, lower binding energy CT₂ state. The energy and lifetime of the CT states are functions of the size of the C₇₀ nanocrystallites which is quantitatively understood in terms of a quantum confinement model. The ratio of the CT₂-to-CT₁ population increases as the relative volume of the C₇₀ crystalline phase increases. The delocalized CT₂ state exhibits $> 91 \pm 2$ % dissociation efficiency in HJs with a 90% C₇₀ concentration. The contribution of CT₂ dominates the charge generation in highly dilute DBP:C₇₀ HJs.

2.1.1 CT state energy spectrum in DBP/C₇₀ bulk heterojunctions

To study the CT state energies in DBP/C₇₀ BHJs, we deposit organic thin films with various D/A ratios in a VTE chamber with base pressure $\sim 2 \times 10^{-7}$ torr. Both C₇₀ and DBP were purified via vacuum thermal gradient sublimation.¹¹⁷ The 54 nm thick DBP:C₇₀ blend films (with C₇₀ volume concentrations of 0%, 10%, 25%, 50%, 65%, 80%, 90%, 95%, 100%) were grown on sapphire substrates for obtaining steady-state PL spectra. The samples were excited in vacuum at a wavelength of $\lambda = 442$ nm using a continuous wave (CW) He-Cd laser. The EL from forward-biased OPVs was investigated using the device structure: ITO/10 nm MoO₃/54 nm DBP:C₇₀/8 nm bathophrenanthroline (Bphen)/100 nm Al. All spectra were collected normal to the substrate using a fiber-coupled monochromator (Princeton Instruments SP-2300i) equipped with both a Si charge-coupled device (CCD) array (PIXIS:400) and an InGaAs photoreceiver with sensitivity from $\lambda = 800$ to 1700 nm (Newport Model 2153). Time-resolved PL measurements were performed using a time-correlated single photon counter (PicoHarp 300) coupled to a Si single photon avalanche detector (PDM Series). The samples were excited at $\lambda = 480$ nm using 150 fs pulses at a 1 kHz repetition rate from a Ti:sapphire laser (Clark-MXR CPA-series) pumped optical parametric amplifier (TOPAS-C). A $\lambda = 800$ nm cut-off long-pass filter was used to remove DBP and C₇₀ emission to isolate the CT state spectra.

Figure 2.1(a) shows the EL spectra of OPVs with different DBP:C₇₀ blends at +3 V forward bias. The EL resulting from two CT states in the near-infrared ($\lambda = 1.0 - 1.6\text{eV}$) is easily distinguished from the singlet emission of neat C₇₀ and DBP at $\lambda > 1.6\text{ eV}$. We denote the low and high energy states as CT₁ and CT₂, respectively. The EL spectrum from the 50% C₇₀ blend is relatively structureless. The CT state energy increases as the C₇₀ concentration is either decreased or increased away from 50%, where the CT₂ state becomes dominant for blends with > 65% C₇₀ concentration. The low energy EL shoulder for > 65% C₇₀ blends is associated with the separate CT₁ state. Surprisingly, insignificant DBP or C₇₀ Frenkel exciton emission appears in the blends even with highly asymmetric blend concentrations (95% or 10% C₇₀) due to the efficient recombination of injected negative and positive charges at the HJ. As the drive voltage increases from +1 V to +5 V in Fig. 2.1(b), the low energy EL shoulder from the device with 90% C₇₀ slightly decreases in intensity, while the peak energy remains unchanged at $1.41 \pm 0.01\text{ eV}$. The EL peak of the 50% C₇₀ device has a minor blue shift of $20 \pm 5\text{ meV}$ as the voltage is increased from +1 V to +5 V.

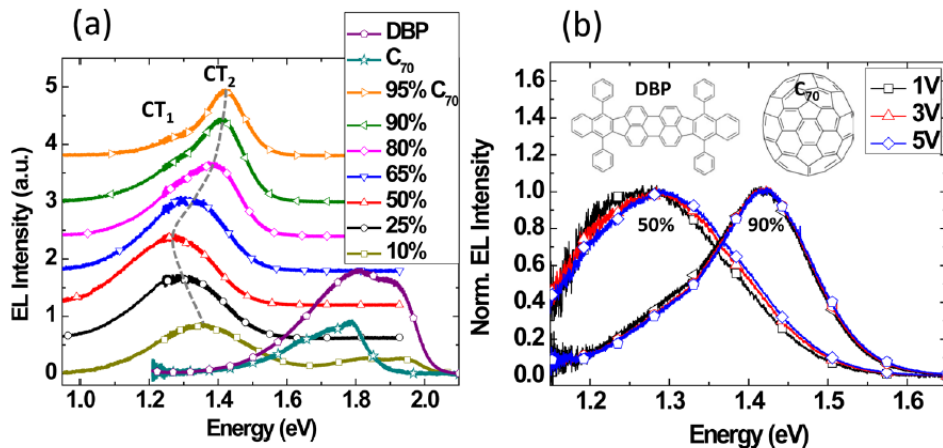


Figure 2.1 (a) Electroluminescence (EL) spectra from OPVs with different C₇₀ concentrations in blends with DBP under +3V forward bias. The spectra above and below 1.22 eV are detected by a Si CCD and a InGaAs photoreceiver, respectively. The spectra are offset for clarity. Two charge transfer excitons are labelled CT₁ and CT₂. The spectra from neat DBP and C₇₀ are shown for comparison. (b) Voltage dependence of EL with 90% and 50% C₇₀ concentrations in DBP.

The PL spectra from various thin film blends at 20K are shown in Fig. 2.2(a). CT state emission appears in the same energy range as from EL for all blends tested, whereas the CT₂-to-CT₁ intensity ratio is larger than that in EL, with intensity ratios calculated based on Gaussian fits to the spectra of 3.0 ± 0.4 , 2.7 ± 0.5 , 1.9 ± 0.6 , 1.3 ± 0.6 for 95%, 90%, 80%, and 65% C₇₀ concentration, respectively. At < 65% concentration, the PL spectra become structureless and it is no longer possible to resolve the two charge transfer features. The CT₂-to-CT₁ intensity ratio does not change as the excitation energy varies from 2.80 eV to 1.60 eV. No C₇₀ or DBP Frenkel exciton emission is observed for blends with C₇₀ concentrations between 90% and 25%, indicating ~100% exciton diffusion and charge transfer efficiency at the interface. The CT state energies as a function of C₇₀ concentration are provided in Fig. 2.2(b).

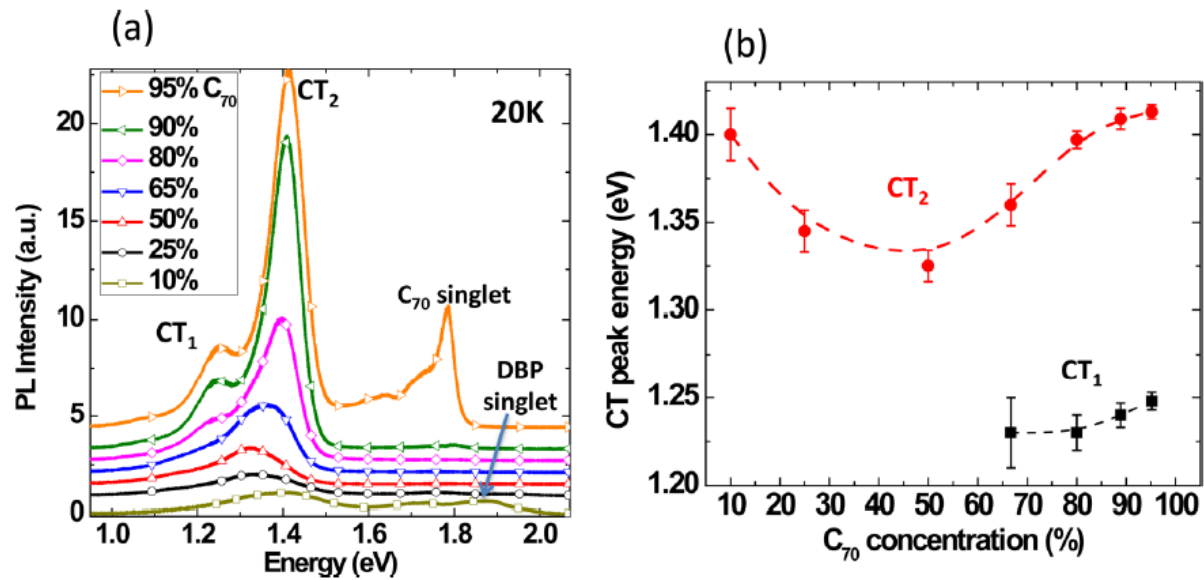


Figure 2.2 (a) Steady-state photoluminescence spectra from DBP/C₇₀ blends excited by a $\lambda = 442$ nm wavelength laser at 20 K. Both CT and monomer singlet emission spectra are noted. The spectra are offset for clarity. (b) CT exciton energies vs C₇₀ concentration. The curves are a guide for the eye.

2.1.2 Morphology study of DBP/C₇₀ bulk heterojunctions

The sample morphology was characterized by grazing incidence X-ray diffraction at a fixed incidence angle of 0.2° using Cu-K α radiation using a Rigaku diffractometer. The nanocrystalline structures were visualized using a JEOL 2100F high resolution transmission electron microscope (HRTEM) at an accelerating voltage of 80kV. The organic films were deposited on Si substrates pre-coated with a 10 nm thick layer of MoO₃, subsequently lifted off by dissolving the MoO₃ in deionized water and then captured by a Cu TEM grid. The X-ray diffraction spectra of DBP:C₇₀ blends with various D/A ratios are shown in Fig. 2.3(a). The peak at $10.3 \pm 0.1^\circ$ corresponds to diffraction from the (111) crystal planes of the C₇₀ FCC structure.¹¹⁸ Blending with DBP results in broadened and less well-defined diffraction peaks. The average C₇₀ nanocrystallite diameters calculated using the Scherrer equation¹¹⁹ are 11.6 ± 0.1 , 10.8 ± 0.2 , 5.6 ± 0.2 , 4.1 ± 0.3 nm, 3.3 ± 0.5 nm for neat C₇₀, 95%, 90%, 80%, and 65% C₇₀ blends, respectively. The diffraction patterns become structureless for blends with C₇₀ concentration < 65%, indicating a lack of crystalline formation to the resolution of this method. No evidence for DBP crystallization is found at any blend concentration studied. High resolution TEM images for four representative blended samples are provided in Fig. 2.3(b). The neat C₇₀ film has 10 to 20 nm diameter interconnected nanocrystalline domains, whereas 95% C₇₀ in DBP results in ~ 10 nm C₇₀ nanocrystallites isolated by disordered regions where DBP and C₇₀ are mixed. For 90% C₇₀, the domain diameters are decreased yet further, and are increasingly isolated by amorphous regions. Finally, the 50% C₇₀ blend shows no evidence for nanocrystallites at any scale.

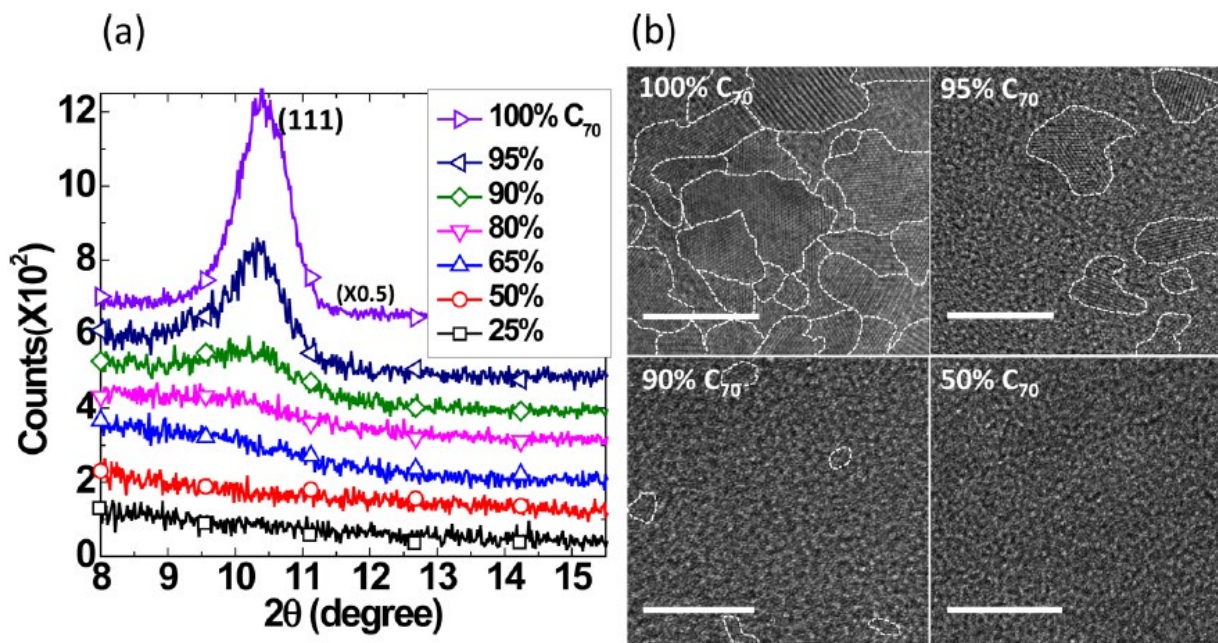


Figure 2.3 (a) Intensity of the (111) C_{70} X-ray diffraction peak of several DBP/ C_{70} blends whose C_{70} concentrations are provided in the legend. (b) Transmission electron microscope images of blends with different C_{70} concentrations. Crystalline C_{70} domain boundaries are outlined in white. Scale bars in the lower left of each micrograph are 20 nm.

2.1.3 Time-resolved PL

The dynamics of CT state recombination were studied using time-resolved PL at room temperature and 20K, with results in Fig. 2.4. At room temperature, the transient is fit by a single lifetime of $\tau = 0.55 \pm 0.05$ ns with no dependence on C_{70} concentration (see Fig. 2.4(b)). At 20K, non-radiative recombination is diminished, leading to an increase in CT lifetime that is dependent on concentration. The time-resolved PL of CT₁ and CT₂ are separately determined by illumination through $\lambda = 950$ nm long-pass and 900 nm band-pass filters, respectively. The best fits are biexponential for both regions, yielding two similar characteristic lifetimes except that the slope intersection point for the transient at $\lambda > 950$ nm region is lower than that near 900nm due to the different intensities of the two CT states. The lifetimes of CT₁ and CT₂ vs. C_{70} concentration have

similar trends, remaining relatively unchanged at $< 65\%$ C_{70} concentration and increased by a factor of two as concentration is increased from 65% to 95%.

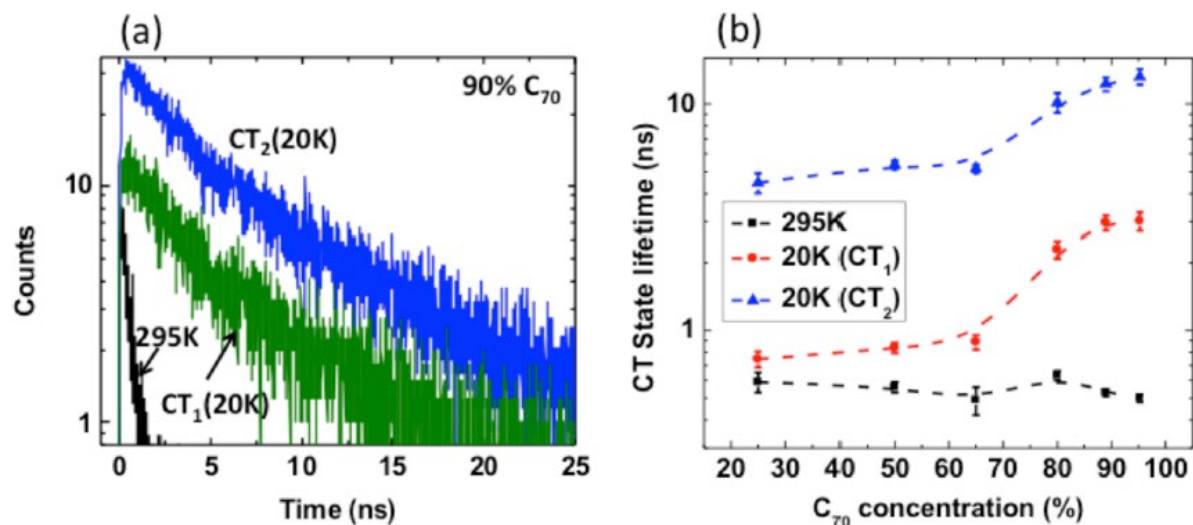


Figure 2.4 (a) Time-resolved PL for a DBP/ C_{70} blend with 90% C_{70} at 295 K and 20 K. (b) CT state lifetime vs C_{70} concentration at 295 and 20K. The error bars are the 95% confidence intervals. The data points are connected by curves to guide the eye.

2.1.4 Reverse-biased EQE and IQE

To study the dissociation efficiency of two CT states, the *EQE* of reverse-biased OPVs with 90% and 50% C_{70} concentrations, and their *IQE* vs. photon energy are measured and calculated. The OPVs were excited by monochromated light from a Xe arc-discharge lamp chopped at 200 Hz. A current amplifier (Keithley 480) was used to provide a voltage bias and further amplify the photocurrent before measurement with a lock-in amplifier. Optical constants (i.e. the real and imaginary parts of the index of refraction) of the neat and blended films were measured by variable angle spectroscopic ellipsometry. As shown in Fig. 2.5, both *EQE* spectra show a shoulder at $< 1.70 \pm 0.02$ eV that is absent in devices with either a neat C_{70} or DBP

photoactive layer. We attribute this feature to direct CT state absorption and exciton dissociation at the interface.¹²⁰ At 90% C₇₀ concentration shown in Fig. 2.5(a), *IQE* remains constant at photon energies $>1.55 \pm 0.02$ eV, while it substantially decreases from 0.91 ± 0.02 to 0.20 ± 0.01 as the photon energy decreases from 1.55 to 1.30 eV. At 50% C₇₀ concentration shown in Fig. 6(b), the *IQE* decreases from 0.71 ± 0.01 to 0.40 ± 0.09 .

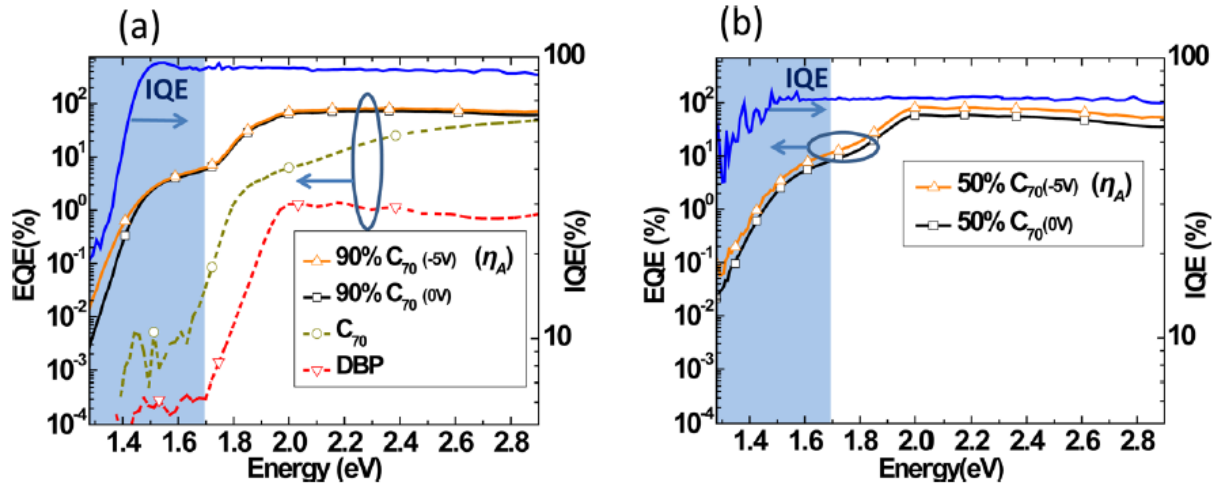


Figure 2.5 External quantum efficiency at 0 and -5 V reverse bias for OPVs with (a) 90% C₇₀ concentration in DBP, neat C₇₀, and neat DBP; (b) 50% C₇₀ concentration in DBP. The EQE at -5 V is equal to η_A . The internal quantum efficiency spectra for two blends are shown with blue lines.

The *IQE* spectrum in Fig. 2.5(a) has three distinct regions, (i) $E_{ph} > 1.70 \pm 0.02$ eV, where DBP or C₇₀ Frenkel excitons are excited, and can subsequently transfer to CT states leading to dissociation. (ii) 1.55 ± 0.02 eV $< E_{ph} < 1.70 \pm 0.02$ eV, where CT₂ states are directly excited. (iii) $E_{ph} < 1.55 \pm 0.02$ eV, where localized CT₁ states are predominantly excited. The *IQE* in regions (i) and (ii) are 0.91 ± 0.02 , suggesting that the relative contributions of CT₁ and CT₂ to the photocurrent remain unchanged across these two regions. As shown in the steady-state PL spectra

at 90% C₇₀ concentration in Fig. 2.2(a), nearly 100% of the Frenkel excitons generated in DBP and C₇₀ transfer to interfacial CT states. Assuming that a is the fraction of CT₂ states and $(1-a)$ is the fraction of CT₁ states generated at the HJ at $E_{ph} > 1.55 \pm 0.02$ eV, and that only CT₁ is generated at $E_{ph} = 1.30$ eV, then:

$$\begin{aligned} IQE &= a \cdot \eta_{diss}(CT_2)\eta_{CC} + (1-a) \cdot \eta_{diss}(CT_1)\eta_{CC} = 0.91 \pm 0.02, & E_{ph} > 1.55 \pm 0.02 \text{ eV} \\ IQE &\approx \eta_{diss}(CT_1)\eta_{CC} = 0.20 \pm 0.01, & E_{ph} = 1.30 \text{ eV} \end{aligned} \quad (2.1.1)$$

Since the value of a and $\eta_{diss}\eta_{CC}$ are in the range of 0 and 1, using Eq. (2.1.1) we infer that $0.91 \pm 0.02 < \eta_{diss}(CT_2)\eta_{CC} < 1$, $0.88 \pm 0.03 < a < 1$. This implies that greater than 88% of excitons generated at $E_{ph} > 1.55 \pm 0.02$ eV are CT₂ states at 90% C₇₀ concentration. The dissociation efficiency of CT₂ is greater than 91%, leading to efficient photogeneration in the OPV. In contrast, the OPV with 50% C₇₀ concentration shown in Fig. 2.5(b) exhibits a low IQE due to a decreased population of CT₂ states in the amorphous blends. These provide an explanation for the very high efficiencies observed in significantly diluted-donor blends in this materials system. This differs from material systems examined by Vandewal, et al., who find that IQE is independent of the photon energy, and where the lowest energy CT state contributes to efficient photocurrent generation.

2.1.5 TDDFT calculation

Quantum chemical calculations were carried out using DFT/TDDFT in the Gaussian 09w package. Calculations were performed on various monomer, dimer and trimer combinations of the C₇₀ and DBP molecules. The geometries were optimized using the B3LYP functional and 6-31G(d) basis set. Based on the optimized structures, TDDFT was used to obtain the electron densities and energy levels of excited states based on the B3LYP functional and 6-31G(d) basis set.

The calculated singlet Frenkel/CT exciton energies are shown in Fig. 2.6(a). The C_{70} monomer has the lowest singlet energy of $E_S = 2.04$ eV, while the DBP monomer has $E_S = 2.18$ eV. Other high energy singlet states are also shown. The singlet energies of the DBP- C_{70} physical dimer, trimer (one DBP-two C_{70} molecules) and tetramer (one DBP-three C_{70} molecules) that lie below the DBP and C_{70} monomer states are CT states. We note that these calculations consider only a few of the many possible DBP- C_{70} molecular configurations, with those provided here serving as examples. The charge density distribution of CT states shown in Fig. 2.6(b) indicates that the electron (purple) and hole (yellow) densities are on C_{70} and DBP, respectively. Including more C_{70} into the complex leads to moderate electron delocalization and creates several higher energy CT states. The calculated oscillator strengths of dimer CT states are in the range of 10^{-4} to 10^{-3} , which are 10^2 to 10^3 times lower than for the monomers, but higher than for trimer and tetramer CT states.

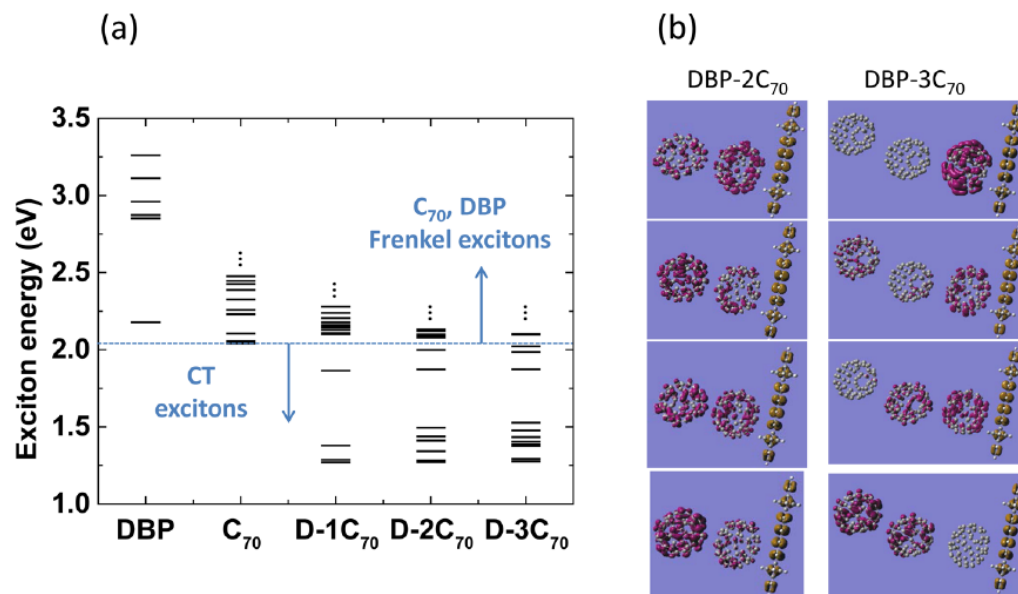


Figure 2.6 (a) Calculated singlet energies of different monomer, dimer, trimer, and tetramer combinations of DBP and C_{70} using TDDFT. On the abscissa, DBP is abbreviated as D. (b) Visualized charge density difference analysis of the first four CT states of the DBP- C_{70} dimer (left) and trimer (right) complexes. The electron (purple) and the hole (yellow) density distributions are located on the C_{70} and DBP molecules, respectively.

2.1.6 Confined Schrödinger equation calculation

Luminescent spectra in Figs. 2.1 and 2.2 show that CT exciton energies, E_{CT} , in DBP:C₇₀ blends increase as the C₇₀ concentration is either increased or decreased away from 50%. This trend is strikingly different from that reported for other material combinations, where the E_{CT} decreases monotonically as the fullerene concentration increases. The change of dielectric constant for different blend ratios has typically been invoked to explain the shift in E_{CT} . However, the optical dielectric constant (ϵ_r) of DBP:C₇₀ blend increases monotonically with C₇₀ concentration (x_{C70}), which fits to $\epsilon_r = 3.88 + 0.0064 \cdot x_{C70}$. While this behavior may result in the spectral shift observed in CT₁, it nevertheless fails to explain the trend of CT₂ with an energy minimum at 50% C₇₀ and the change in slope toward an apparent asymptote at > 80% C₇₀ concentration. Furthermore, the shift cannot be explained by the solid-state solvation effect¹²¹ since both DBP and C₇₀ are non-polar molecules.¹²²

Alternatively, the shift in CT₂ energy can be attributed to the change in exciton binding energy as a result of CT delocalization and quantum confinement in the C₇₀ nanocrystals or DBP aggregates.¹²³⁻¹²⁴ As shown in Fig. 2.7, depending on the local aggregation sizes of donor or acceptor molecules, the CT states can have different levels of delocalization, resulting in different binding energies. As the C₇₀ concentration increases to > 50%, the electron on a C₇₀ nanocrystal bound to the hole on DBP is delocalized over several C₇₀ molecules (*cf.* Fig. 2.6(b)), leading to a decrease in the binding energy and therefore an increase of CT state energy. Similarly, as the C₇₀ concentration decreases below 50%, the DBP aggregate size increases, allowing for increasing hole delocalization.

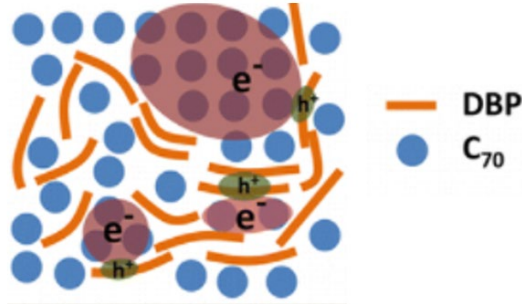


Figure 2.7 Schematics of CT delocalization in various nano morphological environments.⁷⁶

To model the CT states at $> 50\%$ C_{70} concentration, we assume for simplicity that the C_{70} domain is spherical with radius $\langle r_0 \rangle$ estimated from XRD data in Fig. 2.3(a), and is located tangent to the x-y plane. An electron within the domain is confined by a potential barrier $\phi_b = 0.5$ eV on the boundary, which corresponds to the difference between the LUMO energies of DBP and C_{70} . The hole bound to that electron is fixed on a DBP molecule at $\mathbf{a} = (0, 0, -0.4$ nm), where 0.4 nm is the distance to the neighboring C_{70} obtained from DFT geometric optimization.

We assume that the electron mobility in C_{70} is at least as large or larger than the hole in DBP, and hence can occupy a greater volume as noted by Peumans and Forrest. The electron Hamiltonian is then:

$$H = -\frac{\hbar}{2m^*} \nabla^2 + V(\mathbf{r}),$$

$$V(\mathbf{r}) = \begin{cases} -\frac{e^2}{4\pi\epsilon_0\epsilon_{r_{C70}}|\mathbf{r}-\mathbf{a}|} & (|\mathbf{r}-\mathbf{r}_0| < r_0) \\ -\frac{e^2}{4\pi\epsilon_0\epsilon_{r_{DBP}}|\mathbf{r}-\mathbf{a}|} + \phi_b & (|\mathbf{r}-\mathbf{r}_0| > r_0) \end{cases}, \quad (2.1.2)$$

where m^* is the electron effective mass, r_0 is the C_{70} domain radius, and $|\mathbf{r} - \mathbf{a}|$ is the distance between the hole and the electron. The relative dielectric constants are $\epsilon_{r_C_{70}} = 4.60$ and $\epsilon_{r_DBP} = 3.92$ at $\lambda = 900$ nm.

We obtained the energy eigenvalues of the Hamiltonian with and without the potential $V(\mathbf{r})$, yielding the energy of the Coulombically bound and unbound electron states, respectively. The energy difference between them corresponds to the CT binding energy, shown in Fig. 2.7(a). The electron density of a Coulombically bound state for a C_{70} domain radius $\langle r_0 \rangle = 2$ nm is shown in the inset of Fig. 2.7(a). The calculated binding energies fit reasonably well with the measured E_{CT} after including the 1.52 eV energy difference between the DBP HOMO and the C_{70} LUMO.

We can apply the same approach to analyze the energy of holes located on DBP aggregates at C_{70} concentrations $< 50\%$. However, crystallographic data show no evidence for DBP nanocrystals at any concentration. Thus, our analysis assumes cofacial stacking¹²² of only a few DBP molecules to a thickness, d , at the interface, with the bound electron fixed on the adjacent C_{70} molecule. Calculation of the eigenenergies for the hole using a Hamiltonian similar to Eq. (2.1.2) suggests that stacks of only 4 ± 1 DBP molecules can lead to the shifts in CT_2 spectra in Fig. 2(b) observed at high DBP concentrations. Since most of the DBP region is highly disordered, the fits are not as convincing as for C_{70} nanocrystallites in Fig. 2.7(a).

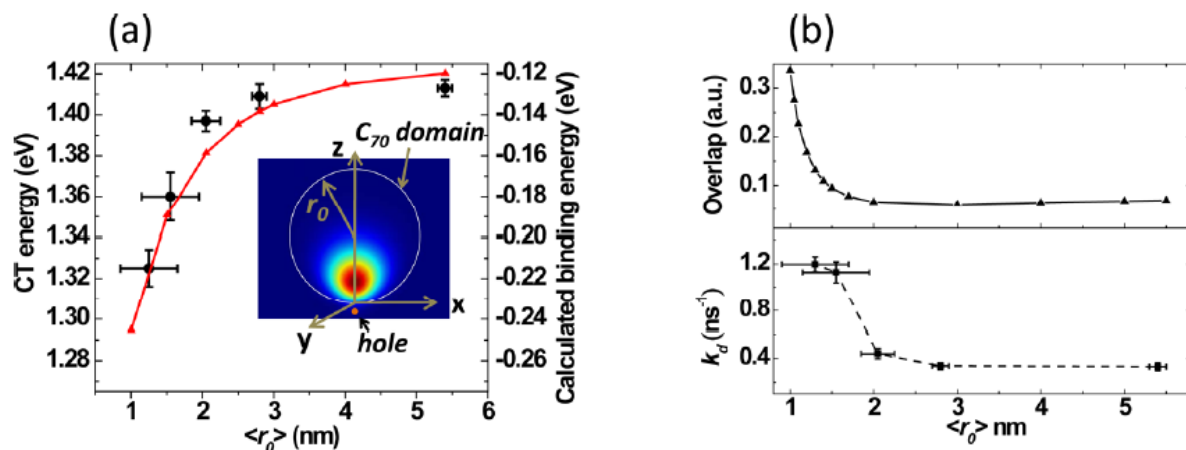


Figure 2.8 (a) Measured peak energies of CT₂ states (data points) and calculated CT binding energies (red line) as functions of C₇₀ domain radius, $\langle r_0 \rangle$. Inset: Calculated electron density distribution for a domain with $\langle r_0 \rangle = 2$ nm. (b) (Top) Calculated probability density overlap J vs $\langle r_0 \rangle$. (Bottom) Measured recombination rate k_d for CT₂ vs $\langle r_0 \rangle$.

As inferred from the TEM images in Fig. 2.3(b), the C₇₀ crystalline phase coexists with the amorphous DBP:C₇₀ mixed phase at high C₇₀ concentrations. Charge transfer excitons in the amorphous regions are more localized than in the crystalline domains.¹²⁵ As a result, two discrete CT peaks are found in the PL spectra of thin film blends with > 65% C₇₀, at which point C₇₀ nanocrystallites with diameters > 4 nm appear. The population of CT₂ excitons significantly decreases at C₇₀ concentrations < 65% due to the decrease of C₇₀ nanocrystallites, thereby resulting in a decrease in CT₂ emission intensity.

The different lifetimes of CT₁ and CT₂ result in a biexponential PL decay at 20K as shown in Fig. 2.4(a). We find that the CT₂ lifetime, as in the case of its binding energy, is also dependent on the C₇₀ domain size, with the lifetime increasing with $\langle r_0 \rangle$ as shown in Fig. 2.7(b). Quantum confinement in the C₇₀ domains leads to an increase in the overlap of the electron and hole probability density as $\langle r_0 \rangle$ decreases, resulting in a concomitant increase in the CT₂ recombination rate. To model this dependence, we calculate the overlap of the probability density of the excited ($|\psi_{CT}|^2$) and ground states ($|\psi_G|^2$), i.e. $J = \int |\psi_{CT}|^2 |\psi_G|^2 dr^3$, where ψ_G is the electron

wavefunction at the DBP HOMO obtained from TDDFT calculations. The overlap integral, J , vs. C_{70} domain radius is shown in Fig. 2.7(b), upper panel, which qualitatively agrees with the trend observed for the decay rate of CT_2 , *i.e.*, $k_d (=1/\tau)$ in the lower panel. A quantitative prediction of CT lifetime vs. the domain size requires an accurate knowledge of the electron wavefunction phase, which can only be obtained from a description of the actual C_{70} molecular configurations in the solid. This makes an accurate calculation of the transition oscillator strength as a function of $\langle r_0 \rangle$ impossible using our current approach.

For the largest C_{70} nanocrystalline domains, the more delocalized CT states with lower binding energy may also suffer from a higher probability of exciton dissociation than for the localized CT_1 states. Absent charge extraction, however, the dissociated electron eventually recombines with the hole to reform a CT exciton at the HJ, which further increases its lifetime. The CT_1 lifetime vs. C_{70} concentration in Fig. 2.4(b) is similar with that of CT_2 . Although spatially separated by different phases, some of the delocalized CT_2 excitons may transfer *via* exchange interactions to CT_1 , or execute a diffusive random walk along the interface and relax to a strongly bound CT_1 state. Thus, a change in the CT_2 lifetime may also result in changes in the observed CT_1 lifetime.

2.2 Charge Transfer States in DBP/ C_{70} Alternating-layer Structures

In Section 2.1, the delocalization of CT states is controlled by varying the D/A ratio in the BHJ. However, this is an indirect way to control the crystalline domain sizes of C_{70} . In this section, we directly control the DBP and C_{70} domain sizes by growing alternating, ultrathin layers of C_{70} and DBP with the degree of CT localization determined by the individual layer thicknesses. In addition, to better understand the mechanisms governing charge extraction, a kinetic Monte Carlo

(KMC) simulation model is applied to quantitatively simulate the nanomorphology of the active dilute donor layers. We find that even in the most dilute blends, planar DBP molecules stack into continuous percolating paths that enable efficient hole extraction.

2.2.1 Samples of alternating DBP and C₇₀ layers

In Section 2.1, the shift in CT₂ peak energy with DBP concentration was attributed to reduced C₇₀ crystallite diameters that confine the CT states. Moreover, the DBP concentration also affects the absorption spectrum. To understand the origin of the spectral energy shifts, we control the degree of excited state localization by growing alternating multilayer stacks of DBP and C₇₀ to gain insights into the mechanisms affecting states in the blends of similar ratios of the two constituents. Samples are grown on solvent-cleaned (100) Si substrates by VTE in a chamber with a base pressure of 10⁻⁷ torr. Prior to growth, both C₇₀ and DBP are purified once via vacuum thermal gradient sublimation.¹²⁶ During the growth of the alternating multilayer samples, temperatures of both sources are adjusted to give a stable growth rate of 0.1 Å/s while two independently controlled source shutters are used to switch between DBP and C₇₀ after each layer growth is completed. The PL spectra of the samples were measured in vacuum using a continuous wave He-Cd laser excitation source at a wavelength of 442 nm. Spectra were collected through a 550 nm long-pass filter and coupled into a monochromator using a fiber (Princeton Instruments SP-2300i). The signal was detected using a Si charge-coupled device array (PIXIS:400).

To confirm that manufactured samples indeed have alternating layer structures, cross-sectional STEM measurements were performed. To enhance the contrast between donor and acceptor layers, Br-dressed DBP molecules synthesized by Luminescence Technology Corp are used for STEM samples (Appendix A).¹²⁷ The multilayer stacks are capped with a C₇₀ neat layer and a 100 nm thick Ag protection layer. The sample was then cut into thin slices using FIB milling

(FEI Nova 200 Nanolab SEM/FIB). The sample thicknesses were estimated to be tens of nanometers. The samples were then examined using a JEOL 2100F high-resolution TEM at an accelerating voltage of 200 kV.

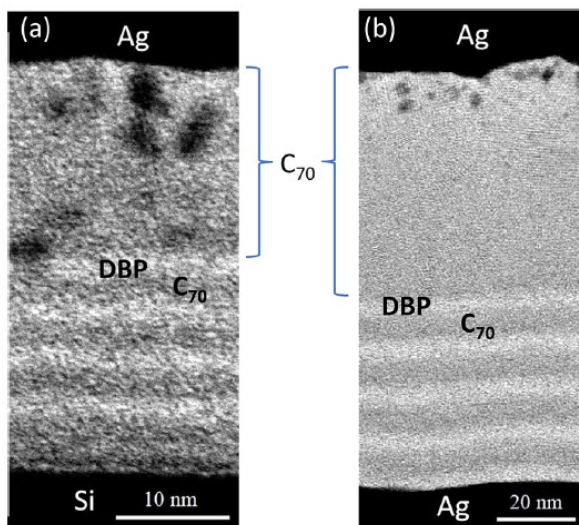


Figure 2.9 (a) Bright field (BF) cross-sectional scanning transmission electron microscopic image of 5 pairs of 2 nm thick alternating layers capped by a 20 nm thick C_{70} layer and a 150 nm thick Ag protection layer. The dark spots are due to Ag diffusion from the contact. (b) Image of 5 pairs of 5 nm thick alternating layers capped by a 20 nm thick C_{70} layer and a 50 nm thick Ag layer.

Figures 2.8 (a) and (b) show bright field cross-sectional scanning transmission electron microscopy (STEM) images of multilayer stacks with alternating layer thicknesses of 2 nm and 5 nm. To increase the imaging contrast between C_{70} and DBP molecules, two H atoms are substituted with Br atoms in the DBP molecules to create a contrast difference with the C_{70} layer (see Appendix A). Each sample contains 5 pairs of DBP and C_{70} layers capped by a C_{70} layer with the same thickness as the multilayer stack, and a 100 nm of Ag. Individual layers as thin as 2 nm are clearly identified in the images in Fig. 2.8.

2.2.2 CT state energy spectrum in DBP/C₇₀ alternating layer structures

Figure 2.9 (a) shows the normalized room temperature PL spectra from DBP and C₇₀ stacks with various layer thicknesses. All samples have a total thickness of 400 nm. The spectra are compared with that of a 1:1 mixed layer sample. The mixed sample has a lowest CT₂ peak energy $E_2 = 1.33 \pm 0.01$ eV. As the alternating layer thicknesses increase from 1 nm to 5 nm, E_2 blue shifts to 1.43 ± 0.02 eV.

The model used to calculate the CT peak energies of multilayer stacks is identical to that used in Section 2.1.6 except that the hole is placed at the center of the ultrathin DBP layer to account for their relative delocalization. Since the volume and ratio of materials in all the samples are equal, the energy shift of the CT₂ peak is attributed to quantum confinement as the individual layer thicknesses decrease. A previously developed quantum mechanical model⁷⁶ is modified to calculate the binding energy between electron and hole of the CT₂ states with various alternating layer thicknesses. The experimental and simulated results are shown in Fig. 2.9 (b). The calculated energy shift reasonably agrees with experiment except for the sample with 1 nm thick layers. This is possibly due to incomplete layer coverage for the thinnest sample, leading to reduced confinement.

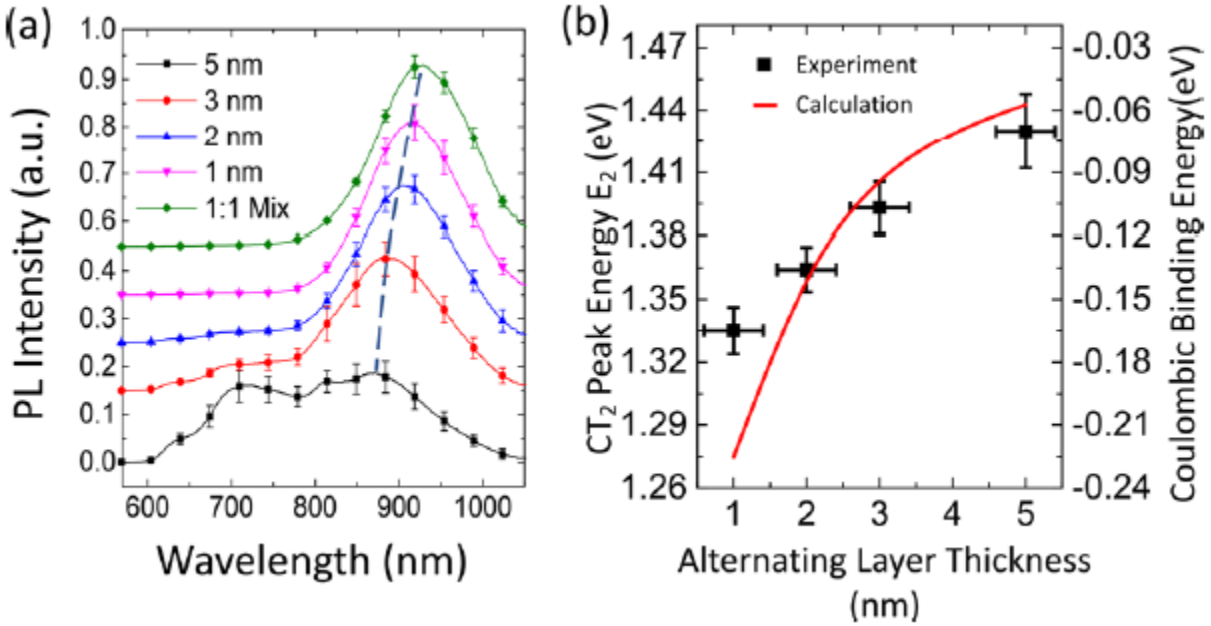


Figure 2.10 (a) Room temperature photoluminescence (PL) spectra of multilayer stacks consisting of alternating layers of DBP and C_{70} and a 1:1 mixed sample. To achieve a total thickness of 40 nm, the multilayer stacks with alternating layer thicknesses of 1, 2, 3, and 5 nm contain 20, 10, 7, and 4 pairs of DBP and C_{70} layers, respectively. The spectra are normalized to the same integrated intensity, and are offset for clarity. (b) Photoluminescence peak energies of CT_2 states, E_2 , and calculated Coulombic binding energies vs layer thickness.

Confinement of CT states partially explains the optimal OPV performance with DBP concentration of only 10%. The electron and hole wavefunction overlap increases as the volume containing the CT state decreases, resulting in a larger recombination rate and a smaller dissociation efficiency compared with that of the delocalized CT states. Previous studies have also shown that an increased CT state energy leads to a higher V_{oc} . Thus, a low DBP concentration benefits OPV performance due to the existence of CT states with higher energies.

2.2.3 Nanomorphology of DBP/ C_{70} alternating layer structures

The question remains as to how the holes are efficiently extracted from such dilute donor layers as used in the DBP: C_{70} blends. The answer lies in the details of the blend morphology at the nanometer scale, which we simulated via a KMC model based on the Van der Waals attraction

between molecules (see Section 2.2.5). The simulation results provide the average nanocrystalline C_{70} cluster radius $\langle r \rangle$ (circles), which was compared with values inferred from the Scherrer approximation of the X-ray diffraction pattern (squares) shown in Fig. 2.10 (a). As the DBP concentration increases from 5% to 50%, $\langle r \rangle$ decreases from 5.2 ± 0.9 nm to 1.3 ± 0.2 nm in the simulated mixed layer, which agrees with experiment. In Fig. 2.10 (b), $\langle r \rangle$ extracted from simulations is used to calculate E_2 , (circles) using the excited state confinement model. Black squares show E_2 measured for the blends.

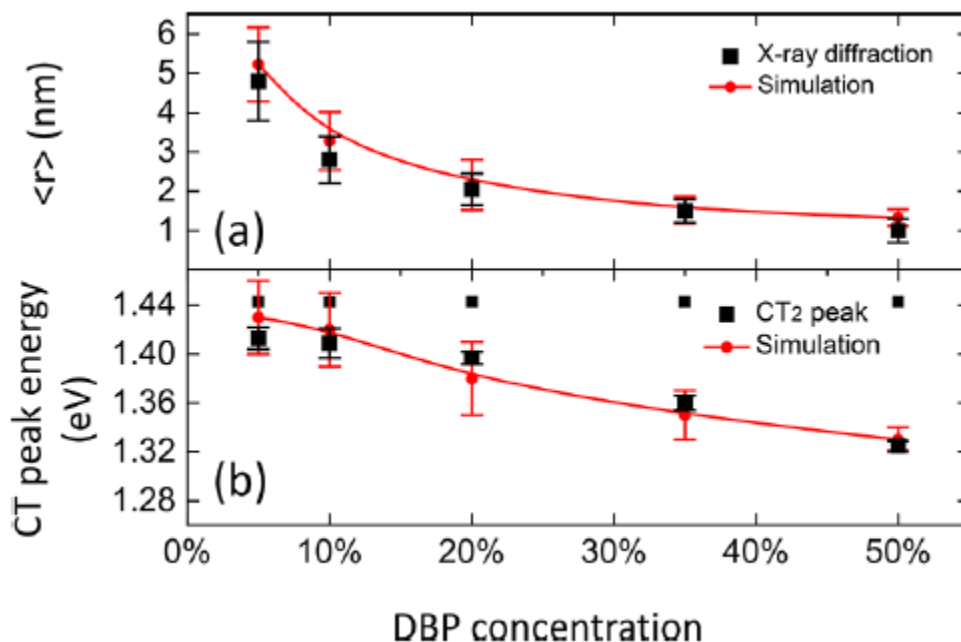


Figure 2.11 (a) Average C_{70} cluster radius $\langle r \rangle$ vs DBP concentration in DBP: C_{70} blends. The radii obtained from X-ray diffraction and KMC simulations (circles) are indicated. Error bars for the X-ray diffraction data arise from uncertainties in line widths at half maxima. Error bars are standard deviations of the simulated cluster size distributions. (b) Measured (squares) and calculated (circles) E_2 based on the simulated nanocrystallite radius, $\langle r \rangle$, vs DBP concentration. The error bars for the PL data arise from Gaussian fits to the CT_2 peak while the error bars for the simulated results are standard deviations of the cluster size distributions.

2.2.4 Kinetic Monte Carlo simulation of DBP/C₇₀ blend

Holes resulting from exciton dissociation are extracted through contiguous, percolating paths formed by DBP molecules. However, DBP concentrations of only ~10% could potentially impede hole extraction due to the formation of discontinuous networks. To understand the hole extraction process, therefore, we use kinetic Monte Carlo simulation to analyze the aggregation of DBP molecules in mixed HJs.

Following Peumans, et al.³¹ and Yang, et al.,¹²⁸ molecules fill sites starting at the substrate surface in a face-centered cubic (FCC) lattice with a lattice constant of 1.06 nm, consistent with the crystal structure of C₇₀. Each DBP molecule has a length of 2.15 nm and can contact between 16 to 22 C₇₀ molecules. Given its large size compared with C₇₀, each DBP molecule is allowed to occupy two adjacent fcc sites, resulting in a coordination number of 18. The intermolecular binding energies for molecules in various configurations are evaluated using the Forcite molecular dynamics module in Materials Studio®. To simulate the deposition dynamics, a two-step process is employed: single molecule deposition followed by full sample annealing. In the first step, a molecule normally incident to the substrate lands at a random location at the growth surface, and attempts to move to adjacent vacant sites. An attempt is accepted if the target site has a lower total energy than its initial site, otherwise the attempt is accepted with a reduced probability of $P(\Delta E) = \exp(-\Delta E/kT)$, where ΔE is the difference between the total binding energies of the target and initial sites, k is Boltzmann's constant and $T = 300\text{K}$ is the temperature. The number of attempts a molecule is allowed to make is used as a parameter to control the average sizes of the molecular aggregates. For DBP molecules, there is an extra rotational attempt where one end of the DBP molecule stays in its original site while the other end attempts to move to an adjacent vacant site, or exchange with an adjacent C₇₀. To account for the many-body dynamics during deposition, full

sample annealing occurs after every 1,000 molecules are deposited. During this step, the 1,000 molecules are allowed to move to adjacent sites. The attempts follow the same rules as in the single molecule deposition process. Full sample annealing significantly reduces the computational intensity compared with real-time simulations in which the dynamics of all molecules are simultaneously considered. This enables the simulation of systems with a very large number of molecules ($\sim 10^6$).

The morphology of the simulated blend is evaluated by determining the C_{70} aggregate size. Spheres with increasing diameters are compared with the C_{70} cluster shape. The diameter of the largest sphere that can fit within the C_{70} cluster with a volume shape mismatch below 5% is used to characterize the C_{70} aggregate size. From X-ray diffraction data, the diffracted intensity from a spherical cluster containing N molecules is proportional to N^2 . Therefore, the average radius of a simulated blend is derived using an average with weight of r^6 .

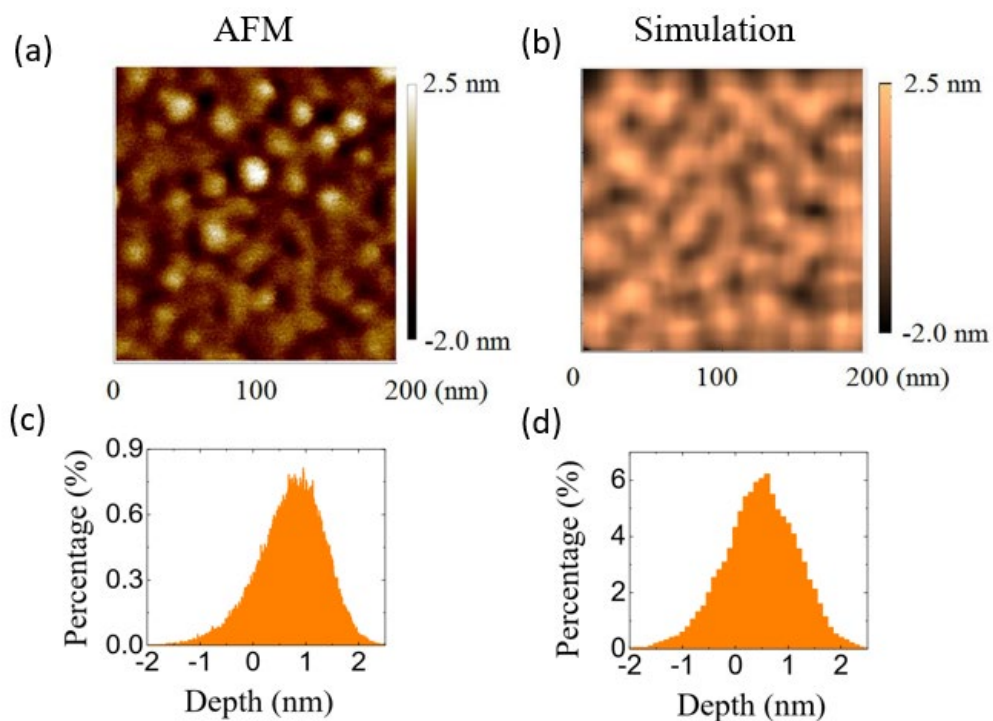


Figure 2.12 (a) Atomic force microscopic (AFM) image of the top surface of a neat C_{70} film. (b) Top surface of a simulated C_{70} film. (c) Histogram of surface roughness of the film in (a). (d) Histogram of surface roughness of the simulated film in (b).

Figure 2.12 (a) shows the atomic force microscopic (AFM) image of the top surface of a neat C_{70} film. We compare it with the top surface of a simulated C_{70} film as shown in Fig. 2.12 (b). The surface roughness histograms of the measured and simulated C_{70} films are shown in Figures 2.12 (c) and (d) respectively. The number of annealing attempts each C_{70} molecule makes in the simulated deposition process before adding the next molecule is decided by matching Fig. 2.12 (d) to (c).

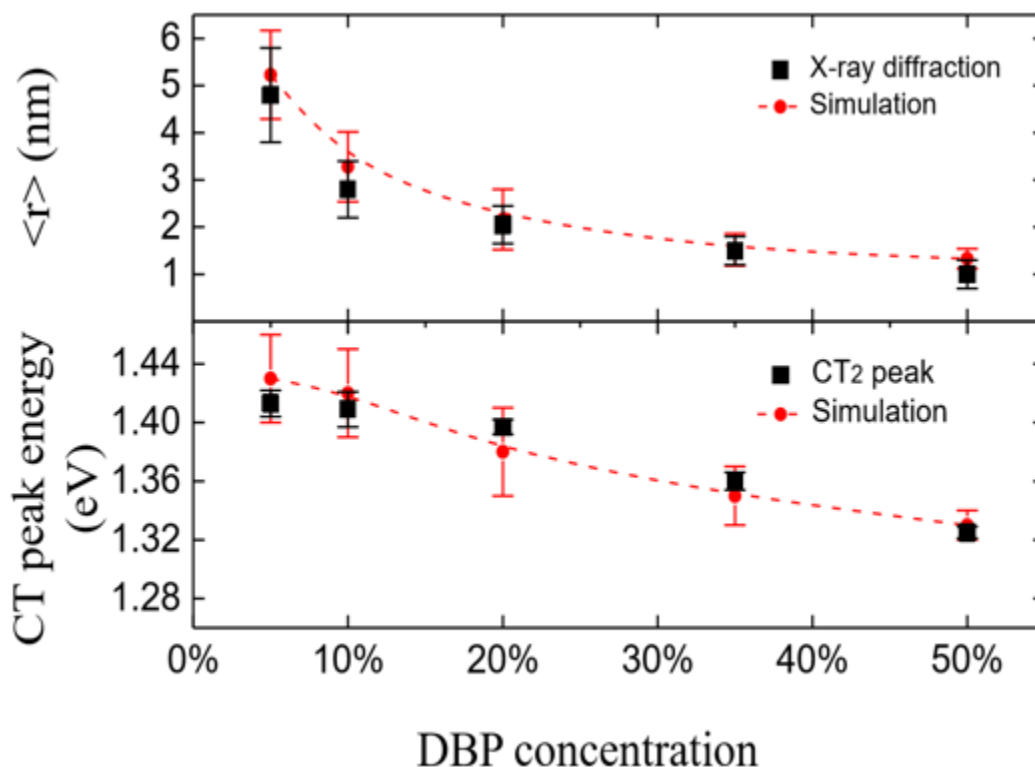


Figure 2.13 Measured and simulated average C_{70} domain sizes and CT_2 peak energies vs. DBP concentration

Figure 2.13 shows the measured and simulated average C_{70} domain sizes at various DBP concentrations. The number of annealing attempts each DBP molecule makes in the simulated deposition process before adding the next molecule is decided by fitting the simulated average C_{70} domain sizes to the measured results at various DBP concentrations.

Figure 2.14 (a) shows a 10-nm-deep slice of simulated mixed active layers with 11 mol% DBP. The evaporated molecules are incident from the top onto the surface of the film with the anode at the base. The 80-nm-thick film has a rough surface and a modest density of voids. Here, the C_{70} regions are shown in blue, and the green areas are DBP molecules that form into percolating paths to the anode. The red areas, which are in a substantial minority, are isolated islands of DBP disconnected from the anode.

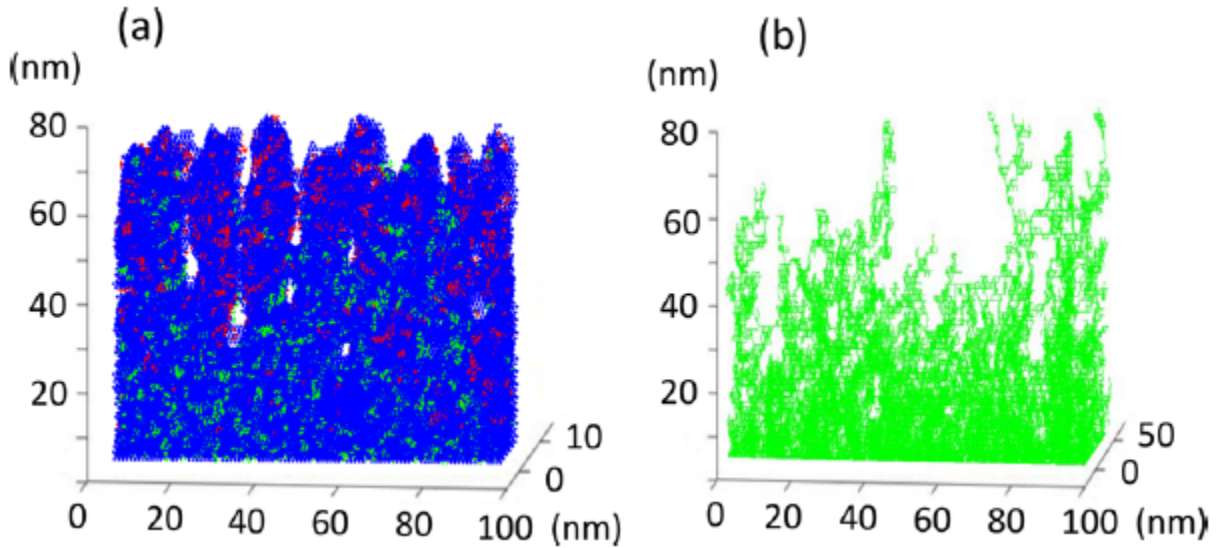


Figure 2.14 (a) Three-dimensional simulation of a 10 nm deep by 80 nm thick slice of a 1:8 DBP: C_{70} blended HJ. Growth is simulated by molecules arriving at top of the surface starting at the anode lying at the bottom. Blue areas are C_{70} molecules. Green (red) areas are DBP molecules that form (do not form) percolating paths to the anode. Note the voids in the thin film. The simulation comprises 600,000 molecules. (b) Three-dimensional simulation of the DBP percolating paths of a 50 nm deep and 80 nm thick vertical slice of a blend with 10 mol % DBP in C_{70} . The C_{70} molecules are not shown. Percolating paths are identified by connecting adjacent DBP molecules with green lines.

Figure 2.14 (b) shows only those percolating paths in DBP that extend from the anode into the active layer of a 50-nm-deep by 80-nm-thick slice. During deposition the planar DBP molecules form continuous π - π stacks that exclude C_{70} molecules from their interstices, thus minimizing the total energy of the blend. The stacks increase the probability of the formation of percolating paths to the anode even at very high dilutions. We define the 2D density of paths using:

$$\rho(z) = \frac{N_p(z)}{A}, \quad (2.2.1)$$

where $N_p(z)$ is the number of DBP molecules forming into continuous regions in a single layer at a distance z from the anode, and A is the anode contact area. Figure 2.12 shows the 2D density of percolating paths in the substrate plane in a blend with 10% DBP versus the distance from the anode. The simulation follows:

$$\rho(z) = \rho_0(z)e^{-\frac{z}{\zeta}}, \quad (2.2.2)$$

shown by the line in Fig. 2.15 (b). Here, ρ_0 is the 2D density of percolating paths originating at the anode, and from the fit, $\zeta = 33 \pm 5$ nm is the characteristic percolation length, which is comparable to the typical active layer thickness using this material combination. At $d = 50$ nm, which is the typical active layer thickness of an OPV cell, then $\rho \approx 0.05$ nm⁻², corresponding to a mean distance between percolating paths of 4.5 nm. This is well below the C₇₀ exciton diffusion length (~ 8 nm), suggesting that the holes can be extracted throughout the active layer with a DBP concentration of only 10 mol.%.

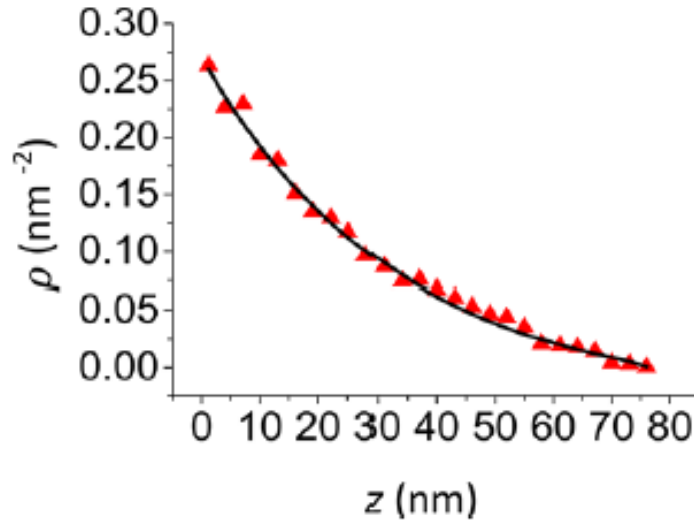


Figure 2.15 Two-dimensional density of DBP percolating paths, ρ , in the substrate plane as a function of distance from the anode, z (triangles). An exponential fit to the data is shown by the line.

Figure 2.15 (a) also shows that a fraction of DBP clusters form isolated islands where holes can be trapped following exciton dissociation. Dissociation on islands is therefore limited by the recombination rate of the previously dissociated charges within a particular island. Due to the spatial separation and energetic barriers of the trapped holes and free electrons delocalized among C₇₀ molecules, the hole recombination rate is expected to be low compared with the charge

extraction rate. In steady state, therefore, the exciton dissociation rate on isolated DBP islands is smaller than within the percolating paths. This is supported by the high peak internal quantum efficiencies of devices at donor concentrations of $\sim 10\%$.

With these analyses, we can summarize the performance of DBP:C₇₀ mixed HJs at low DBP concentrations. Photogeneration is the product of four steps: exciton generation through light absorption with efficiency η_A , exciton diffusion to donor-acceptor interfaces with efficiency η_{diff} , exciton dissociation into charge carriers with efficiency η_{diss} , and charge collection at electrodes with efficiency η_{CC} . Reverse-biased *EQE* measurements suggest that η_A has only a weak dependence on DBP concentration. Significant quenching of bulk exciton emission in the PL spectrum indicates that $\eta_{diff} \approx 1$ even at low DBP concentrations. On the other hand, formation of CT₂ at low DBP concentrations results in a larger η_{diss} as well as a higher V_{OC} . The KMC simulations show that η_{CC} is also high due to the formation of DBP percolating paths at concentrations as low as 10%. Taken together, the unique stacking properties of DBP lead to its high absorption and charge collection properties, that persist even when the fraction of DBP molecules is small compared with the C₇₀ acceptor in the blends.

2.3 Charge Transfer States in Nonfullerene Acceptor-Based OPVs

The energy loss experienced by OPVs is the difference between the photogenerated exciton energy of donor or acceptor (E_{ex}) and the V_{OC} . It sets the fundamental limits of open circuit voltage and hence the efficiency of OPVs. This loss can be as large as 0.7 eV using fullerene acceptors, although NFAs show promise for reducing this to ≤ 0.5 eV. In this Section, we systematically quantify the relationship between charge transfer energy loss (ΔE_{CT}), the non-radiative recombination loss, exciton binding energy, and intra- and inter-molecular electron-phonon

couplings. Density functional theory and comprehensive quantum mechanical modeling is used to associate molecular volume, effective conjugation length, and the nonbonding character of molecules to these several sources of energy loss.

2.3.1 Energy loss in nonfullerene acceptor-based OPVs

Excitons in organic semiconductors are tightly bound electron-hole pairs with binding energies of $E_B = 0.2$ to 1.5 eV.¹²⁹⁻¹³² A large driving force is therefore required to overcome the binding energy to separate the electron and hole in the photocurrent generation process. This force is commonly provided by the offset of the lowest unoccupied molecular orbital (LUMO) and highest occupied MO (HOMO) energies, i.e. ΔE_{LUMO} and ΔE_{HOMO} , respectively, between donor and acceptor molecular layers in a type-II heterojunction (HJ). As a result, the dissociation process incurs an energy loss during charge transfer (CT) at the interface, that is

$$\Delta E_{CT} = E_{ex} - E_{CT} \approx \Delta E_{HOMO(LUMO)} - E_B, \quad (2.3.1)$$

where E_{ex} is the exciton energy of the donor or acceptor that is generally equal to the HOMO-LUMO energy gap less E_B . Also, E_{CT} is the CT state energy. Additional losses are due to both radiative (ΔE_r) and nonradiative (ΔE_{nr}) recombination in the charge separation and extraction processes, i.e.

$$\Delta E_{rec} = E_{CT} - qV_{OC} = \Delta E_r + \Delta E_{nr}, \quad (2.3.2)$$

where V_{OC} is the open circuit voltage and q is the electron charge.¹³³ Therefore, the total energy loss at the donor-acceptor HJ is:

$$E_{loss} = \Delta E_{CT} + \Delta E_{rec} = E_{ex} - qV_{OC}. \quad (2.3.3)$$

Heterojunctions employing fullerene derivatives usually suffer from a loss of $E_{loss} > 0.7$ eV. The ΔE_{CT} required for efficient charge generation via excitation of the fullerene acceptor is higher than via excitation from the donor in a polymer:fullerene bulk HJ.¹³⁴ Alternatives for fullerene

acceptors have therefore been sought to reach a smaller E_{loss} while extending the absorption spectrum into the infrared. The development of NFAs with acceptor-donor-acceptor (a-d-a) or perylene diimide (PDI)-based molecular motifs give freedom to tune the molecular energetics, absorption spectra and thin film morphologies through molecular design.¹³⁰⁻¹³² As a result, HJs using NFAs show ΔE_{CT} as low as 0.1 to 0.2 eV, and a total $E_{loss} \leq 0.5$ eV.^{48, 135-137} This is compared to fullerene-based HJs that require $\Delta E_{CT} > 0.3$ eV for efficient charge generation, leading to a higher E_{loss} .¹³⁸⁻¹⁴⁰ While mechanism of energy losses have been discussed qualitatively or studied with specific focus over years,^{133, 141-143} to our knowledge, there is no *quantitative* analysis as to why NFAs have lower energy losses than the fullerenes. As a result, unambiguous guidelines for molecular designs that lead to lower losses have yet to be articulated.

2.3.2 Semiclassical Marcus charge transfer theory

We use semiclassical Marcus charge transfer theory to quantify both the charge transfer, k_{CT} , and non-radiative recombination, k_{nr} , rates. These rates are used to analyze the energy losses, ΔE_{CT} and ΔE_{nr} , as functions of E_B and the intra- and inter-molecular electron-phonon coupling. We compare the energy losses during exciton dissociation of a family of NFAs and fullerenes in type II BHJs, where k_{CT} vs. ΔE_{CT} are studied using temperature dependent transient PL spectroscopy, and ΔE_{nr} is analyzed by the electroluminescence quantum yield of the CT states. The large and rigid molecular backbone of thiophene-based NFA, and the presence of non-bonding orbitals introduced by cyano or chloride group substitutions, extend the electron density distribution along the molecules to reduce E_B , electron-phonon coupling, and hence reduce energy losses. Calculations using DFT and quantum mechanical modeling lead to comprehensive strategies for the design of molecular structures with low energy losses.

We focus our attention on comparing charge transfer of excitons from a variety of acceptor to donor molecules. The transition from an acceptor exciton (A^*) to a CT state (A^-/D^+) is illustrated in Fig. 2.16(a). In semiclassical Marcus theory,¹⁴⁴⁻¹⁴⁵ the rate k_{CT} for non-adiabatic transfer is given by:

$$k_{CT} = \frac{2\pi}{\hbar} V^2 F = \frac{2\pi}{\hbar} V^2 \left[\frac{1}{\sqrt{4\pi\lambda_O k_B T}} \sum_{n'} (-S)^n \frac{S^{n'}}{n!} \exp\left(-\frac{(-\Delta E_{CT} + \lambda_O + n'\hbar\langle\omega_I\rangle)^2}{4\lambda_O k_B T}\right) \right]. \quad (2.3.4)$$

Here, $V = \langle\psi_{A^*D}|H|\psi_{A^-D^+}\rangle$ is the electronic coupling between the acceptor excited state (ψ_{A^*D}) and CT ($\psi_{A^-D^+}$) wavefunctions, H is the Hamiltonian, F denotes the nuclear Franck-Condon factor, λ_O is the intermolecular reorganization energy, k_B is the Boltzmann constant, and T is the temperature. Also, S is the mean intramolecular electron-phonon coupling constant known as the Huang-Rhys factor given by $S = \lambda_I/\hbar\langle\omega_I\rangle$ where λ_I is the intramolecular reorganization energy incorporating all the coupled modes. Often, but not exclusively, the intramolecular phonon modes can be subsumed into a single mode with mean energy $\hbar\langle\omega_I\rangle$, since the dominant mode in organic molecules is carbon-carbon (C-C) bond stretching with $\hbar\langle\omega_I\rangle \approx 0.17$ eV. The Gibbs free energy for charge transfer in Eq. 2.3.4 is:

$$\begin{aligned} -\Delta E_{CT} = E_{CT} - E_{ex} &\approx |E_{HOMO_D} - E_{LUMO_A}| - (|E_{HOMO_A} - E_{LUMO_A}| - E_B) \\ &= -(\Delta E_{HOMO} - E_B), \end{aligned} \quad (2.3.5)$$

where $E_{HOMO_{D(A)}}$ and $E_{LUMO_{D(A)}}$ are the HOMO and LUMO energy of donor (acceptor) molecule, respectively. Here, the contribution of entropy to the free energy for charge transfer is neglected.

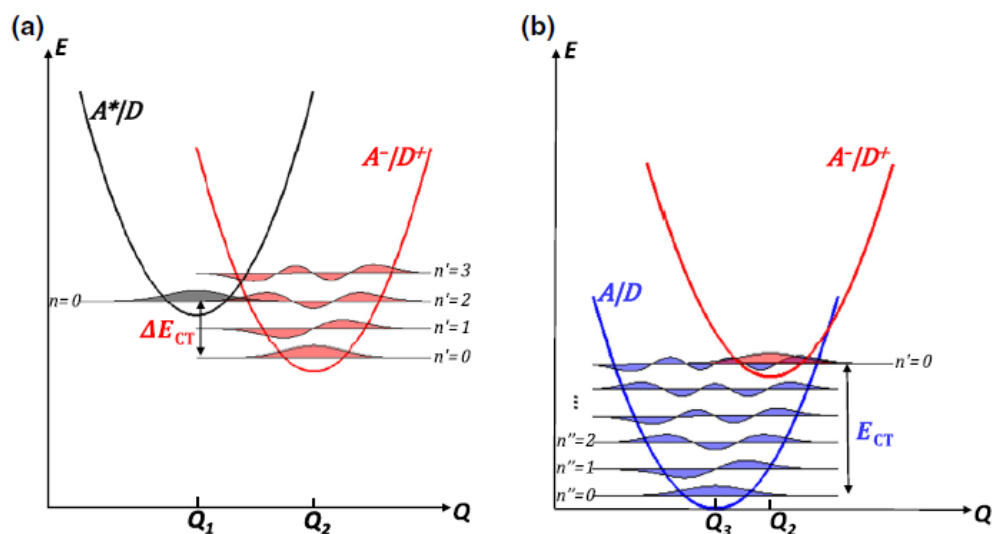


Figure 2.16 Energy diagrams of (a) charge transfer from the acceptor exciton (A^*) to the charge transfer (CT) state (A^-/D^+), and (b) nonradiative recombination from the CT state (A^-/D^+) to the ground state (A/D). The Gibbs free energies are ΔE_{CT} in (a) and E_{CT} in (b). Symmetric parabolic potentials are assumed for the initial and final states. The vibrational levels (n , n' , and $n'' = [0, 1, 2, \dots]$) are equally spaced. Equilibrium configurations of A^*/D , A^-/D^+ , and A/D manifolds are indicated by Q_1 , Q_2 and Q_3 , respectively.¹⁴⁶

The Franck-Condon factor, F , in Eq. 2.3.4 contains contributions from high frequency intramolecular phonon modes ($\hbar\omega_I \gg k_B T$) and low frequency intermolecular modes in the medium ($\hbar\omega_O \ll k_B T$). The high frequency modes are quantum mechanically treated with distinct energy levels ($n = [0, 1, 2 \dots]$) as depicted in Fig. 2.16(a). It assumes that the transition occurs from the lowest vibrational state ($n = 0$) of acceptor excitons (A^*) to the vibrational state n' in the CT (A^-/D^+) manifold. The Frank-Condon integral of the transition is hence simplified to $\exp(-S) \frac{S^{n'}}{n!'}$. The contribution of low frequency intermolecular modes is, however, lumped into λ_O in the classical Arrhenius-type exponential in Eq. 2.3.1.

The reorganization energy, λ , during charge transfer is the sum of intramolecular (λ_I) and intermolecular (λ_O) contributions. Intramolecular reorganization arises from local electron-phonon

coupling leading to a nuclear coordinate displacement $\langle \Delta Q \rangle$ between two equilibrium positions Q_1 and Q_2 (or Q_2 and Q_3 in Fig. 2.16(b)). In the harmonic approximation,

$$\lambda_I = \frac{1}{2} (M \langle \omega_I \rangle^2) \langle \Delta Q \rangle^2, \quad (2.3.6)$$

$$S = \frac{1}{2} \left(\frac{M \langle \omega_I \rangle}{\hbar} \right) \langle \Delta Q \rangle^2, \quad (2.3.7)$$

where M is the reduced nuclear mass of the system.

Intermolecular reorganization is due to the electronic polarization, and consequently the lattice relaxation of the surrounding medium. The magnitude of λ_0 can be estimated using the classical approach of Marcus.¹⁴⁷ Assuming a spherically symmetric charge distribution on the donor and acceptor, and treating the medium as an isotropic dielectric continuum, we have:

$$\lambda_0 = \frac{e^2}{4\pi\epsilon_0} \left(\frac{1}{\epsilon_{opt}} - \frac{1}{\epsilon_s} \right) \left(\frac{1}{2r_D} + \frac{1}{2r_A} - \frac{1}{R_{DA}} \right), \quad (2.3.8)$$

where ϵ_{opt} and ϵ_s are the optical and static dielectric constants, respectively, $r_{D(A)}$ is the radius of donor (acceptor), and R_{DA} is the distance between acceptor and donor molecules.

Non-radiative recombination energy losses (ΔE_{nr}) that occur through coupling from the CT (A^-/D^+) to the ground state (A/D) is illustrated in Fig. 2.16(b). There, the transfer rate is:

$$k_{nr} = \frac{2\pi}{\hbar} V'^2 \frac{1}{\sqrt{4\pi\lambda_0' k_B T}} \sum_{n''} (-S') \frac{S'^{n''}}{n''!} \exp \left(- \frac{(-E_{CT} + \lambda_0' + n'' \hbar \langle \omega_I \rangle)^2}{4\lambda_0' k_B T} \right), \quad (2.3.9)$$

where, $V' = \langle \psi_{A^-D^+} | H | \psi_{AD} \rangle$ is the electronic coupling between the CT and ground states. The Gibbs free energy in Eq. 2.3.9 is equal to the CT state energy gap E_{CT} . The energy loss, ΔE_{nr} , is given by:

$$\Delta E_{nr} = k_B T \ln \left(\frac{1}{\eta_{EL}} \right) = k_B T \ln \left(\frac{k_r + k_{nr}}{k_r} \right), \quad (2.3.10)$$

Here, η_{EL} is the internal quantum efficiency of the CT state electroluminescence.

To achieve low energy loss, the bulk exciton binding energy, E_B , needs to be minimized to decrease the potential offset (ΔE_{HOMO}) required for efficient charge transfer (c.f. Eq. 2.3.5). Secondly, decreasing both intra- and intermolecular electron-phonon coupling leads to an increased k_{CT} at a minimum cost of ΔE_{CT} , as well as a decrease in k_{nr} and thus ΔE_{nr} .

The k_{CT} as a function of ΔE_{CT} was studied by blending a family of non-fullerene and fullerene acceptors with a variety of donors in a wide energy gap poly(methyl methacrylate) (PMMA) reference at a concentration of 2 ± 1 wt%. The mixture was dissolved in chlorobenzene at a concentration of 20 mg mL^{-1} , and then spin-coated onto a Si substrate to form 100 nm thick films. Donors were chosen to have non-overlapping absorption spectra with the acceptors such that excitons are generated only on the acceptor molecules using appropriately chosen excitation wavelengths. In these dilute blends, the acceptor domains are small compared to the exciton diffusion length. This simplifies the analysis by eliminating the dynamics of exciton diffusion. Then, k_{CT} is calculated from the difference between the acceptor exciton lifetime in the type-I PMMA-acceptor HJ and that at the type-II donor-acceptor HJ.

Exciton dynamics were measured by time-resolved PL using a time-correlated single photon counter (PicoHarp 300, PicoQuant GmbH) coupled to a Si single photon avalanche detector (PDM Series, PicoQuant GmbH). The acceptor molecules were excited at $\lambda = 725 \text{ nm}$ for NFAs, and 560 nm for fullerene derivatives using 150 fs pulses at a 1 kHz repetition rate from a Ti:sapphire laser (CPA-2110, Clark-MXR Inc.)-pumped optical parametric amplifier (TOPAS-C, Coherent). Charge transfer dynamics vs. temperature in the range between 295 K and 25 K were obtained in a closed-cycle cryostat (SHI-4-5, Janis Research Company LLC).

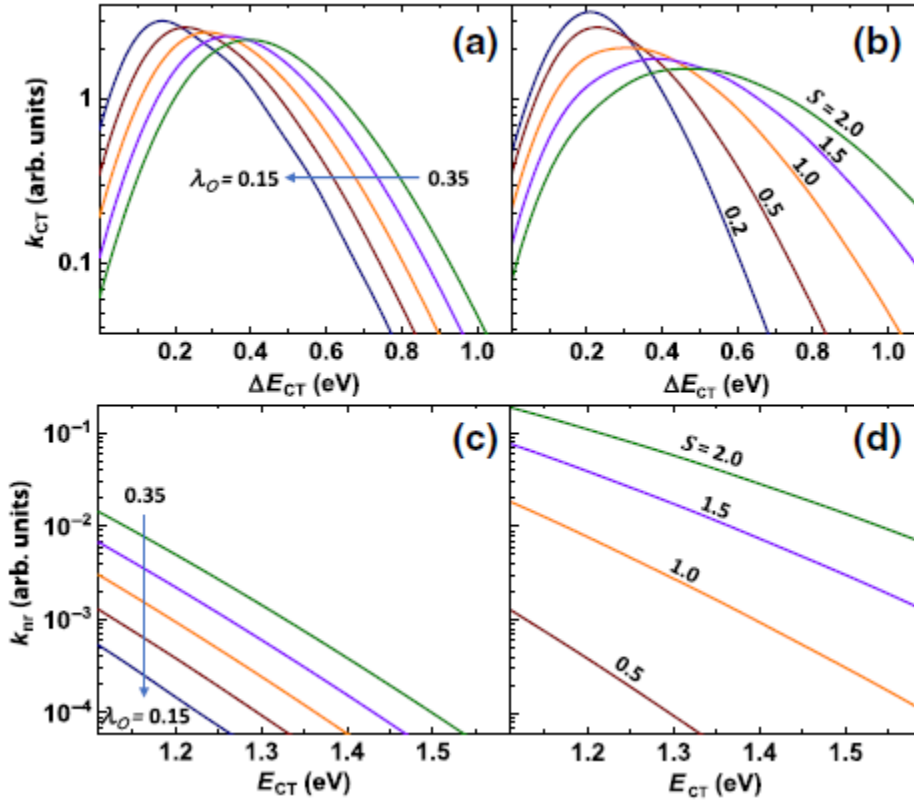


Figure 2.17 Charge transfer rate, k_{CT} , vs the energy loss on CT state formation, ΔE_{CT} , as functions of (a) the intermolecular reorganization energy, λ_0 , and (b) intramolecular coupling strength, S . (c) Nonradiative recombination rate k_{nr} vs E_{CT} as functions of λ_0 and (d) S .

Calculations of k_{CT} and k_{nr} using Eqs. (2.3.4) and (2.3.9) at $T = 300\text{ K}$ are shown in Fig. 2.17. For convenience, we set V^2 and V'^2 equal to unity. Figures 2.17(a) and (b) show that reducing λ_0 and S , respectively, lead to an increased maximum in k_{CT} that occurs at a lower ΔE_{CT} . Note that k_{nr} vs. E_{CT} in Figs. 2.17(c) and (d) have a Marcus inverted relationship in the range of E_{CT} we consider. This is a version of the “energy gap law”^{142, 148} where k_{nr} decreases with increasing E_{CT} . Decreasing λ_0 and S further reduces k_{nr} at a given E_{CT} , and hence non-radiative recombination ΔE_{nr} , according to Eq. 2.3.10. All four figures show that a decrease of S results in a more pronounced change of k_{CT} and k_{nr} than that for λ_0 .

2.3.3 Exciton binding energy vs. molecular size

The parameters, E_B , S and λ_0 in Eqs. 2.3.4, 2.3.5 and 2.3.9 that determine energy losses are closely correlated with the molecular structure. We, therefore, systematically analyzed the exciton binding energies, molecular polarizabilities and intramolecular reorganization of fullerenes and NFAs by DFT. The exciton binding energy is $E_B = (E_- + E_+) - (E_{gnd} + E_{ex})$, where E_- and E_+ are the optimized energies of radical anions and cations of the molecule, respectively. Also, E_{gnd} and E_{ex} are the ground and first singlet excited state energies, respectively.

Molecular level electron density distributions of NFAs and fullerenes, and their energy levels were modeled using DFT/ TDDFT in the Gaussian 09w package.¹⁴⁹ The calculation of exciton binding energy and reorganization energy was based on the B3LYP functional and the 6-31G(d) basis set. Molecular solvation effects are considered by combining the DFT calculations with the Polarizable Continuum Model.¹⁵⁰ Figure 2.18 shows the molecular structures of the archetypical a-d-a type NFAs. The electron-donating conjugate backbone is capped with two electron-withdrawing side groups. The electron and hole distributions of the excited state along the long molecular axis of BT-CIC is shown in Fig. 2.18(b). The conjugated electron system is shown by the bold, red line bridging the electron-donating thiophene backbone to the electron deficient cyano and Cl groups. This charge distribution results in symmetric intramolecular charge transfer (ICT) from the middle to two ends of the molecule upon optical excitation. Also, the relative segregation of electron and hole densities results in a reduced E_B (see below). Two other molecules with a different number of thiophene rings, and hence a shorter conjugated backbone with reduced ICT are shown for comparison in Fig. 2.18(c).

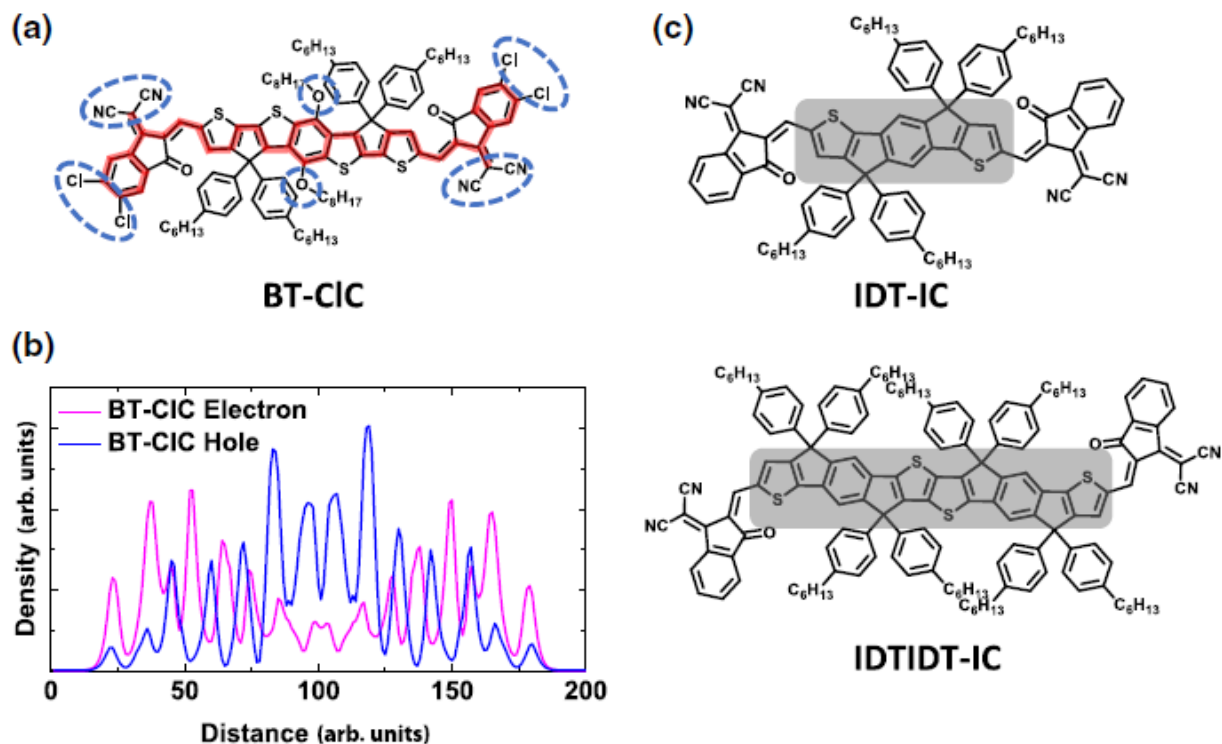


Figure 2.18 (a) The molecular structure of BT-C1C. The red bold line traces the electron-conjugation path comprising alternating C-C single and double bonds. Blue dashed circles indicate the electron-rich (i.e., oxy-) and deficient (i.e., chloro- and cyano-) moieties that affect the electron distributions in the molecules. (b) The electron and hole density distributions along the molecular length of BT-C1C calculated using DFT. (c) The molecular structural formulas of IDT-IC and IDTIDT-IC that have different lengths of the electron-donating cores as indicated in the shaded regions.

Figure 2.19(a) shows calculated E_B of a variety of fullerenes and NFAs vs. the *effective molecular volume*. All the chemical names and structures of the fullerenes and NFAs are listed in the Supplementary Information. The effective molecular volume $v = l \cdot w \cdot h$ is determined from the molecular length l , width w , and height h that are defined by a box whose boundaries are at the distance where electron density falls below 0.02 au^{-3} . Figure 2.19(a) shows that the exciton binding energy E_B decreases with increasing v . Also, the slope of E_B vs. v decreases until $v > 1.5 \text{ nm}^3$. Figure 2.19(b) shows the calculated static polarizabilities, α_{xx} , along the molecular length, l of this same population of acceptors. Since the electron distribution is spread along the conjugated molecular donating backbone unit, α_{xx} increases with l , along the backbone. This corresponds to

the x coordinate, and y and z along w and h , respectively. The full polarizability tensors of the molecules are provided in the Table 2.3.1.

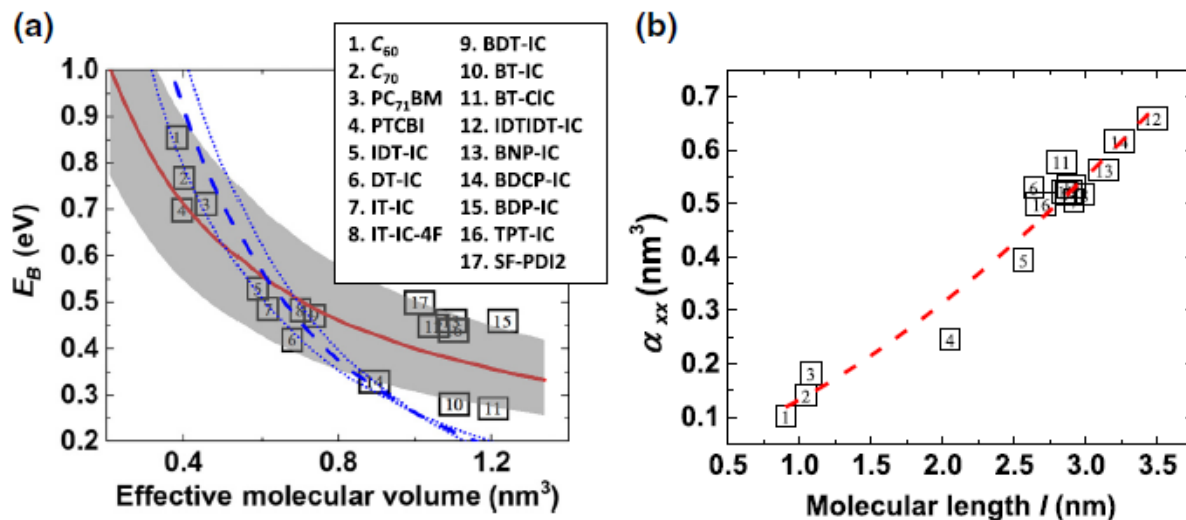


Figure 2.19 Exciton binding energy, E_B , found via DFT vs effective molecular volume for several acceptor molecules indicated in legend whose molecular formulas are in Appendix A. The red solid line is a fit assuming electron confinement within the effective molecular volume for each molecule. The calculation assumes a dielectric parameter, $f = 5.4$. The shaded area is the 95% confidence band. The blue dashed line assumes f depends on molecular polarizability from (b). The confidence limits of the calculations are shown by dotted lines. (b) The calculated molecular polarizability along the molecular longitudinal axis, α_{xx} , vs the effective molecular length l . The dashed line is the fit using an empirical power law described in text.

Table 2.1 The calculated polarizability (Unit: nm³) tensor of fullerenes and NFAs.

	α_{xx}	α_{yx}	α_{yy}	α_{zx}	α_{zy}	α_{zz}
C ₆₀	0.102	0.000	0.102	0.000	0.000	0.102
C ₇₀	0.141	0.000	0.127	0.000	0.000	0.127
PC ₇₁ BM	0.182	-0.006	0.145	-0.004	-0.002	0.141
PTCBI	0.246	0.003	0.081	0.000	0.000	0.019
IDT-IC	0.394	0.012	0.165	-0.006	0.002	0.084
DT-IC	0.530	-0.031	0.167	0.000	0.000	0.087

IT-IC	0.505	0.001	0.172	0.000	0.000	0.089
IT-IC-4F	0.517	-0.014	0.174	0.000	0.000	0.090
BDT-IC	0.519	0.031	0.175	0.000	0.000	0.089
BT-IC	0.523	0.031	0.183	0.000	0.003	0.094
BT-CIC	0.579	-0.043	0.200	-0.002	0.002	0.096
IDTIDT-IC	0.660	-0.022	0.236	0.000	0.000	0.151
BNP-IC	0.563	0.036	0.190	-0.002	0.005	0.097
BDCP-IC	0.616	-0.034	0.197	0.005	0.001	0.098
BDP-IC	0.533	-0.053	0.185	0.003	0.001	0.095
TPT-IC	0.499	0.043	0.167	-0.004	0.003	0.095

The intramolecular reorganization energy on electron transfer is $\lambda_I^- = (E_0^* - E_0) + (E_-^* - E_-)$, where E_0 and E_- are the energies of the neutral and radical anion molecules in their optimized geometries, respectively, and E_0^* and E_-^* are energies of the neutral and radical anion molecules in the unrelaxed geometries, respectively. Table 2.3.2 lists the calculated λ_I^- of PC₇₁BM and three a-d-a type NFAs in Fig. 2.20(a) and (c). Non-fullerene acceptors have smaller intramolecular reorganization energies on electron transfer than PC₇₁BM. Introducing electron-donating oxy-, electron-withdrawing cyano-, and chloro- moieties (Fig. 2.20(a)), or extending the conjugation length of the middle subgroup (Fig. 2.20(c)) further reduce λ_I^- .

Table 2.2 The intramolecular reorganization energy upon electron transfer λ_I^- of archetypical fullerenes and NFAs.

	PC ₇₁ BM	IDT-IC	IDTIDT-IC	BT-CIC
--	---------------------	--------	-----------	--------

λ_I^- (eV)	0.180	0.179	0.101	0.157
--------------------	-------	-------	-------	-------

The k_{CT} from BT-CIC (or BT-IC), IT-IC and fullerene derivatives are measured as functions of ΔE_{CT} , with the results shown in Fig. 2.17. The NFA-based HJs show non-monotonic changes of k_{CT} as ΔE_{CT} increases, indicative of the Marcus normal (non-shaded) and inverted (shaded) regimes that are separated by the ΔE_{CT} at which k_{CT} is maximized. The k_{CT} of fullerene derivatives in Fig. 2.17(c) however do not reach a maximum, but rather increase monotonically until $\Delta E_{CT} = 0.6$ eV which is at energies short of the inverted region.

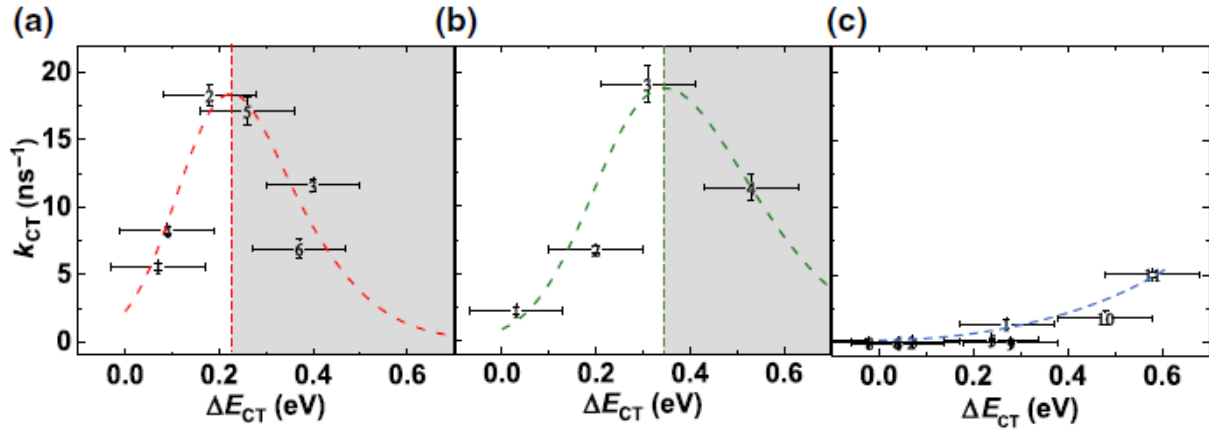


Figure 2.20 Measured k_{CT} vs ΔE_{CT} for HJs comprising (a) 1. BT-IC/PBDBT, 2. BT-IC/J61, 3. BT-IC/P3HT, 4. BT-CIC/PCDTBT, 5. BT-CIC/PBDBT, 6. BT-CIC/J61, (b) 1. IT-IC/PCDTBT, 2. IT-IC/PBDBT, 3. IT-IC/J61, 4. IT-IC/P3HT, and (c) 1. PC₇₁BM/F8T2, 2. PC₇₁BM/F8, 3. PC₇₁BM/F8BT, 4. ICBA/F8T2, 5. PC₆₁BM/F8T2, 6. PC₆₁BM/F8, 7. PC₆₁BM/F8BT, 8. C₇₀/CBP, 9. C₇₀/TCTA, 10. C₇₀/NPD, and 11. C₇₀/TPTPA. The dashed lines in (a) and (b) are the fits using semi-classical Marcus theory [Eq. (2.3.4) in text]. The blue dashed line in (c) is a guide to the eye. Nonshaded sections are the Marcus normal regions, and shaded sections are the inverted regions. All molecular structural formulas are found in Appendix A.

We also measured k_{CT} as a function of temperature for two HJs, BT-IC/PBDBT and IT-IC/PBDBT, with results shown in Fig. 2.21 (a) and (b), respectively. Both systems show two distinct regimes with a transition at $T_X = 120$ K. At $T > T_X$, k_{CT} decreases rapidly with temperature, characteristic of thermally activated behavior for charge transfer. At lower

temperatures (i.e., $T < T_X$), k_{CT} becomes relatively temperature independent due to the dominance of tunneling in the charge transfer process.

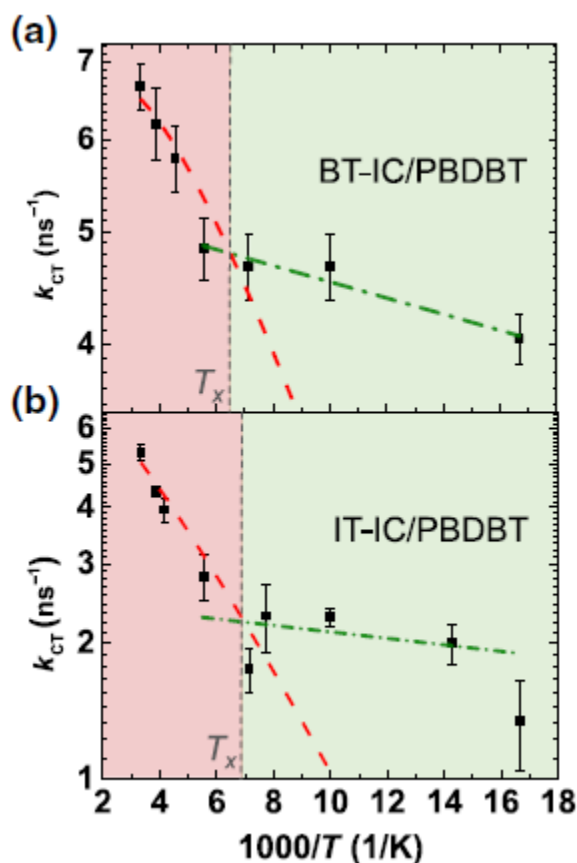


Figure 2.21 Measured k_{CT} vs temperature, T , for (a) BT-IC/PBDBT and (b) IT-IC/PBDBT HJs. The dashed lines are the fits assuming thermal activation.

2.3.4 EL and EQE spectra of OPVs with various BHJs

Nonradiative coupling between the CT and ground states possesses the same Franck-Condon factor as in radiative coupling.¹⁴² We therefore measured the Frank-Condon shift between absorption and emission spectra of CT state to probe the electron-phonon coupling strength during the nonradiative recombination. OPVs are fabricated with structures: ITO/ZnO/BHJ/MoO₃/Al. The 20 nm thick ZnO layer was spin-coated onto a precleaned, UV-ozone-treated ITO anode,

followed by 30 min thermal annealing at 150 °C in air. The 100 nm thick BHJ layer was spin-coated on the ZnO, followed by thermal evaporation of a 10 nm thick MoO₃ buffer and a 100 nm thick Al cathode at a chamber base pressure of 2×10^{-7} torr. The external quantum efficiency was measured using the photocurrent of devices coupled to a lock-in amplifier (Stanford Research Systems SR830) while being excited by monochromated light from a Xe arc-discharge lamp chopped at 200 Hz. Photoluminescence and EL spectra were measured using a fiber-coupled monochromator (Acton series SP2300i, Princeton Instruments) equipped with a Si charge-coupled device array (PIXIS:400, Princeton Instruments).

Electroluminescence spectra of PC₇₁BM/PBDBT and IT-IC/PBDBT OPVs in Fig. 2.22 show CT emission peaks at 1.23 ± 0.01 eV and 1.37 ± 0.01 eV, respectively. We extract the CT state absorption spectra by Gaussian fits of external quantum efficiency spectra at the low energy shoulders using the same full width half maximum (FWHM) as the corresponding emission spectrum. The Frank-Condon shift of the PC₇₁BM/PBDBT HJ is $E_{FC} = 0.45 \pm 0.02$ eV, while for IT-IC/PBDBT, $E_{FC} = 0.22 \pm 0.02$ eV.

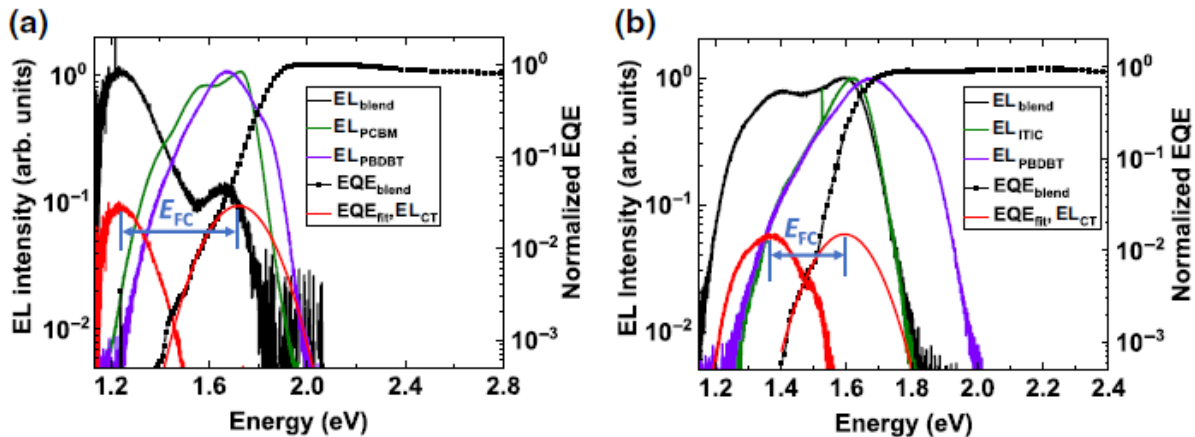


Figure 2.22 Electroluminescence (EL) and external quantum efficiency (EQE) spectra of OPVs based on (a) neat IT-IC, PBDBT, and their blended heterojunction. (b) Neat PC₇₁BM, PBDBT, and their blended heterojunction. The CT state emission at low energy is extracted from the EL spectra by subtracting the spectra from the neat layers. The CT state absorption spectra are extracted by a Gaussian fit of the EQE spectra along the low energy shoulders. The arrows between the short lines indicate the Franck-Condon shift, E_{FC} , of the CT spectra.

2.3.5 Strategies to design molecules with low energy losses

For a given offset of the donor and acceptor HOMO energies, the Gibbs free energy of hole transfer from acceptor to donor, $\Delta E_{CT} = \Delta E_{HOMO} - E_B$, is maximized by minimizing the acceptor exciton binding energy and hence increase k_{CT} in the Marcus non-inverted regime. The combined influences of molecular size, conjugation length, and strength of the electron donating and withdrawing groups determines the amount of ICT in the acceptors,¹⁴⁹⁻¹⁵² ultimately determines E_B . The molecular size and the availability of sp^2 hybridized atoms in the molecules determine the extent of conjugation, and hence the mean separation of the electron and hole orbital distributions. A rigid coplanar structure of a-d-a type small molecule NFAs ensures that the electron wavefunction is delocalized over the entire molecular backbone, unlike polymers that can twist at the C-C single bonds that ultimately terminates the extent of the excited state.¹⁵³ This is apparent from the DFT calculations of the electron and hole densities of BT-CIC in Fig. 2.18(b). The oscillations in the densities are due to variations in electron and hole wavefunctions at each of the thiophene rings as well as the end caps. The low electron concentration at the molecular center of mass relative to the capping groups results from their electron donating and withdrawing character, respectively, and leads to a reduction in the electron-hole (i.e., exciton) binding energy.

To estimate the effects of molecular size on the exciton binding energy, we use a simplified electron wavefunction for a particle in a three dimensional box, i.e. $\Psi_{n_x, n_y, n_z} = \sqrt{\frac{8}{v}} \sin\left(\frac{n_x \pi x}{l}\right) \sin\left(\frac{n_y \pi y}{w}\right) \sin\left(\frac{n_z \pi z}{h}\right)$, where n_x, n_y, n_z are the quantum numbers. This fits the result in Fig. 2.18(a), whereby the E_B vs. effective molecular volume monotonically decreases,

independent of the details of the molecules studied (i.e., fullerenes or NFAs). For this analysis, we assume an average molecular height of $h = 0.3$ nm and width $w = 0.8$ nm and vary the length l according to the dimensions of the molecule. As noted above, l is taken between points where the electron density falls below 0.02 au^{-3} . Then the wavefunctions Ψ_{n_x, n_y, n_z} and exciton binding energies are solved using Schrödinger's equation to give the binding energy:

$$E_B = q^2 \int \frac{|\Psi_{0,0,0}(\mathbf{r}_h)|^2 \cdot |\Psi_{1,0,0}(\mathbf{r}_e)|^2}{f \cdot 4\pi\epsilon_0 |\mathbf{r}_h - \mathbf{r}_e|} d\mathbf{r}_h^3 d\mathbf{r}_e^3. \quad (2.3.11)$$

where the hole and electron wavefunctions are $\Psi_{0,0,0}$ and $\Psi_{1,0,0}$, respectively, \mathbf{r}_h and \mathbf{r}_e are the coordinate vector of hole and electron, respectively, q is the electron charge. Here, f is a fitting parameter that accounts for the relative dielectric constant of the molecule. The solid line in Fig. 2.19(a) corresponds to $f = 5.4$, which approximately fits the entire population of acceptors studied. This is indeed remarkable, given that the molecular structures vary significantly from molecule to molecule, and from highly symmetric fullerenes to planar NFAs. The shaded region depicts the 95% confidence band between $f = 6.8$ and 4 . The deviations of the data from the solid line are associated with details of the molecular structures that impact the molecular polarizabilities and relative dielectric constants in the solid.

As shown in Fig. 2.19(b), the polarizability α_{xx} vs. molecular length l follows an empirical power dependence,^{5, 154}

$$\alpha_{xx} = \alpha_0 + \alpha_1 l^n. \quad (2.3.12)$$

Here, α_0 is the polarizability of terminal bonds such as C-H, α_1 is related to the polarizability of conjugated or non-conjugated chains of length l . A fit to the data gives $\alpha_0 = 0.035 \pm 0.075 \text{ nm}^3$,

$\alpha_1 = 0.098 \pm 0.060 \text{ nm}^3$, and $n = 1.51 \pm 0.44$. A superlinear increase of polarizability ($n > 1$) is due to the contributions of conjugation and ICT.¹⁵¹ The relationship between the dielectric constant of the medium and the polarizabilities of each constituent, α_i , is given by the Clausius-Mosotti relationship:

$$\frac{\varepsilon - 1}{\varepsilon + 2} = \sum_i \frac{N_i \alpha_i (4\pi \varepsilon_0)}{3\varepsilon_0}. \quad (2.3.13)$$

where the molecular packing density is N_i . The effect of dielectric constant change on E_B can be estimated by using Eq. 2.3.12 and 2.3.13 to replace f of Eq. 2.3.11 and assuming an isotropically polarizable medium comprising randomly oriented molecules with $N = 1.3 \text{ nm}^{-3}$ to yield the dash line in Fig. 2.19(a). The fit closely follows the data for molecules 1 to 11 compared to the that using a constant f , despite a slight overestimation due to simplifications used to approximate molecular structure. The less accurate fits to molecules 12, 13, 15 - 17 is attributed to molecular bends that disturbs the electron distribution to increase E_B .

Achieving a maximum k_{CT} at a small energy loss, ΔE_{CT} , and a minimum k_{nr} requires simultaneously reducing both the intra- and intermolecular electron-phonon coupling. We have shown that λ_0 can be reduced by increasing the extent of electron conjugation. The intramolecular coupling S also changes with the size and rigidity of the molecules. Studies of oligoacenes, polythiophenes, fused thiophenes, etc.¹⁵⁵ have shown that $S \propto \frac{1}{N_{C-C}} \propto \frac{1}{n}$, where, N_{C-C} is the number of carbon-carbon bonds, and n is the number of aromatic rings. Bond length adjustment is smaller when accommodating a more delocalized charge distribution. In NFAs, extending the conjugation length along the donor subgroup is one of the effective methods, as shown in Table 1. Another feature of molecules that leads to a reduced S as shown in Fig. 2.18 (a) is the nonbonding character of the molecules. Calculations suggest that the primary intramolecular mode appears

along the conjugated carbon chains forming the backbone, indicated by the bold line tracing the conjugation path. The presence of nonbonding orbitals in the cyano, chloro or oxy groups introduce lone pair electrons that do not participate in bonding, and that avoid electron-phonon coupling. At the same time, the cyano and chloro groups can attract electrons and reduce the charge density along the backbones. This, in turn, reduces local electron-phonon coupling.

A result of low local electron-phonon coupling, S , and small intermolecular coupling λ_O in NFAs, the cost of Gibbs free energy $-\Delta E_{CT}$ for achieving a maximum k_{CT} is lower than that of the more compact fullerenes. In particular, HJs using BT-IC achieves a maximum k_{CT} at only $\Delta E_{CT} = 0.22$ eV,⁴⁸ which is slightly lower than IT-IC, of $\Delta E_{CT} = 0.35$ eV. Equation 2.3.4 is applied to fit both Fig. 2.20 and the temperature dependent results above T_X in Fig. 2.21. From the fits, we obtain $\lambda_O = 0.21 \pm 0.03$ eV and $S = 0.30 \pm 0.10$ for BT-CIC (BT-IC)/donor HJs, and $\lambda_O = 0.35 \pm 0.11$ eV and $S = 0.54 \pm 0.12$ for IT-IC/donor HJs. In contrast, fullerene/donor HJs show an unconstrained fit where $\lambda_I + \lambda_O > 0.6$ eV.

Charge transfer states are characterized by the strength of electron-phonon coupling and reorganization energy, λ_{CT} , during recombination, that can be determined via their Frank-Condon shifts as shown in Fig. 2.22. The Frank-Condon shift is twice the total reorganization energy, i.e., $E_{FC} = 2\lambda_{CT}$, yielding $\lambda_{CT} = 0.11$ eV for IT-IC/PBDBT compared to $\lambda_{CT} = 0.23$ eV for PC₇₁BM/PBDBT. This results in a higher k_{nr} of the latter system, according to Fig. 2.17. Thus, $\eta_{EL} = \frac{k_r}{k_r + k_{nr}}$ is higher in the IT-IC/PBDBT HJ. Calculations of the non-radiative recombination loss using Eq. 2.3.10 and η_{EL} of IT-IC/PBDBT and PC₇₁BM/PBDBT HJs yield a 0.05 ± 0.01 eV smaller ΔE_{nr} in IT-IC system, leading to the generally higher power conversion efficiencies observed for NFA vs. fullerene based OPVs

The foregoing understanding of the dependence of energy loss on molecular structure, suggests molecular design strategies that can further reduce energy loss. Currently, all a-d-a-type NFAs have symmetric electron-withdrawing end groups that possess a nearly zero dipole moment. However, asymmetric electron withdrawing end groups in a-d-a molecules can provide freedom to tune the dipole moment and further reduce E_B , S , and λ_0 by changing the effective intramolecular electron-hole separation and molecular packing in bulk heterojunctions. Additionally, the relationship between molecular dimension, rigidity and energy loss obtained from our analysis points to the benefits of enlarging the molecular volume. However, there is a limit to the extent to which the length of the donor backbone can be increased. When the backbone is too long, total intermolecular interactions applied on the backbone can be large enough to cause bending or distortion and hence terminating the effective conjugation length. However, extending the conjugation into two and three dimensions provides can further reduce E_B , S , and λ_0 , as compared to one-dimensional conjugation used up to now. This additional degree of freedom may also enhance the intermolecular π - π interactions along all directions, leading to increased charge carrier mobilities. Indeed, early demonstrations of increasing the molecular volume in two dimensions based on dithienopicenocarbazole-based a-d-a-type¹⁵⁶ or spiro-fused perylene diimide NFAs¹⁵⁷ provide an illustration of the benefit of this molecular design.

2.4 Conclusions

We studied the relationship between CT state energies and levels of quantum confinement in DBP:C₇₀ BHJs and alternating layer stacks. The change of C₇₀ domain size leads to a change in the CT exciton binding energy and lifetime, which is accurately fit by assuming that the electron and hole Coulombically bound across the HJ are confined within their separate domains. Two discrete CT peaks are attributed to the delocalized and localized CT excitons in crystalline C₇₀ and

amorphous DBP:C₇₀ mixed phases, respectively. As the fractional volume of the C₇₀ crystalline phase increases with C₇₀ concentration or alternating layer thickness, an increased probability for generation of delocalized CT₂ states leads to efficient photogeneration in the surprisingly dilute DBP:C₇₀ HJs. Kinetic Monte Carlo simulations of the deposition process illustrate the formation of DBP percolation pathways which allows hole collection in BHJs with low donor concentrations.

For BHJs of NFAs, we applied the semi-classical Marcus theory to quantify the impact of exciton binding energy and electron-phonon coupling in both charge transfer loss and nonradiative recombination loss. The calculations fit to the experimental results of charge transfer and recombination loss using a variety of fullerene derivatives and thiophene-based NFAs paired with donor molecules. Our analysis unambiguously points out the benefits of enlarging the conjugated volume and introducing non-bonding characters by electron-donating and -withdrawing moieties in the reducing the sources of energy loss and provides guidelines for future molecular design.

Chapter 3

Interfacial Energy Loss in Organic Photovoltaics

3.1 Introduction

As described in Section 2.3, the energy loss, usually defined as the energy difference between the optical gap and the open circuit voltage, V_{oc} , is a defining feature of OPV performance.¹⁴⁷ Many studies of energy losses incurred during photogeneration including the ones in Chapter 2 have focused primarily on the role of CT states in BHJ OPVs.^{76, 90, 158-160} However, CT states are not the only source of energy loss. In this section, we reveal that the interfaces between the organic BHJ and the buffer layers can be as a significant source of energy loss in DBP/C₇₀ OPVs, along with several commonly used ABLs including MoO_x, PEDOT:PSS and HAT-CN.¹⁶¹⁻¹⁶⁴ The energy landscape near the active region/ABL interface is studied using ultraviolet photoelectron spectroscopy (UPS). We find that for MoO_x and PEDOT:PSS, there is frontier energy level bending near the active region/ABL interface that leads to energy losses.¹⁶⁵ By independently controlling the D/A ratio of the BHJ near the active region/ABL interface, V_{oc} can be varied over a range of 120 ± 10 mV independent of the J_{sc} and FF . Kinetic Monte Carlo (kMC) simulations are used to quantitatively evaluate the interfacial energy loss by simulating the charge dynamics near the active region/ABL interface. Inserting a thin layer of acceptor between

the BHJ and certain anode buffer layers is found to reduce the energy loss and increase the V_{oc} compared with conventional device architectures.

3.2 Identifying the Interfacial Energy Loss

3.2.1 Theoretical derivations

We start the investigation by focusing on archetype DBP/ C_{70} based OPVs with a MoO_x ABL and a bathophenanthroline (BPhen) cathode buffer layer. To study the interface and the bulk properties separately, we insert a thin anode interface layer (AIL) between the BHJ (hereafter referred to as the bulk layer) and the ABL with various C_{70} concentrations (x) from that in the bulk layer (y), as shown in Fig. 3.1(a). MoO_x is a commonly used anode buffer material with a work function of 6.8 eV.¹⁶³ Photogenerated holes are extracted through the MoO_x by recombining with electrons injected from the anode.^{161, 166} It has been reported that, due to the high work function of MoO_x , electrons in the HOMO of the donor transfer into the MoO_x conduction band (CB), pinning its Fermi level to near the organic HOMO.^{74, 161, 166-167} The electric field from the resulting static interface dipole causes the orbital energies near the interface to bend towards the lower binding energy direction, while also broadening the density of states (DOS) on the organic side of the interface.^{73, 165, 168}

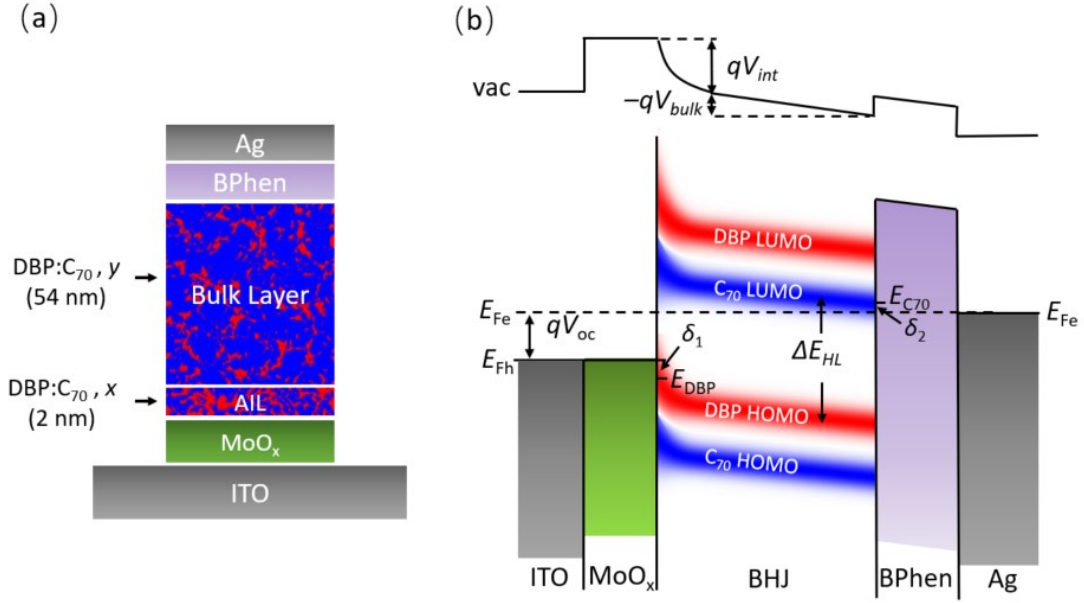


Figure 3.1 (a) OPV structure with the active region divided into the interface and the bulk regions with C_{70} concentrations of x and y , respectively. (b) Energy level diagram of a DBP/ C_{70} OPV at open circuit. The blurred red/blue lines represent the DBP/ C_{70} HOMOs with a finite width of the density of states.

Figure 1(b) shows the energy level diagram of the OPV at open circuit. We assume the hole quasi-Fermi level E_{Fh} is at δ_1 above the DBP HOMO level on the anode side, E_{DBP} , and electron quasi-Fermi level E_{Fe} is at δ_2 below the C_{70} LUMO level on the cathode side, E_{C70} . Note δ_1 and δ_2 can be either positive or negative based on the energy alignment on the interfaces. Then E_{DBP} and E_{C70} have following relationship:

$$E_{DBP} = E_{C70} - \Delta E_{HL} - qV_{bulk} + qV_{int}, \quad (3.2.1)$$

where ΔE_{HL} is the energy offset between C_{70} LUMO and DBP HOMO, V_{bulk} is the voltage drop across the bulk active layer, V_{int} is the voltage drop across the AIL due to the presence of a static interface dipole and q is the elementary charge. Note that the direction of V_{int} is defined as opposite to that of V_{bulk} and the external device voltage, V , by convention. Therefore, V is:

$$qV = E_{Fe} - E_{Fh} = (E_{C70} - \delta_2) - (E_{DBP} + \delta_1) = \Delta E_{HL} - \delta_2 - \delta_1 + qV_{bulk} - qV_{int}, \quad (3.2.2)$$

Figure 3.2(a) shows the energy level diagram near the BHJ/MoO_x interface, with the electron and hole currents represented by blue and yellow arrows, respectively. When forward-biased, electrons transfer from the organic HOMO into MoO_x, leaving holes in the organic that flow into the BHJ and recombine with electrons injected from cathode. This is the dark current J_D . Under illumination, a photocurrent, J_{ph} , generated in the active region flows through the ABL interface where photogenerated holes recombine with electrons in the MoO_x. While J_D depends on both the interface and bulk properties, J_{ph} depends primarily on recombination in the bulk, provided that interface recombination is insignificant. Under open-circuit conditions, $J_D = -J_{ph}$ and the total current is zero.

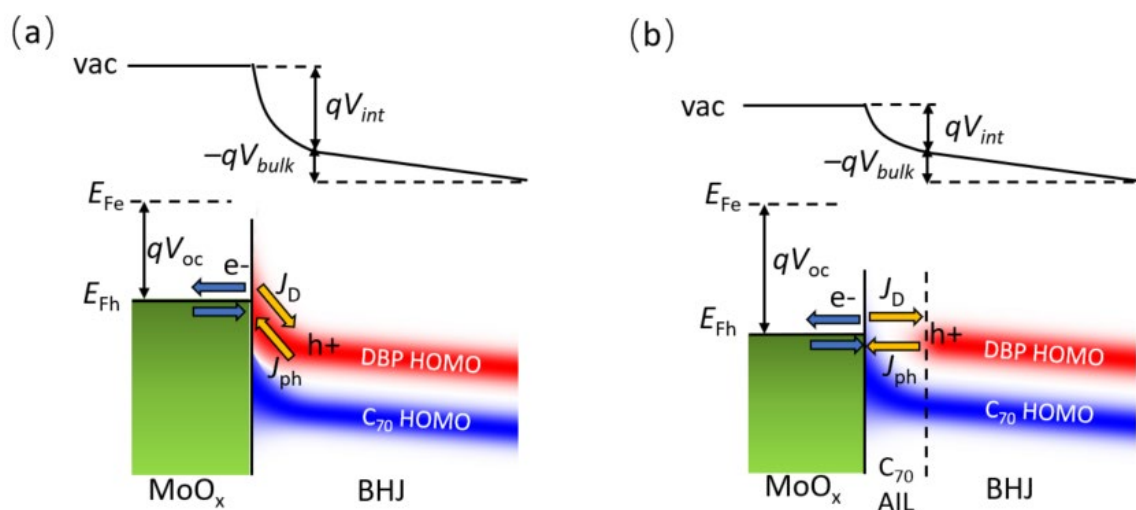


Figure 3.2 (a) Energy level diagram near the interface between a DBP/C₇₀ mixed layer and MoO_x at open circuit. The blue and yellow arrows represent the flow of electrons and holes, respectively. (b) Energy level diagram near the interface between a DBP/C₇₀ mixed layer and MoO_x at open circuit when a 2-nm-thick neat C₇₀ anode interface layer (AIL) is inserted between the bulk layer and the MoO_x.

Because the BHJ blend morphology is isotropic, photogenerated charges require the guidance of the electric field in the BHJ to reach the electrodes. The direction of J_{ph} is decided by

the sign of V_{bulk} . Thus it follows that when $V_{\text{bulk}} = 0$, then $J_{\text{ph}} = 0$. Assuming the current dependences of δ_1 , δ_2 and V_{int} are small, Eq. (3.2.2) becomes:

$$qV(J_{\text{ph}} = 0) = \Delta E_{\text{HL}} - \delta_2 - \delta_1 - qV_{\text{int}}. \quad (3.2.3)$$

Then, using Eq. (3.2.2) and (3.2.3):

$$V = V(J_{\text{ph}} = 0) + V_{\text{bulk}}. \quad (3.2.4)$$

This scenario suggests that reducing V_{int} may be an effective way to reduce energy losses at the active region/ABL interface. To achieve this objective, we can eliminate the DBP in the AIL, as shown in Fig. 3.2(b). The deeper HOMO of C_{70} pins the Fermi level of MoO_x , resulting in a reduced V_{int} . Hole transport between the DBP HOMO in the bulk and the C_{70} HOMO in the AIL is required to extract photogenerated holes.⁶³ As long as the AIL is thin, this transport can be via tunneling and hence is *non-dissipative*. Therefore, V_{oc} will undergo a rigid shift without a change in V_{bulk} and J_{ph} .

3.2.2 Impact of interfacial energy loss on J-V characteristics

To test the dependence of energy loss on the properties of the AIL, we fabricated the following devices: indium tin oxide (ITO) /ABL/ C_{70} :DBP (2 nm, x) / C_{70} :DBP (54 nm, y) / BPhen (8 nm) /Ag (100 nm), where $x = 0\%$ to 100% , and $y = 20\%$ to 90% are the C_{70} concentrations in the interface and bulk layers, respectively (see Fig. 3.1(a)). The ITO coated glass substrates were solvent-cleaned and exposed to ultraviolet ozone for 10 min before use. The ABLs studied are MoO_x , PEDOT:PSS and HAT-CN. The PEDOT:PSS solution (Clevios P VP AI 4083 from Heraeus Clevios™) was filtered with a $0.45 \mu\text{m}$ Nylon syringe filter and spin coated onto the substrate at 6,000 rpm for 60 s. The sample is then annealed at $150 \text{ }^\circ\text{C}$ for 30 min. The thickness of the PEDOT:PSS layer was measured to be 40 – 50 nm using an ellipsometer. The 10-nm-thick MoO_x and HAT-CN ABLs are deposited along with the other layers using VTE at rates between

0.2 to 1.6 Å/s in a chamber with a base pressure of 10^{-7} Torr. The mixed active layers were co-deposited at a rate of 0.2 Å/s for DBP, while the deposition rate for C_{70} was adjusted to achieve the desired volume ratio. The devices were tested in a glovebox filled with ultrapure N_2 (< 1 ppm O_2 and H_2O) in the dark and under simulated AM1.5G illumination from a calibrated solar simulator at an intensity of 100 mW/cm^2 (1 sun equivalent).

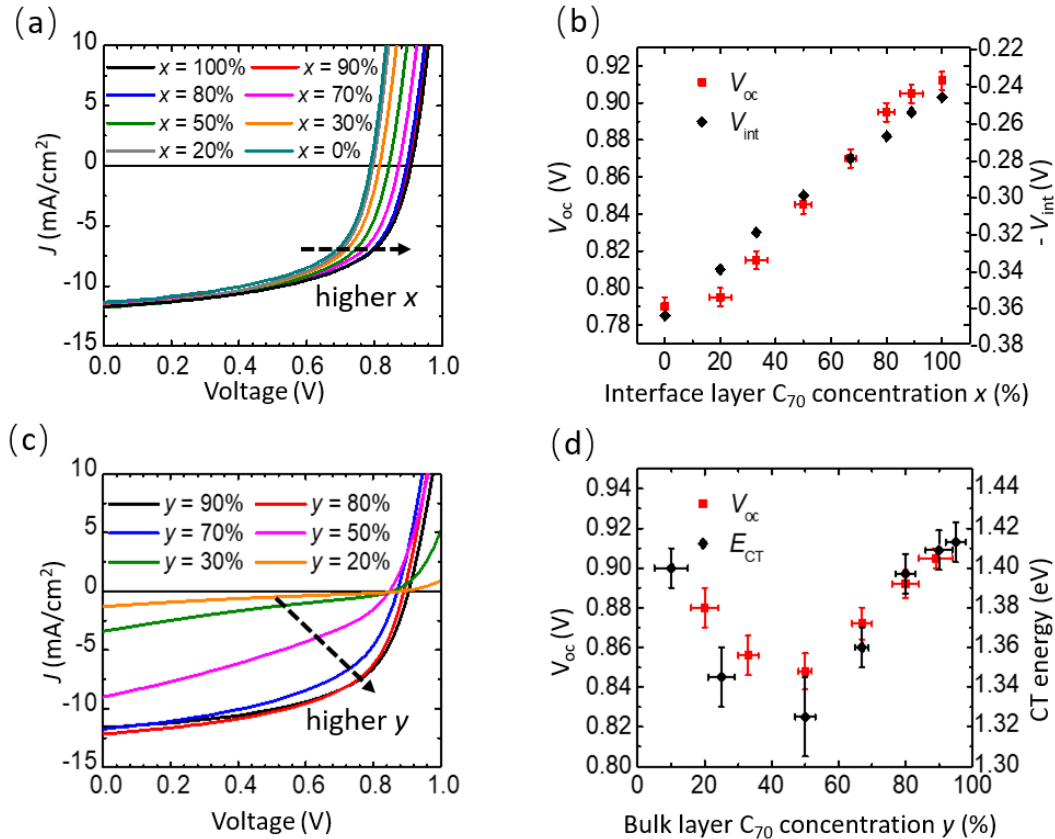


Figure 3.3 (a) Current density-voltage (J - V) characteristics under one sun simulated AM1.5G illumination of OPVs with identical C_{70} concentrations in the bulk of $y = 90\%$, and various C_{70} concentrations, x , in AIL. (b) Open circuit voltage, V_{oc} (red squares) and simulated interfacial potential drop, V_{int} (black diamonds) vs. x . (c) J - V characteristics of OPVs with $x = 100\%$, and various y . (d) Device V_{oc} (red squares) and charge transfer state energy measured from photoluminescence spectra (black diamonds) vs. y .

Figure 3.3(a) shows the J - V characteristics of OPVs for MoO_x as the ABL, a bulk layer C_{70} concentration of $y = 90\%$, and various C_{70} concentrations, x , in the AIL. As x increases, the measured J - V characteristics rigidly shift to higher voltage, as shown in Fig. 3(b) (squares), whereas J_{sc} is nearly unchanged. The V_{oc} difference, ΔV , between devices with a neat C_{70} AIL and

a neat DBP AIL is 0.12 ± 0.01 V. The calculated values of V_{int} at various x , are also plotted in Fig. 3.3(b) (diamonds), showing quantitative agreement with measurement.

Figure 3.3(c) shows the J - V characteristics of devices with constant AIL C_{70} concentration ($x = 100\%$) and various y , with V_{oc} shown in Fig. 3.3(d) (squares) along with CT state energies acquired from their PL spectra (diamonds).⁷⁶ The V_{oc} and CT exciton energy have similar dependences on y , both showing a minimum near $y = 50\%$, which has previously been shown to be due to the minimization of C_{70} or DBP aggregate formation.^{76, 90, 158-159}

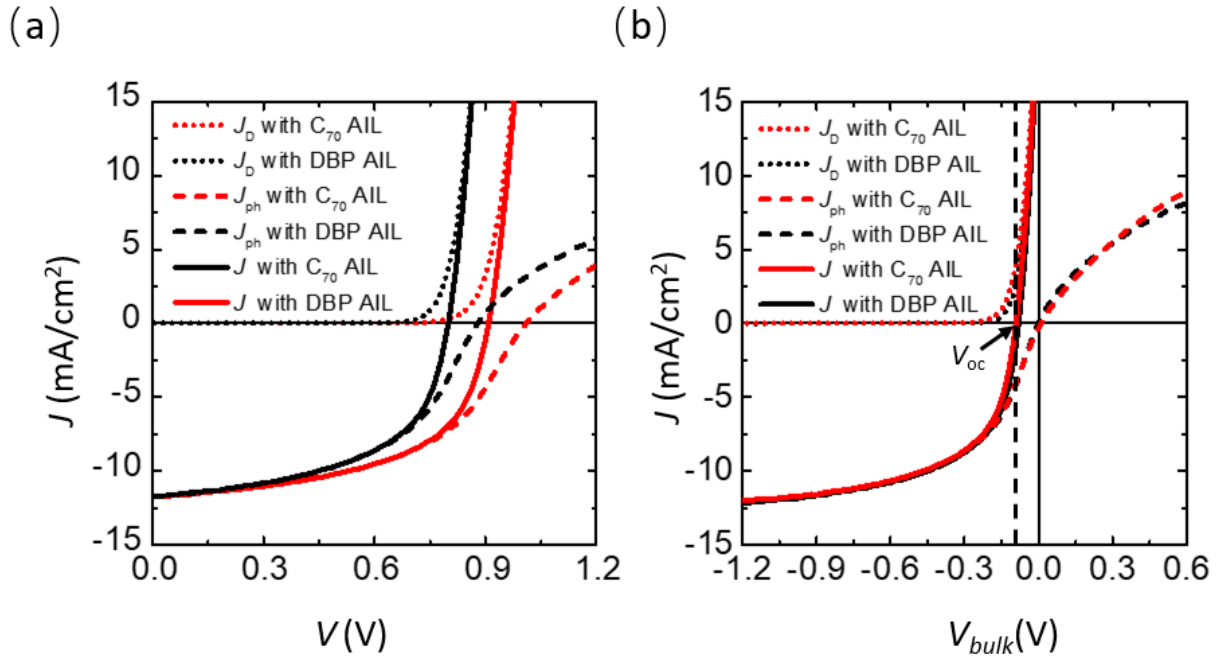


Figure 3.4 (a) J - V characteristics for the dark current density J_D (dotted), photocurrent density J_{ph} (dash) and total current density J (solid) of devices with a C_{70} (red), and a DBP AIL (black). (b) The same J - V characteristics as in (a) replotted with reference to voltage across the active layer, V_{bulk} . The vertical dashed line corresponds to V_{oc} .

To separate the dependences of J_D , J_{ph} and J on voltage, we calculate J_{ph} by subtracting J_D from the total current, J , and plot the contributions in Fig. 3.4(a) for devices with either a C_{70} AIL

or a DBP AIL. Using Eq. (3.2.4), we replot the J - V characteristics in Fig. 3.4(a) with reference to V_{bulk} for each device in Fig. 3.4(b).

Figure 3.5 shows the J - V characteristics of OPVs with $y = 80\%$ and AILs of various thickness. As the AIL thickness increases from 0 to 5 nm, V_{oc} increases while the J_{sc} remains nearly constant. This shows that holes can effectively tunnel through an acceptor layer up to 5 nm. When the AIL is 8-nm-thick, however, J_{sc} and FF decrease and the curve exhibits a weak inflection near V_{oc} .

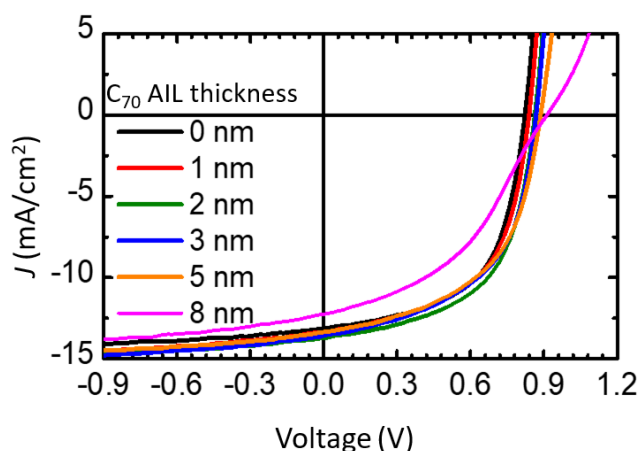


Figure 3.5 J - V characteristics of OPVs with a neat C_{70} AIL of various thicknesses. The bulk layer of all devices consists of DBP as donor and C_{70} as acceptor with $y = 80\%$.

3.2.3 Interfacial dipoles on BHJ/MoO_x interface

Besides AIL, the voltage shift also depends on C_{70} concentration, y , in the bulk. Figure 3.6(a) shows the illuminated J - V characteristics of OPVs with a C_{70} AIL (solid line) and a DBP AIL (dashed line), and $y = 90\%$ (red), 50% (blue) and 30% (black), respectively. For $y = 90\%$ and 50%, different AILs exhibit rigid horizontal shifts of their J - V characteristics. The voltage shift $\Delta V = 0.02 \pm 0.01$ V for devices with $y = 50\%$, is smaller than that for devices with $y = 90\%$ ($\Delta V =$

0.12 ± 0.01 V). For $y = 30\%$, the J - V characteristics show only a weak photoresponse with a high resistance in the forward biased direction.

To determine the electric field and potential drop across the active region/ABL interface, studies must consider the nanoscale connectivity between donor and acceptor molecules within the BHJ. For this purpose, Monte Carlo simulations provide a suitable method for modeling the discrete paths and electron transfer processes taken by individual charges across the AIL, as well as the hole dynamics in the active region. For $y > 50\%$, V_{int} has a weak dependence on J as shown in Fig. 3.6(a). Thus, we need only to calculate V_{int} at open circuit ($J = 0$) to describe the rigid shift in the J - V characteristics. There are three charge transfer processes considered in the simulation: electron transfer from the organic to the MoO_x layer, recombination of electrons in MoO_x with holes in the organic, and hole diffusion in the organic. The simulation consists of a 100 nm x 100 nm x 10 nm thick organic layer where the molecules form a simple cubic lattice with a 1 nm lattice constant. The frontier orbital energies of the organics are assumed to be accurately described by a Gaussian distribution with a standard deviation of 0.1 eV.¹⁶⁹⁻¹⁷⁰ Initially, both the MoO_x and organic layer are neutral. As the simulation proceeds, electrons transfer from the HOMOs of both the donor and acceptor to the MoO_x conduction band (CB) due to its high work function (6.7 eV), leaving behind holes in the organic layer.¹⁷⁰⁻¹⁷³ The charge transfer rate from organic molecules to MoO_x is assumed to follow Miller-Abrahams hopping:

$$P = P_0 \begin{cases} \exp\left(-\frac{E_F - E_i}{kT}\right); & E_F > E_i, \\ 1; & E_F < E_i, \end{cases} \quad (3.2.5)$$

where E_F is the MoO_x Fermi level, E_i is the HOMO energy of molecule i , P_0 is the maximum hopping rate that is proportional to the overlap between the electron wavefunctions in the organic and MoO_x , k is the Boltzmann constant, and T is the temperature.

Electrons in MoO_x CB can also transfer back into the organic by recombining with holes near the interface. The recombination rate is also calculated using Eq. (3.2.5) with E_F and E_i swapped. Thermal equilibrium is reached when the electron transfer is balanced by electron-hole recombination across the interface. The holes in the organic layer can also diffuse among neighboring molecules. For either the recombination or diffusion event to happen, there is a wait time:

$$\tau = -\frac{\ln(X)}{P}, \quad (3.2.6)$$

where X is a random number between 0 and 1. The transfer event with the smallest wait time τ happens first. After each event, the energy of every organic site is updated based on the electric field from the charges using:

$$E_i = E_{i0} - \int_{z_0}^{z_i} F(z) \cdot dz, \quad (3.2.7)$$

where E_{i0} is the HOMO energy when $F = 0$, z_i is the distance of molecule i perpendicular to the interface, z_0 is the z -coordinate for a molecule in the bulk (taken at 10 nm from the interface), and $F(z)$ is the electric field. The electric field from the holes is given by:

$$\mathbf{F}_{\text{hole}}(\mathbf{r}_i) = \sum_j \frac{q}{4\pi\epsilon_0\epsilon_r |\mathbf{r}_i - \mathbf{r}_j|^2} \hat{\mathbf{r}}_{ij}, \quad (3.2.8)$$

where \mathbf{r}_i is the coordinate of a site i , \mathbf{r}_j is the coordinate of a hole at j , $\hat{\mathbf{r}}_{ij}$ is the unit vector between the hole and \mathbf{r}_i , ϵ_0 is the *vacuum* permittivity, and ϵ_r is the dielectric constant of the organic. To reduce the computational workload, we set a cutoff radius of 4 nm for calculating the electric field from holes. $F_{\text{hole}}(z)$ is calculated by taking average of the $F_{\text{hole}}(\mathbf{r}_i)$ over all sites in a certain plane.

Due to the high conductivity ($\sigma \sim 10^{-2}$ S/m)¹⁷⁴ and static dielectric constant ($\epsilon_r \sim 18$)¹⁷⁵ of MoO_x compared to the organic blend (e.g. $\sigma \sim 10^{-6}$ S/m¹⁷⁶ and $\epsilon_r \sim 4$ for C₇₀¹⁷⁷), we consider

all the transferred electrons uniformly distribute at the MoO_x surface.¹⁷⁸⁻¹⁷⁹ The electric field on the organic side is thus a constant:

$$F_{\text{electron}}(z) = \frac{\sigma}{2\varepsilon_0\varepsilon_r}, \quad (3.2.9)$$

where σ is the electron surface density. Due to energetic disorder in the organic thin film, holes diffuse among molecules and distribute across a few interfacial molecular layers. The asymmetric distribution of electrons and holes results in an interface dipole, and hence the energy level shift observed in Fig. 3.8. The electric potential φ in Fig. 3.6(b) and 6(c) was calculated using:

$$\varphi(z_i) = \int_{z_{\text{bulk}}}^{z_i} F(z) \cdot dz, \quad (3.2.10)$$

where $z_{\text{bulk}} = 10$ nm by assuming the electric field at 10 nm is zero.

Hole diffusion is also simulated using Eq. (3.2.5), where P_0 is now proportional to the overlap between the HOMOs of two neighboring molecules. Although the absolute values of P_0 have no effect on the simulation results, the ratio between the P_0 values for the two processes matter. We introduce the parameter, $\alpha = P_{0\text{diff}}/P_{0\text{trans}}$, where $P_{0\text{diff}}$ is the maximum hopping rate for hole diffusion among organic molecules, and $P_{0\text{trans}}$ is maximum hopping rate for charge transfer between the MoO_x layer and the organic layer. The V_{int} in Fig. 3.6(b) and 3.6(c) was calculated with $\alpha = 130$. The large value of α is due to the smaller overlap between the organic HOMOs and the electron wavefunctions in the MoO_x CB compared with the overlap between organic HOMOs.

The simulated results of the hole density ρ_h (histogram) and potential shift from the bulk $\Delta\varphi$ (lines) near the active region/ABL interface for devices with a C₇₀ AIL or a DBP AIL and $y = 90\%$ and 50% are plotted in Fig. 3.6(b) and 3.6(c). The V_{int} is equal to $\Delta\varphi$ at $z = 0$ nm.

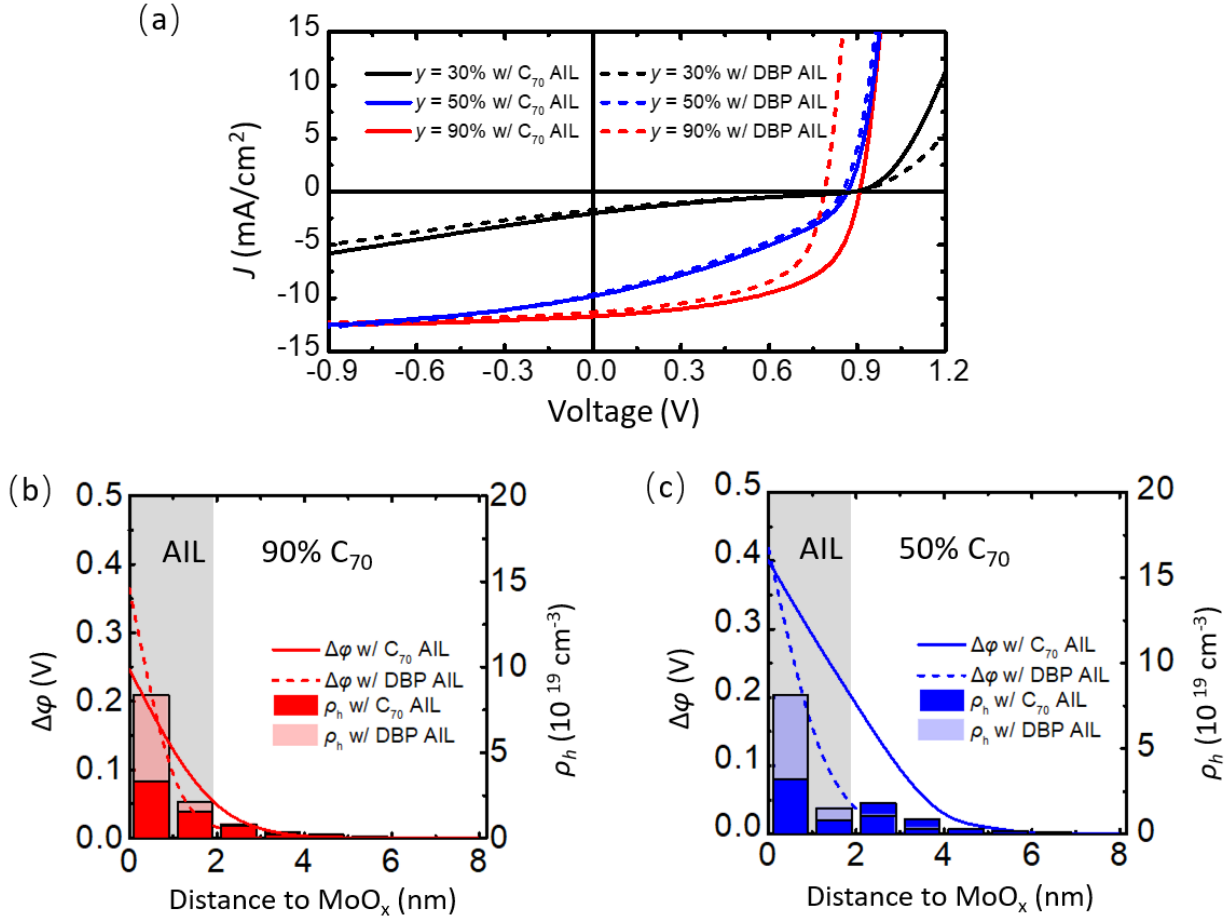


Figure 3.6 (a) J - V characteristics of OPVs with $x = 100\%$ (solid line) and $x = 0\%$ (dash line) when $y = 90\%$ (red), 50% (blue) and 30% (black), respectively. (b) Simulated hole density ρ_h (histogram) and electric potential shift from the bulk $\Delta\phi$ (lines) near the active region/anode buffer layer (ABL) interface for devices with a C₇₀ or a DBP AIL with $y = 90\%$. (c) Simulated ρ_h (histogram) and $\Delta\phi$ (lines) near the active region/ABL interface for devices with a C₇₀ IL or a DBP IL with $y = 50\%$.

Similar rigid shift of the J - V characteristics are observed for devices with a PEDOT:PSS ABL with a voltage shift of 0.07 ± 0.01 V. The J - V characteristics of OPVs under illumination with a PEDOT:PSS ABL are shown in Fig. 3.7(a) with $y = 90\%$ and a C₇₀ AIL (black) or a DBP AIL (red). The device with a C₇₀ AIL shows a larger V_{oc} but a similar J_{sc} and FF as the device with a DBP AIL, which is comparable to the case with a MoO_x ABL. The OPV J - V characteristics with a HAT-CN ABL are shown in Fig. 7(b) with $y = 90\%$ and a C₇₀ AIL (black) or a DBP AIL (red). The device with a C₇₀ AIL shows a reduced V_{oc} and FF .

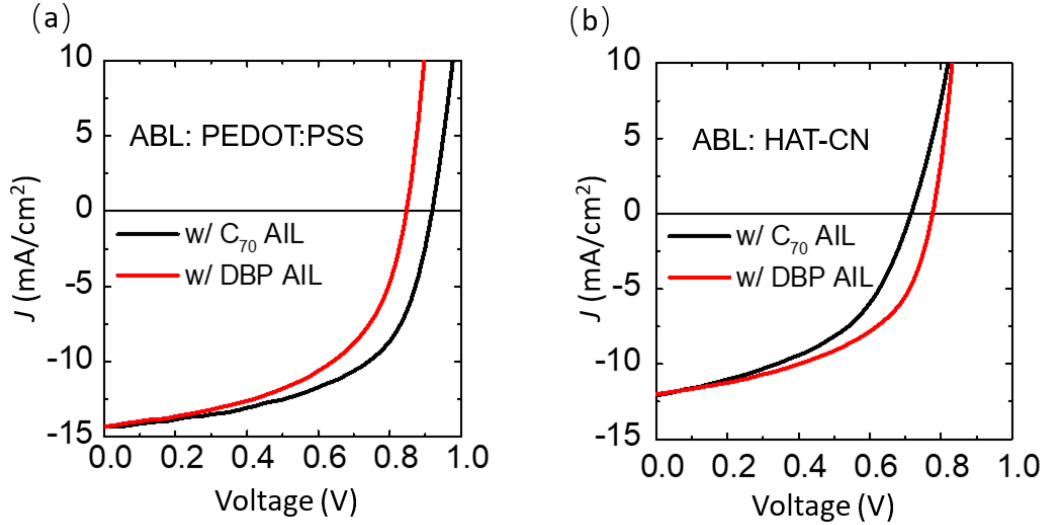


Figure 3.7 (a) J - V characteristics of OPVs with PEDOT:PSS as the anode buffer layer (ABL), with a C₇₀ AIL (black) and a DBP AIL (red) when $y = 90\%$. (b) J - V characteristics of OPVs with HAT-CN as the ABL, with a C₇₀ (black) and a DBP AIL (red) when $y = 90\%$.

The HOMO energies of organic active layers near the active region/ABL interface are measured by growing organic films of various thicknesses onto the ABL, which was deposited on ITO/glass. Samples are deposited in the same VTE chamber as the OPVs and PL samples, and transferred into a vacuum chamber with base pressure of 10^{-7} Torr. The HOMO energy is measured using UPS with a 21.2 eV UV photon source at - 8.0 V bias. The measured HOMO energies proximal to ABL interface are shown in Fig. 3.8. For MoO_x and PEDOT:PSS, there is bending of the organic HOMO energy near the ABL. The energy bending has previously been shown to result from a static interface dipole formed by electron transfer from the active region to the MoO_x and PEDOT:PSS^{161, 166, 180-184}. The total bending in the C₇₀ HOMO energy is 0.4 ± 0.2 eV for MoO_x, and 0.2 ± 0.1 eV for PEDOT:PSS. The energy bending extends over a distance of $\lambda = 30 \pm 10$ Å from the ABL interface. For C₇₀/HAT-CN interface, no energy bending is observed.

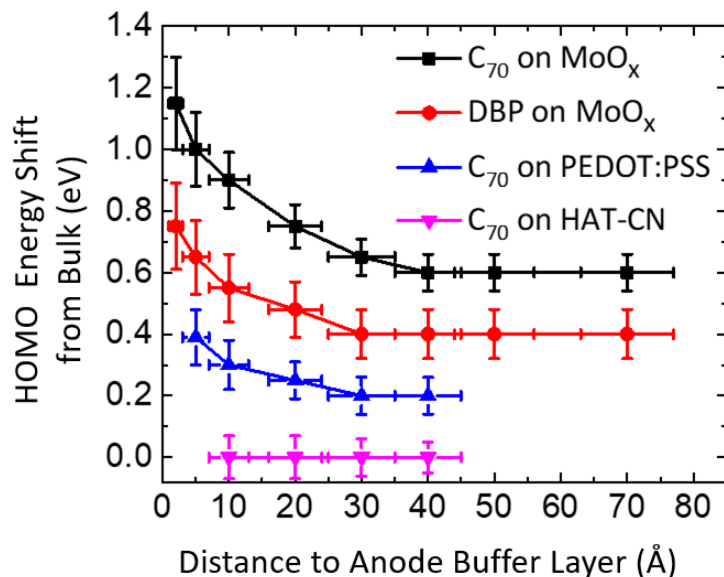


Figure 3.8 Highest occupied molecular orbital (HOMO) energy bending (relative to the bulk) vs. distance from the ABL interface for C₇₀/MoO_x interface (black), DBP/MoO_x interface (red), C₇₀/PEDOT:PSS interface (blue) and C₇₀/HAT-CN interface (pink) measured by ultraviolet photoelectron spectroscopy. The vertical error bars represent the energy resolution of the measurement and the horizontal error bars represent the uncertainty of the organic layer thickness.

3.3 Reducing the Interfacial Energy Loss with an Acceptor Anode Interface

Layer

3.3.1 Interfacial voltage loss and interfacial D/A ratio

The dependence of V_{oc} on C₇₀ concentration in the AIL, x (Fig. 3.3(b)) and in the bulk, y (Fig 3.3(d)) reveals the different origins of the energy losses in the two active region sections. For $y = 90\%$, V_{oc} and the simulated V_{int} show similar monotonic dependences on x (see Fig. 3.4(b)). This indicates that the energy loss at the active region/ABL interface is governed by V_{int} as described in Section II. However, the energy loss in the bulk layer is closely related to the CT state energy in the bulk, as suggested by the similar dependences on y of V_{oc} and CT energy when x is fixed (see Fig. 3.3(d)).

As shown in Fig. 3.4(a), both J_D and J_{ph} feature a rigid shift relative to the device voltage, V , depending on the composition of the AIL. When plotted with reference to V_a in Fig. 3.4(b), the J_{ph} - V_a relationships for the two devices are almost identical in the region of $J_{ph} < 0$, showing that photogeneration in the BHJs is indeed governed by V_a and is unaffected by V_{int} , in agreement with the simulations. Both devices show V_{oc} at $V_a = -0.10 \pm 0.01$ V, as denoted by the vertical dash line. The device with a C₇₀ AIL has a slightly higher J_D at a given V_a , which is possibly due to a reduced hole injection barrier.⁷⁴

Besides AIL, the voltage shift also depends on C₇₀ concentration, y , in the bulk. As y changes from 90% to 50%, ΔV between devices with a C₇₀ and a DBP AIL drops from 0.12 ± 0.01 V to 0.02 ± 0.01 V, as shown in Fig. 3.6(a). When $y = 90\%$, ρ_h near the interface is lower with a C₇₀ AIL compared with that with a DBP AIL, leading to a 30% drop in V_{int} (0.37 V to 0.25 V), see Fig. 3.6(b). When $y = 50\%$, the device with a C₇₀ AIL still has lower ρ_h near the interface as shown in Fig. 3.6(c). But due to the higher DBP concentration in the bulk compared with the C₇₀ AIL, a portion of holes diffuse into the bulk, resulting in a larger average electron-hole separation. As a result, V_{int} for devices with a C₇₀ or DBP AIL are similar. When the bulk layer has only 30% C₇₀, the device J - V characteristics no longer show a rigid horizontal shift and the shape changes from that of the devices with thinner AILs (black lines in Fig. 3.6), suggesting the formation of an energy barrier with impedance to charge extraction.¹⁸⁵

3.3.2 Hole transporting mechanism of the acceptor interface layer

Holes traverse the AIL across thicknesses comparable to the sum of energy bending region thickness λ (30 ± 10 Å as shown in Fig. 3.8) plus the hole tunneling distance through the organic, which can be as large as 4 nm.⁶³ As shown in Fig. 3.5, V_{oc} increases with AIL thicknesses < 5 nm, while J_{sc} remains nearly unaffected. When the AIL thickness is 8 nm, however, it exceeds the

tunneling length and thus acts as a hole-blocking layer, leading to distorted J - V characteristics with a reduced J_{sc} and FF . At this point, charges must transfer across the barrier by thermionic emission, which is inherently dissipative. While this may appear as an increase in V_{oc} , it is accompanied by a decrease in J_{ph} and fill factor, thus reducing the power conversion efficiency of the solar cell.

3.3.3 Anode interface layer with other active layers

Apart from DBP/C₇₀, we also tested the effect of an acceptor AIL on two other D/A systems: 2-[(7-[4-[N,N-Bis(4-methylphenyl)amino]phenyl]-2,1,3-benzothiadiazol-4-yl)methylene]propanedinitrile (DTDCPB)/C₇₀ and 2-[[7-(5-N,N-Ditolylaminothiophen-2-yl)-2,1,3-benzothiadiazol-4-yl]methylene]malononitrile (DTDCTB)/C₆₀. Table 3.2.1 shows device characteristics of the three D/A material systems with and without the acceptor AIL. All three systems show improvement in V_{oc} and PCE with an acceptor AIL.

Table 3.1 Device performance using various active layers with and without an acceptor anode interface layer (AIL).

Device Active Layer	J_{sc} [mA/cm ²]	V_{oc} [V] ^b	FF ^b	PCE [%]
DBP/C ₇₀ (1:4, 60 nm)	12.6 ± 0.2	0.86	0.54	5.8 ± 0.1
DBP/C ₇₀ (1:4, 60 nm) ^a	12.6 ± 0.2	0.88	0.54	6.0 ± 0.1
DTDCPB/C ₇₀ (1:2, 80 nm)	13.9 ± 0.2	0.90	0.70	9.2 ± 0.2
DTDCPB/C ₇₀ (1:2, 80 nm) ^a	14.1 ± 0.2	0.94	0.71	9.8 ± 0.2
DTDCTB/C ₆₀ (1:3, 80 nm)	10.4 ± 0.3	0.80	0.47	3.9 ± 0.2
DTDCTB/C ₆₀ (1:3, 80 nm) ^a	10.6 ± 0.3	0.84	0.46	4.1 ± 0.2

^a Device has a 3-nm-thick acceptor AIL

^b Errors are ± 0.01

3.4 Conclusions

In this chapter, we have shown that a static dipole at the active region/ABL interface introduces energy loss. By removing the donors near the active region/ABL interface, the loss can be reduced by up to 30%. A change in interfacial energy loss results in a concomitant change in V_{oc} , while J_{sc} and FF remain unaffected. The V_{oc} can be controlled over a range of 120 ± 10 meV by varying the D/A ratio near the interface. We attributed the change in V_{oc} to the change in the potential drop across the interface dipole layer at various interfacial D/A ratios, which was supported by Monte Carlo simulations. A significant outcome of our work is the demonstration of a counterintuitive but effective strategy to reduce the energy loss by inserting a thin electron accepting layer between the active region and the anode buffer. A primary condition for this layer is that it must be sufficiently thin to support non-dissipative charge tunneling, resulting in an increase in V_{oc} without a decrease in current or fill factor.

This work illuminates the different roles played by the interface and bulk layers in the photogeneration process, showing that their compositions should be independently controlled to optimize OPV performance. It also shows that tunneling can be an effectively way for hole transport at a distance up to 5 nm.

Chapter 4

Bulk Quantum Efficiency of Organic Photovoltaics

In this chapter, a method is introduced to analyze the performance of BHJs of OPVs by calculating its “bulk quantum efficiency” (BQE), a quantity related to the recombination losses within the BHJ, but not in the surrounding device layers. By applying the method to both vacuum- and solution-processed OPVs with various BHJ, buffer layers and interface layer compositions, we show that measurements of the BQE isolates the properties of the BHJ from other device layers and interfaces.

4.1 Theory

The internal quantum efficiency (IQE) is defined as the ratio of the number of extracted photogenerated charge carrier pairs to the number of absorbed photons. The IQE is less than unity in the presence of recombination. If the charge carriers are localized, the IQE can be written as:

$$\text{IQE}(V) = \frac{J_{ph}(V)}{q\Phi\eta_{abs}} = (1 - r_{bulk}(V_{bulk})) \cdot (1 - r_{edge}(V_{edge})), \quad (4.1.1)$$

where q is the elementary charge, Φ is the incident photon flux and η_{abs} is the absorption efficiency. Also, $J_{ph}(V)$ is the photocurrent density at the applied voltage, V , and is equal to the difference between total current density, J_{tot} , and dark current, J_{dark} . The recombination efficiencies in the BHJ and at the edges are given by r_{bulk} and r_{edge} , with corresponding voltage

drops V_{bulk} and V_{edge} , respectively. The V_{bulk} is the macroscopic voltage drop across the BHJ and is given by:

$$V_{bulk} = - \int_0^D F(z) dz, \quad (4.1.2)$$

where D is the BHJ thickness, z is the distance to the anode and F is the average electric field component along the z direction. Due to random orientation of the donor-acceptor interfaces, local electric field can be in random directions microscopically and $F(z)$ may be not uniform. But F should be monotonic and point from the cathode to the anode for efficient charge extraction to happen. We assume the charge recombination only depends on the local electric field. The first term, $(1 - r_{bulk}(V_{bulk}))$, is the BQE. We write V_{edge} as:

$$V_{edge} = V_{int} + AJ_{tot}R_{edge}, \quad (4.1.3)$$

where V_{int} is the sum of voltages across various interfaces, R_{edge} is the sum of the resistances of all edge layers, and A is the device area. To proceed, two assumptions are made: (i) $r_{bulk} \approx 0$ when V_{bulk} is large; (ii) $AJ_{tot}R_{edge} \ll V_{int}$, and the dependence of V_{int} on applied voltage is much smaller than V_{bulk} . This latter assumption is based on the understanding that V_{int} is primarily due to dipoles resulting from the work function difference across the interface. On the other hand, this may not be correct in the presence of a large, mid-energy gap interfacial trap state density.^{74, 183-184, 186} Assumption (i) results since both geminate and non-geminate recombination vanish at high electric fields.¹⁸⁷⁻¹⁸⁹ Assumption (ii) requires the buffer layers to have low resistance compared to the bulk (which is a combination of the junction and internal layer resistances). Therefore, at large reverse bias, Eq. (4.1.1) becomes:

$$IQE|_{-V \rightarrow \text{large}} = \frac{J_{sat}}{q\Phi\eta_{abs}} \approx 1 - r_{edge}(V_{edge}), \quad (4.1.4)$$

where J_{sat} is the saturated photocurrent density at large reverse bias. Then, using Eq. (4.1.1) and (4.1.4):

$$\text{BQE}(V_{bulk}) = (1 - r_{bulk}(V_{bulk})) \approx \frac{\text{IQE}(V)}{\text{IQE}|_{-V \rightarrow \text{large}}} = \frac{J_{ph}(V)}{J_{sat}}. \quad (4.1.5)$$

This quantity is the charge collection probability, or normalized photocurrent that has been previously introduced.¹⁹⁰⁻¹⁹¹ In this work we show that BQE is the quantum efficiency specific only to the BHJ, and is independent of the edges in the device. Although BQE is expected to depend on light intensity when high order events (e.g., exciton-exciton annihilation) or charge accumulations are present, we find the BQE- V_{bulk} characteristic is almost independent of intensity at 100 mW/cm² or lower in the junctions studied (see Section 4.3.1).

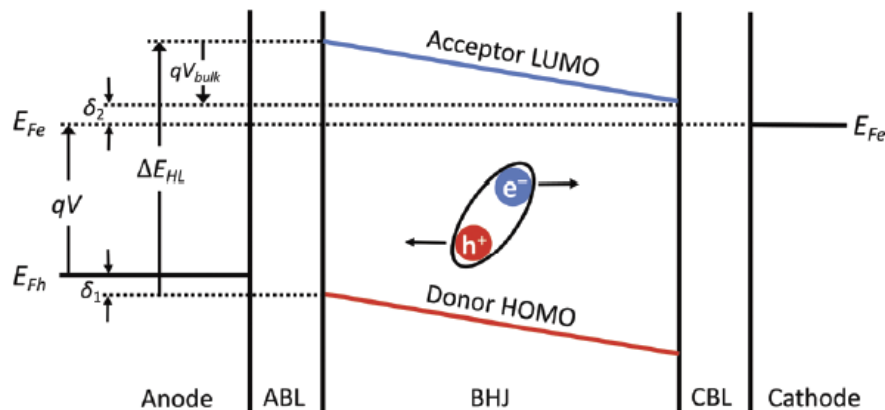


Figure 4.1 Energy level diagram of an OPV under forward bias that is smaller than the open-circuit voltage. The hole quasi-Fermi energy, E_{Fh} , is pinned at δ_1 above the donor HOMO level on the anode side while the electron quasi-Fermi energy, E_{Fe} , is at δ_2 below the acceptor LUMO level on the cathode side. The schematic indicates the flow directions of the photogenerated charges from an exciton.

Figure 4.1 shows the energy level diagram of an OPV under a forward bias of $V < V_{oc}$ with a schematic indicating the flow directions of the photogenerated charges from an exciton. We assume the hole quasi-Fermi level (E_{Fh}) is pinned at δ_1 above the HOMO level of the donor on the

anode side (E_D), and electron quasi-Fermi level (E_{Fe}) is pinned at δ_2 below the LUMO level of the acceptor on the cathode side (E_A). Then:

$$qV = E_{Fe} - E_{Fh} = (E_A - \delta_2) - (E_D - \delta_1) = \Delta E_{HL} - qV_{edge} - qV_{bulk}, \quad (4.1.6)$$

where ΔE_{HL} is the energy offset between the acceptor LUMO and the donor HOMO, and $V_{edge} = \delta_1 + \delta_2$. For convenience, the $V_{bulk} > 0$ is defined as opposite to that of V , since V_{bulk} and V have opposite signs under OPV operation.

To help understand the relationship between V and V_{bulk} , we assume in an “ideal OPV”, all contacts are ohmic and $V_{edge} = 0$. Figure 4.2(a) shows the energy level diagram of the ideal OPV under reverse bias, $V < 0$. According to Eq. (4.1.6), $V_{bulk} = \Delta E_{HL}/q + |V|$. When at short-circuit, as shown in Fig. 4.2(b), $V = 0$ and $V_{bulk} = \Delta E_{HL}$; When under solar cell working condition, $V > 0$ and $V_{bulk} = \Delta E_{HL}/q - V$, as shown in Fig. 4.2(c); Figure 4.2(d) shows the condition when there is no electric field in the BHJ and $V = \Delta E_{HL}/q$, $V_{bulk} = 0$.

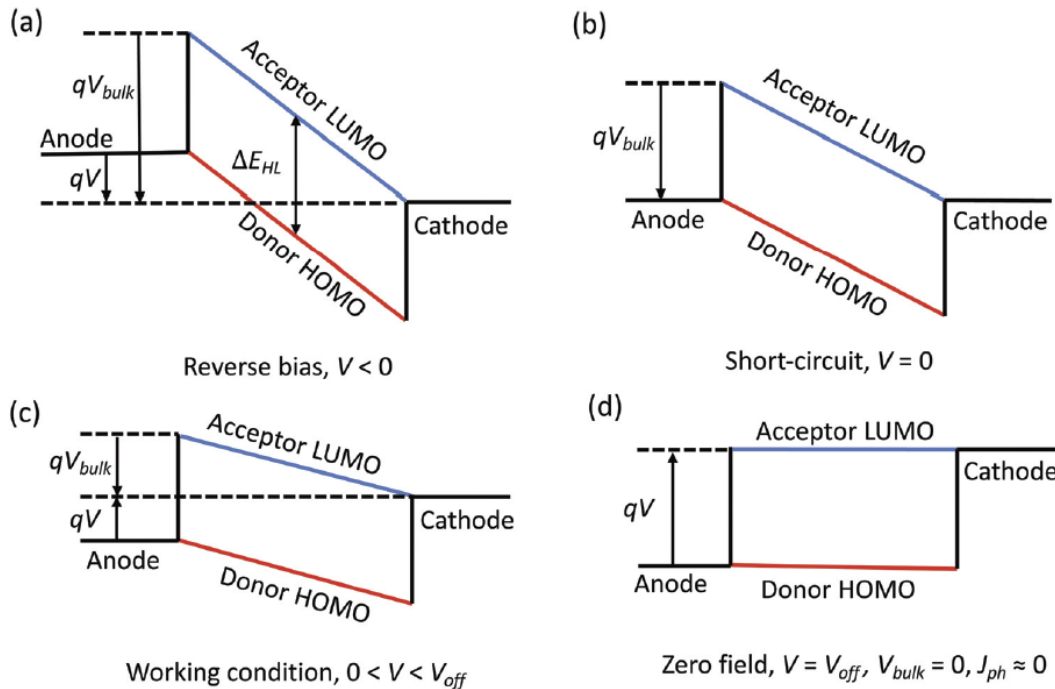


Figure 4.2 (a) Energy level diagram of an “ideal OPV” of which all contacts are ohmic under reverse bias. (b) Energy level diagram of an ideal OPV at short-circuit. (b) Energy level diagram of an ideal OPV under solar cell working condition. (d) Energy level diagram of an ideal OPV when there is no electric field in the BHJ.

Due to the random orientation of dissociating interfaces and localized charge states in organic BHJs, photogenerated charges usually suffer heavier recombination losses compared with inorganic p-n junctions. Under the condition in Fig. 4.2d, there is no electric field in the BHJ to help photogenerated charges to overcome the Coulombic attraction and guide them towards the respective electrodes, the probability for the charges to contribute to photocurrent through random walking is therefore low. Here we make an approximation that $J_{ph} = 0$ when $V_{bulk} = 0$ and call it assumption (iii). This assumption could be invalid under following conditions: the BHJ has a structural orientation (e.g., a bi-layer structure), leading to an oriented diffusion J_{ph} ; the charges experience band-like transport with no recombination loss (e.g., inorganic semiconductors); the

photogenerated charge density is high and form a density gradient throughout the BHJ. These conditions are further discussed in later sections. Using assumption (iii), Eq. (4.1.6) becomes:

$$V|_{J_{ph}=0} = V_{off} = \frac{\Delta E_{HL}}{q} - V_{edge}, \quad (4.1.7)$$

where we rename $V|_{J_{ph}=0}$ as V_{off} , referring to the offset voltage between V and V_{bulk} . Using Eqs. (4.1.6) and (4.1.7), we obtain:

$$V_{bulk} = V_{off} - V. \quad (8)$$

Note that although Eq. (4.1.4) and (4.1.7) are helpful for understanding the physical origins of J_{sat} and V_{off} , $BQE(V_{bulk})$ can be directly obtained from $J_{ph}(V)$ through Eq. (4.1.5) and (4.1.8). Step-by-step guidance to calculating $BQE(V_{bulk})$ is provided in SI.

To sum up, our theory rests on three assumptions: (i) $r_{bulk} \approx 0$ when V_{bulk} is large; (ii) the dependence of V_{int} on applied voltage is much smaller than V_{bulk} ; (iii) when $V_{bulk} = 0$, $J_{ph} = 0$. When these assumptions are valid, then $BQE(V_{bulk})$ is a property of the BHJ alone, and consequently is independent of other layers and interfaces within the device. Recombination outside of the BHJ affects J_{sat} as shown in Eq. (4.1.4), while voltage drops outside the BHJ affect V_{off} as in Eq. (4.1.7).

4.2 Experimental Verification

4.2.1 BQE of DBP:C₇₀ OPVs with various ABLs

To test that BQE- V_{bulk} characteristic depends only on photogeneration originating in the BHJ, OPV devices with various BHJs, buffer layers and interface qualities are fabricated. All OPVs were fabricated on ITO coated glass substrates (Lumtec Corp.) with a sheet resistance of 15 Ω /sq. The ITO anodes were patterned into 2 mm wide strips. The substrates were cleaned using a

detergent (tergitol solution) and solvents (acetone and isopropanol) and exposed to ultraviolet ozone for 10 min prior to thin film deposition. For vacuum-processed OPVs, the substrates were transferred into a vacuum thermal evaporation (VTE) chamber with a base pressure of 10^{-7} torr, and all layers were deposited at rates between 0.2 to 1.6 Å/s. The deposition rates and thicknesses were measured using quartz crystal monitors and calibrated post-growth using variable-angle spectroscopic ellipsometry. Metal cathodes were deposited through 2 mm wide shadow mask openings oriented orthogonal to the ITO strips, forming device areas of 4 mm². The J - V characteristics were measured inside a N₂ glovebox at room temperature using a semiconductor parameter analyzer (Agilent 4156C) with a 1kW m⁻² simulated AM 1.5G illumination source. Fluctuations in contact resistance during the J - V measurement results in randomness in the J_{ph} near $V_{bulk} = 0$. In this case, the V_{off} is determined by aligning the rising edges of the BQE- V_{bulk} curves (see Section 4.3.3).

Figure 4.3(a) shows the BQE- V_{bulk} characteristics of OPVs with identical BHJs comprising DBP as the donor and C₇₀ as the acceptor, but with a variety of anode buffer layers (ABLs). The device structures are: ITO 150nm/ABL 10 nm/DBP:C₇₀, 1:8, 54 nm/BPhen 7 nm/Ag 100 nm as shown in the inset. For ease in comparing the BQE- V_{bulk} characteristic, we define V_{80} as the V_{bulk} required to achieve a BQE of 80%, i.e.:

$$V_{80} = V_{bulk} |_{\text{BQE}=80\%}, \quad (4.2.1)$$

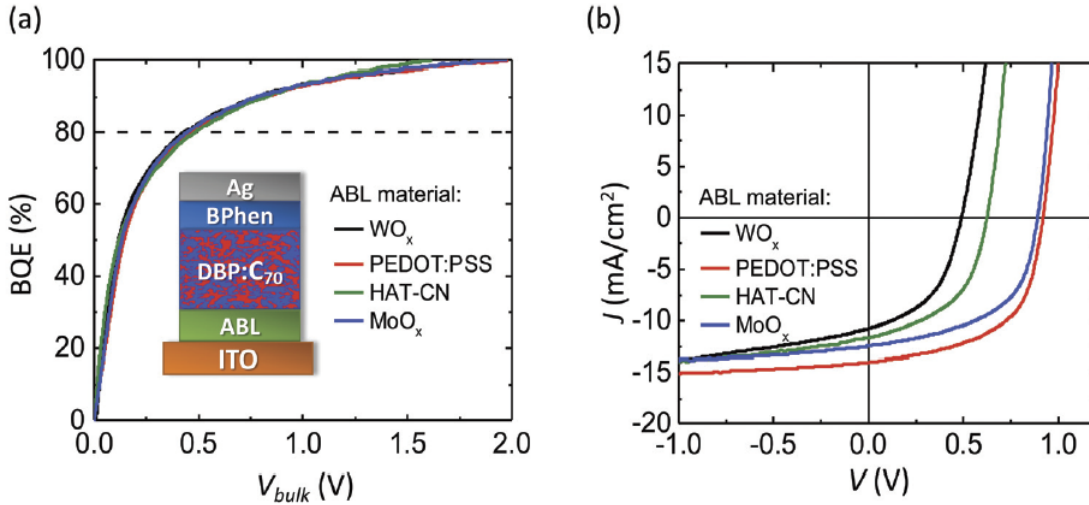


Figure 4.3 (a) BQE- V_{bulk} characteristics of OPVs with identical bulk heterojunction (BHJ) layers of DBP as the donor and C₇₀ as the acceptor (1:8 by volume, 54 nm), and various anode buffer layers (ABLs). Inset: Device structure. (b) Current density-voltage (J - V) characteristics of devices in (a).

The charge extraction from a BHJ is more efficient when V_{80} is small. The V_{80} along with V_{off} , J_{sat} and PCEs are provided in Table 4.2.1. The BHJ itself has been reported to be highly stable under intense sun light exposure, albeit with different cathode and anode buffers than used here.¹⁹² The J - V characteristics of each device are shown in Fig. 4.3(b). Although V_{OC} , J_{SC} and FF depend on the choice of ABL, their BQE- V_{bulk} characteristics are almost identical. With different ABLs, the V_{80} are similar, while V_{off} and J_{sat} vary significantly. The J_{sat} is chosen to equal J_{ph} at -1 V.

4.2.2 BQE of DTDCPB:C₇₀ OPVs with various AILs

Previously, it has been found that a thin anode interface layer (AIL) inserted between the ABL and BHJ determines the interface voltage, which contributes to V_{edge} .¹⁸⁶ Figure 4.4(a) shows the BQE- V_{bulk} characteristics of OPVs with identical BHJs and a 3-nm-thick AIL of various materials. The device structures are: ITO 150nm/ MoO_x 10 nm/AIL 3nm/DTDCPB:C₇₀, 1:2, 80

nm/BPhen 7 nm/Ag 100 nm as shown in the inset. The J - V characteristics of each device are shown in Fig. 4.4(b), with V_{off} , J_{sat} , V_{80} and PCEs listed in Table 4.2.2. The V_{off} is a sensitive function of the AIL composition, although the BQE- V_{bulk} characteristics are similar due to the use of the same BHJ in each device.

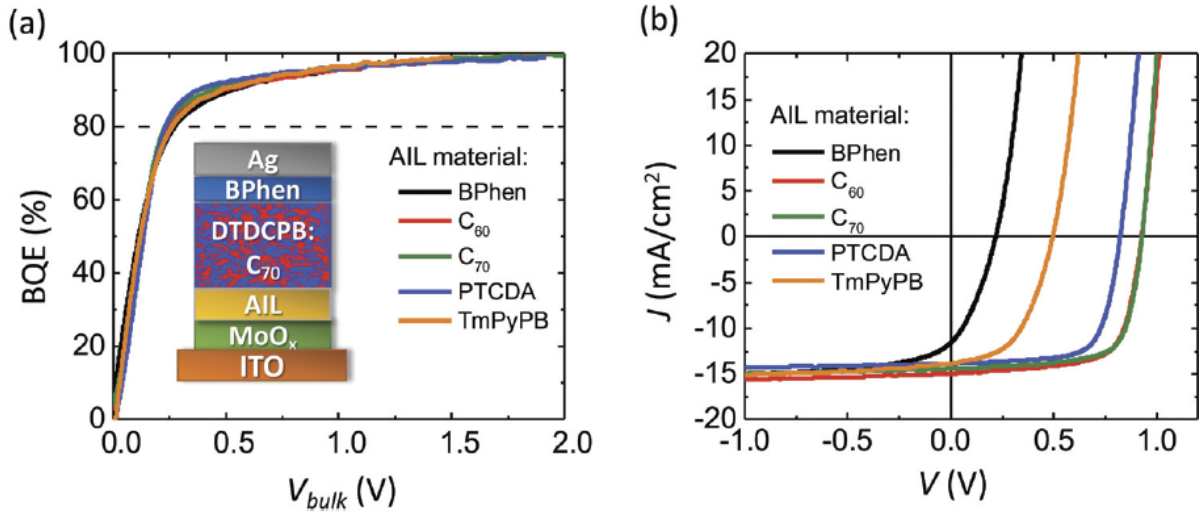


Figure 4.4 (a) BQE- V_{bulk} characteristics of OPVs with identical BHJs of DTDCPB as the donor and C_{70} as the acceptor (1:2 by volume, 80 nm) and various anode interface layers (AILs). Inset: Device structure. (b) J - V characteristics of devices in (a).

Table 4.1 Device characteristics of OPVs with a DBP: C_{70} BHJ and various anode buffer layer (ABL) materials.

ABL material	V_{off} (V)	J_{sat} (mA/cm ²)	V_{80} (V)	PCE (%)
WO _x	0.50 ± 0.01	12.9 ± 0.3	0.43 ± 0.03	2.5 ± 0.3
PEDOT:PSS	0.99 ± 0.01	15.0 ± 0.3	0.46 ± 0.03	7.2 ± 0.3
HAT-CN	0.63 ± 0.01	13.7 ± 0.3	0.48 ± 0.03	4.1 ± 0.2
MoO _x	0.97 ± 0.01	13.8 ± 0.3	0.44 ± 0.03	5.5 ± 0.2

Table 4.2 Device characteristics of OPVs with a DTDCPB:C₇₀ BHJ and various anode interface layer (AIL) materials.

AIL material	V_{off} (V)	J_{sat} (mA/cm ²)	V_{80} (V)	PCE (%)
BPhen	0.22 ± 0.01	15.4 ± 0.3	0.27 ± 0.02	0.8 ± 0.1
C ₆₀	1.02 ± 0.01	15.6 ± 0.3	0.24 ± 0.02	9.4 ± 0.2
C ₇₀	1.05 ± 0.01	14.9 ± 0.3	0.23 ± 0.02	9.3 ± 0.2
PTCDA	0.94 ± 0.01	14.3 ± 0.3	0.22 ± 0.02	8.0 ± 0.2
TmPyPB	0.50 ± 0.01	15.3 ± 0.3	0.24 ± 0.02	4.4 ± 0.2

4.2.3 BQE of OPVs with gradient D/A ratios

As discussed in Section 4.1.1, a BHJ with a structural orientation may lead to a non-zero J_{ph} even when $V_{bulk} = 0$, causing assumption (iii) to be invalid. To evaluate the effectiveness of the BQE analysis under such conditions, OPVs with graded mixing ratios in the BHJs and MoO_x or HAT-CN as the ABL are fabricated with the BQE- V_{bulk} characteristics shown in Fig. 4.5(a). The device structures are: ITO 150nm/ABL 10 nm/ /DTDCPB:C₇₀, gradient mixing ratios, 80 nm/BPhen 7 nm/Ag 100 nm, as shown in the inset. The gradients in C₇₀ concentrations in the legend are from the anode to the cathode side. The J - V characteristics are shown in Fig. 4.5(b), with device parameters provided in Table 4.2.3. The BQE- V_{bulk} characteristics are same for devices with similar gradient mixing ratios, while J_{sat} , V_{off} and PCEs vary for different ABLs. The results show that BQE analysis is still able to effectively separate the bulk from edges for inhomogeneous BHJs.

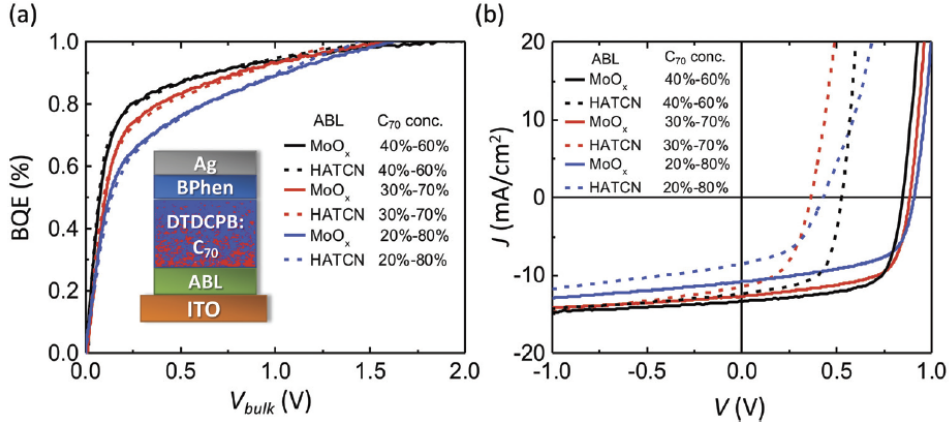


Figure 4.5 (a) BQE- V_{bulk} characteristics of DTDCPB: C_{70} OPVs with gradient C_{70} concentrations from the anode to the cathode side (80 nm), and various anode buffer layers (ABLs). Inset: Device structure. (b) Current density-voltage ($J-V$) characteristics of devices in (a).

Table 4.3 Device characteristics of OPVs with gradient mixed DTDCPB: C_{70} BHJs and various anode buffer layers (ABL). The C_{70} concentrations are referenced from the anode to the cathode side.

ABL material	C_{70} conc.	V_{off} (V)	J_{sat} (mA/cm^2)	V_{80} (V)	PCE (%)
MoO _x	40%-60%	0.85 ± 0.01	14.7 ± 0.3	0.24 ± 0.02	7.4 ± 0.1
HAT-CN	40%-60%	0.61 ± 0.01	14.3 ± 0.3	0.26 ± 0.02	4.0 ± 0.2
MoO _x	30%-70%	0.88 ± 0.01	14.1 ± 0.3	0.38 ± 0.02	7.1 ± 0.2
HAT-CN	30%-70%	0.36 ± 0.01	14.6 ± 0.3	0.42 ± 0.02	2.0 ± 0.2
MoO _x	20%-80%	0.91 ± 0.01	12.9 ± 0.3	0.62 ± 0.02	5.7 ± 0.2
HAT-CN	20%-80%	0.43 ± 0.01	11.7 ± 0.3	0.63 ± 0.02	1.7 ± 0.2

4.2.4 BQE of solution-processed NFA-based OPVs

We also determined the BQE of solution-processed inverted OPVs with PCE-10 as the donor and BT-CIC as the acceptor.⁴³⁻⁴⁴ The device structures are: ITO 150nm/CBL 30 nm/PCE-10:BT-CIC, 1:1.5, 80 nm/AIL 3nm/MoO_x 10 nm/Al 100 nm. The ZnO CBL was spun onto the substrates at 4000 rpm for 1 min using a sol-gel ZnO precursor solution (Sigma-Aldrich Inc.), and then thermally annealed at 160°C for 30 min in air. The SnO₂ CBL was deposited from a

nanocrystal dispersion (Sigma-Aldrich Inc.). The SnO₂ dispersion was diluted to 0.4 wt% by adding isopropanol and spun onto the substrates at 4000 rpm for 1 min. The sample was then thermally annealed in air for 30 min at 160°C. The C₆₀-SAM (1-Material Inc.) was dissolved at 1.5 mg/mL in chlorobenzene(CB):tetrahydrofuran(THF) (2:1 vol%) solution and stirred at 300 rpm overnight. The solution was then spin-coated at 3500 rpm for 1 min, and thermally annealed at 110°C for 10 min. A second spin-coating using CB:THF (2:1 vol%) solution spun at the same speed was applied on top of the film to remove residual C₆₀-SAM molecules that are not chemically bonded to the surface. The PCE10:BT-CIC blend was dissolved at a total concentration of 16 mg/mL in 9:1 CB:chloroform solution with a 1:1.5 weight ratio, and stirred at 300 rpm overnight at 65°C. The solution was subsequently spun onto the sample at 4000 rpm for 1 min. The AIL, MoO_x and Al cathode were deposited via the same procedures as the vacuum-processed OPVs.

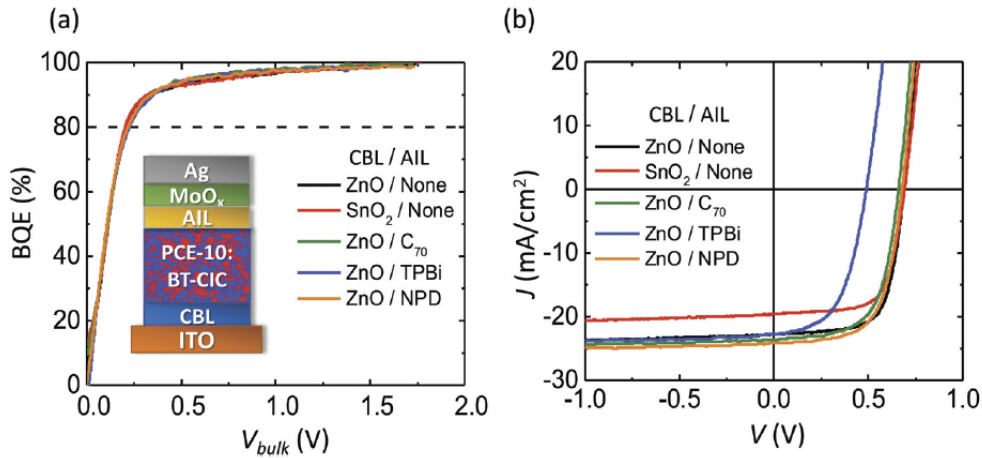


Figure 4.6 (a) BQE- V_{bulk} characteristics of OPVs with identical BHJs of PCE-10 as the donor and BT-CIC as the acceptor (1:1.5 by weight, 80 nm) and various cathode buffer layer (CBL)/AIL compositions. Inset: Device structure. (b) J - V characteristics of devices in (a).

Figure 4.6(a) shows BQE- V_{bulk} characteristics of the OPVs with two different CBLs (ZnO and SnO₂) and various AILs. The device structures are shown in the inset. Their J - V characteristics

are shown in Fig. 4.6(b), and device parameters are provided in Table 4.2.4. Again, all devices have almost identical BQE- V_{bulk} characteristics. The OPV with a SnO₂ CBL has J_{sat} that is 3 mA/cm² smaller than that with a ZnO CBL, while various AILs primarily affect the V_{off} .

Table 4.4 Device characteristics of inverted OPVs with a PCE-10:BT-CIC BHJ and various cathode buffer layer (CBL) and AIL compositions.

CBL / AIL	V_{off} (V)	J_{sat} (mA/cm ²)	V_{80} (V)	PCE (%)
ZnO / None	0.74 ± 0.01	24.1 ± 0.3	0.21 ± 0.02	10.0 ± 0.2
SnO ₂ / None	0.77 ± 0.01	21.1 ± 0.3	0.22 ± 0.02	9.1 ± 0.2
ZnO / C ₇₀	0.72 ± 0.01	24.3 ± 0.3	0.22 ± 0.02	9.7 ± 0.2
ZnO / TPBi	0.52 ± 0.01	24.0 ± 0.3	0.21 ± 0.02	5.9 ± 0.2
ZnO / NPD	0.74 ± 0.01	25.1 ± 0.3	0.21 ± 0.02	10.4 ± 0.2

4.3 Details of BQE analysis

Conventional metrics used to analyze OPV performance such as V_{OC} , J_{SC} and FF often have entangled correlations with the device structure, making it difficult to evaluate the effectiveness of a particular layer in the photogeneration process. On the other hand, BQE, J_{sat} and V_{off} , can separate the BHJ properties from the edges. As shown in Figs. 4.3a, 4.4a, 4.5a and 4.6a, devices with different ABL, CBL or AIL layers have similar BQE- V_{bulk} characteristics. Indeed, the BQE- V_{bulk} characteristics are unaffected even for layers that severely reduce PCE (e.g., WO_x ABLs and BPhen AILs) and BHJs with varying mixing ratios across the active region. The impacts of the contacts, buffer layers and interfaces are incorporated in V_{off} and J_{sat} , which depend on voltage drops and recombination at the edges, respectively. For clarification, BQE analysis being able to separate the bulk properties from the edges for material systems studied, is an experimental

observation. The proposed theory in Section 4.1 is an effort to explain this observation and does not affect the experimental effectiveness of BQE analysis. Several details of calculating BQE is discussed here.

4.3.1 Determination of the saturation current

The BQE is calculated using $J_{ph}(V = -1V)$ as the saturation photocurrent, J_{sat} . However, to accurately calculate the BQE, J_{sat} should be at a reverse bias that is large enough such that $BQE \rightarrow 1$ (see Eq. (4.1.3)). To test the effect of the choice of J_{sat} , we compare the BQE calculated using $J_{sat} = J_{ph}(V = -1V)$, BQE_{-1V} , with the BQE calculated using $J_{sat} = J_{ph}(V = -5V)$, BQE_{-5V} . Figure 4.7(a) shows the $BQE_{(-1V)}$ and $BQE_{(-5V)}$ vs. V_{bulk} for a PCE-10:BT-CIC OPV aged for 46 days. It can be seen that $BQE_{(-1V)}$ overestimates BQE by approximately 10% assuming $BQE_{(-5V)}$ is the actual BQE. However, $BQE_{(-1V)}$ and $BQE_{(-5V)}$ have the same dependence on V_{bulk} for $V > -1V$, as shown in Fig. 4.7(b). Therefore, although the absolute values of BQE can be slightly larger than their actual values, their relative changes vs. V_{bulk} are accurate. This overestimation of BQE is higher when the BQE is lower, resulting in an underestimation of ΔBQE . Choosing J_{sat} to be at a larger reverse bias is preferred.

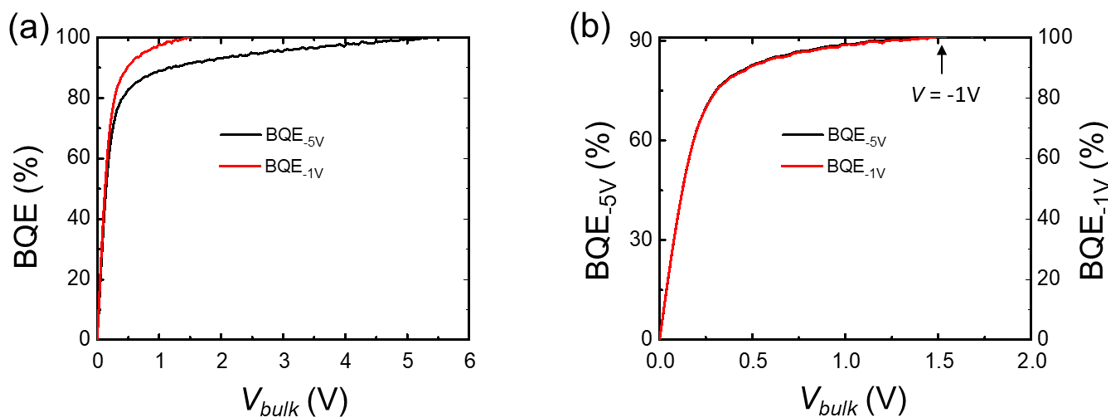


Figure 4.7 (a) $BQE-V_{bulk}$ characteristics of a PCE-10:BT-CIC OPV aged for 46 days using $J_{sat} = J(-1V)$ and $J_{sat} = J(-5V)$. (b) $BQE-V_{bulk}$ characteristics in (a) plotted on different vertical scales.

4.3.2 The intensity dependence of BQE

The BQE (as well as the r_{bulk} and r_{edge} in Eq. (4.1.1)) can have a light intensity dependence when multiparticle interactions are active. Figure 4.8 shows the $J_{ph}-V$ characteristics normalized to the J_{ph} (-1V) for a DBP:C₇₀ OPV at various white light illumination intensities. The shape of the $J_{ph}-V$ characteristics saturates when the intensity is > 0.38 sun intensity, suggesting that the effects of higher-order mechanisms are negligible. This also makes BQE immune to errors related to the fluctuation in the light intensity during $J-V$ measurement. The different shapes of J_{ph} at low intensities are likely due to a calculation error when injection current (J_{inj}) increases with light intensity due to photoconductivity.¹⁹³ As a result, $J_{ph} = J - J_{dark}$ includes not only the photocurrent, J_{ph} , but also the increase in injection current, ΔJ_{inj} . This affects the shape of $J_{ph}-V$ characteristics at $V > V_{oc}$ where J_{inj} is increasingly important. This increase in injected current is small and only causes a change of the $J_{ph}-V$ shape when the J_{ph} is also small. Assuming $J_{ph-norm}(100\%)$ is the normalized photocurrent, the increase of injected current at 0.14% sun is: $\Delta J_{inj} = J_{ph-norm}(0.14\%) - J_{ph-norm}(100\%)$, as shown by the dashed line in Fig. 4.8(a). Figure 4.8(b) show the responsivity vs. light intensity of the OPV. The almost constant responsivity also suggests that the low charge density approximation is valid and multiparticle interactions are negligible.

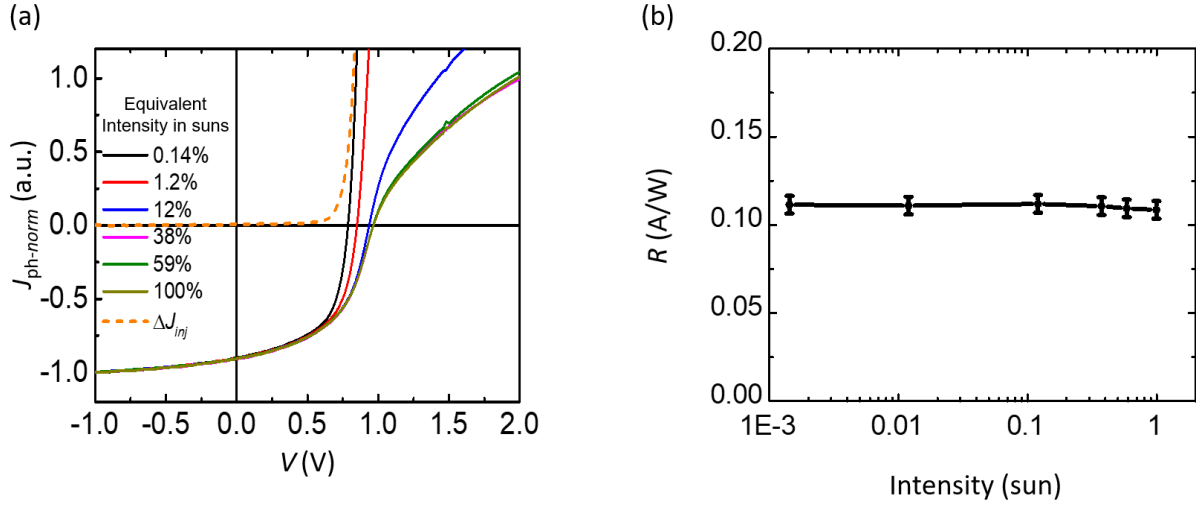


Figure 4.8 (a) Normalized photocurrent J_{ph} vs. voltage characteristics of a DBP:C₇₀ OPV under various illumination intensities, and the increase in injection current, ΔJ_{inj} . (b) The responsivity vs. light intensity.

4.3.3 Correction to BQE due to poor contact

Although BQE is not dependent on J_{dark} , the calculation of J_{ph} relies on the value of J_{dark} . When the contact is unstable (e.g., if Al contact is oxidized or the probes are not in solid contact with the electrodes), the J_{inj} under illumination may not equal J_{dark} even at light intensities comparable to 1 sun, causing an error in J_{ph} near the $V_{bulk} = 0$ where $J_{dark} \approx J_{ph}$. Figure 4.9(a) shows the J_{ph} - V characteristics of four identical PCE-10:BT-CIC OPVs on the same substrate but with different contact conditions. Due to poor contact, the shapes of the J_{ph} near the $V_{bulk} = 0$ differ, causing an error in determining the V_{off} . In Fig. 4.9(b), the BQE- V_{bulk} characteristics of the four devices are aligned by the linear sections on the rising edges to correct the error caused by the poor contacts. As a result, the BQE- V_{bulk} curves after correction may not cross the origin.

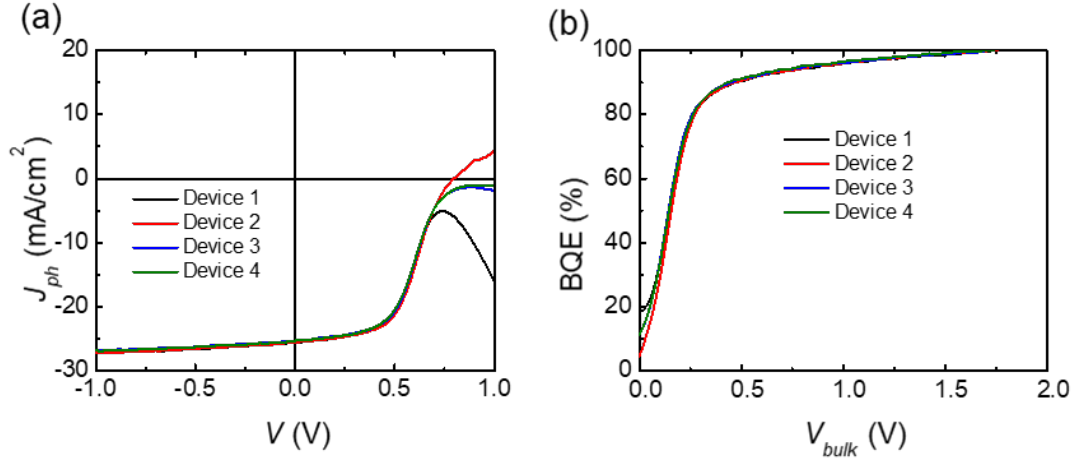


Figure 4.9 (a) J_{ph} - V characteristics of four identical PCE-10:BT-CIC OPVs on the same substrate with various contact conditions. (b) Corrected BQE- V_{bulk} characteristics of devices in (a).

4.3.4 Step-to-step guidance of BQE calculation

To get BQE- V_{bulk} characteristics as well as J_{sat} and V_{off} for an OPV, the J - V characteristics in the dark, $J_D(V)$, and under illumination, $J(V)$, are needed. The BQE- V_{bulk} characteristics can be achieved as follows:

1. Calculate the photocurrent: $J_{ph}(V) = J(V) - J_D(V)$;
2. Determine J_{sat} which is the value of J_{ph} at a certain reverse bias. It is recommendable to choose a large reverse bias as discussed above;
3. Determine V_{off} which is the value of V where $J_{ph} = 0$;
4. Calculate BQE- V_{bulk} characteristics:

$$\text{BQE}(V_{bulk}) = \frac{J_{ph}(V_{off} - V_{bulk})}{J_{sat}}, \quad (4.3.1)$$

In the case of a poor contact as discussed above, the BQE- V_{bulk} curve near $V_{bulk} = 0$ can be distorted, leading to a randomness in V_{off} . Figure 4.10(a) shows J_{ph} - V characteristics of the same device with solid and poor contact. As a result, V_{off} of the poor contact curve is larger. To correct for this error, we recommend extending the linear section on the rising edge of the BQE- V_{bulk} curve

as shown in Fig. 4.10(b) and adjust the BQE- V_{bulk} curve horizontally as well as the V_{off} value so that the extended line crosses the origin.

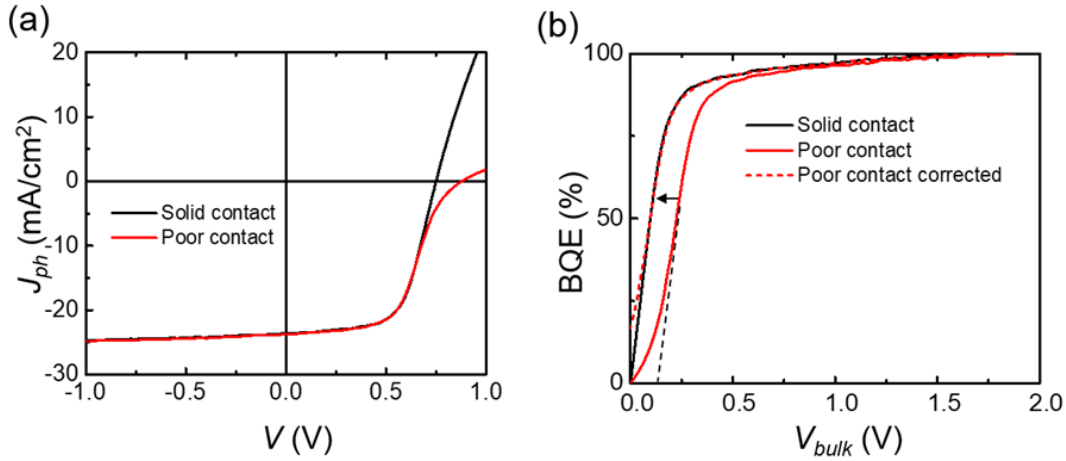


Figure 4.10 (a) J_{ph} - V characteristics of a PCE-10:BT-CIC OPV with solid and poor contact. (b) As-calculated BQE- V_{bulk} characteristics for solid and poor contact devices and corrected BQE- V_{bulk} characteristics for the poor contact device.

4.3.5 OPVs with Energy Barriers

In previous work, we show that in DBP:C₇₀ OPVs, a thin layer of C₇₀ AIL inserted between the BHJ and the anode buffer layer reduces the energy loss at the BHJ/anode buffer interface and hole collection is achieved through tunneling through the AIL. However, when the AIL thickness surpasses the hole tunneling distance, the AIL introduces an energy barrier and becomes a hole blocking layer, leading to a S-shaped J - V characteristic.¹⁸⁶ This S-shape has been suggested to be due to the accumulation of photogenerated charges at the energy barrier.¹⁹⁴ Figure 4.11(a) shows the J - V characteristics of DBP:C₇₀ OPVs with various mixing ratios and C₇₀ AILs with various thicknesses and the as-calculated BQE- V_{bulk} characteristics are shown in Fig. 4.11(b). The J - V characteristics become S-shaped with thick AILs due to the energy barrier between the AIL and

the BHJ for holes. As a result, the calculated BQEs also become S-shaped and can no longer represent the charge collection properties of the BHJs.

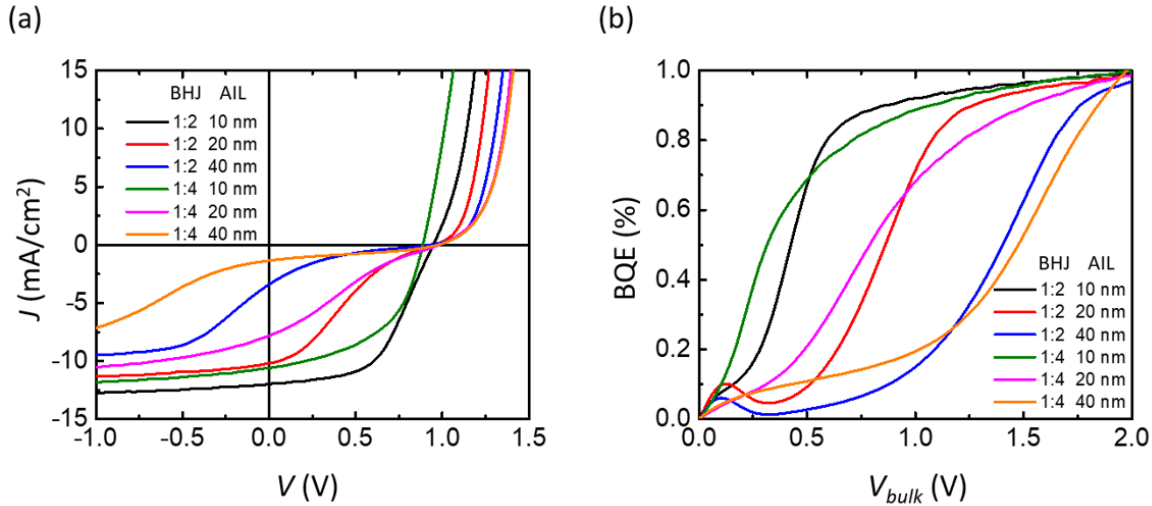


Figure 4.11 (a) J - V characteristics of DBP:C₇₀ OPVs with various mixing ratios and C₇₀ AILs of various thicknesses. (b) As-calculated BQE- V_{bulk} characteristics for OPVs in (a).

4.4 Conclusions

In this chapter, we introduced a method to analyze OPV performance by directly measuring the charge photogeneration efficiency within the BHJ using the bulk quantum efficiency that is extracted directly from the OPV J - V characteristics. The BQE analysis was used to separate the properties of the BHJ from the device peripheral regions (interfaces, buffer layers, contacts) for both vacuum- and solution-processed OPVs. Compared with conventional metrics such as V_{OC} , J_{SC} and FF, the BQE, V_{off} and J_{sat} , introduced in this work are determined by either the active or the edge regions, providing physical insights into the photogeneration process. This method is derived for systems with localized charge carriers and isotropic dissociating interfaces, and thus might have broader applications such as for perovskite solar cells.

Chapter 5

Photodegradation of Organic Photovoltaics

Aside from the efficiency, device stability is also an importance aspect of OPV performance. Due to the low binding energy of Coulombic force that hold molecules together, organic semiconductors are more vulnerable than traditional inorganic semiconductors, which could be a bottleneck for their mass application. With that been said, many recent works have shown that many of the mechanisms that causing OPVs to have a short lifetime can be prevented and the organic BHJs can be intrinsically very stable. In this section, we mainly focus on photodegradation of NFA based OPVs.

5.1 Photo-stability of DBP:C₇₀ OPVs

A pervasive myth associated with OPVs is that the materials are intrinsically vulnerable to degradation and morphological instabilities in the BHJ over the short term.¹⁹⁵⁻¹⁹⁷ However, this myth is challenged by the very long extrapolated lifetimes (27,000 years) recently demonstrated in an archetype, thermally evaporated fullerene-based material system,¹⁹² providing a proof-of-concept that OPVs can have exceptional operational lifetimes.

The OPV structure studied is: ITO 150nm/MoO_x 10 nm/DBP:C₇₀, 1:8, 54 nm/C₇₀ 9nm/TPBi: C₇₀, 1:1, 10nm/TPBi 3nm/Ag 100 nm. The OPVs were fabricated on ITO coated glass substrates (Lumtec Corp.) with a sheet resistance of 15 Ω/sq. The ITO anodes were patterned into

2 mm wide strips. The substrates were cleaned using a detergent (tergitol solution) and solvents (acetone and isopropanol) and exposed to ultraviolet ozone for 10 min prior to thin film deposition. The substrates were transferred into a VTE chamber with a base pressure of 10^{-7} torr, and all layers were deposited at rates between 0.2 to 1.6 Å/s. The deposition rates and thicknesses were measured using quartz crystal monitors and calibrated post-growth using variable-angle spectroscopic ellipsometry. Metal cathodes were deposited through 2 mm wide shadow mask openings oriented orthogonal to the ITO strips, forming device areas of 4 mm². The simulated solar illumination was produced using a large-area Xe-arc lamp filtered to approximate an AM1.5G reference, and the intensity was calibrated to 1 sun intensity (1 kW m⁻²) using a calibrated Si photodiode (National Renewable Energy Laboratory). The 27 suns white light source was achieved using high-intensity white LED arrays. The intensity was calibrated using the as-grown PCE-10:BT-CIC OPV in Fig. 8a. The OPV is illuminated using a solar simulator and the J_{sc} is recorded as $J_{sc, AM 1.5G}$. The OPV is then illuminated by the LED array with the intensity concentrated with a silver-coated reflective tube and a 10% transmissive neutral-density filter. The power of the LED array was adjusted so that the OPV produces a J_{sc} equivalent to $2.7J_{sc}$ at AM 1.5G.¹⁹²

Figure 5.1(a) shows the Normalized PCE plotted against ageing time under illumination equivalent to 9.5 ± 1.4 , 20 ± 3 and 37 ± 5.5 Suns. The device ages very slowly at the intensity of 1 Sun and the stability is hard to be directly characterized. Therefore, lifetimes at higher intensities are used to study the lifetime at 1 Sun, which is extrapolated to be over 5×10^7 h.

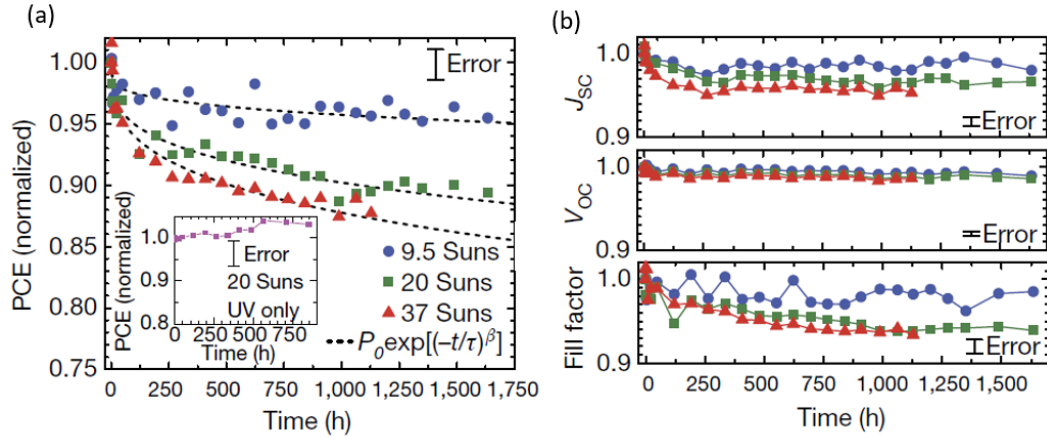


Figure 5.1 (a) Normalized PCE plotted against ageing time under illumination equivalent to 9.5 ± 1.4 , 20 ± 3 and 37 ± 5.5 Suns. Stretched exponential fits to each PCE against time dataset are shown by dashed lines. The inset shows PCE plotted against time for an OPV aged under ultraviolet illumination equivalent to 20 Suns. (b) Normalized J_{sc} , V_{oc} and FF plotted against ageing time under illumination equivalent to 9.5 ± 1.4 , 20 ± 3 and 37 ± 5.5 Suns.

5.1.1 BQE analysis for DBP:C₇₀ OPVs

We apply the BQE analysis developed in Chapter 4 to study the OPV degradation. Figure 5.2(a) shows the BQE- V_{bulk} characteristics of an OPV with DBP:C₇₀ BHJ aged under a white LED array which delivers an equivalent intensity of 27 suns (27 kW/m^2 , lacking UV content).¹⁹² The inset shows V_{80} vs. aging time. After 1000 h, V_{80} increases by approximately 0.2 V. The V_{off} and J_{sat} vs. time are shown in Figure 5.2(b). The V_{off} remains stable while J_{sat} decreases by approximately 10%.

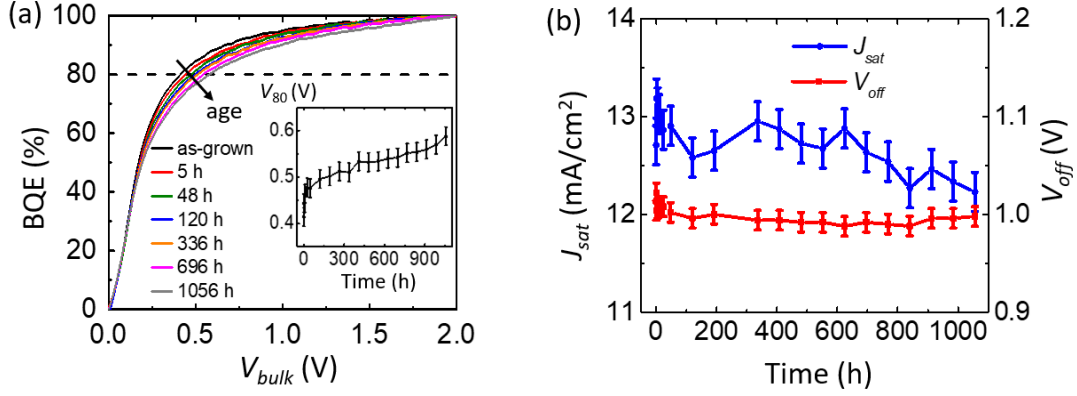


Figure 5.2 (a) BQE- V_{bulk} characteristics of a DBP:C₇₀ OPV aged under white light with an intensity equivalent to 27 suns. Inset: V_{80} vs. aging time. (b) V_{off} and J_{sat} vs. aging time.

5.1.2 BQE degradation equation due to a low concentration of traps

As an OPV ages, its BQE decreases. To understand the aging process, we assume that conductivity within the BHJ is due to thermally assisted hopping, and that trap sites with energy ΔE_t within the energy gap are generated over time. The thermal activated rate for a charge to escape a trap site, k_{esc} , is:¹⁹⁸

$$k_{esc} = k_0 \exp\left(-\frac{\Delta E_t}{kT}\right), \quad (5.1.1)$$

where k_0 is a constant, k is the Boltzmann constant and T is the temperature. In an electric field F , the energy barrier for thermal activation is lowered to $\Delta E_t - qFd$, where d is the distance between neighboring sites. Assuming a uniform electric field in a BHJ of thickness D , then $F = V_{bulk}/D$.

The probability for a trapped charge to recombine is then:

$$P_{rec} = \frac{k_{rec}}{k_{rec} + k_{esc}} = \frac{k_{rec}}{k_{rec} + k_0 \exp\left(-\frac{\Delta E_t - \frac{qV_{bulk}d}{D}}{kT}\right)}, \quad (5.1.2)$$

where k_{rec} is the recombination rate of trapped charges. In the low trap site density limit where every photogenerated charge gets trapped at most once prior to extraction, the decrease in BQE is:

$$\begin{aligned} \Delta BQE &= BQE_0 P_{trap} P_{rec} = BQE_0 P_{trap} \frac{k_{rec}}{k_{rec} + k_0 \exp\left(-\frac{\Delta E_t - \frac{qV_{bulk}d}{D}}{kT}\right)} \\ &= BQE_0 \left[\frac{P_{trap}}{1 + C_{esc} \exp\left(\frac{V_{bulk}}{V_{esc}}\right)} \right], \end{aligned} \quad (5.1.3)$$

where BQE_0 is the BQE of the unaged device, and P_{trap} is the probability for photogenerated charges to become trapped during extraction. Also:

$$C_{esc} = \frac{k_0}{k_{rec}} \exp\left(-\frac{\Delta E_t}{kT}\right), \quad (5.1.4a)$$

$$V_{esc} = \frac{kTD}{qd}. \quad (5.1.4b)$$

Here, the escape constant, C_{esc} , is the ratio of the escape to the recombination rate at zero electric field, and V_{esc} is the escape voltage. It follows that for efficient charge extraction, V_{bulk} must be larger than V_{esc} . Note that Eq. (5.1.3) is derived in the low trap density limit, and does not include other degradation mechanisms such as morphological changes over time.

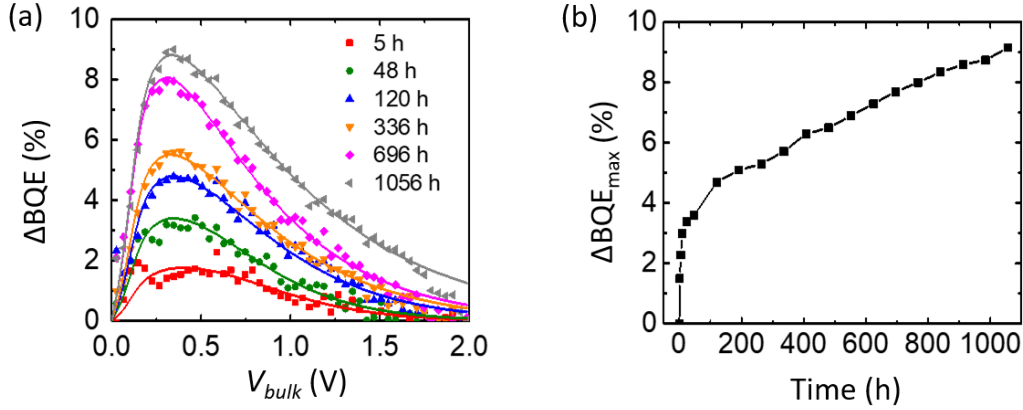


Figure 5.3 (a) Experimental (symbols) and fitted (lines) values of the decrease in BQE relative to the as-grown device (ΔBQE) vs. V_{bulk} at various aging times. (b) Maximum values of ΔBQE vs. aging time.

Figure 5.3(a) shows the change in BQE, ΔBQE , relative to the device prior to aging. The experimental (symbols) and results fit to Eq. (5.1.3) (lines) are in reasonable agreement, assuming $V_{esc} = 0.5$ V, which corresponds to a site distance $d = 4.1$ nm. Values of fitting parameters, P_{trap} , C_{esc} and V_{esc} , for each line are provided in SI. Figure 5.3(b) shows the maximum value of ΔBQE vs. aging time. Since $\Delta BQE \propto P_{trap}$, the results suggest that the trap site density increases linearly with time after an initial burn-in.

5.1.3 Partially aged device

To separate the contributions of the MoO_x layer and the MoO_x/BHJ interface from the BHJ in the BQE decrease in Fig. 5.2(a), the MoO_x and the lower 10 nm of the BHJ were deposited on two identical ITO coated glass substrates in the VTE chamber and encapsulated in N_2 atmosphere. One sample (later fabricated into the partly aged device) was exposed to 27 suns for 17 days while the other (later fabricated into the as-grown device) was kept in darkness. Then both sample packages were opened and the remaining device layers including 44 nm thick BHJ, BPhen and Ag cathodes were deposited in the VTE chamber using the same procedures as the vacuum-processed OPVs. After the $J-V$ measurement, the as-grown device was aged at 27 suns for 17 days which is referred

to as the fully aged device, as shown in Fig. 5.4(a). The BQE- V_{bulk} characteristics of the partly aged device are compared with those of the as-grown device and the fully aged device, as shown in Fig. 5.4(b). The device parameters of the unaged and aged devices are provided in Table 5.1.1. Although the MoO_x layer and the MoO_x/BHJ interface experience intense light exposure, the partly aged device has almost identical BQE- V_{bulk} characteristics as the as-grown device. The V_{off} and J_{sat} of the partly aged device, however, drop significantly.

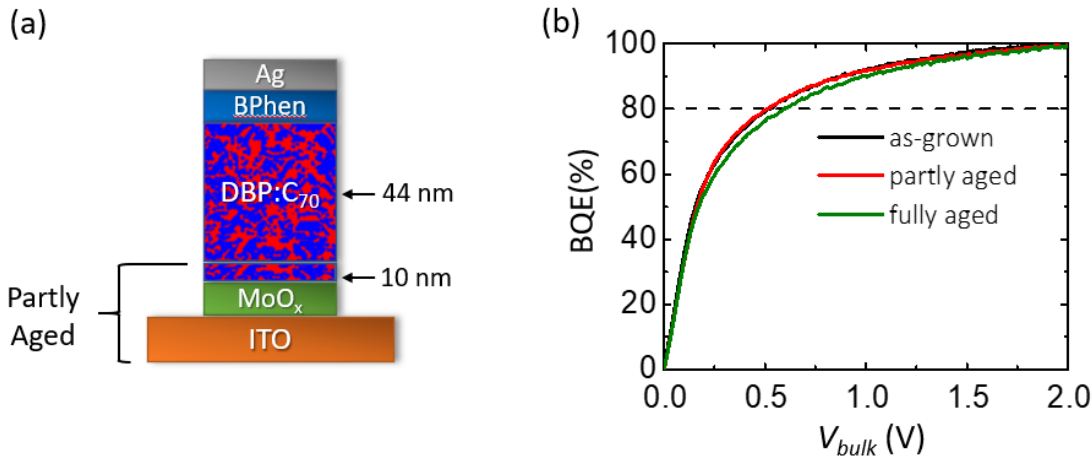


Figure 5.4 (a) Structure of the partly aged and fully aged OPVs. The ITO layer, MoO_x layer and bottom 10 nm of the BHJ were aged under white light with an intensity equivalent to 27 suns for 17 days in the partly aged device. (b) BQE- V_{bulk} characteristics of the partly aged device, the as-grown device, and the fully aged device.

Table 5.1 Device characteristics of DBP:C₇₀ OPVs with various aging procedures.

Device	V_{off} (V)	J_{sat} (mA/cm ²)	V_{80} (V)	PCE (%)
As-grown	0.94 ± 0.01	13.3 ± 0.3	0.52 ± 0.03	5.3 ± 0.2
Partly Aged	0.82 ± 0.01	12.7 ± 0.3	0.52 ± 0.03	4.5 ± 0.2
Fully Aged	0.94 ± 0.01	12.8 ± 0.3	0.60 ± 0.03	5.1 ± 0.2

Several mechanisms can lead to the degradation of OPV performance: morphological changes¹⁹⁹⁻²⁰¹ or chemical changes (e.g., photo-bleaching and molecule fragmentation)^{192, 202-203} in the BHJ, degradation of the electrodes,²⁰⁴⁻²⁰⁵ degradation of the buffer layers,²⁰⁶⁻²⁰⁹ chemical reactions and diffusion between BHJ and edge layers, etc.²¹⁰⁻²¹³ As shown in Figs. 5.2(a) and (b), the BQE of the DBP:C₇₀ OPV decreases under illumination, whose trend can be fit with Eq. (5.1.3) as shown in Fig. 5.3(a). The V_{off} remains almost constant, suggesting that there is no significant increase in the voltage across the interface during aging. The J_{sat} experiences a decrease of 1 mA/cm², which may be due to increased trapping within the buffer layers.

In the partly aged device in Fig. 5.4(a), only the lower section was exposed to illumination. As a result, this device has nearly identical BQE- V_{bulk} characteristics as the as-grown device, while the BQE of the fully aged device is reduced, as shown in Fig. 5.4(b). This suggests that the MoO_x and the MoO_x/BHJ interface are not responsible for the decrease in BQE observed in Fig. 5.2(a). The J_{sat} of the partly aged device is similar to that of the fully aged device, which is 0.5 mA/cm² smaller than that of the as-grown device, as shown in Table 5.1.1, indicating that aging of the lower edge layers (nearest the substrate) account for the decrease in J_{sat} observed in Fig. 5.2(b). The partly aged device has a V_{off} that is 0.12 V smaller compared with that of the as-grown and fully aged devices. This is possibly due to an energy barrier between the aged and unaged parts of the BHJ.

5.2 Photo-stability of NFA-based OPVs

Compared to the highly stable devices employing a C₇₀ acceptor with its high bond-dissociation energy, the most efficient NFAs contain multiple thiophene units with relatively weak chemical bonds that are dissociated at high UV and IR light intensities.¹⁹⁵⁻¹⁹⁷ Therefore, it remains

an open question as to what the degradation mechanisms are of solution processed systems based on NFAs. Beyond changes in the active BHJ in both materials and morphology, the properties of organic/electrode interfaces can also affect cell performance over time. Although strategies have been proposed to modify materials interfaces to suppress the degradation, to our knowledge, long term stable NFA-based solar cells under simulated air mass (AM) 1.5G irradiation have not yet been realized.¹⁴⁻¹⁷ The causes of instability for these high performance NFAs systems are also still not well understood. This motivates and encourages us to investigate the correlation between materials, film morphology, device architecture and their relationship to the reliability of NFA OPVs. In this sub-section, we study a material system used for semitransparent solar cell modules consisting of the commonly used donor, PCE-10, and an archetype near infrared (NIR) absorbing non-fullerene acceptor, BT-CIC to study the photodegradation of NFA-based OPVs.

5.2.1 BQE analysis for PCE-10:BT-CIC OPVs

Figure 5.5(a) shows the BQE- V_{bulk} characteristics of an OPV aged under 1 sun intensity, simulated AM1.5G illumination from a Xe-arc lamp. The device structure is: ITO 150nm/ZnO 30 nm/PCE-10:BT-CIC, 1:1.5, 80 nm/MoO_x 10 nm/Al 100 nm. The V_{80} experiences a significant increase of 0.4 V after 300 h, see inset. Figure 5.5(b) shows the V_{off} and J_{sat} vs. time. The V_{off} drops by 0.15 V during aging, while the J_{sat} drops by 3.5 mA/cm². Figure 5.5(c) shows the experimental (symbols) and fitted (lines) ΔBQE vs. V_{bulk} . The average V_{esc} is 0.2 V, corresponding to a site distance $d = 10$ nm. The fitted lines depart from the experimental data at large V_{bulk} , suggesting that the low trap site density assumption used to derive Eq. (5.1.3) is invalid. The maximum values of ΔBQE vs. aging time are shown in Fig. 5.5(d), where it is observed that the decrease in BQE saturates after 300 h.

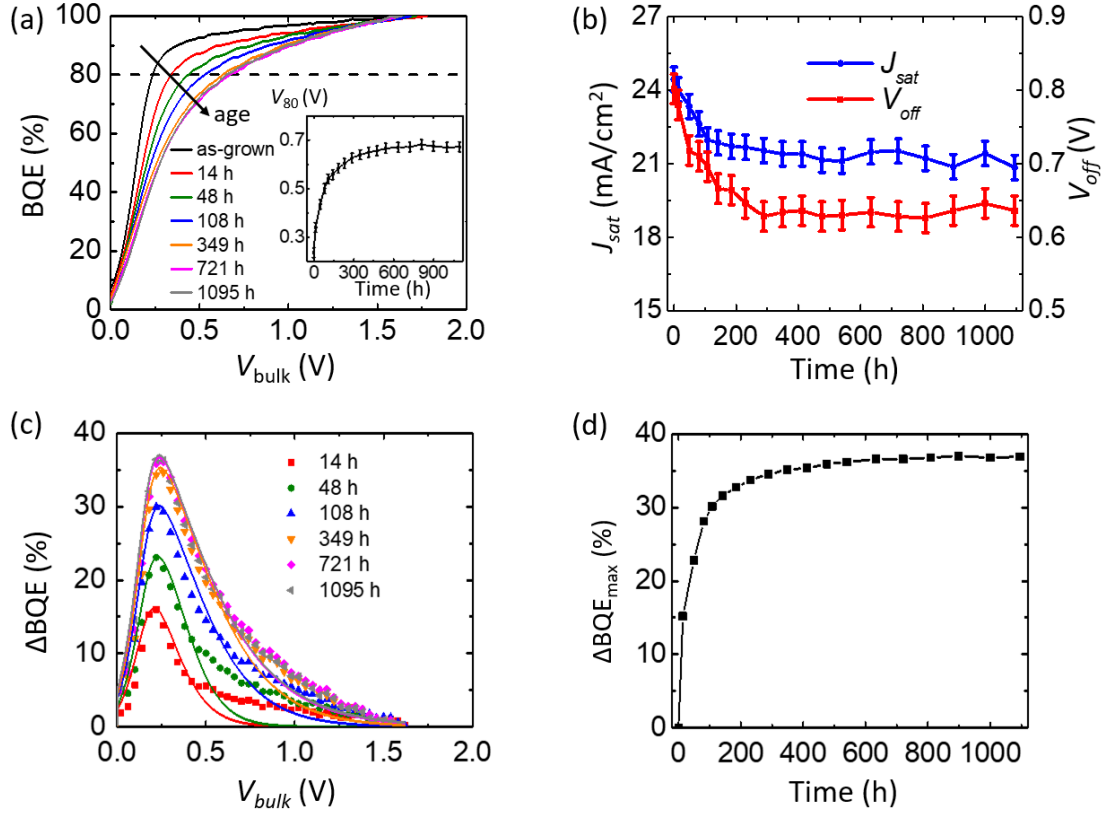


Figure 5.5 (a) BQE- V_{bulk} characteristics of an inverted OPV with a PCE-10:BT-CIC BHJ and a ZnO CBL aged under simulated AM 1.5G illumination. Inset: V_{80} vs. aging time. (b) V_{off} and J_{sat} vs. aging time. (c) Experimental (symbols) and fitted (lines) decrease in BQE (ΔBQE) vs. V_{bulk} vs. aging time. (d) The maximum values of ΔBQE vs. aging time.

The BQE decreases relative to the fresh device with a 0.4 V increase in V_{80} after 1000 h of aging under 1 sun intensity, simulated AM1.5G illumination, as shown in Fig. 5.5(a). The V_{off} drops by 0.15 V while the J_{sat} decreases by 3.5 mA/cm² (see Fig. 5.5(b)). The fitted lines depart from the experimental data at large V_{bulk} in Fig. 5.5(c), suggesting the existence of trapped charges even at large V_{bulk} . This is possibly because a high trap site density results in multiple trapping events for each charge during charge extraction, increasing the recombination probability beyond that predicted by Eq. (5.1.3) at large V_{bulk} . The ΔBQE saturates after 300 h, as shown in Fig. 5.5(d).

5.2.2 Photocatalytic reaction between NFA and ZnO

It has been reported that NFA molecules can experience photocatalytic reaction with ZnO. The absorption loss of encapsulated PCE-10 and BT-CIC on ZnO films aged under high intensity UV (365 nm LED, 60 suns, equivalent) is shown in Fig. 5.6 (a) and(b). Contrary to previous studies where PCE-10 on ZnO showed no degradation over 1400 h, UV soaking for ~30 h bleaches the BT-CIC. This is attributed to the photo-oxidation of the exocyclic double bond in BT-CIC that interrupts the π -conjugation, thus decreasing its absorbance²¹⁰⁻²¹¹.

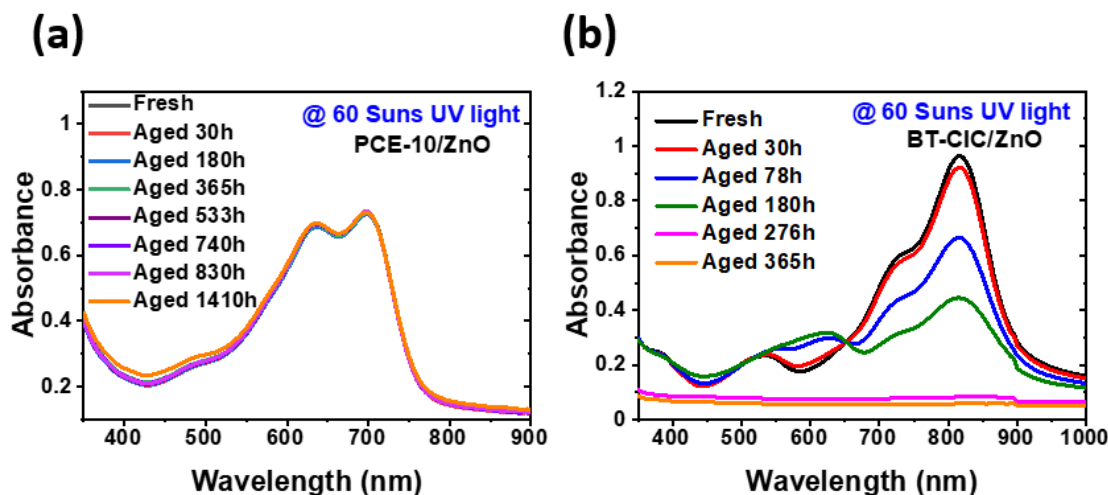


Figure 5.6 UV-Vis absorption spectra plotted vs. aging time under ultraviolet illumination with intensity equivalent to 60 suns of thin film of (a) PCE-10 on ZnO, (b) BT-CIC on ZnO.

5.2.3 IC-SAM protection layer

To suppress the reaction between NFA and ZnO, we insert an IC-SAM at the BHJ/ZnO interface. With insertion of the IC-SAM, no bleaching of BT-CIC and PCE-10:BT-CIC blend films is observed, and the intramolecular charge transfer peak maintains both its shape and intensity, as shown in Fig. 5.7(a) and (b).

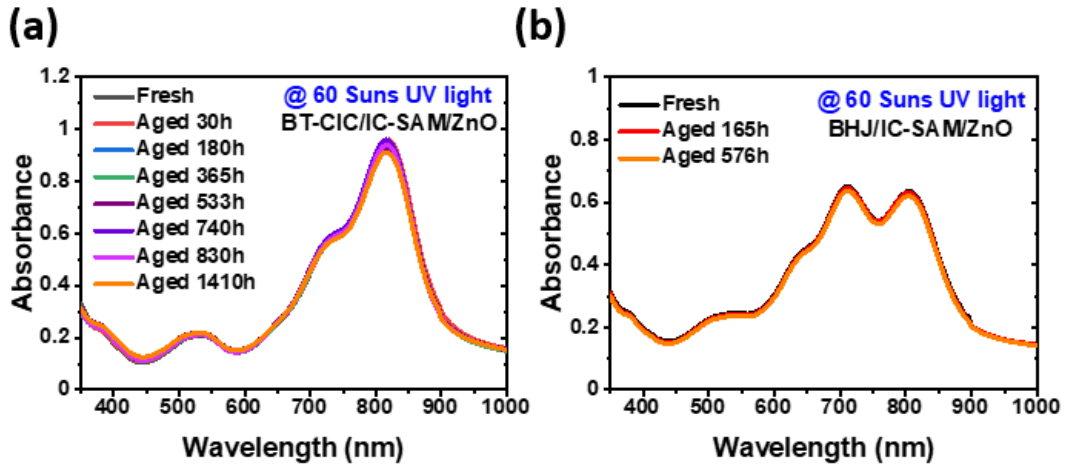


Figure 5.7 UV-Vis absorption spectra plotted vs. aging time under ultraviolet illumination with intensity equivalent to 60 suns of thin film of (a) BT-CIC/IC-SAM/ZnO, (b) PCE-10:BT-CIC/IC-SAM/ZnO.

With the IC-SAM inserted between the BHJ and ZnO, the BHJ is protected from the ZnO induced degradation. Figure 5.8(a) shows the BQE the time evolution of BQE- V_{bulk} characteristics of the control device under simulated AM 1.5G illumination with the V_{off} change in the inset. Both the BQE and the V_{off} experience fast decrease, suggesting both the BHJ and the edges are degrading. Figure 5.8(b) shows the BQE the time evolution of BQE- V_{bulk} characteristics of an OPV with an IC-SAM inserted between the BHJ and the ZnO. The change of V_{off} is shown in the inset. The decrease of BQE and V_{off} are significantly suppressed compared with the control device.

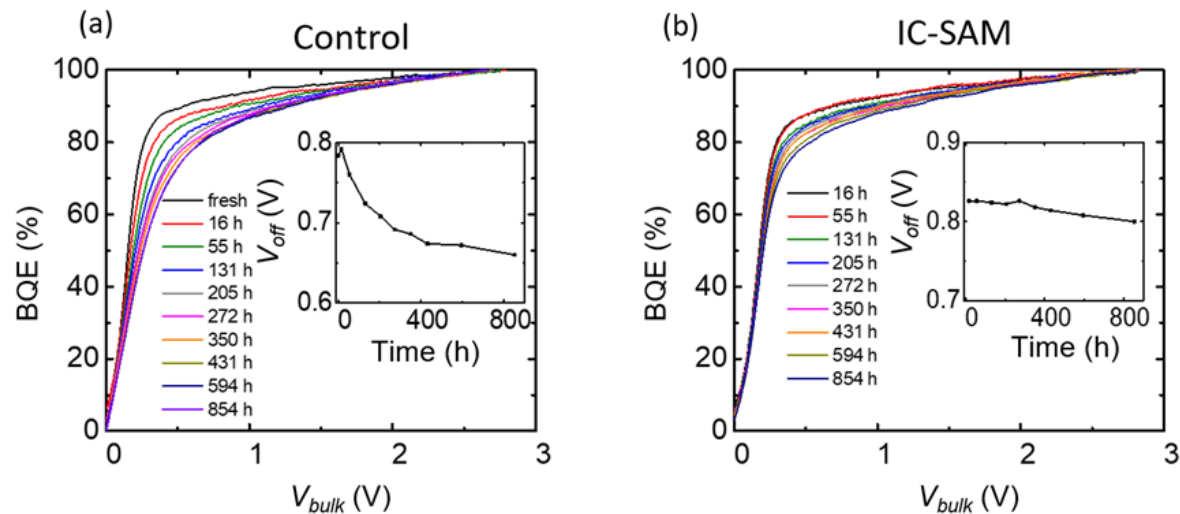


Figure 5.8 (a) Time evolution of BQE- V_{bulk} characteristics of a PCE-10:BT-CIC control OPV under simulated AM 1.5G illumination. Inset: V_{off} vs. aging time. (b) Time evolution of BQE- V_{bulk} characteristics of a PCE-10:BT-CIC OPV with an IC-SAM inserted between the BHJ and the ZnO layer under simulated AM 1.5G illumination. Inset: V_{off} vs. aging time.

5.2.4 GIWAXS and TEM study

The morphological stability of the PCE-10:BT-CIC (1:1.5, w/w) film was further investigated using grazing incidence wide angle X-ray scattering (*GIWAXS*), and carbon K-edge resonant soft X-ray scattering (RSoXS) as functions of aging under AM 1.5G, 1 sun intensity illumination. The samples were prepared on Si wafers in a similar manner to the devices. The thin films were measured at beamline 7.3.3 at the Advanced Light Source (ALS),²¹⁴ Lawrence Berkeley National Lab (LBNL). The x-ray energy was 10 keV and the scattering patterns were recorded on a 2D image plate (Pilatus 1M) with a pixel size of 172 μm (981×1043 pixels). The samples were ~ 10 mm long in the direction of the beam path, and the detector was located at a distance of 300 mm from the sample center (distance calibrated by a AgB reference). The incidence angle was 0.16° . Resonant soft x-ray scattering with photon energy of 283.6 eV was performed at beamline

11.0.1.2 of LBNL.²¹⁵ Thin films were transferred onto a Si₃N₄ substrate and the experiment was done in the transition mode.

As shown in Fig. 5.9(a), the GIWAXS diffraction profile of the PCE-10:BT-CIC blend film shows a (010) peak in the out-of-plane direction at $\sim 1.8 \text{ \AA}^{-1}$, and a (100) diffraction peak in the in-plane direction at 0.30 \AA^{-1} characteristic of BT-CIC. No changes in coherence lengths were observed in the diffraction profiles after aging. Further, both fresh and aged PCE-10:BT-IC blends show the same multi-length-scale morphology with one peak at $q = 0.10 \text{ nm}^{-1}$ (corresponding to a distance of 63 nm) and another at 0.28 nm^{-1} (22 nm). This suggests that the PCE-10:BT-CIC BHJ is stable itself.

To gain more insights to the role of IC-Sam, we prepare cross-sectional slice of the OPV device by focused ion beam (FIB) milling (FEI Nova 200 Nanolab SEM/FIB) and glued by Pt soldering onto a FIB lift-out grid rod. The sample was then transferred into a TEM chamber (JEOL 2010F) to take images. The absorbance of thin films is collected using a calibrated PerkinElmer Lambda 1050 ultraviolet-visible spectrometer. Transmission electron microscopy (TEM) images of thin cross-sectional slices of the OPVs without, and with the IC-SAM interface buffer are shown in Fig. 5.9(b) and (c), respectively. We find that the unprotected interface between ZnO and the BHJ appears broad, which is possibly due to the reaction between the BHJ and ZnO. In contrast, when the IC-SAM is placed between the ZnO and the BHJ, we observe a sharp boundary between layers. The boundary remains sharp even after ageing, as shown in Fig. 5.9(d).

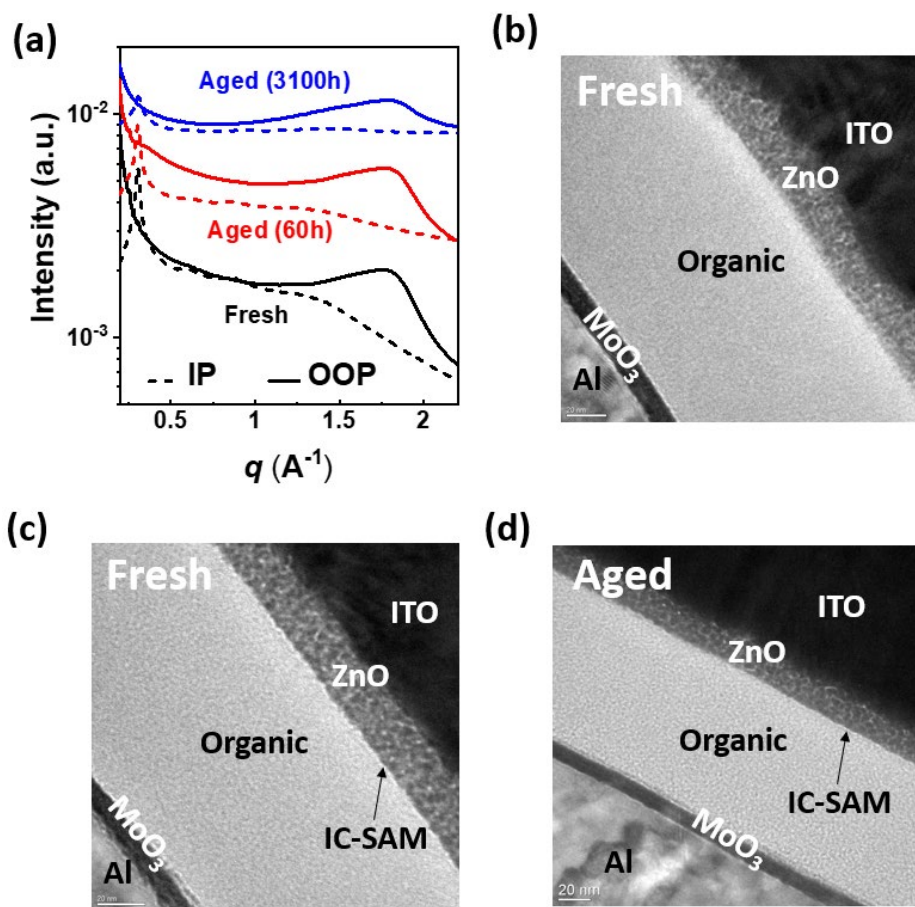


Figure 5.9 (a) In-plane (dotted line) and out-of-plane (solid line) sector-averaged profiles extracted from grazing incidence wide-angle x-ray scattering (GIWAXS) patterns, q is the scattering vector. (b) TEM image of cross-sectional slices of a fresh PCE-10:BT-CIC device without an interface buffer layer. (c) Fresh PCE-10:BT-CIC device with an IC-SAM layer inserted at the ZnO/BHJ interface. (d) Aged PCE-10:BT-CIC device with an IC-SAM layer inserted at the ZnO/BHJ interface under 27 ± 3.8 suns illumination for 870 h.

5.2.5 UV induced degradation

Although the IC-SAM suppresses the reaction between BHJ and ZnO, the BQE still experience a decrease as shown in Fig. 5.8(b). We found that this bulk degradation is mainly induced by the UV part of the illumination. Figure 5.10 shows the Time evolution of BQE- V_{bulk} characteristics of a PCE-10:BT-CIC OPV with an IC-SAM inserted between BHJ and ZnO and a UV filter (cutoff at 400 nm) under simulated AM 1.5G illumination with the change of V_{off} shown in the inset. The BQE decrease is significantly suppressed compared with Fig. 5.8(b). This result

shows that the NFA-based BHJ can be intrinsically stable under white light when externally induced mechanisms are stopped.

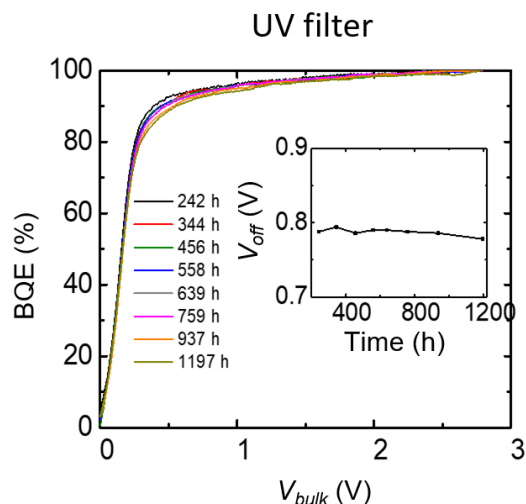


Figure 5.10 Time evolution of BQE- V_{bulk} characteristics of a PCE-10:BT-CIC OPV with an IC-SAM inserted between BHJ and ZnO and a UV filter (cutoff at 400 nm) under simulated AM 1.5G illumination. Inset: V_{off} vs. aging time.

However, in reality, it is impossible to install laboratory level UV filters for all OPV devices. To solve this problem, we developed a spin coated 600 nm thick ZnO film on the external surface of the glass substrate that effectively blocks radiation at wavelengths < 400 nm. Figure 5.11 shows the transmittance spectra of the fresh stand-alone filter, as well as one aged for 1500 h at 1 sun intensity in air. Compared to the bare glass substrate, the one comprising the ZnO filter exhibits negligible transmission at wavelengths < 375 nm, with approximately 6% Fresnel reflection loss at > 400 nm. The performance of the device with ZnO coating retained 95% of its initial PCE after 340 h, which is equivalent to 11 years of accumulated UV photons from outdoor exposure. In contrast, the PCE of the device lacking the ZnO coating declined by 66% over this same period.

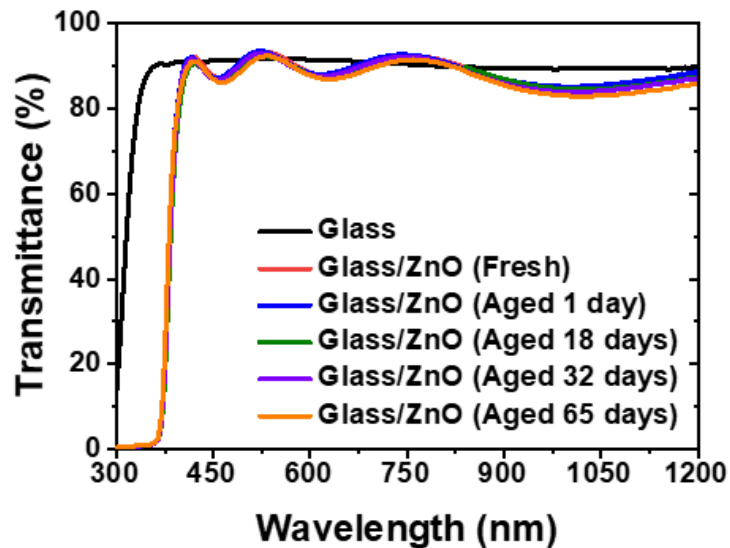


Figure 5.11 Transmittance spectra of the glass substrate with and without the ZnO coating with various aging periods.

5.2.6 Light intensity dependence of OPV photostability

With the IC-SAM suppressing the reaction between BHJ and ZnO and the UV filter to protect the BHJ from high energy photons, the OPV is very stable under one Sun illumination. To better understand the intensity dependence of the intrinsic photodegradation of the BHJ, the devices are tested under high intensity white light LEDs.

The changes of BQEs over time of the OPVs under 10 Suns, 20 Suns and 27 Suns white light illumination are shown in Fig. 5.11 (a), (b) and (c). The changes of V_{off} over time are shown in Fig. 5.11 (d), (e) and (f). It can be seen that the OPV performance degradation is mainly due to the degradation of the BHJs while the changes in the edges are relatively small.

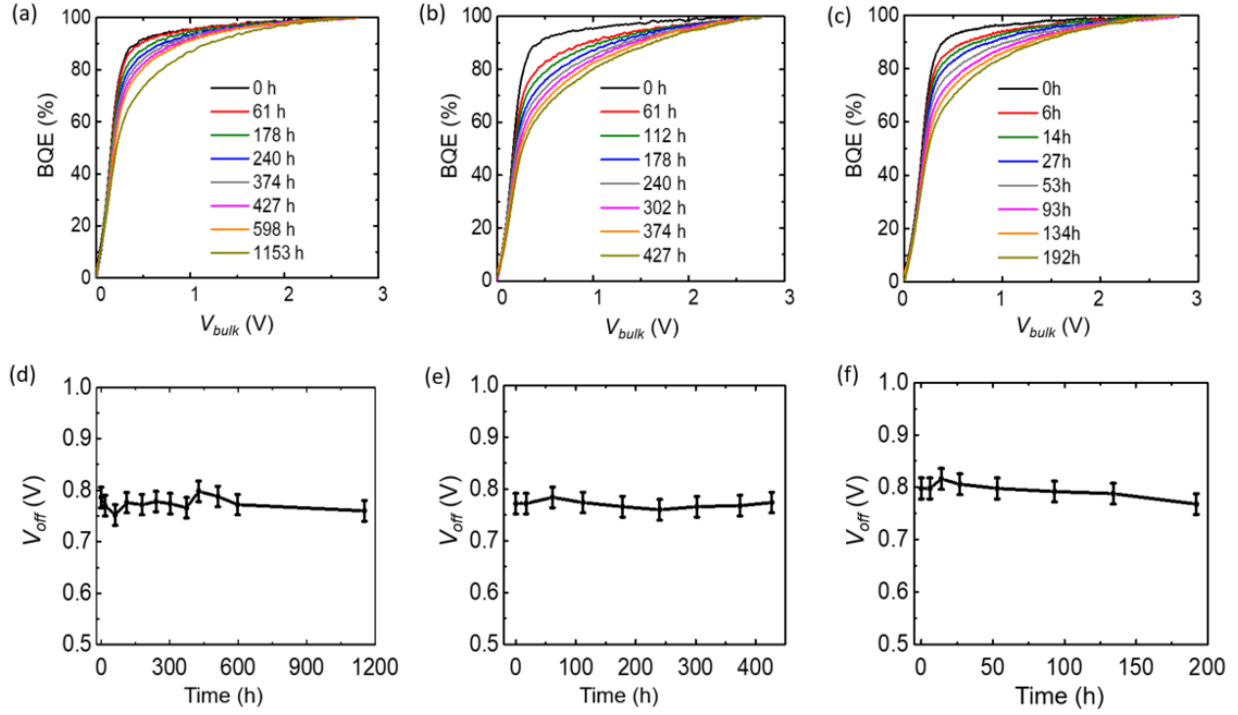


Figure 5.12 (a), (b), (c) Change of BQE over time of BT-CIC:PCE-10 OPVs under white light illumination equivalent to 10, 20 and 27 Suns. (d), (e), (f) Change of the V_{off} over time under white light illumination equivalent to 10, 20 and 27 Suns.

The decrease of BQE can be explained by an increase of trap state density inside the BHJs, which is proportional to the maximum value of the BQE decrease, ΔBQE_{max} .²¹⁶ We define the equivalent 1-sun exposure time, t_{1sun} , as:

$$t_{1-sun} = \left(\frac{I}{I_{sun}} \right)^2 \cdot t, \quad (5.2.1)$$

where I is the illumination intensity, I_{sun} is the solar illumination intensity, t is the aging time.

Figure 5.13 shows the maximum values of BQE decrease, $\Delta\text{BQE}_{\text{max}}$, vs. $t_{1\text{-sun}}$ under various white light intensities. All three lines are almost linear to the t_{square} with similar gradients. This suggests that the creation rate of trap states inside the BHJs is proportional to $t_{1\text{-sun}}$. This coincides with second-order events such as exciton-exciton annihilations of which the rates are also proportional to $t_{1\text{-sun}}$.

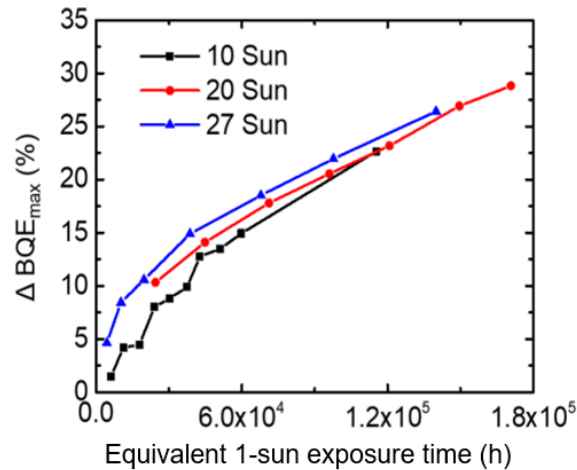


Figure 5.13 Maximum values of BQE decrease, $\Delta\text{BQE}_{\text{max}}$, vs. squared aging time, t_{square} , of BT-CIC:PCE-10 OPVs under various white light intensities.

With the suppression of externally induced degradations by inserting protection layers on the anode and cathode buffer layer interfaces and separate the BHJs degradation from the edges using BQE analysis, we show that intrinsic photo-degradation rates of NFA based BHJs are proportional to the square of light intensity. Such a simple quantitative relationship provides insightful information to the understanding of fundamental degradation mechanisms of OPVs. Based on the results, we propose that the intrinsic photo-degradation of NFA based BHJs are mainly due to trap states created by second-order events such as exciton-exciton annihilation inside the BHJs. ²¹⁷⁻²¹⁹

5.3 Conclusions

Using various experimental tools and the BQE analysis, we show that the photodegradation of OPVs with various BHJ materials are due to different mechanism. In vacuum deposited DBP:C₇₀ devices, the photodegradation mainly affects the BHJ and can be described by an increase in trap state density. The photodegradation of the NFA solar cells have two externally induced sources. A photocatalytic reaction between the BHJ and ZnO, and the UV illumination. The former can be effectively suppressed by inserting an IC-SAM layer between the BHJ and ZnO layer. The latter can be suppressed by the integration of a simple ZnO UV filter layer to the distal surface of the glass substrate. With the two externally induced degradation mechanisms suppressed, the rate of intrinsic photodegradation of the BHJ is found to be proportional to the square of light intensity. This suggests that second-order events such as exciton-exciton annihilation could be a main source of intrinsic photodegradation of OPV BHJs.

Chapter 6

Thermal Stability of Organic Photovoltaics

In real applications, solar cells are often exposed to temperatures that are much higher than lab conditions.²²⁰⁻²²¹ Depending on the installation conditions, the solar cells in outdoor applications can experience temperatures as high as 80°C. Therefore, it is necessary to study the thermal stability of OPVs. However, NFA- based OPVs often have poor thermal stabilities, significantly limiting their outdoor applications.²²²⁻²²⁶ In this chapter, we characterize the thermal stabilities at temperatures up to 80°C of inverted NFA-based OPVs and study the mechanisms behind various channels of thermal degradation.

6.1 Thermal Degradation of inverted NFA-based OPVs

6.1.1 J-V characteristics and EQE

We fabricate OPVs on ITO coated glass substrates (Lumtec Corp.) with a sheet resistance of 15 Ω /sq. The ITO anodes were patterned into 1 mm wide strips. The substrates were cleaned using a detergent (tergitol solution) and solvents (acetone and isopropanol) and exposed to ultraviolet ozone for 15 min. The ZnO layer was fabricated by spinning a sol-gel ZnO precursor solution (Sigma-Aldrich Inc.) at 4,000 rpm for 1 min and thermally annealed in air at 160 °C for 30 min. The IC-SAM was dissolved at 1 mg/mL in Methanol and stirred at 300 rpm at 65 °C

overnight. The solution was then spun at 3,500 rpm for 1 min, followed by thermally annealing at 110 °C for 10 min. After the annealing, pure methanal solution was spun on the IC-SAM at 3,500 rpm for 1 min to remove residual IC-SAM molecules that are not chemically bonded to the ZnO. The PCE-10:BT-CIC powder was dissolved in 9:1 chlorobenzene:chloroform solution at a total concentration of 16 mg/mL and stirred at 300 rpm at 65 °C overnight. The solution is then spun onto the sample at 4,000 rpm for 1 min. The PM6:Y6 power was dissolved in chloroform at a total concentration of 20 mg/mL and stirred at 300 rpm at 65 °C overnight. The solution is then spun onto the sample at 4,000 rpm for 1 min. The film is then thermally annealed at 110 °C for 10 min.

The MoO_x layers and Ag electrodes were deposited in a VTE chamber with a base pressure of 10⁻⁷ Torr. The MoO_x was deposited at 0.6 Å/s. The Ag was deposited with a ramping rate from 0.1 to 1 Å/s. The deposition rates and film thicknesses were monitored by quartz crystal monitors and calibrated post-growth using variable-angle spectroscopic ellipsometry. The Ag electrodes were deposited through 2 mm wide shadow mask openings oriented orthogonal to the ITO strips, forming device areas of 2 mm². After the deposition of the electrodes, the devices were encapsulated in N₂ atmosphere.

The encapsulated devices were thermally aged on hotplates at various temperatures in air in a windowless room with lights turned off. The *J-V* characteristics were measured inside a N₂ glovebox at room temperature using a parameter analyzer (Agilent 4156C) with a 1 kW m⁻² simulated AM 1.5G illumination source.

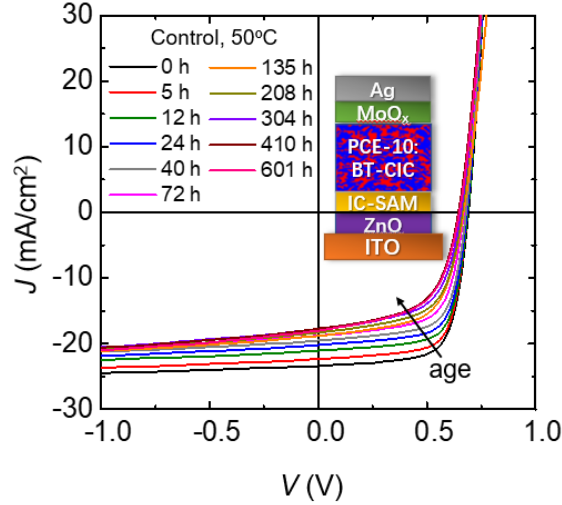


Figure 6.1 Time evolution of J - V characteristics of a PCE-10:BT-CIC device when heated under 50 °C in the dark. Inset: Device structure.

Figure 6.1 shows the time evolution of the current density-voltage (J - V) characteristics of an OPV held for extended periods in the dark at 50°C. The control device structure shown in the inset of Fig. 6.1(a) is: ITO 150nm/ZnO 30 nm/IC-SAM/PCE-10:BT-CIC, 1:1.5, 80 nm/MoO_x 10 nm/Ag 100 nm (control). The IC-SAM prevents photocatalytic reactions between ZnO and NFA BHJs as shown in Chapter 5. After 600 h, the short-circuit current (J_{sc}) decreased from 23.4 ± 0.3 mA/cm² to 18.0 ± 0.3 mA/cm², the open-circuit voltage (V_{oc}) from 0.69 ± 0.01 V to 0.64 ± 0.01 V, the fill factor (FF) from 0.69 ± 0.01 to 0.58 ± 0.01 , and PCE from 11.3 ± 0.2 % to 6.6 ± 0.2 %.

At higher temperature, surprisingly, we observed a recovery in PCE and the EQE, which is quite abnormal for thermal degradation of solar cells. As shown in Fig. 6.2 (a), at 80°C, the J - V characteristics degrade rapidly in the first 8 h, but the J_{sc} recovers at 62 h, while the V_{oc} is still smaller compared with the as cast device. The EQE spectrum decreases and recovers with no significant change in the wavelength dependence, as shown in Fig. 6.2(b).

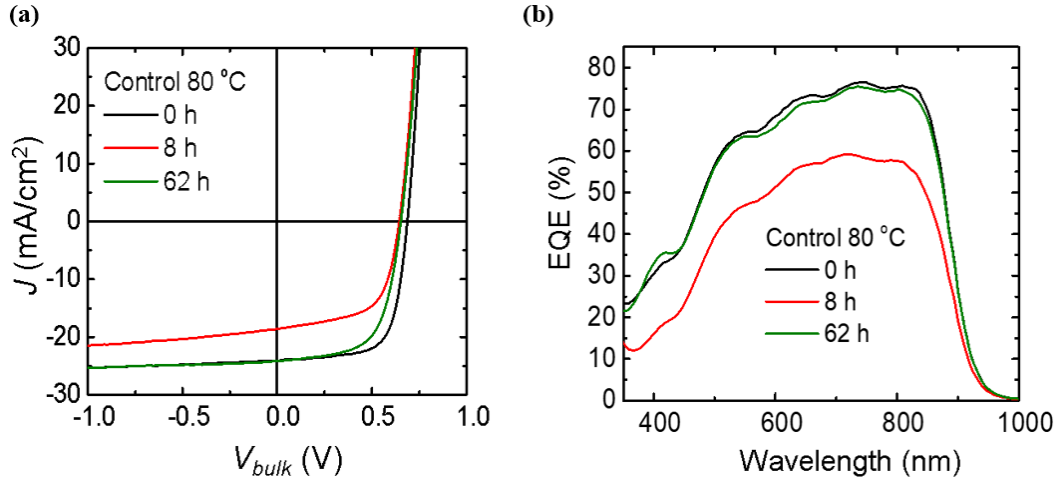


Figure 6.2 (a) J - V characteristics of a PCE-10:BT-CIC control device when heated under 80 °C after various aging periods. (b) External quantum efficiency (EQE) spectra of the control device when heated under 80 °C after various aging periods.

6.1.2 C₇₀ anode interlayer

To test if this thermal degradation is related to the BHJ/MoO_x interface, we insert a 2-nm-thick C₇₀ layer between the BHJ and MoO_x in a buffered device that is otherwise identical to the control.¹⁸⁶ Figure 6.3 shows the time evolution of the J - V characteristics at 50°C of the buffered device. The degradation rate is significantly suppressed from that of the control, with only a small PCE drop, from 10.8 ± 0.2 % to 10.4 ± 0.2 % after 600 h. This suggests that the BHJ/MoO_x interface plays an important role in the thermal degradation of this device.

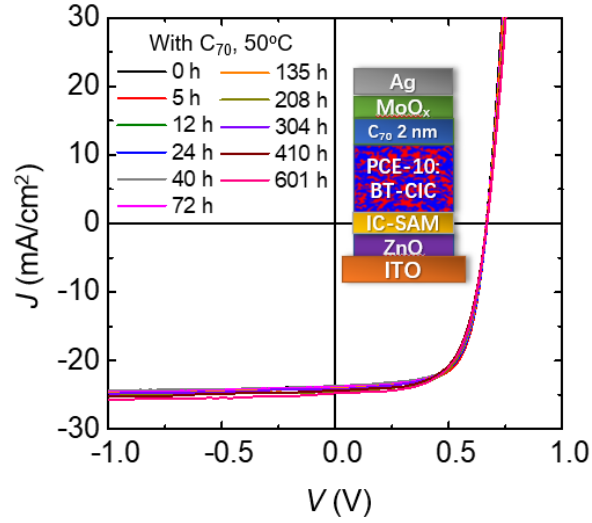


Figure 6.3 Time evolution of J - V characteristics of a PCE-10:BT-CIC device with a 2 nm thick C_{70} layer inserted between the MoO_x and BHJs when heated under 50 °C in the dark. Inset: Device structure.

Figure 6.4 shows the PCE time evolution of control (solid lines) and buffered (dashed lines) devices heated in the dark at several temperatures. At all temperatures, the addition of the C_{70} buffer improves the thermal stability. The device T_{80} at 80 °C increases from 20 min to 800 h with the C_{70} buffer inserted. The control devices at 70 °C and 80 °C show a recovery in their PCEs after initial decrease, forming a check-mark shaped aging pattern. The T_{80} at 80 °C improves from 20 min to 800 h.

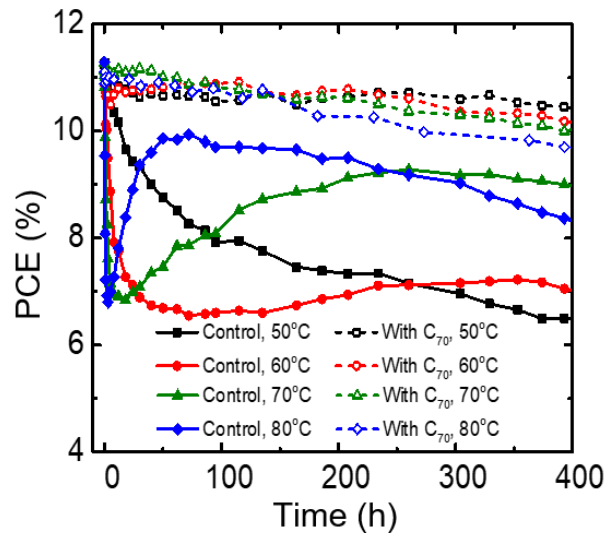


Figure 6.4 Time evolution of PCEs of control devices (solid lines) and devices with the C_{70} protection layer (dash lines) heated under various temperatures. The errors of the PCEs are $\pm 0.2\%$ but not plotted for clarity.

OPVs with PM6 as the donor and Y6 as the acceptor have reached single cell PCEs over 18%.^{34, 227-228} Figure 6.5 shows the PCE time evolution of PM6:Y6 OPVs with D/A ratios of 1:2 (black) and 1:1 (red) without (solid lines) and with (dashed lines) the C_{70} layer. The device structures are: ITO 150nm/ZnO 30 nm/ PM6:Y6, 130 nm/ C_{70} , 2 nm (not in control devices)/MoO_x 10 nm/Ag 100 nm. The results are similar to those of the PCE-10:BT-CIC devices except for a burn-in effect, where the PCE rapidly increases in the first hour of thermal ageing, possibly due to a morphology change.

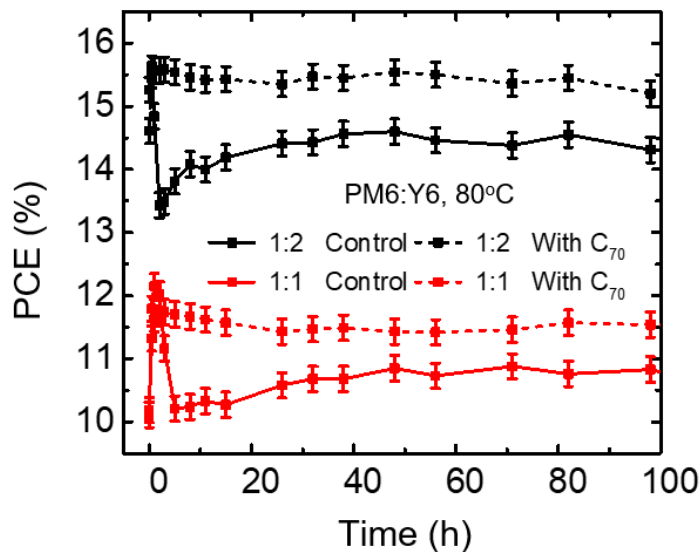


Figure 6.5 PCE time evolution of PM6:Y6 OPVs with donor/acceptor ratios of 1:2 (black) and 1:1 (red) without (solid lines) and with (dash lines) the C₇₀ protection layer.

6.1.3 BQE analysis

To understand which layers of the device are most responsible for changes in PCE over time, we apply the BQE analysis developed in Chapter 4. As discussed above, BQE is a quantity that measures the photogeneration properties of the BHJ, and does not depend on the peripheral layers, or the “edges”. The V_{off} depends on the voltage drop at the edges.

Figure 6.6(a) and (b) show the time evolution of the BQE- V_{bulk} characteristics of the control and buffered devices, respectively, heated in the dark at 80 °C. To better visualize the change of BQE over time, the time evolutions of V_{80} , as defined in Eq. (4.2.1), are plotted in the insets. The larger the V_{80} is, the worse is the photogeneration property of the BHJ. The V_{80} of the control device increases rapidly in the first 5 hours but decreases and stabilizes after 40 hours, while the V_{80} of the buffered device remain constant for the whole ageing period of 600 h. The time evolutions of V_{off} at several temperatures of control and buffered devices are shown in Fig 6.6 (c)

and (d), respectively. The V_{off} of the control devices show monotonic decreases of 0.12 ± 0.01 V(80°C), 0.08 ± 0.01 V(70°C), 0.07 ± 0.01 V(60°C), 0.04 ± 0.01 V(50°C) over 600 h. The V_{off} of the buffered devices show smaller decrease of 0.07 ± 0.01 V (80°C), 0.03 ± 0.01 V(70°C), 0.03 ± 0.01 V(60°C), 0.02 ± 0.01 V(50°C) over 600 h.

From the BQE analysis, we identify two thermal degradation modes: (1) a temperature-induced change in the BHJ featured by the decrease and recovery of the BQE, which can be almost fully arrested by adding a thin C_{70} layer at the BHJ/MoO_x interface; and (2) an increased voltage loss at the edges as inferred by the monotonic decrease of V_{off} . This voltage loss has been previously attributed to increased interfacial dipoles between the BHJ and buffer layers.¹⁸⁶ Note that the magnitude of the decrease in V_{off} is reduced by either eliminating the IC-SAM on the cathode side or adding the C_{70} layer on the anode side. In the following sections, we mainly focus on mode (1), which is related to the abnormal check-mark aging pattern of the PCE.

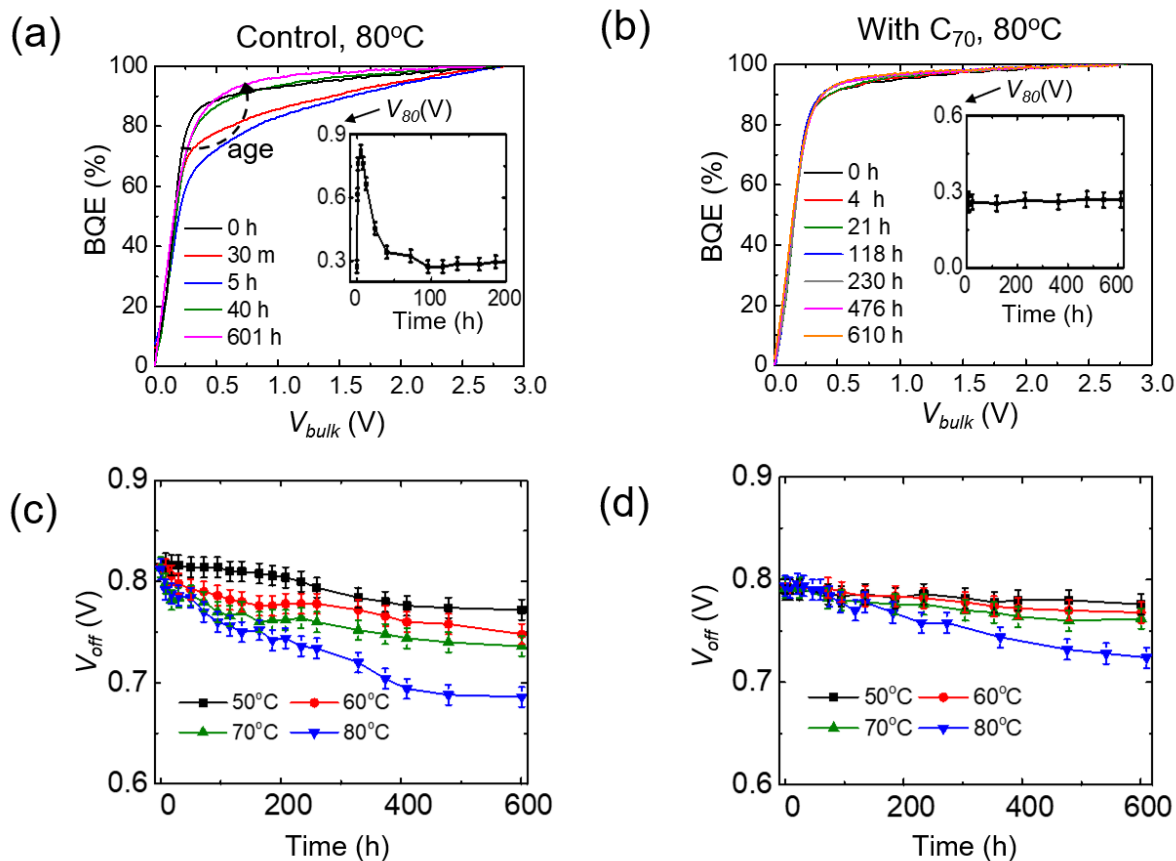


Figure 6.6 (a) Time evolution of BQE- V_{bulk} characteristics of a control device at 80°C. Inset: time evolution of the V_{80} . (b) Time evolution of BQE- V_{bulk} characteristics of a buffered device at 80°C. Inset: time evolution of time evolution of the V_{80} . (c) Time evolution of V_{off} of control devices at various temperatures. (d) Time evolution of V_{off} of buffered devices at various temperatures.

6.1.4 STEM and EDS mapping

To gain more insights into the causes of mode (1), we examined the interfaces in thin slices of devices with and without C_{70} buffer via STEM and energy dispersive spectroscopy (EDS) mapping. The cross-sectional slices of OPVs were carved out of the OPV device by FIB milling (FEI Nova 200 Nanolab SEM/FIB) and glued by Pt soldering onto a FIB lift-out grid rod. The sample is then thinned down to electron-transparent before transferred into a STEM system (Thermo Fisher Talos F200X G2 S/TEM) for STEM and EDS mapping.

Figure 6.7(a) shows the STEM image collected by a bright-field (BF) detector of a control device heated in the dark for 700 h at 80 °C. Figure 6.7(b) shows an image of the BHJ/MoO_x interface collected by a low-angle annular dark field (LAADF) detector. Figure 6.7(c) shows the Cl weight concentration distributions of the as-cast device with C₇₀ layer, thermally aged device with C₇₀ layer, and the thermally aged control device with the horizontal axis aligned to that of Fig. 6.7(a). Figure 6.7(d) shows the EDS Cl concentration map near the BHJ/MoO_x interface with the horizontal axis aligned to that of Fig. 6.7(b). A high concentration of Cl is observed at the BHJ/MoO_x interface in the thermally aged control device but not in the as-cast control device and thermally aged device with C₇₀ layer. The Cl concentration can be distinguished in the LAADF image (vertical bright line in the middle of Fig. 6.7(b)) but not in the BF image. Among the materials comprising the device, only BT-CIC contains Cl. These results suggest that during the thermal aging of the control device, the Cl in the BHJ redistributes and moves toward the BHJ/MoO_x interface.

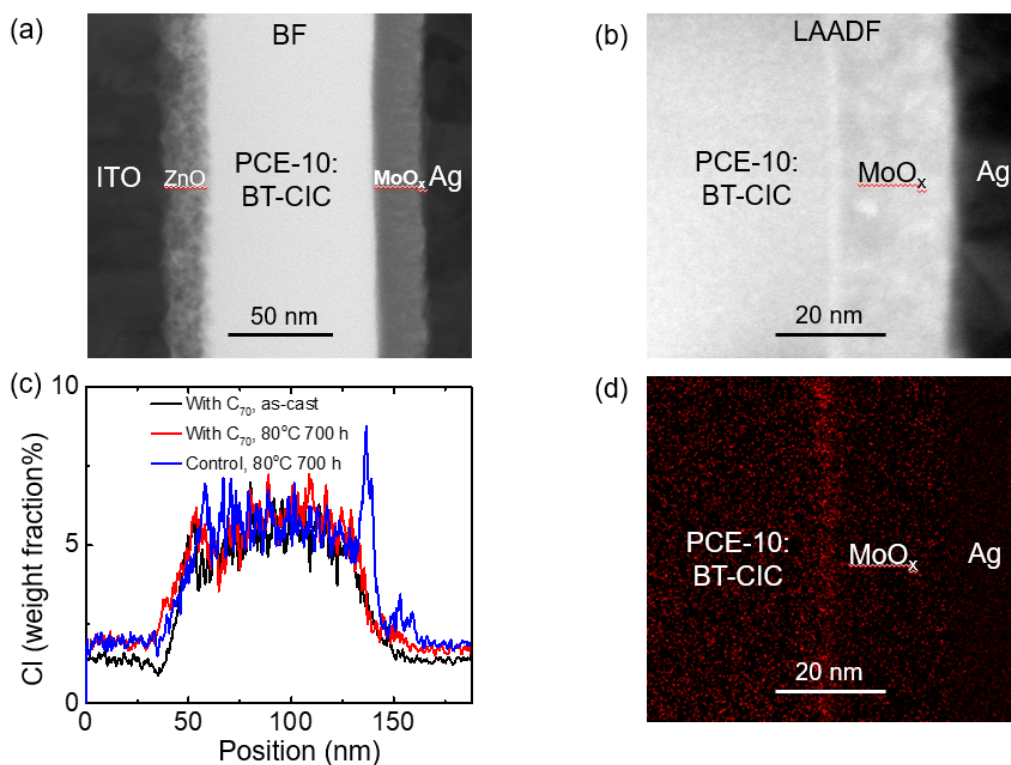


Figure 6.7 (a) STEM image collected by a bright-field (BF) detector of a control device heated in the dark for 700 h at 80°C. (b) Zoomed in STEM image of the BHJ/MoO_x interface collected by a low-angle annular dark field (LAADF) detector. (c) The EDS Cl weight concentration distributions of the as-cast device with a C₇₀ layer, thermally aged device with a C₇₀ layer and the thermally aged control device with the horizontal axis aligned to that in (a). (d) The Cl weight concentration map near the BHJ/MoO_x interface with the horizontal axis aligned to that in (b).

6.1.5 XPS study of BHJ/MoO_x interface

To understand the origin of the high Cl concentration at the BHJ/MoO_x interface in the thermally aged control, we used X-ray photoelectron spectroscopy (XPS) to examine the MoO_x surface. Samples with structures: ITO (150 nm)/MoO_x (10 nm)/organic layer were fabricated and thermally aged before submersion into chlorobenzene to dissolve the organic layer. Figures 6.8 (a)-(d) show the XPS spectra of Mo 3d peaks of samples fabricated with PCE-10:BT-CIC, 1:2 or neat BT-CIC layers held at room temperature (RT) or 90°C. The spectra are fit with multiple Gaussian peaks using CasaXPS.²²⁹ Both blend and BT-CIC samples show reduced intensities of Mo⁵⁺ relative to Mo⁶⁺ peaks after the aging, suggesting that the MoO_x is oxidized. The blend layer

samples show a sulfur (S) 2s peak at 228.3 eV, suggesting the existence of residual thiophene, which exists in both BT-CIC and PCE-10, on the MoO_x surface. The S 2s peak is missing in samples with neat BT-CIC layers indicating their complete removal by the chlorobenzene treatment.

Figures 6.8 (e)-(h) show the measured and fit XPS spectra of the Cl 2p peaks of blend and neat BT-CIC layers held at RT or 90°C. While the Cl signals in the blends may be from residual molecules left on the MoO_x surface, the Cl in neat BT-CIC are due to chlorination of MoO_x since the BT-CIC molecules are completely removed according to Fig. 6.8 (c) and d. Chlorination is possible due to the smaller energy of the C-Cl bond (327 kJ/mol or 3.39 eV) compared that of Mo-Cl (365 kJ/mol or 3.78 eV).²³⁰⁻²³¹ Hence, this atomic exchange is net exothermic. One possible product is MoCl₂O₂.

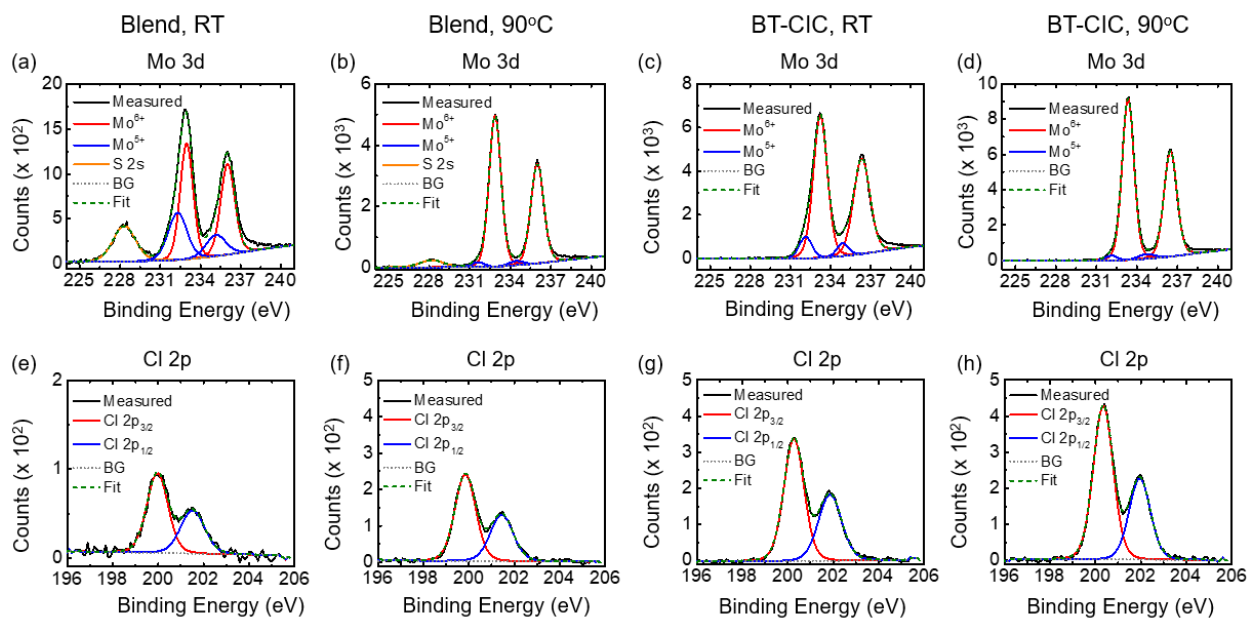


Figure 6.8 X-ray photoelectron spectra (XPS) of the Mo 3d signal of MoO_x layers fabricated with a (a) PCE-10:BT-CIC 1:2 blend layer, held at room temperature (RT), (b) PCE-10:BT-CIC 1:2 blend layer, held at 90°C, (c) neat BT-CIC layer, held at RT, and (d) neat BT-CIC layer, held at 90°C for 100 h. XPS spectra of Cl 2p of MoO_x layers fabricated with a (e) PCE-10:BT-CIC 1:2 blend layer, held at RT, (f) PCE-10:BT-CIC 1:2 blend layer, held at 90°C, (g) neat BT-CIC layer, held at RT, and (h) neat BT-CIC layer, held at 90°C for 100 h.

Given these results, we can infer a likely mechanism leading to degradation mode (1) of the control device. Due to the redox reaction between the BT-CIC and MoO_x observed by XPS, the BT-CIC molecules near the BHJ/MoO_x interface lose Cl to the MoO_x, driving a thermally activated redistribution of Cl toward the BHJ/MoO_x, leading to the change of BQE in Fig. 6.6(a). The insertion of the C₇₀ layer at the BHJ/MoO_x interface prevents interactions between BT-CIC and the MoO_x, thus eliminating processes leading to mode (1).

6.2 Thermal Degradation of conventional structured NFA-based OPVs

6.2.1 *J-V characteristics*

In solution processed OPVs, spin coating of successive layers must be done with orthogonal solvents to prevent destruction of previously fabricated layers. As a result, conventional structured OPVs often have different buffer layer choices as the inverted OPVs. We tested the thermal stability of conventional structured OPVs with various ABL and CBL combinations. We will use ABL_CBL to refer to the device with a particular buffer layer combinations. The device structures are: ITO 150nm/ABL 10 nm/ PCE-10:BT-CIC, 1:1.5, 80 nm/CBL 10 nm/Ag 100 nm. Figure 6.9 shows the time evolution of the of *J-V* characteristics at 80°C of OPVs with ABL/CBL combinations of (a) PEDOT:PSS/TmPyPB, (b) MoO_x/BPhen, (c) PEDOT:PSS/PDINO. All devices experience rapid thermal degradation.

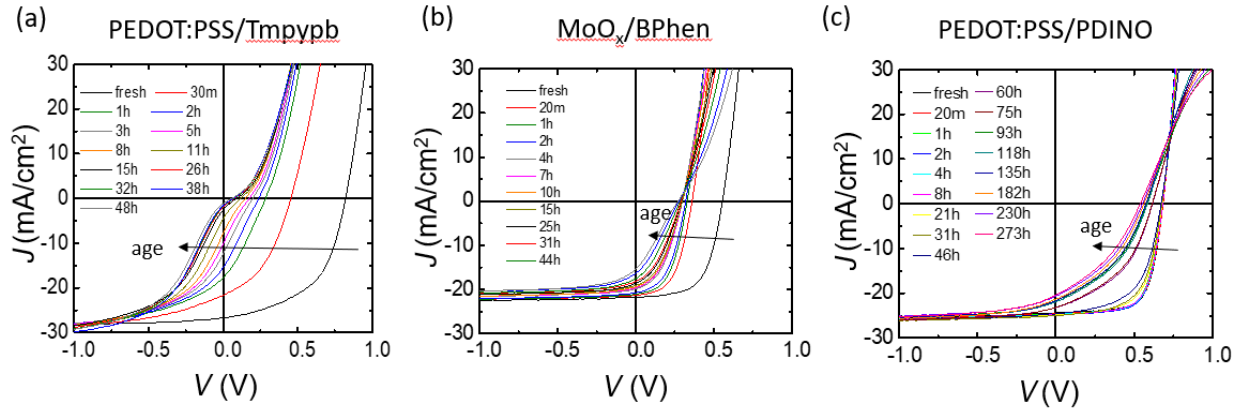


Figure 6.9 Time evolution of J - V characteristics at 80°C of OPVs with ABL/CBL combinations of (a) PEDOT:PSS/TmPyPB, (b) MoO_x/BPhen, (c) PEDOT:PSS/PDINO.

The PCE time evolution under 80°C is shown in Fig. 6.10. Most devices show poor thermal stability with the PCE decrease by more than 50% within 100 hours. The MoO_x_PDINO device shows a similar mode (1) recovery pattern as the control device. The mode (1) recovery pattern is not observed in MoO_x_TmPypb and MoO_x_BPhen devices possibly due to the mode (2) degradation is too fast.

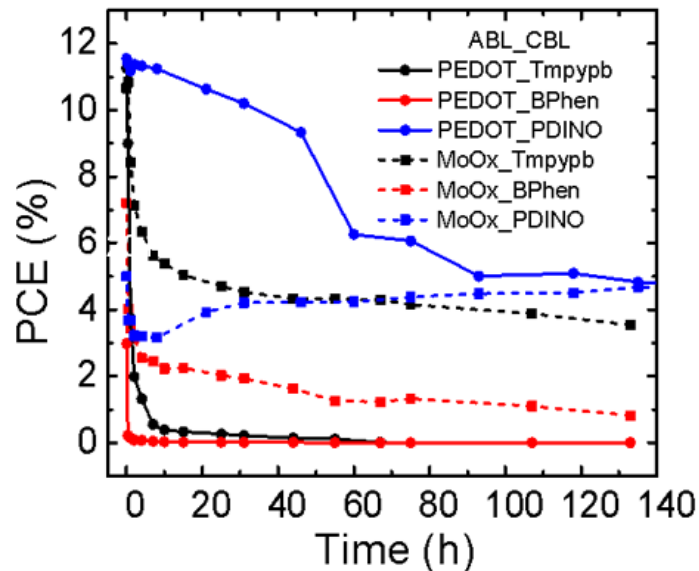


Figure 6.10 PCE time evolution under 80°C of conventional structured OPVs with various ABL/CBL combinations.

6.2.2 BQE analysis

We apply the BQE analysis to study if the bulk or the edges cause the PCE decrease. Figure 6.11 shows the time evolution of of BQE- V_{bulk} characteristics under 80 °C of the MoO_x_BPhen device with the V_{off} change shown in the inset. It can be seen that the rapid decrease of V_{off} is the main cause for the PCE decrease, while the change in BQE is small. This suggests that the buffer layers are the main reasons for the thermal degradation of conventional-structured OPVs. This agrees with the results of inverted OPVs as NFA-based solution processed BHJs are intrinsically stable at high temperatures.

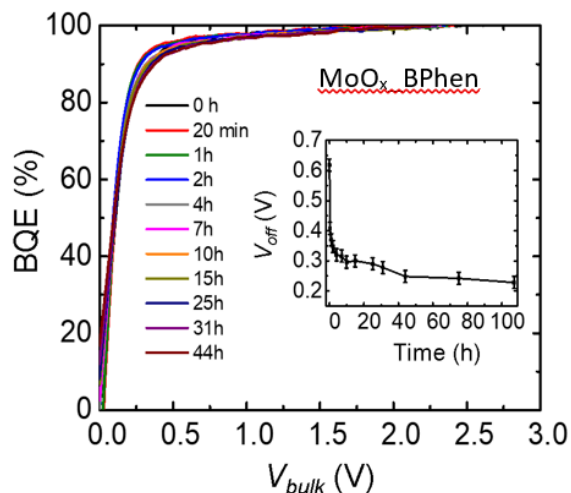


Figure 6.11 Time evolution of BQE- V_{bulk} characteristics under 80 °C of the MoO_x_BPhen device. Inset: Time evolution of V_{off} .

6.3 Thermal Degradation vs. Photodegradation

Table 6.1 summarizes the thermal and photodegradation mechanisms encountered so far for PCE-10:BT-CIC based inverted OPVs and methods to suppress them. In Chapter 5, we studied two externally induced photodegradation modes, the photocatalytic reaction between NFA-based BHJ and ZnO, and UV induced damage. The former causes decomposition of BT-CIC, leading to a degradation to both the BHJ and the edges. This reaction can be suppressed by inserting an IC-

SAM or C₆₀-SAM between the BHJ and ZnO. The latter mainly affects the BHJ and can be suppressed by adding a cost-efficient UV-absorbing ZnO layer on the distal surface of the device. With these two mechanisms suppressed, there is only a slow intrinsic degradation left, leading to an operational lifetime of 30 years.²³² In this chapter, we introduced 2 thermal degradation modes. Mode (1) is likely due to a thermally activated Cl redistribution process inside the BHJ driven by a redox reaction at the BHJ/MoO_x interface (one possible product is MoCl₂O₂), resulting in a check-mark shaped aging pattern featured by a rapid BQE decrease at the beginning followed by a slower recovery. This mode can be effectively arrested by inserting a 2-nm-thick C₇₀ buffer between the BHJ and MoO_x. Mode (2) is featured by a monotonically increasing interfacial voltage loss. This mode is partially related to the chlorination of MoO_x and can be reduced by the insertion of C₇₀ buffer.

Table 6.1 Effects of various photo and thermal degradation mechanism and methods to suppress them.

Mechanism	Type	Effects	Method to Suppress	Section
Photocatalytic reaction between BHJ and ZnO	Photo	Decrease of BQE and V_{off}	Inserting an IC-SAM or C ₆₀ -SAM between the BHJ and ZnO	5.2.2-5.2.4
UV exposure	Photo	Decrease of BQE	Adding a UV-absorbing ZnO coating on the distal surface of the device	5.2.5
Intrinsic photodegradation of the BHJ under white light	Photo	Decrease of BQE		5.2.6
Cl redistribution in the BHJ	Thermal	Check-mark shaped aging pattern of BQE	Inserting a 2-nm-thick C ₇₀ layer between the BHJ and MoO _x	6.1.1-6.1.5
Thermally induced interfacial voltage loss	Thermal	Decrease of V_{off}		6.1.3

Figure 6.12 shows a schematic of the photo- and thermal degradation mechanisms related to the anode and cathode edges and interlayers to suppress them.

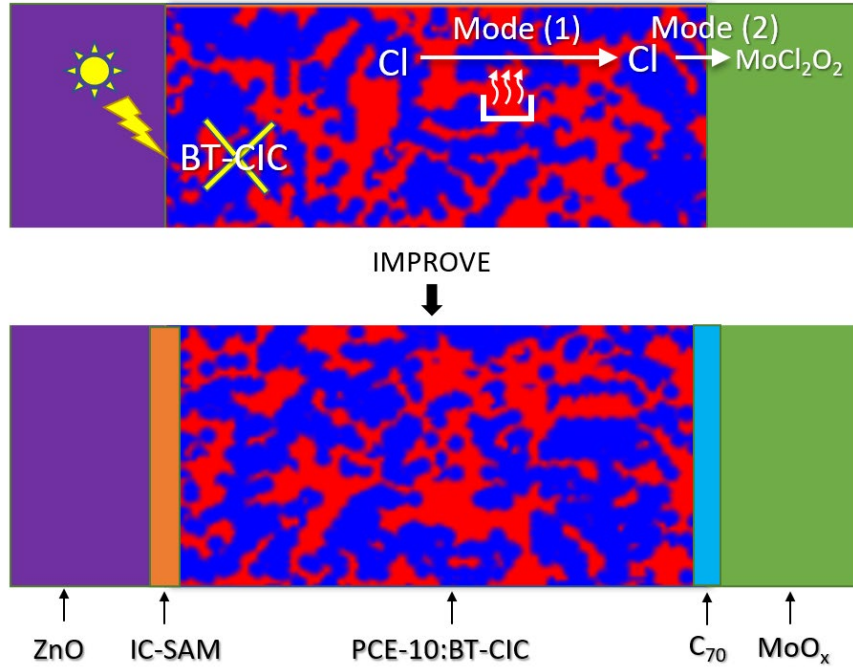


Figure 6.12 Schematic of the photo- and thermal degradation mechanisms related to the anode and cathode edges and interlayers to suppress them.

With the C₇₀ layer at the BHJ/MoO_x interface, mode (1) is almost fully stopped. In this case, thermal degradation is governed by a voltage loss at the edges while the BHJ remains almost unchanged. This is in contrast to the photodegradation of the same device under white light, where the degradation is primarily within the BHJ.

Figure 6.13(a) shows the time evolution of BQE- V_{bulk} characteristics of a PCE-10:BT-CIC OPV with both a C₇₀ anode interlayer and an IC-SAM cathode interlayer at 80°C. The time evolution of V_{off} is shown in the inset. Figure 6.13(b) shows the time evolution of BQE- V_{bulk} characteristics of the same device under the illumination of white light that is equivalent to 20

Suns with the V_{off} change shown in the inset. The photodegradation mainly affects the BHJ while the thermal degradation mainly affects the edges.

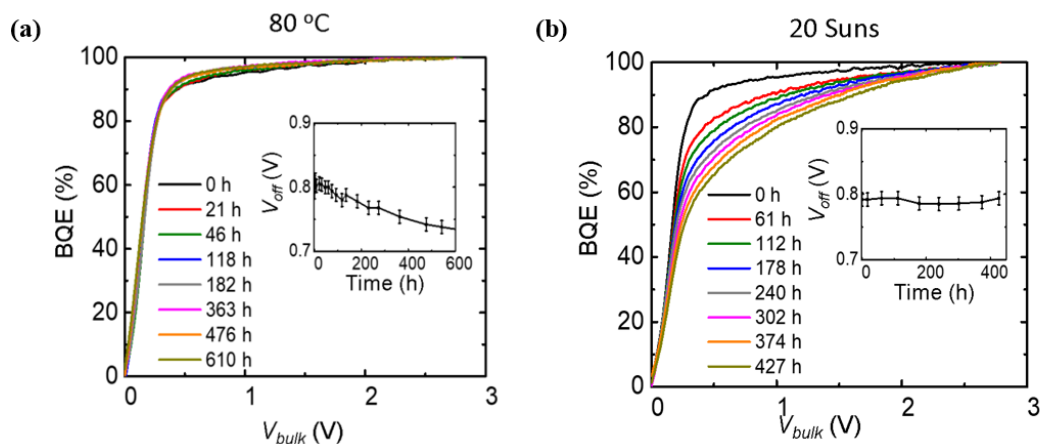


Figure 6.13 (a) Time evolution of BQE- V_{bulk} characteristics under 80 °C of inverted PCE-10:BT-CIC device with the C_{70} anode protection layer and the IC-SAM cathode protection layer. Inset: Time evolution of V_{off} . (b) Time evolution of BQE- V_{bulk} characteristics of the same device under illumination of white light that is equivalent to 20 Suns. Inset: Time evolution of V_{off} .

As discussed in Section 5.2.6, the photodegradation of the BHJ is likely related to second-order events such as exciton-exciton interactions. The mechanism behind the thermal degradation of the edges, however, is not clear. Even though the degradation mechanisms are not fully understood, knowing which layers are degrading provides guidelines for improving OPV stabilities.

6.4 Conclusions

In this chapter, we identify two different thermal degradation modes in inverted NFA-based OPVs with MoO_x as the anode buffer layer. Mode (1) results in a rapid 40% decrease of PCE followed by a slower recovery, forming a check-mark shaped degradation pattern. This mode

affects the BHJ and could be caused by a redox reaction between BHJ and MoO_x. A thin C₇₀ layer added between the MoO_x and BHJs can effectively stop this mode. Mode (2) appears as a monotonically increasing voltage loss in the edges but does not affect the BHJ. This mode can be partially suppressed by the C₇₀ protection layer. We also studied the thermal stabilities of conventional structured NFA-based OPVs. However, all devices studied show poor thermal stabilities. The BQE analysis show that the degradation mainly origins from the edges. These results suggest that the solution-processed NFA-based BHJs can be intrinsically thermally stable and the thermal degradation is usually induced by the edge layers.

Chapter 7

Outlook

7.1 Unanswered Questions

7.1.1 Channeling photocurrent outside the device area

So far all our studies have focused on the vertical direction (perpendicular to the substrate) assuming the device is uniform in the horizontal plane. However, this may not be the case near the device edge or when defects are presented. To map the photocurrent distribution in the horizontal plane, we constructed a photocurrent mapping system. As shown in Figure 7.1 (a), the OPV device is placed on a motorized translation stage. A chopped 532 nm laser beam is focused onto the OPV through an objective lens (Olympus, 50x). The size of the focus beam spot is about 1 μm . The stage can be finely controlled to move in the horizontal plane with a sub-micrometer resolution, while the photocurrent from the device is recorded by a lock-in amplifier (Stanford Research Systems SR830).²³³

We use the system to study the photocurrent distribution near the edge of a PCE-10:BT-CIC device. The device structure is: ITO 150nm/ZnO 30 nm/ PCE-10:BT-CIC, 1:1.5, 80 nm/MoO_x 10 nm/Ag 100 nm. As shown in Fig. 7.1(b), we observe photocurrent outside the device area where there is no Ag layer (anode). We name this photocurrent from outside the device area the

channeling photocurrent, J_{ch} , which results in an overestimation of OPV efficiency especially when the device area is small.²³⁴⁻²³⁶

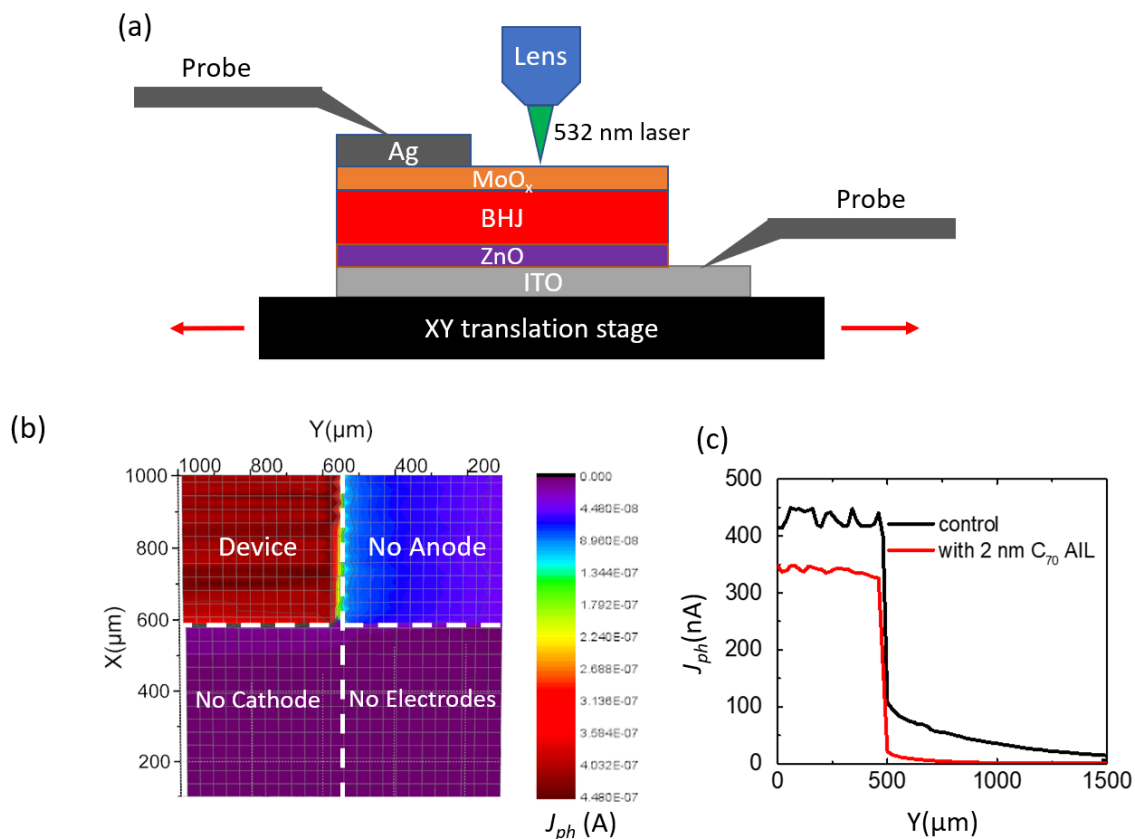


Figure 7.1 (a) Schematic of photocurrent mapping system. (b) Photocurrent distribution near the edge of a PCE-10:BT-CIC OPV device. (c) Photocurrent distribution along the Y axis for OPVs with and without a 2 nm C₇₀ anode interlayer.

With a 2 nm C₇₀ layer between the BHJ and MoO_x, J_{ch} disappears, as shown in Fig. 7.1 (c), suggesting that J_{ch} is related to the MoO_x layer. To study this, we fabricated devices with MoO_x that only partially extended from the device area in the Y direction, as shown by the microscope image in Fig. 7.2(a). Figure 7.2 (b) shows the photocurrent distribution of devices that has full coverage of MoO_x along the Y direction (black), has partial coverage of MoO_x along the Y direction (red) and has no MoO_x coverage beyond the device area (blue), respectively. This shows that the channeling current depends on the MoO_x layer, possibly by partially playing the role as

the top contact due to its high conductivity.²³⁴⁻²³⁷ However, further study is required to explain why the insertion of C_{70} layer eliminates the channeling photocurrent.

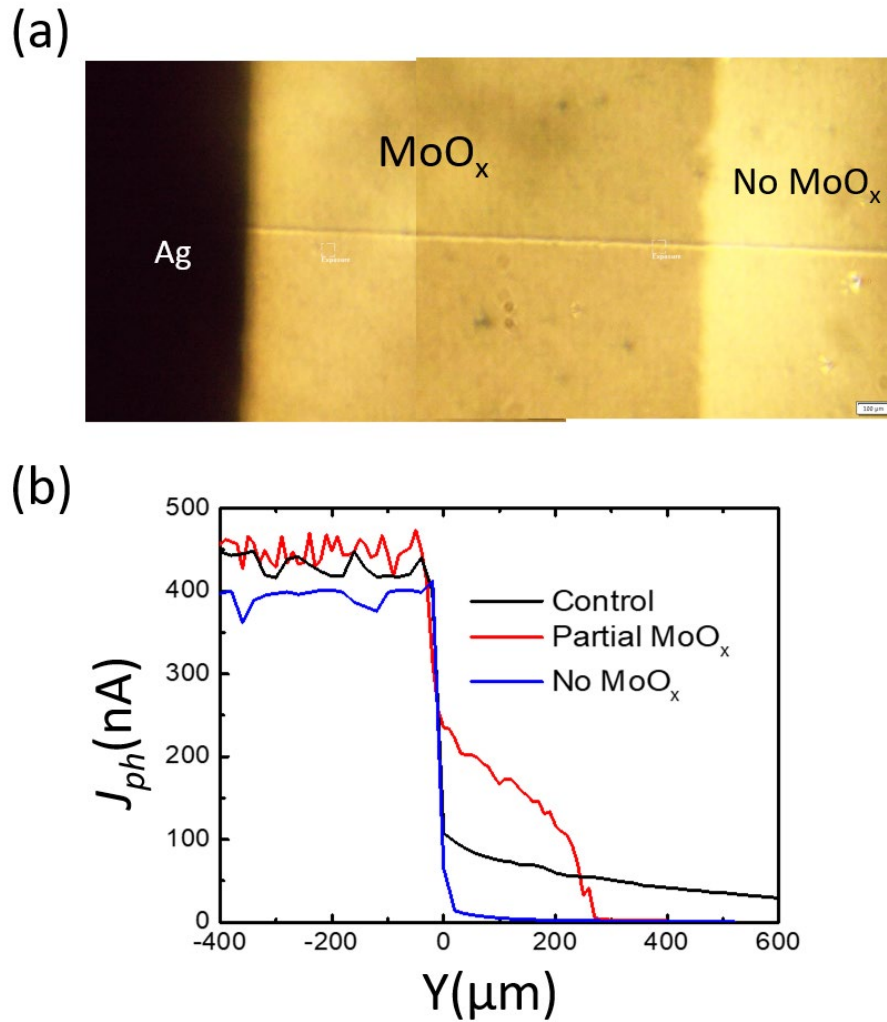


Figure 7.2 (a) Optical microscope image near the device edge where the MoO_x only extend out from the device area by 300 μm . (b) Photocurrent distribution of devices that: has full coverage of MoO_x along the Y direction (black), has partial coverage of MoO_x along the Y direction (red) and has no MoO_x coverage beyond the device area (blue), respectively.

We also studied the effect of thermal aging to the photocurrent distribution. As shown in Figure 7.3, after 44 h of aging at 80°C, the channeling photocurrent disappears while the device photocurrent decreases. This might be related to the redox reaction between the BHJ and the MoO_x

described in Chapter 6. However, future studies, e.g., the change of conductivity of MoO_x after the redox reaction with BT-CIC, are required to fully understand the mechanisms related to the channeling photocurrent.

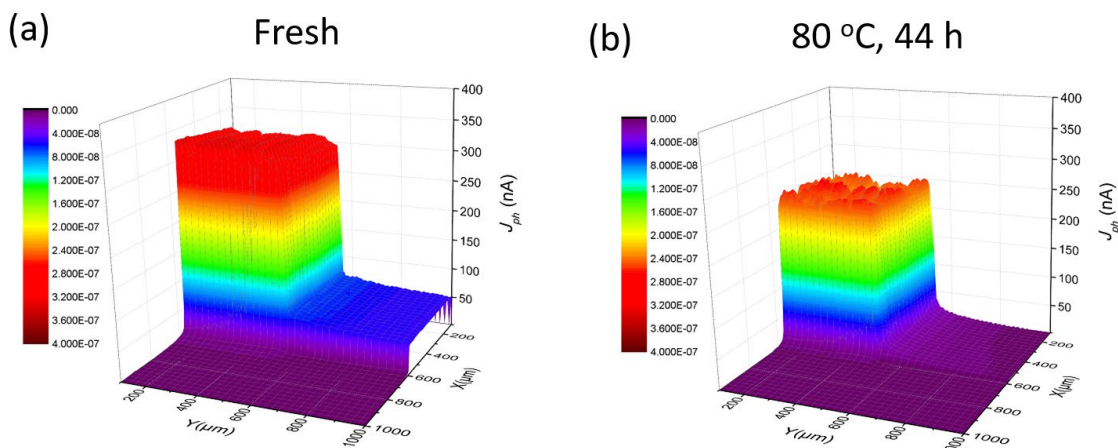


Figure 7.3 Photocurrent distribution near the device edge for (a) the as-cast device, (b) the device aged at 80°C for 44 h.

7.1.2 *J-V characteristics and BQE at low temperatures*

In practice, OPVs usually operate at temperatures equal to, or above room temperature. However, a study of device performance at low temperatures will help understand the physics of photogeneration process. Figure 7.4 (a) shows the *J-V* characteristics at various temperatures of a PCE-10:BT-CIC OPV device with the same structure as the control device in Section 7.1.1. As the temperature is lowered, the *J-V* characteristics show an S-shape, causing the FF and J_{sc} to significantly decrease. The S-shape suggests the existence of an energy barrier at low temperature as discussed in Section 4.3.5.^{165, 185, 194, 238} The energy barrier disappears at high temperatures possibly due to the thermal broadening of energy levels of organic molecules. Due to the S-shape, the BQE analysis cannot be applied to this device.²¹⁶

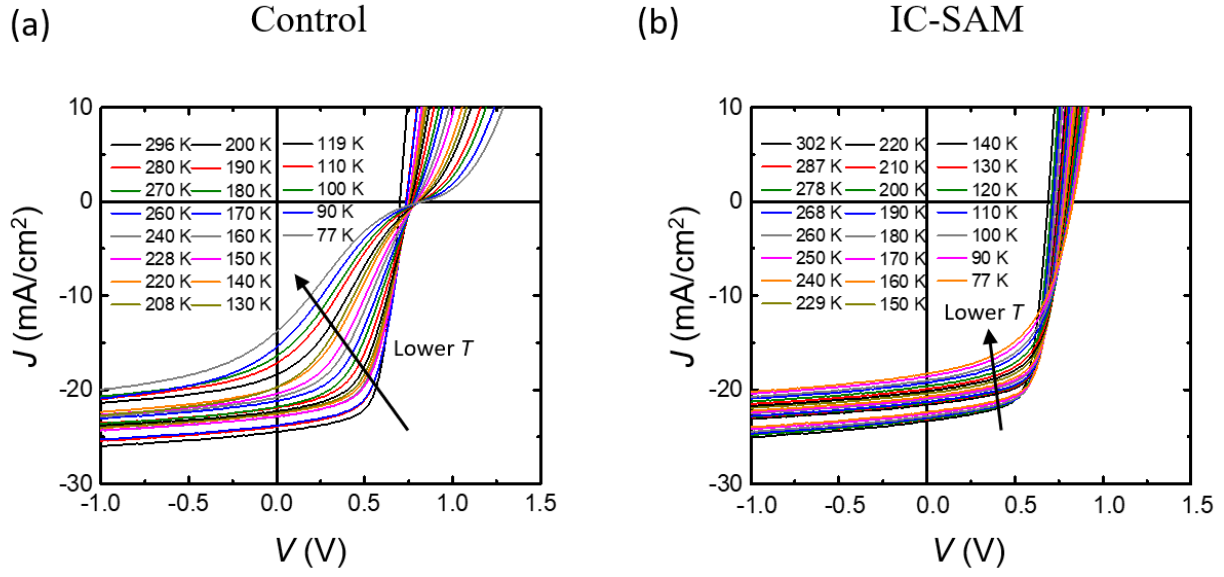


Figure 7.4 The J - V characteristics at various temperatures of (a) a control OPV device, (b) an OPV device with an IC-SAM between the BHJ and ZnO.

When there is an IC-SAM between the BHJ and the ZnO, there is no S-shape in the J - V characteristics. The change mainly appears as a decrease in the J_{sc} and an increase in the V_{oc} . We apply the BQE analysis as shown in Figure 7.5 (a) and (b). As the temperature decreases, the BQE decreases, meaning more electric field in the BHJ is required to extract the photogenerated charges. The J_{sat} decreases at low temperature, suggesting more recombination loss at the edges. The V_{off} increases at lower temperatures. This could be due to the narrowing of the HOMO and LUMO levels at low temperatures, effectively increase the HOMO-LUMO offset which is related to the V_{off} (Chapter 4).^{216, 239-240} However, further studies on related quantities, e.g., CT binding energies and charge mobilities at low temperatures, are required to fully understand the role of IC-SAM and the temperature dependence of BQE, J_{sat} and V_{off} .

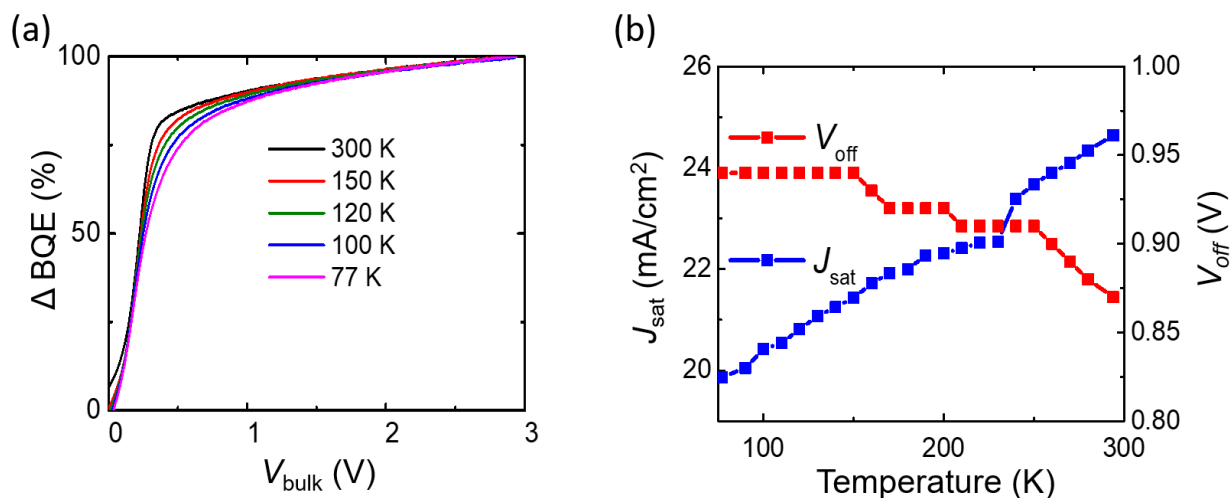


Figure 7.5 (a) BQE- V_{bulk} characteristics of the device with IC-SAM at various temperatures. (b) The V_{off} and J_{sat} of the device with IC-SAM at various temperatures.

7.2 Proposed Future Work

7.2.1 Physical meaning of BQE- V_{bulk} characteristics

Although the BQE analysis has been proven to effectively separate the properties of the BHJ from the device edges, a quantitative understanding of the physical meaning of the BQE- V_{bulk} characteristics is lacking. As shown in Section 7.1.2, temperature plays an important role in BQE- V_{bulk} characteristics. Intuitively, other quantities related to charge dissociation and collection, such as CT binding energies, charge mobilities, D/A ratios and BHJ thickness, should all play roles in the BQE- V_{bulk} characteristics.^{63, 132, 241-245} More research with these quantities should be performed in order to achieve an analytical or computational expression for the BQE- V_{bulk} characteristics. Then, the design and optimization the BHJ to achieve high performance can be simplified. Also, the BQE- V_{bulk} characteristics of BHJs with various materials systems, D/A ratios and thicknesses should be summarized and documented to help the design of OPVs.

7.2.2 Understanding OPV edges

All improvement methods described in Chapter 3, 5 and 6 are done by designing the edge structures of OPV devices, showing the importance of these layers on OPV performance. However, there are still mechanisms in the edges, e.g., Section 6.1.5 and Section 7.1.2, that are not fully understood. Specifically, more material science and chemistry studies should be done to understand the redox reaction between the BHJ and MoO_x interface. More energetic studies should be done on the effect of IC-SAM on the BHJ/ZnO interface to understand the low temperature behavior observed in Fig. 7.4.

In general, values of J_{sat} and V_{off} of OPV devices with different buffer layers/BHJ combinations should be summarized and documented. Rules for choosing compatible buffer layer materials should be developed to minimize the recombination and voltage losses at the edges.

7.2.3 Understanding the photodegradation mechanisms

In Chapter 5, we proposed a hypothesis about the intrinsic photodegradation mechanisms in NFA-based OPVs, where second-order events, such as exciton-exciton annihilation, may be a cause for the BQE decrease.^{217, 219} However, more controlled experiments should be done to test this hypothesis.

Firstly, the dependence of exciton density and polaron density on the rate of BQE decrease in Fig. 5.13 should be studied via controlling the D/A ratio in the BHJ and at various bias voltages. Secondly, studies on the change of energy levels in the BHJ during the photodegradation should be done to understand the decrease of BQE. Additionally, the dependence of the decreasing rate of BQE in Fig. 5.13 on molecular structures should be studied to help the design of molecules with better photostabilities.

7.3 Outlook for Organic Solar Cells

In this thesis, we have shown that with proper design, OPVs are capable of having both excellent photo- and thermal stabilities. With continuous improvements in molecule and device structure design, there is no doubt that OPV PCE will surpass 20% in the near future.³⁵ Meanwhile, techniques for large scale applications are being developed (Fig. 7.6).²⁴⁶ With all of this progress, OPVs have never been closer to industrial level applications.

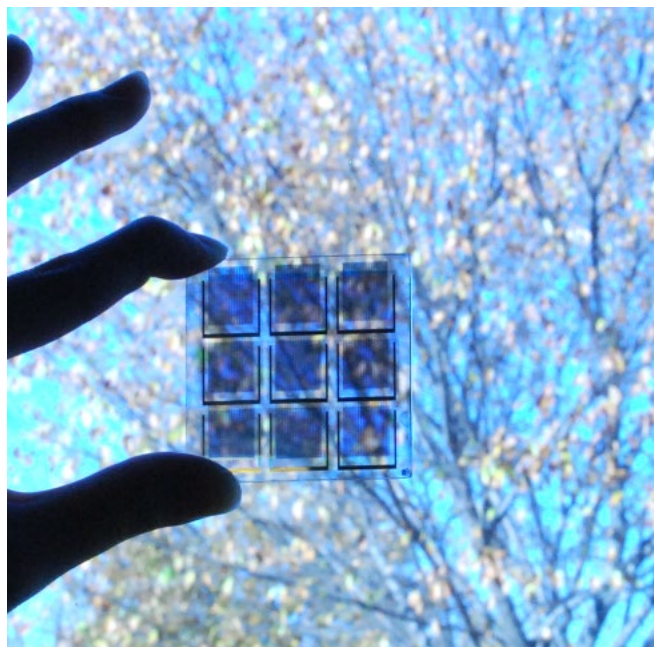


Figure 7.6 A semi-transparent OPV module developed by the OCM group at University of Michigan, Ann Arbor.²⁴⁶

Although it is still hard for OPVs to challenge the traditional solar cell industry with current efficiency and cost, the unique advantages of OPVs, such as color tunability, flexibility and semi-transparency, provide opportunities of unique applications.

One of the most promising applications is semi-transparent OPVs which can be integrated into windows.^{41, 43, 246-250} Due to the high color tunability of organic semiconductors, molecules such as BT-CIC are designed to absorb only the near-infrared portion of the solar spectrum while

still providing over 10% PCE. Combined with the existing glass industry, this could be a non-negligible source of clean energy for buildings.

Another potential application is flexible OPVs.²⁵¹⁻²⁵³ Flexibility is a major advantage granted by organic semiconductors. With appropriate substrates and electrodes, OPVs can easily be made flexible. Although currently the need for flexible OPVs is small, as the industry develops, flexible OPVs could become an important source of energy for the wearable devices.²⁵⁴ Figure 7.7 shows an example where OPVs are used to power wearable sensors.²⁵⁵

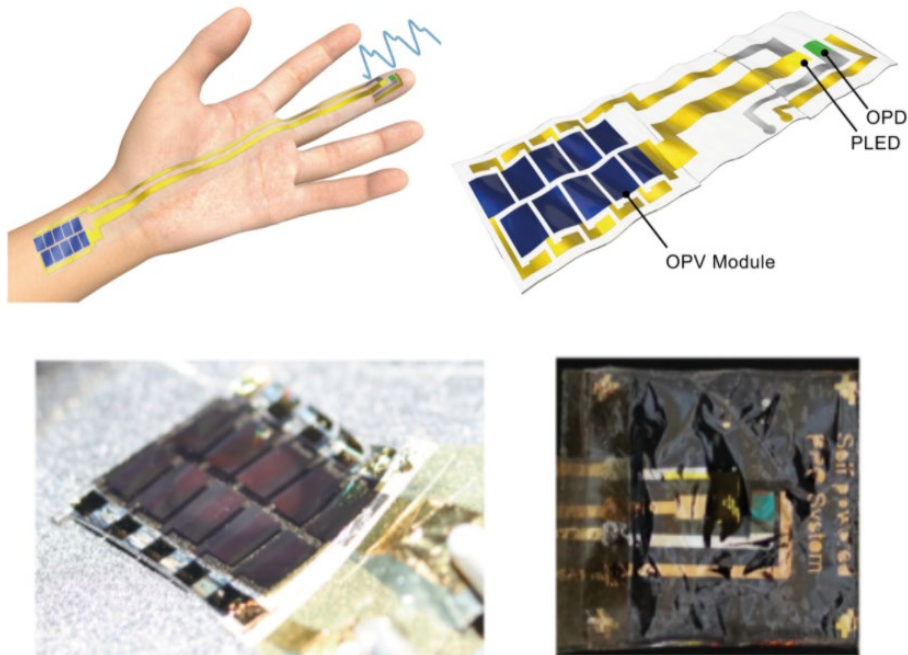


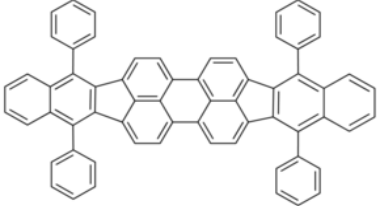
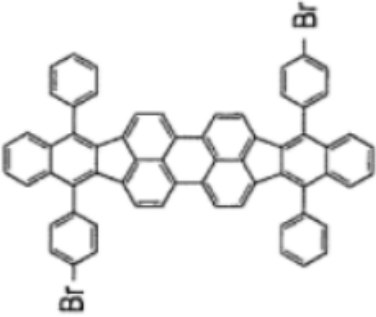
Figure 7.7 Schematics of the ultraflexible, self-powered photoplethysmogram (PPG) sensor on a human hand.²⁵⁵


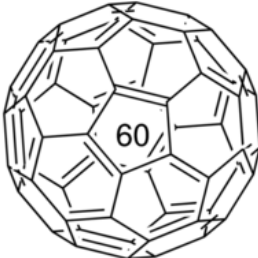
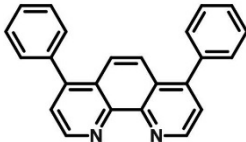
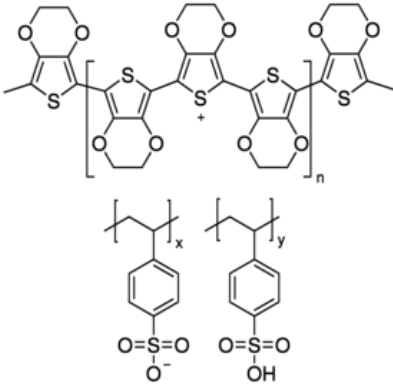
Appendices

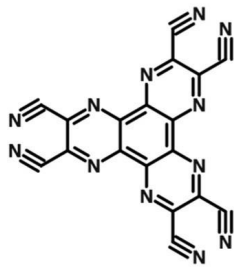
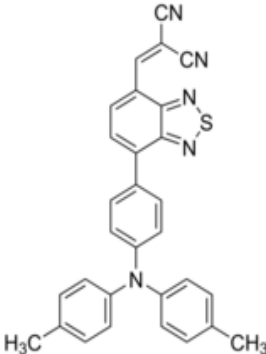
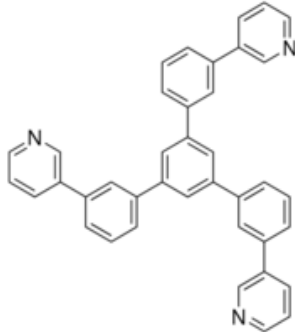
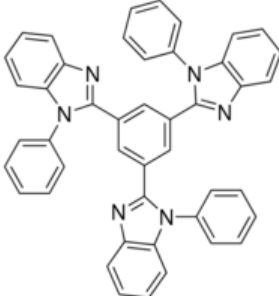
Appendix A

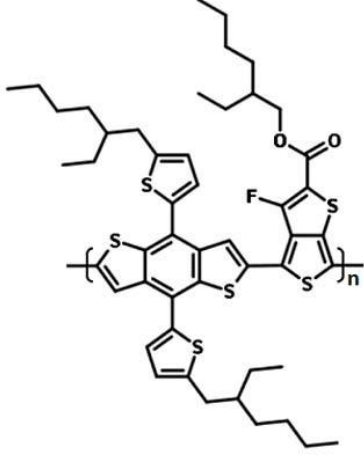
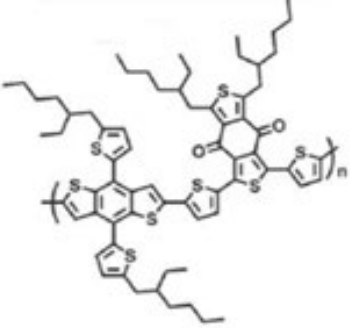
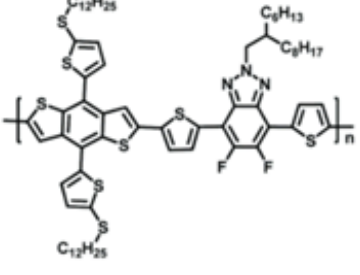
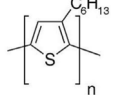
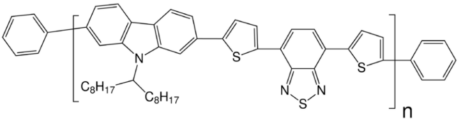
Chemical Structures and Full Chemical Names of Molecules

Table A.0.1 Chemical structures and short names of molecules

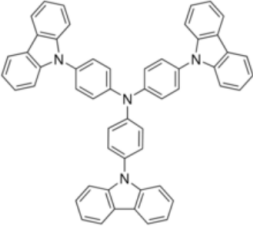
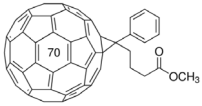
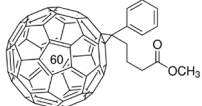

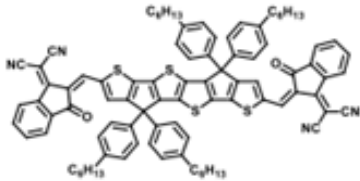
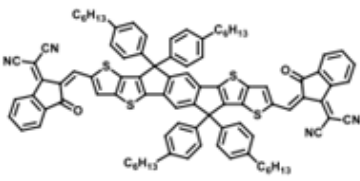
Short Name	Full Chemical Name	Chemical Structure
DBP	5,10,15,20-Tetraphenylbisbenz[5,6]indeno[1,2,3-cd:1',2',3'-lm]perylene	
DBP-Br		

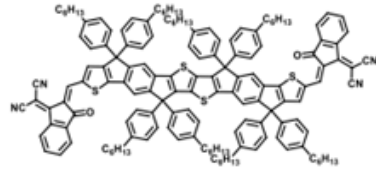
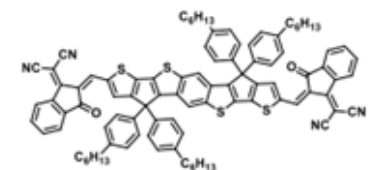
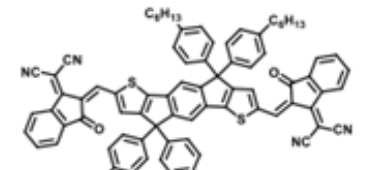
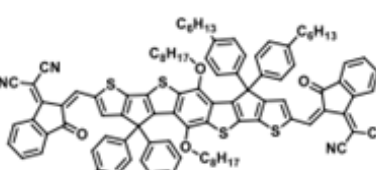
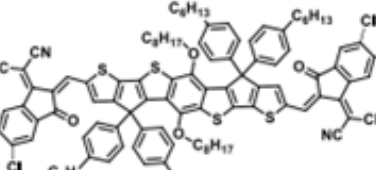
C ₇₀	[5,6]-Fullerene-C70	
C ₆₀	Fullerene-C ₆₀	
BPhen	Bathophenanthroline	
PEDOT:PSS	Poly(3,4-ethylenedioxythiophene)- poly(styrenesulfonate)	

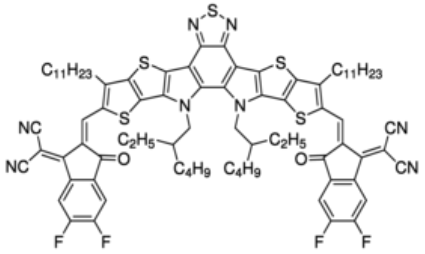
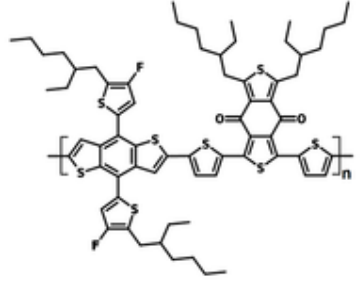
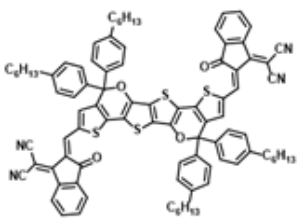
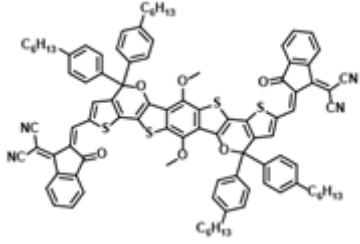
HAT-CN	1,4,5,8,9,11-Hexaazatriphenylenehexacarbonitrile	
DTDCPB	2-[(7-[4-[<i>N,N</i> -Bis(4-methylphenyl)amino]phenyl]-2,1,3-benzothiadiazol-4-yl)methylene]propanedinitrile	
TmPyPB	1,3,5-Tri(<i>m</i> -pyridin-3-ylphenyl)benzene, 1,3,5-Tris(3-pyridyl-3-phenyl)benzene	
TPBi	2,2',2''-(1,3,5-Benzinetriyl)-tris(1-phenyl-1- <i>H</i> -benzimidazole)	

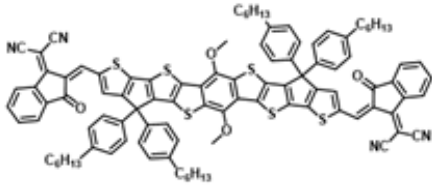
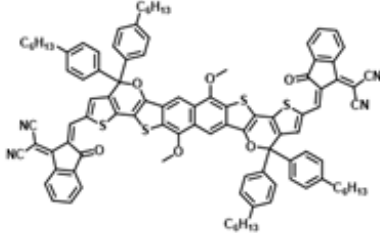
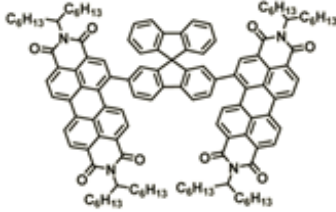
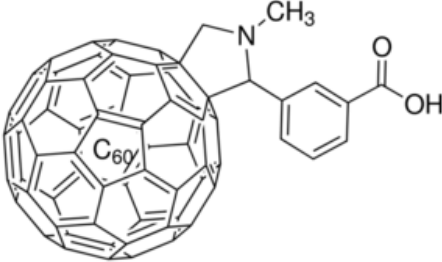
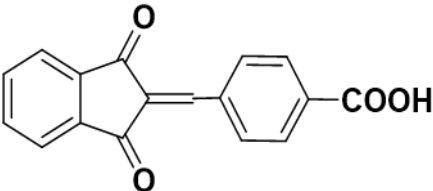
PCE-10	Poly[4,8-bis(5-(2-ethylhexyl)thiophen-2-yl)benzo[1,2-b;4,5-b']dithiophene-2,6-diyl-alt-(4-(2-ethylhexyl)-3-fluorothieno[3,4-b]thiophene)-2-carboxylate-2,6-diyl]]	 <p>The structure shows a polymer chain with two alternating units. The first unit is a benzobisthiophene core with two 2-ethylhexyl groups at the 4 and 8 positions. The second unit is a thienothiophene core with a fluorine atom at the 3-position and a 2-ethylhexyl group at the 4-position, and a carboxylate group at the 2-position.</p>
PBDBT	Poly[(2,6-(4,8-bis(5-(2-ethylhexyl)thiophen-2-yl)benzo[1,2-b:4,5-b']dithiophene))-alt-(5,5-(1',3'-di-2-thienyl-5',7'-bis(2-ethylhexyl)benzo[1',2'-c:4',5'-c']dithiophene-4,8-dione))]	 <p>The structure shows a polymer chain with two alternating units. The first unit is a benzobisthiophene core with two 2-ethylhexyl groups at the 4 and 8 positions. The second unit is a dione-benzobisthiophene core with two 2-ethylhexyl groups at the 1' and 3' positions.</p>
J61	Poly[4,8-bis(5-(2-ethylhexyl)thiophen-2-yl)benzo[1,2-b:4,5-b']dithiophene-co-2',1',3'-benzotriazole]	 <p>The structure shows a polymer chain with two alternating units. The first unit is a benzobisthiophene core with two 2-ethylhexyl groups at the 4 and 8 positions. The second unit is a benzotriazole core with two 2-ethylhexyl groups at the 2' and 3' positions.</p>
P3HT	Poly(3-hexylthiophene-2,5-diyl)	 <p>The structure shows a polymer chain with a single unit of 3-hexylthiophene-2,5-diyl.</p>
PCDTBT	Poly[[N-9'-heptadecanyl-2,7-carbazole-alt-5,5-(4',7'-di-2-thienyl-2',1',3'-benzothiadiazole)], Poly[[9-	 <p>The structure shows a polymer chain with two alternating units. The first unit is a carbazole core with a heptadecanyl group at the 9' position. The second unit is a benzothiadiazole core with two 2-thienyl groups at the 4' and 7' positions.</p>

	(1-octylnonyl)-9H-carbazole-2,7-diyl]-2,5-thiophenediyl-2,1,3-benzothiadiazole-4,7-diyl-2,5-thiophenediyl]	
F8BT	Poly(9,9-dioctylfluorene-alt-benzothiadiazole), Poly[(9,9-dioctylfluorenyl-2,7-diyl)-alt-(benzo[2,1,3]thiadiazol-4,8-diyl)]	
F8T2	Poly(9,9-dioctylfluorene-alt-bithiophene), Poly[(9,9-dioctylfluorenyl-2,7-diyl)-co-bithiophene], Poly[[2,2'-bithiophene]-5,5'-diyl(9,9-dioctyl-9H-fluorene-2,7-diyl)]	
CBP	4,4'-Bis(N-carbazolyl)-1,1'-biphenyl	
TPTPA	Tris(4-(5-phenylthiophen-2-yl)phenyl)amine	
NPD	N,N'-Di(1-naphthyl)-N,N'-diphenyl-(1,1'-biphenyl)-4,4'-diamine	

TCTA	Tris(4-carbazoyl-9-phenyl)amine	
PC ₇₁ BM	6,6-Phenyl C ₇₁ butyric acid methyl ester	
PC ₆₁ BM	6,6-Phenyl C ₆₁ butyric acid methyl ester	
PTCBI	Bisbenzimidazo[2,1-a:2',1'-a']anthra[2,1,9-def:6,5,10-d'e'f']diisoquinoline-10,21-dione	
DT-IC	(5,5,10,10-tetrakis(4-hexylphenyl)-thiophene-thieno[3,2-b]thiophene-thiophene)bis(2-(3-oxo-2,3-dihydroinden-1-ylidene)malononitrile)	
ITIC	3,9-bis(2-methylene-(3-(1,1-dicyanomethylene)-indanone))-5,5,11,11-tetrakis(4-hexylphenyl)-dithieno[2,3-d:2',3'-d']-s-indaceno[1,2-b:5,6-b']dithiophene	

IDTIDT-IC		
BDT-IC	(5,5,12,12-tetrakis(4-hexylphenyl)-dithienyl[1,2-b:4,5-b']benzodithiophene-2,7-diyl)bis(2-(3-oxo-2,3-dihydroinden-1-ylidene)malononitrile)	
IDT-IC	(4,4,9,9-tetrakis(4-hexylphenyl)-4,9-dihydro-s-indaceno[1,2-b:5,6-b']dithiophene-2,7-diyl)bis(2-(3-oxo-2,3-dihydroinden-1-ylidene)malononitrile)	
BT-IC	(8,15-dibutyloxy-tetrakis(4-hexylphenyl)-(5,5,12,12-tetrakis(4-hexylphenyl)-dithienyl[1,2-b:4,5-b']benzodithiophene-2,7-diyl)bis(2-(3-oxo-2,3-dihydroinden-1-ylidene)malononitrile)	
BT-CIC	4,4,10,10-tetrakis(4-hexylphenyl)-5,11-(2-ethylhexyloxy)-4,10-dihydrodithienyl[1,2-b:4,5b']benzodithiophene-2,8-	

	diyl)bis(2-(3-oxo-2,3-dihydroinden-5,6-dichloro-1-ylidene)malononitrile)	
Y6	(2,2'-((2Z,2'Z)-((12,13-bis(2-ethylhexyl)-3,9-diundecyl-12,13-dihydro-[1,2,5]thiadiazolo[3,4-e]thieno[2,"3":4',5']thieno[2',3':4,5]	
PBDB-T-2F (PM6)	Poly[(2,6-(4,8-bis(5-(2-ethylhexyl)-3-fluoro)thiophen-2-yl)-benzo[1,2-b:4,5-b']dithiophene))-alt-(5,5-(1',3'-di-2-thienyl-5',7'-bis(2-ethylhexyl)benzo[1',2'-c:4',5'-c']dithiophene-4,8-dione)]	
TPT-IC		
BDP-IC		

BDCP-IC		
BNP-IC		
SF-PDI2		
C ₆₀ -SAM	4-(1',5'-Dihydro-1'-methyl-2'H-[5,6]fullereno-C ₆₀ -I _h -[1,9-c]pyrrol-2'-yl)benzoic acid	
IC-SAM	4-((1,3-dioxo-1,3-dihydro-2H-inden-2-ylidene)methyl)benzoic acid	

Appendix B

Ultralong-Range Energy Transport in Disordered Organic Semiconductors at Room Temperature via Coherent Exciton-Polariton Propagation

Long range excited state energy transport is a fundamental process in natural photosynthesis. As such, it can be exploited in numerous optoelectronic applications, such as organic photovoltaics and light-emitting devices.²⁵⁶⁻²⁵⁷ As discussed in Section 1.2, in a molecular system, the excitation energy is localized in Frenkel excitons with large binding energies, and their transport occurs by near-field Förster or Dexter intermolecular hopping that is severely limited by a combination of the intrinsic dynamic disorder as well as considerable static disorder in amorphous films. Compared with excitons, long range photon propagation has only limited interactions with the solid. Thus, a promising means to improve energy transport is to strongly couple excitons with photons in an optical cavity, forming new quantum mechanical quasi-particles called exciton-polaritons.²⁵⁸⁻²⁶² Polaritons partially inherit the light effective mass and delocalization properties rendered by their photonic component, and thus are potentially immune from interactions with local defects and disorder common to molecular solids.²⁶³⁻²⁶⁵ Coherent coupling with an extended and propagating photon mode can lead to rapid and long-range transport that differs from the slow and short-range diffusion of more massive excitons.²⁶⁶⁻²⁶⁷

In this work, we investigate room temperature polariton propagation in an all-dielectric photonic structure comprising a disordered molecular thin-film of DBP deposited onto the surface of a distributed Bragg reflector (DBR). Similar to the surface confined and propagating modes of one-dimensional or two-dimensional photonic crystals,²⁶⁸⁻²⁶⁹ the truncated periodic multilayers of DBR support a Bloch surface mode, of which its strong electric-field enhancement and low optical loss is ideal for strong coupling with excitons and long-range transport applications.²⁷⁰⁻²⁷¹ Angular reflectivity measurements show two anti-crossing polariton branches with a giant vacuum Rabi splitting energy of 480 meV due to ultra-strong coupling between 0-0 vibronic of the molecular excitons and Bloch surface modes. Using spatial and momentum-resolved photoluminescence imaging measurements, we observe polariton transport over distances of at least 100 μm , and a halo-like intensity pattern due to polariton self-interference. Our model of polariton transport indicates that the hole size is determined by the coherence length correlated to phase-breaking by inelastic scattering, while the total propagation distance depends on the attenuation coefficient that includes material absorption and other scattering processes.

The sample consists of a DBR comprising 4 pairs of ZnS/MgF₂ followed by a 20 nm-thick DBP film on a 180 micrometer-thick fused silica substrate via vacuum thermal evaporation, and finally encapsulated before measurement. The DBR supports a single transverse-electric (TE) Bloch surface wave (BSW) above the total internal reflection (TIR) angle ($\theta_{TIR} = 42^\circ$). The angular reflectivity and photoluminescence spectra were measured using a k-space microscope comprising an inverted microscope with a 1.40 NA, 100X objective (Olympus), a white lamp source (for reflectivity), TM-polarized $\lambda = 532$ nm ultrafast pulsed laser source (Toptica Fibre-Pro, for PL), a k-space lens, a TE polarizer, a $\lambda = 600$ nm long pass filter (for PL), and a spectrometer (Acton SpectraPro SP-2500) with a 1024 x 1024 CCD camera (PIX 1024B, Princeton Instruments). The

photoluminescence images were collected by the k-space microscope in a transmission geometry. A 1 μm diameter TM-polarized pulsed Gaussian laser beam was focused on the surface of the DBP layer with a 0.5NA, 50X objective from the DBP side, and the emission was collected with another 1.40 NA, 100X objective from the substrate side. Before projecting it to the spectrometer or camera, delay lenses were used to reconstruct k-space and real-space, where a slit filter in k-space or a pinhole filter in real-space was placed as designed.

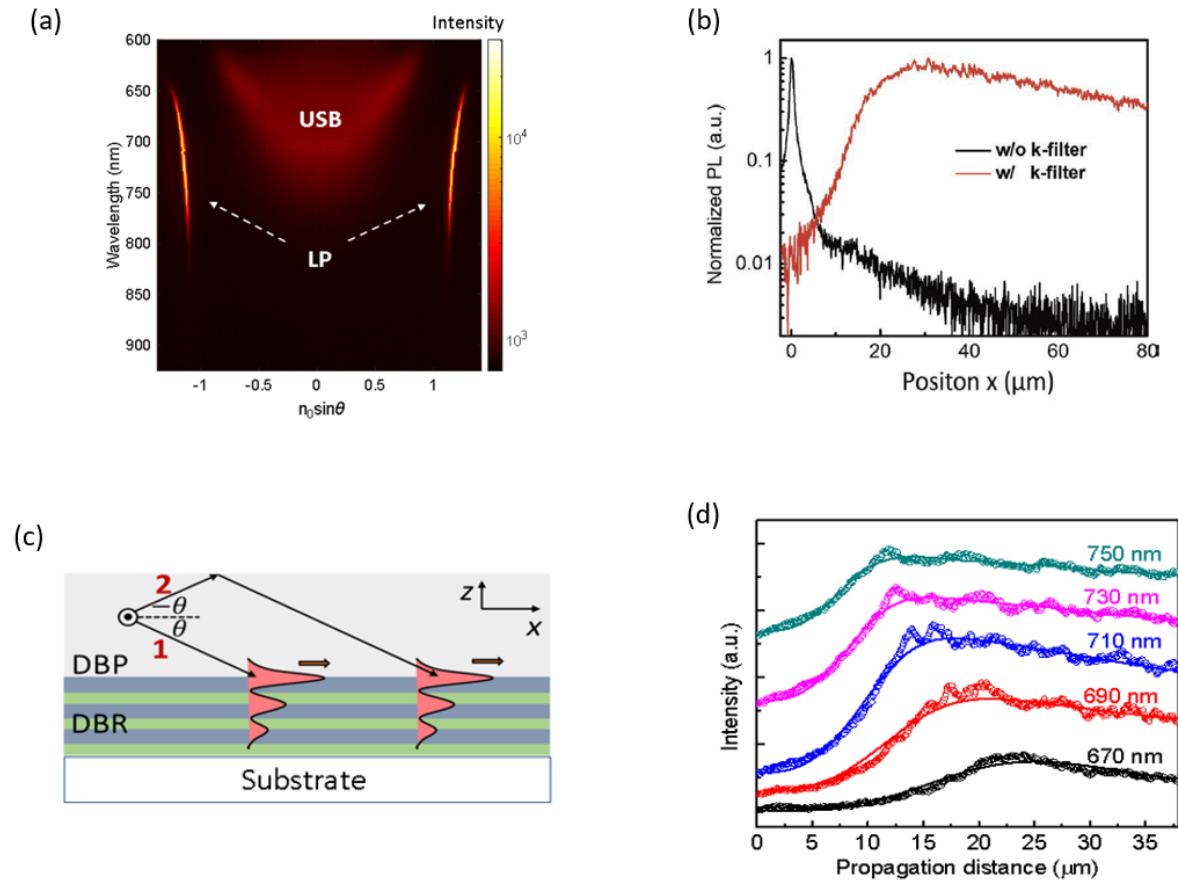


Figure B1. (a) Transverse electric (TE) angular PL spectra of the lower polariton brach (LP) of ultra-strong coupled polariton mode using a laser excitation wavelength at 532 nm and a long-pass filter cutting off at 600 nm. (b) PL emission intensity distribution along the propagation direction with (black) and without (red) a k-space filter. (c) The self-interference model proposed to explain the hollow pattern of polariton propagation. The emission from an exciton experience two light paths before exciting the polariton mode at the organic/DBR interface. One light path includes a total internal reflection on the DBP top surface, resulting in a phase delay. Therefore, the wavefronts experience destructive interference in the excitation area, resulting in a low intensity. As the polariton mode propagates, decoherence accumulates and intensity increases. (d) Propagation profiles at various wavelength. The calculated profiles (solid lines) are fitted to the measured data (circular dots) using the self-interference model in (c).^{26, 272}

Figure B1(a) shows the room temperature TE angular photoluminescence emission spectrum of an encapsulated sample. At $\theta > \theta_{TIR}$, only the lowest polariton branch LP is observed, and the maximum intensity is close to the emission peak of the 0-2 vibronic, indicating phonon-assisted polariton relaxation.²⁶⁷ After non-resonant excitation, photogenerated hot excitons rapidly relax to the exciton reservoir where they radiatively decay via weakly-coupled localized modes, such as leakage from the USB at $\theta < \theta_{TIR}$. At the same time, excitons in the reservoirs populate the LP polariton states via phonon-assisted recombination and/or radiative pumping.²⁶⁷ As polaritons have large group velocities, they rapidly propagate in-plane, away from the pumping region. Thus, the lifetimes and group velocities of polaritons in the LP branch determine the spatial extent of the quasiparticle distribution.

To track the polariton propagation, we image the spatial distribution of photoluminescence via non-resonantly exciting the sample with a tightly focused laser beam using the setup in the transmission configuration, and the pumping light cannot be coupled into any surface modes of sample due to energy and momentum mismatch. The photoluminescence image is now dominated by an intense and bright exciton emission at the excitation spot due to the Gaussian spatial profile of the 1 μm diameter laser beam. Outside of this bright spot, relatively weaker emission radially spreads beyond the field of view. To rule out this weakly-coupled exciton emission leakage from the USB, we place a slit filter in the reconstructed in-plane momentum k -space behind the imaging collection lens in the detection channel, and select only the high- k polariton emission at $\theta > \theta_{TIR}$. The polariton emission propagating in the direction selected by the slit is shown in Fig. B1(b). Surprisingly, the polariton emission intensity is weak near the excitation spot, has a peak at a distance of approximately 20 μm , and then exponentially decays along the propagating path beyond the field of view that extends to 80 μm . For comparison, the emission profile taken in the

absence of a k -space filter is also shown in Fig. B1(b), where a long and weak emission tail overlaps with the narrow and intense peak at the pumping position.

We attribute the polariton propagation pattern to self-interference between two light paths illustrated in Figure B1(c). The polariton mode is either directly excited by the radiation field of an exciton (path 1), or after experiencing TIR (path 2) from the DBP film surface. The phase difference between the two paths results in destructive interference at the pumping site. As the polariton mode propagates beyond the coherence length approximately corresponding to the radius of the halo, the emission intensity rapidly increases to a maximum, followed by an exponential decay due to scattering and non-negligible material absorption.

For simplicity, we take a pair of planewave components of the spherical dipole radiation field with the same in-plane momentum and calculate the polariton propagation pattern (see Methods). In Figure B1(d), we find that the calculation (solid lines) quantitatively fits the halo-like profile observed in wavelength-resolved propagation measurement (data points). The size of the halo, L_{hole} , is determined by the coherence length, l_{coh} (see Methods), of polariton propagation, which is limited by decoherence mechanisms including scatterings from grain boundaries, surface roughness, and interaction among polaritons and phonons.^{259, 273-274} The hole diameter decreases with increasing wavelength as the polariton mode approaches the air cone at θ_{TIR} .

In conclusion, we have demonstrated exceptionally long range, room temperature transport of strongly coupled exciton-polaritons in a one-sided distributed Bragg reflector, which is orders of magnitude larger than expected for excitons in disordered organic semiconductors. The observed polariton intensity shows a halo-like pattern which is explained by the self-interference of polariton modes. Our work shows that to realize long range and efficient polariton transport in disordered systems, it is essential to eliminate the strongly localized polariton components,

increase the coherence and phase-breaking lengths, as well as reduce other losses, such as absorption and scattering. Compared with short-range Förster and Dexter-mediated exciton diffusion, polaritons provide an alternative path to transport of excitation energy to a remote location. Furthermore, the simplicity of open dielectric optical structures enables a range of device architectures. For example, the robust nature of polaritons can reduce requirements for use of highly ordered solids, leading to, for example, efficient long-range energy harvesting in organic photovoltaics that mimic photosynthetic processes under ambient conditions, while also advancing our understanding of polariton physics.

Bibliography

1. Akamatu, H.; Inokuchi, H., On the Electrical Conductivity of Violanthrone, Iso-Violanthrone, and Pyranthrone. *The Journal of Chemical Physics* **1950**, *18* (6), 810-811.
2. Akamatu, H.; Inokuchi, H.; Matsunaga, Y., Electrical Conductivity of the Perylene–Bromine Complex. *Nature* **1954**, *173* (4395), 168-169.
3. Förster, T., Zwischenmolekulare Energiewanderung Und Fluoreszenz. *Annalen der Physik* **1948**, *437* (1-2), 55-75.
4. Dexter, D. L., A Theory of Sensitized Luminescence in Solids. *The Journal of Chemical Physics* **1953**, *21* (5), 836-850.
5. Marcus, R. A., On the Theory of Electron-Transfer Reactions. Vi. Unified Treatment for Homogeneous and Electrode Reactions. *The Journal of Chemical Physics* **1965**, *43* (2), 679-701.
6. Tang, C. W., Two-Layer Organic Photovoltaic Cell. *Appl. Phys. Lett.* **1986**, *48* (2), 183-185.
7. Tang, C. W.; VanSlyke, S. A., Organic Electroluminescent Diodes. *Appl. Phys. Lett.* **1987**, *51* (12), 913-915.
8. Geffroy, B.; le Roy, P.; Prat, C., Organic Light-Emitting Diode (Oled) Technology: Materials, Devices and Display Technologies. *Polymer International* **2006**, *55* (6), 572-582.

9. Baldo, M. A.; O'Brien, D. F.; You, Y.; Shoustikov, A.; Sibley, S.; Thompson, M. E.; Forrest, S. R., Highly Efficient Phosphorescent Emission from Organic Electroluminescent Devices. *Nature* **1998**, *395* (6698), 151-154.
10. Adachi, C.; Baldo, M. A.; Thompson, M. E.; Forrest, S. R., Nearly 100% Internal Phosphorescence Efficiency in an Organic Light-Emitting Device. *J. Appl. Phys.* **2001**, *90* (10), 5048-5051.
11. Baldo, M. A.; Lamansky, S.; Burrows, P. E.; Thompson, M. E.; Forrest, S. R., Very High-Efficiency Green Organic Light-Emitting Devices Based on Electrophosphorescence. *Appl. Phys. Lett.* **1999**, *75* (1), 4-6.
12. Lamansky, S.; Djurovich, P.; Murphy, D.; Abdel-Razzaq, F.; Lee, H.-E.; Adachi, C.; Burrows, P. E.; Forrest, S. R.; Thompson, M. E., Highly Phosphorescent Bis-Cyclometalated Iridium Complexes: Synthesis, Photophysical Characterization, and Use in Organic Light Emitting Diodes. *J. Am. Chem. Soc* **2001**, *123* (18), 4304-4312.
13. Kamtekar, K. T.; Monkman, A. P.; Bryce, M. R., Recent Advances in White Organic Light-Emitting Materials and Devices (Woleds). *Adv. Mater.* **2010**, *22* (5), 572-582.
14. D'Andrade, B. W.; Forrest, S. R., White Organic Light-Emitting Devices for Solid-State Lighting. *Adv. Mater.* **2004**, *16* (18), 1585-1595.
15. Bernanose, A.; Comte, M.; Vouaux, P., Sur Un Nouveau Mode D'émission Lumineuse Chez Certains Composés Organiques. *J. Chim. Phys.* **1953**, *50*, 64-68.
16. Sekitani, T.; Nakajima, H.; Maeda, H.; Fukushima, T.; Aida, T.; Hata, K.; Someya, T., Stretchable Active-Matrix Organic Light-Emitting Diode Display Using Printable Elastic Conductors. *Nat. Mater.* **2009**, *8* (6), 494-499.

17. Gu, G.; Bulović, V.; Burrows, P. E.; Forrest, S. R.; Thompson, M. E., Transparent Organic Light Emitting Devices. *Appl. Phys. Lett.* **1996**, *68* (19), 2606-2608.
18. Lewis, J., Material Challenge for Flexible Organic Devices. *Materials Today* **2006**, *9* (4), 38-45.
19. Sugimoto, A.; Ochi, H.; Fujimura, S.; Yoshida, A.; Miyadera, T.; Tsuchida, M., Flexible Oled Displays Using Plastic Substrates. *IEEE Journal of Selected Topics in Quantum Electronics* **2004**, *10* (1), 107-114.
20. Park, J.-S.; Chae, H.; Chung, H. K.; Lee, S. I., Thin Film Encapsulation for Flexible Am-Oled: A Review. *Semiconductor Science and Technology* **2011**, *26* (3), 034001.
21. Görrn, P.; Sander, M.; Meyer, J.; Kröger, M.; Becker, E.; Johannes, H.-H.; Kowalsky, W.; Riedl, T., Towards See-through Displays: Fully Transparent Thin-Film Transistors Driving Transparent Organic Light-Emitting Diodes. *Adv. Mater.* **2006**, *18* (6), 738-741.
22. Wager, J. F., Transparent Electronics. *Science* **2003**, *300* (5623), 1245-1246.
23. Bardsley, J. N., International Oled Technology Roadmap. *IEEE Journal of Selected Topics in Quantum Electronics* **2004**, *10* (1), 3-9.
24. Kim, J.; Batagoda, T.; Lee, J.; Sylvinson, D.; Ding, K.; Saris, P. J. G.; Kaipa, U.; Oswald, I. W. H.; Omary, M. A.; Thompson, M. E.; Forrest, S. R., Systematic Control of the Orientation of Organic Phosphorescent Pt Complexes in Thin Films for Increased Optical Outcoupling. *Adv. Mater.* **2019**, *31* (32), 1900921.
25. Deng, H.; Haug, H.; Yamamoto, Y., Exciton-Polariton Bose-Einstein Condensation. *Reviews of Modern Physics* **2010**, *82* (2), 1489-1537.

26. Hou, S.; Khatoniar, M.; Ding, K.; Qu, Y.; Napolov, A.; Menon, V. M.; Forrest, S. R., Ultralong-Range Energy Transport in a Disordered Organic Semiconductor at Room Temperature Via Coherent Exciton-Polariton Propagation. *Adv. Mater.* **2020**, *32* (28), 2002127.
27. Zhang, L.; Wu, F.; Hou, S.; Zhang, Z.; Chou, Y.-H.; Watanabe, K.; Taniguchi, T.; Forrest, S. R.; Deng, H., Van Der Waals Heterostructure Polaritons with Moiré-Induced Nonlinearity. *Nature* **2021**, *591* (7848), 61-65.
28. Song, Y.; Liu, X.; Li, Y.; Nguyen, H. H.; Duan, R.; Kubarych, K. J.; Forrest, S. R.; Ogilvie, J. P. In *Charge Generation Mediated by Bound Polaron Pairs and Delocalized Charge Transfer States in Non-Fullerene Organic Solar Cells*, The 22nd International Conference on Ultrafast Phenomena 2020, Washington, D.C., 2020/11/16; Kärtner, F. K. M. L. R. L. F.; Tahara, T., Eds. Optical Society of America: Washington, D.C., 2020; p Th2A.7.
29. Kippelen, B.; Brédas, J.-L., Organic Photovoltaics. *Energy Environ. Sci.* **2009**, *2* (3), 251-261.
30. Peumans, P.; Yakimov, A.; Forrest, S. R., Small Molecular Weight Organic Thin-Film Photodetectors and Solar Cells. *J. Appl. Phys.* **2003**, *93* (7), 3693-3723.
31. Peumans, P.; Uchida, S.; Forrest, S. R., Efficient Bulk Heterojunction Photovoltaic Cells Using Small-Molecular-Weight Organic Thin Films. *Nature* **2003**, *425* (6954), 158-162.
32. Gomez De Arco, L.; Zhang, Y.; Schlenker, C. W.; Ryu, K.; Thompson, M. E.; Zhou, C., Continuous, Highly Flexible, and Transparent Graphene Films by Chemical Vapor Deposition for Organic Photovoltaics. *ACS Nano* **2010**, *4* (5), 2865-2873.
33. Wang, X.; Zhi, L.; Tsao, N.; Tomović, Ž.; Li, J.; Müllen, K., Transparent Carbon Films as Electrodes in Organic Solar Cells. *Angew. Chem. Int. Ed.* **2008**, *47* (16), 2990-2992.

34. Liu, Q.; Jiang, Y.; Jin, K.; Qin, J.; Xu, J.; Li, W.; Xiong, J.; Liu, J.; Xiao, Z.; Sun, K.; Yang, S.; Zhang, X.; Ding, L., 18% Efficiency Organic Solar Cells. *Sci. Bull.* **2020**, *65* (4), 272-275.
35. Karki, A.; Gillett, A. J.; Friend, R. H.; Nguyen, T.-Q., The Path to 20% Power Conversion Efficiencies in Nonfullerene Acceptor Organic Solar Cells. *Adv. Energy Mater.* **2021**, *11* (15), 2003441.
36. Zhang, M.; Zhu, L.; Zhou, G.; Hao, T.; Qiu, C.; Zhao, Z.; Hu, Q.; Larson, B. W.; Zhu, H.; Ma, Z.; Tang, Z.; Feng, W.; Zhang, Y.; Russell, T. P.; Liu, F., Single-Layered Organic Photovoltaics with Double Cascading Charge Transport Pathways: 18% Efficiencies. *Nat. Commun.* **2021**, *12* (1), 309.
37. Green, M.; Dunlop, E.; Hohl-Ebinger, J.; Yoshita, M.; Kopidakis, N.; Hao, X., Solar Cell Efficiency Tables (Version 57). *Progress in Photovoltaics: Research and Applications* **2021**, *29* (1), 3-15.
38. Jiang, Q.; Zhao, Y.; Zhang, X.; Yang, X.; Chen, Y.; Chu, Z.; Ye, Q.; Li, X.; Yin, Z.; You, J., Surface Passivation of Perovskite Film for Efficient Solar Cells. *Nature Photonics* **2019**, *13* (7), 460-466.
39. Yoshikawa, K.; Kawasaki, H.; Yoshida, W.; Irie, T.; Konishi, K.; Nakano, K.; Uto, T.; Adachi, D.; Kanematsu, M.; Uzu, H.; Yamamoto, K., Silicon Heterojunction Solar Cell with Interdigitated Back Contacts for a Photoconversion Efficiency over 26%. *Nat. Energy* **2017**, *2* (5), 17032.
40. Polman, A.; Knight, M.; Garnett, E. C.; Ehrler, B.; Sinke, W. C., Photovoltaic Materials: Present Efficiencies and Future Challenges. *Science* **2016**, *352* (6283), aad4424.

41. Li, Y.; Guo, X.; Peng, Z.; Qu, B.; Yan, H.; Ade, H.; Zhang, M.; Forrest, S. R., Color-Neutral, Semitransparent Organic Photovoltaics for Power Window Applications. *Proc. Natl. Acad. Sci.* **2020**, *117* (35), 21147-21154.
42. Forrest, S. R., *Organic Electronics: Foundations to Applications*. Oxford University Press: 2020.
43. Li, Y.; Lin, J.-D.; Che, X.; Qu, Y.; Liu, F.; Liao, L.-S.; Forrest, S. R., High Efficiency near-Infrared and Semitransparent Non-Fullerene Acceptor Organic Photovoltaic Cells. *J. Am. Chem. Soc.* **2017**, *139* (47), 17114-17119.
44. Che, X.; Li, Y.; Qu, Y.; Forrest, S. R., High Fabrication Yield Organic Tandem Photovoltaics Combining Vacuum- and Solution-Processed Subcells with 15% Efficiency. *Nat. Energy* **2018**, *3* (5), 422-427.
45. Mehler, A.; Néel, N.; Bocquet, M. L.; Kröger, J., Exciting Vibrons in Both Frontier Orbitals of a Single Hydrocarbon Molecule on Graphene. *J. Phys. Condens. Matter* **2018**, *31* (6), 065001.
46. Mishra, A.; Bäuerle, P., Small Molecule Organic Semiconductors on the Move: Promises for Future Solar Energy Technology. *Angew. Chem. Int. Ed.* **2012**, *51* (9), 2020-2067.
47. Yiu, A. T.; Beaujuge, P. M.; Lee, O. P.; Woo, C. H.; Toney, M. F.; Fréchet, J. M. J., Side-Chain Tunability of Furan-Containing Low-Band-Gap Polymers Provides Control of Structural Order in Efficient Solar Cells. *J. Am. Chem. Soc.* **2012**, *134* (4), 2180-2185.
48. Li, Y.; Zhong, L.; Gautam, B.; Bin, H.-J.; Lin, J.-D.; Wu, F.-P.; Zhang, Z.; Jiang, Z.-Q.; Zhang, Z.-G.; Gundogdu, K.; Li, Y.; Liao, L.-S., A near-Infrared Non-Fullerene Electron Acceptor for High Performance Polymer Solar Cells. *Energy Environ. Sci.* **2017**, *10* (7), 1610-1620.

49. Pope, M.; Kallmann, H. P.; Magnante, P., Electroluminescence in Organic Crystals. *The Journal of Chemical Physics* **1963**, *38* (8), 2042-2043.
50. Choe, J.; Lee, Y.; Park, J.; Kim, Y.; Kim, C. U.; Kim, K., Direct Imaging of Structural Disorder and Heterogeneous Dynamics of Fullerene Molecular Liquid. *Nat. Commun.* **2019**, *10* (1), 4395.
51. Root, S. E.; Savagatrup, S.; Printz, A. D.; Rodriguez, D.; Lipomi, D. J., Mechanical Properties of Organic Semiconductors for Stretchable, Highly Flexible, and Mechanically Robust Electronics. *Chem. Rev.* **2017**, *117* (9), 6467-6499.
52. Bredas, J.-L., Mind the Gap! *Mater. Horiz.* **2014**, *1* (1), 17-19.
53. Huang, X.; Liu, X.; Ding, K.; Forrest, S. R., Is There Such a Thing as a Molecular Organic Alloy? *Mater. Horiz.* **2019**.
54. Huang, X.; Liu, X.; Ding, K.; Forrest, S., Alloy or Blend: Analysis of a Ternary Organic Photovoltaic. 2019; Vol. 2019, p K50.008.
55. Frenkel, J., On the Transformation of Light into Heat in Solids. I. *Physical Review* **1931**, *37* (1), 17-44.
56. Hill, I. G.; Kahn, A.; Soos, Z. G.; Pascal, J. R. A., Charge-Separation Energy in Films of Π -Conjugated Organic Molecules. *Chem. Phys. Lett.* **2000**, *327* (3), 181-188.
57. Bulović, V.; Burrows, P. E.; Forrest, S. R.; Cronin, J. A.; Thompson, M. E., Study of Localized and Extended Excitons in 3,4,9,10-Perylenetetracarboxylic Dianhydride (Ptcda) I. Spectroscopic Properties of Thin Films and Solutions. *Chemical Physics* **1996**, *210* (1), 1-12.
58. Wannier, G. H., The Structure of Electronic Excitation Levels in Insulating Crystals. *Physical Review* **1937**, *52* (3), 191-197.

59. Walle, C. G. V. d.; Neugebauer, J., First-Principles Calculations for Defects and Impurities: Applications to III-Nitrides. *J. Appl. Phys.* **2004**, *95* (8), 3851-3879.
60. Sun, Y.; Giebink, N. C.; Kanno, H.; Ma, B.; Thompson, M. E.; Forrest, S. R., Management of Singlet and Triplet Excitons for Efficient White Organic Light-Emitting Devices. *Nature* **2006**, *440* (7086), 908-912.
61. Dias, F. B.; Bourdakos, K. N.; Jankus, V.; Moss, K. C.; Kamtekar, K. T.; Bhalla, V.; Santos, J.; Bryce, M. R.; Monkman, A. P., Triplet Harvesting with 100% Efficiency by Way of Thermally Activated Delayed Fluorescence in Charge Transfer Oled Emitters. *Adv. Mater.* **2013**, *25* (27), 3707-3714.
62. Katz, H. E.; Lovinger, A. J.; Johnson, J.; Kloc, C.; Siegrist, T.; Li, W.; Lin, Y. Y.; Dodabalapur, A., A Soluble and Air-Stable Organic Semiconductor with High Electron Mobility. *Nature* **2000**, *404* (6777), 478-481.
63. Melianas, A.; Pranculis, V.; Spoltore, D.; Benduhn, J.; Inganäs, O.; Gulbinas, V.; Vandewal, K.; Kemerink, M., Charge Transport in Pure and Mixed Phases in Organic Solar Cells. *Adv. Energy Mater.* **2017**, *7* (20), 1700888.
64. Lu, N.; Li, L.; Geng, D.; Liu, M., A Review for Polaron Dependent Charge Transport in Organic Semiconductor. *Org. Electron.* **2018**, *61*, 223-234.
65. Holstein, T., Studies of Polaron Motion: Part II. The "Small" Polaron. *Annals of Physics* **1959**, *8* (3), 343-389.
66. Warta, W.; Karl, N., Hot Holes in Naphthalene: High, Electric-Field-Dependent Mobilities. *Phys. Rev. B* **1985**, *32* (2), 1172-1182.
67. Electronic and Optical Processes of Organic Semiconductors. In *Electronic Processes in Organic Semiconductors*, 2015; pp 193-305.

68. Moser, M.; Savva, A.; Thorley, K.; Paulsen, B. D.; Hidalgo, T. C.; Ohayon, D.; Chen, H.; Giovannitti, A.; Marks, A.; Gasparini, N.; Wadsworth, A.; Rivnay, J.; Inal, S.; McCulloch, I., Polaron Delocalization in Donor–Acceptor Polymers and Its Impact on Organic Electrochemical Transistor Performance. *Angew. Chem. Int. Ed.* **2021**, *60* (14), 7777-7785.
69. Yan, H.; Chen, Z.; Zheng, Y.; Newman, C.; Quinn, J. R.; Dötz, F.; Kastler, M.; Facchetti, A., A High-Mobility Electron-Transporting Polymer for Printed Transistors. *Nature* **2009**, *457* (7230), 679-686.
70. Frank, B.; Gast, A. P.; Russell, T. P.; Brown, H. R.; Hawker, C., Polymer Mobility in Thin Films. *Macromolecules* **1996**, *29* (20), 6531-6534.
71. Chiang, C. K.; Fincher, C. R.; Park, Y. W.; Heeger, A. J.; Shirakawa, H.; Louis, E. J.; Gau, S. C.; MacDiarmid, A. G., Electrical Conductivity in Doped Polyacetylene. *Physical Review Letters* **1977**, *39* (17), 1098-1101.
72. Shirakawa, H.; Louis, E. J.; MacDiarmid, A. G.; Chiang, C. K.; Heeger, A. J., Synthesis of Electrically Conducting Organic Polymers: Halogen Derivatives of Polyacetylene, (Ch). *Journal of the Chemical Society, Chemical Communications* **1977**, (16), 578-580.
73. Baldo, M. A.; Forrest, S. R., Interface-Limited Injection in Amorphous Organic Semiconductors. *Phys. Rev. B* **2001**, *64* (8), 085201.
74. Kotadiya, N. B.; Lu, H.; Mondal, A.; Ie, Y.; Andrienko, D.; Blom, P. W. M.; Wetzelaer, G.-J. A. H., Universal Strategy for Ohmic Hole Injection into Organic Semiconductors with High Ionization Energies. *Nat. Mater.* **2018**, *17* (4), 329-334.
75. Bakulin, A. A.; Rao, A.; Pavelyev, V. G.; van Loosdrecht, P. H. M.; Pshenichnikov, M. S.; Niedzialek, D.; Cornil, J.; Beljonne, D.; Friend, R. H., The Role of Driving Energy and Delocalized States for Charge Separation in Organic Semiconductors. *Science* **2012**, *335* (6074), 1340.

76. Liu, X.; Ding, K.; Panda, A.; Forrest, S. R., Charge Transfer States in Dilute Donor–Acceptor Blend Organic Heterojunctions. *ACS Nano* **2016**, *10* (8), 7619-7626.
77. Guan, Z. a. L. H.-W. a. C. Y. a. Y. Q. a. L. M.-F. a. N. T.-W. a. T. S.-W. a. L. C.-S., Charge-Transfer State Energy and Its Relationship with Open-Circuit Voltage in an Organic Photovoltaic Device. *J. Phys. Chem. C* **2016**, *120* (26), 14059-14068.
78. Jailaubekov, A. E.; P. Willard, A.; Tritsch, J. R.; Chan, W.-L.; Sai, N.; Gearba, R.; Kaake, L. G.; J. Williams, K.; Leung, K.; Rossky, P. J.; Zhu, X.-Y., Hot Charge-Transfer Excitons Set the Time Limit for Charge Separation at Donor/Acceptor Interfaces in Organic Photovoltaics. *Nat. Mater.* **2013**, *12*, 66-73.
79. Sykes, M., Circumventing the Tradeoff between Optical Absorption and Exciton Diffusion in Organic Photovoltaics. **2015**.
80. Lee, J.; Kim, S.-Y.; Kim, C.; Kim, J.-J., Enhancement of the Short Circuit Current in Organic Photovoltaic Devices with Microcavity Structures. *Appl. Phys. Lett.* **2010**, *97* (8), 083306.
81. Lunt, R. R.; Giebink, N. C.; Belak, A. A.; Benziger, J. B.; Forrest, S. R., Exciton Diffusion Lengths of Organic Semiconductor Thin Films Measured by Spectrally Resolved Photoluminescence Quenching. *J. Appl. Phys.* **2009**, *105* (5), 053711.
82. Yu, G.; Gao, J.; Hummelen, J. C.; Wudl, F.; Heeger, A. J., Polymer Photovoltaic Cells: Enhanced Efficiencies Via a Network of Internal Donor-Acceptor Heterojunctions. *Science* **1995**, *270* (5243), 1789.
83. Halls, J. J. M.; Walsh, C. A.; Greenham, N. C.; Marseglia, E. A.; Friend, R. H.; Moratti, S. C.; Holmes, A. B., Efficient Photodiodes from Interpenetrating Polymer Networks. *Nature* **1995**, *376* (6540), 498-500.

84. Che, X. High Efficiency Single and Multijunction Organic Photovoltaics. University of Michigan, 2018.
85. Shockley, W., The Theory of P-N Junctions in Semiconductors and P-N Junction Transistors. *The Bell System Technical Journal* **1949**, 28 (3), 435-489.
86. Giebink, N. C.; Wiederrecht, G. P.; Wasielewski, M. R.; Forrest, S. R., Ideal Diode Equation for Organic Heterojunctions. I. Derivation and Application. *Phys. Rev. B* **2010**, 82 (15), 155305.
87. Giebink, N. C.; Lassiter, B. E.; Wiederrecht, G. P.; Wasielewski, M. R.; Forrest, S. R., Ideal Diode Equation for Organic Heterojunctions. Ii. The Role of Polaron Pair Recombination. *Physical Review B* **2010**, 82, 155306.
88. Servaites, J. D.; Yeganeh, S.; Marks, T. J.; Ratner, M. A., Efficiency Enhancement in Organic Photovoltaic Cells: Consequences of Optimizing Series Resistance. *Adv. Func. Mater.* **2010**, 20 (1), 97-104.
89. Gilot, J.; Wienk, M. M.; Janssen, R. A. J., Measuring the External Quantum Efficiency of Two-Terminal Polymer Tandem Solar Cells. *Adv. Func. Mater.* **2010**, 20 (22), 3904-3911.
90. Ding, K.; Liu, X.; Forrest, S. R., Charge Transfer and Collection in Dilute Organic Donor–Acceptor Heterojunction Blends. *Nano Lett.* **2018**, 18 (5), 3180-3184.
91. Pandey, R.; Holmes, R. J., Organic Photovoltaic Cells Based on Continuously Graded Donor–Acceptor Heterojunctions. *IEEE Journal of Selected Topics in Quantum Electronics* **2010**, 16 (6), 1537-1543.
92. Baldo, M. A.; Kozlov, V. G.; Burrows, P. E.; Forrest, S. R.; Ban, V. S.; Koene, B.; Thompson, M. E., Low Pressure Organic Vapor Phase Deposition of Small Molecular Weight Organic Light Emitting Device Structures. *Appl. Phys. Lett.* **1997**, 71 (21), 3033-3035.

93. Shtein, M.; Mapel, J.; Benziger, J. B.; Forrest, S. R., Effects of Film Morphology and Gate Dielectric Surface Preparation on the Electrical Characteristics of Organic-Vapor-Phase-Deposited Pentacene Thin-Film Transistors. *Appl. Phys. Lett.* **2002**, *81* (2), 268-270.
94. Qu, B.; Ding, K.; Sun, K.; Hou, S.; Morris, S.; Shtein, M.; Forrest, S. R., Fast Organic Vapor Phase Deposition of Thin Films in Light-Emitting Diodes. *ACS Nano* **2020**, *14* (10), 14157-14163.
95. Shtein, M.; Gossenberger, H. F.; Benziger, J. B.; Forrest, S. R., Material Transport Regimes and Mechanisms for Growth of Molecular Organic Thin Films Using Low-Pressure Organic Vapor Phase Deposition. *J. Appl. Phys.* **2001**, *89* (2), 1470-1476.
96. Yang, F.; Shtein, M.; Forrest, S. R., Controlled Growth of a Molecular Bulk Heterojunction Photovoltaic Cell. *Nat. Mater.* **2005**, *4* (1), 37-41.
97. Søndergaard, R.; Hösel, M.; Angmo, D.; Larsen-Olsen, T. T.; Krebs, F. C., Roll-to-Roll Fabrication of Polymer Solar Cells. *Materials Today* **2012**, *15* (1), 36-49.
98. Søndergaard, R. R.; Hösel, M.; Krebs, F. C., Roll-to-Roll Fabrication of Large Area Functional Organic Materials. *Journal of Polymer Science Part B: Polymer Physics* **2013**, *51* (1), 16-34.
99. Bae, S.; Kim, H.; Lee, Y.; Xu, X.; Park, J.-S.; Zheng, Y.; Balakrishnan, J.; Lei, T.; Ri Kim, H.; Song, Y. I.; Kim, Y.-J.; Kim, K. S.; Özyilmaz, B.; Ahn, J.-H.; Hong, B. H.; Iijima, S., Roll-to-Roll Production of 30-Inch Graphene Films for Transparent Electrodes. *Nature Nanotechnology* **2010**, *5* (8), 574-578.
100. Forrest, S. R., The Path to Ubiquitous and Low-Cost Organic Electronic Appliances on Plastic. *Nature* **2004**, *428* (6986), 911-918.

101. Deibel, C.; Strobel, T.; Dyakonov, V., Role of the Charge Transfer State in Organic Donor-Acceptor Solar Cells. *Adv. Mater.* **2010**, *22* (37), 4097-4111.
102. Charges and Excited States in Organic Semiconductors. In *Electronic Processes in Organic Semiconductors*, 2015; pp 87-191.
103. Loi, M. A.; Toffanin, S.; Muccini, M.; Forster, M.; Scherf, U.; Scharber, M., Charge Transfer Excitons in Bulk Heterojunctions of a Polyfluorene Copolymer and a Fullerene Derivative. *Adv. Funct. Mater.* **2007**, *17* (13), 2111-2116.
104. Bernardo, B.; Cheyns, D.; Verreet, B.; Schaller, R. D.; Rand, B. P.; Giebink, N. C., Delocalization and Dielectric Screening of Charge Transfer States in Organic Photovoltaic Cells. *Nat. Commun.* **2014**, *5*, 3245.
105. Grancini, G.; Polli, D.; Fazzi, D.; Cabanillas-Gonzalez, J.; Cerullo, G.; Lanzani, G., Transient Absorption Imaging of P3ht:Pcbm Photovoltaic Blend: Evidence for Interfacial Charge Transfer State. *J. Phys. Chem. Lett.* **2011**, *2*, 1099-1105.
106. Arndt, A. P.; Gerhard, M.; Quintilla, A.; Howard, I. A.; Koch, M.; Lemmer, U., Time-Resolved Charge-Transfer State Emission in Organic Solar Cells: Temperature and Blend Composition Dependences of Interfacial Traps. *J. Phys. Chem. C* **2015**, *119*, 13516-13523.
107. Weise, G., Absorption and Electroabsorption on Amorphous Films of Polyvinylcarbazole and Trinitrofluorenone. *Phys. Status Solidi A* **1973**, *18*.
108. Zhu, X.-Y.; Yang, Q.; Muntwiler, M., Charge-Transfer Excitons at Organic Semiconductor Surfaces and Interfaces. *Acc. Chem. Res.* **2009**, *42* (11), 1779-1787.
109. Song, Y.; Schubert, A.; Liu, X.; Bhandari, S.; Forrest, S. R.; Dunietz, B. D.; Geva, E.; Ogilvie, J. P., Efficient Charge Generation Via Hole Transfer in Dilute Organic Donor-Fullerene Blends. *The Journal of Physical Chemistry Letters* **2020**, *11* (6), 2203-2210.

110. Cowan, M. L.; Ogilvie, J. P.; Miller, R. J. D., Two-Dimensional Spectroscopy Using Diffractive Optics Based Phased-Locked Photon Echoes. *Chem. Phys. Lett.* **2004**, *386* (1), 184-189.
111. Song, Y.; Liu, X.; Li, Y.; Nguyen, H. H.; Duan, R.; Kubarych, K. J.; Forrest, S. R.; Ogilvie, J. P., Mechanistic Study of Charge Separation in a Nonfullerene Organic Donor–Acceptor Blend Using Multispectral Multidimensional Spectroscopy. *The Journal of Physical Chemistry Letters* **2021**, *12* (13), 3410-3416.
112. Wilcox, D. E.; Lee, M. H.; Sykes, M. E.; Niedringhaus, A.; Geva, E.; Dunietz, B. D.; Shtein, M.; Ogilvie, J. P., Ultrafast Charge-Transfer Dynamics at the Boron Subphthalocyanine Chloride/C₆₀ Heterojunction: Comparison between Experiment and Theory. *J. Phys. Chem. Lett.* **2015**, *6*, 569-575.
113. Shen, X.; Han, G.; Fan, D.; Xie, Y.; Yi, Y., Hot Charge-Transfer States Determine Exciton Dissociation in the Dtdctb/C₆₀ Complex for Organic Solar Cells: A Theoretical Insight. *J. Phys. Chem. C* **2015**, *119*, 11320-11326.
114. Peumans, P.; Forrest, S. R., Very-High-Efficiency Double-Heterostructure Copper Phthalocyanine/C₆₀ Photovoltaic Cells. *Appl. Phys. Lett.* **2001**, *79* (1), 126-128.
115. Piersimoni, F.; Chambon, S.; Vandewal, K.; Mens, R.; Boonen, T.; Gadisa, A.; Izquierdo, M.; Filippone, S.; Ruttens, B.; D’Haen, J.; Martin, N.; Lutsen, L.; Vanderzande, D.; Adriaensens, P.; Manca, J. V., Influence of Fullerene Ordering on the Energy of the Charge-Transfer State and Open-Circuit Voltage in Polymer:Fullerene Solar Cells. *J. Phys. Chem. C* **2011**, *115*, 10873–10880.

116. Xiao, X.; Zimmerman, J. D.; Lassiter, B. E.; Bergemann, K. J.; Forrest, S. R., A Hybrid Planar-Mixed Tetraphenyldibenzoperiflanthene/ C_{70} Photovoltaic Cell. *Appl. Phys. Lett.* **2013**, *102*, 073302.
117. Forrest, S. R., Ultrathin Organic Films Grown by Organic Molecular Beam Deposition and Related Techniques. *Chem. Rev.* **1997**, *97*, 1793-1896.
118. Valsakumar, M. C.; Subramanian, N.; Yousuf, M.; Sahu, P. C.; Hariharan, Y.; Bharathi, A.; Sankara Sastry, V.; Janaki, J.; Rao, G. V. N.; Radhakrishnan, T. S.; Sundar, C. S., Crystal Structure and Disorder in Solid C_{70} . *Phys. Rev. B* **1993**, *48* (12), 9080-9085.
119. Scherrer, P., Bestimmung Der Größe Und Der Inneren Struktur Von Kolloidteilchen Mittels Röntgenstrahlen. *Nachr. Ges. Wiss. Göttingen* **1918**, *26* (1918), 98-100.
120. Wang, Z.; Yokoyama, D.; Wang, X.-F.; Hong, Z.; Yang, Y.; Kidoa, J., Highly Efficient Organic P-I-N Photovoltaic Cells Based on Tetraphenyldibenzoperiflanthene and Fullerene C_{70} . *Energy Environ. Sci.* **2013**, *6*, 234.
121. Madigan, C. F.; Bulovic, V., Solid State Solvation in Amorphous Organic Thin Films. *Phys. Rev. Lett.* **2003**, *91* (24), 247403.
122. Griffith, O. L.; Liu, X.; Amonoo, J. A.; Djurovich, P. I.; Thompson, M. E.; Green, P. F.; Forrest, S. R., Charge Transport and Exciton Dissociation in Organic Solar Cells Consisting of Dipolar Donors Mixed with C_{70} . *Phys. Rev. B* **2015**, *92*, 085404.
123. Liu, X.; Gu, J.; Ding, K.; Fan, D.; Hu, X.; Tseng, Y.-W.; Lee, Y.-H.; Menon, V.; Forrest, S. R., Photoresponse of an Organic Semiconductor/Two-Dimensional Transition Metal Dichalcogenide Heterojunction. *Nano Lett.* **2017**, *17* (5), 3176-3181.
124. Panda, A.; Ding, K.; Liu, X.; Forrest, S. R., Free and Trapped Hybrid Charge Transfer Excitons at a ZnO/Small-Molecule Heterojunction. *Phys. Rev. B* **2016**, *94* (12), 125429.

125. Lunt, R. R.; Benziger, J. B.; Forrest, S. R., Relationship between Crystalline Order and Exciton Diffusion Length in Molecular Organic Semiconductors. *Adv. Mater.* **2010**, *22*, 1233-1236.
126. Forrest, S. R., Ultrathin Organic Films Grown by Organic Molecular Beam Deposition and Related Techniques. *Chem. Rev.* **1997**, *97* (6), 1793-1896.
127. Fujita, T., Organic Electroluminescent Device. Google Patents: 2008.
128. Yang, F.; Forrest, S. R., Photocurrent Generation in Nanostructured Organic Solar Cells. *ACS Nano* **2008**, *2* (5), 1022-1032.
129. Knupfer, M., Exciton Binding Energies in Organic Semiconductors. *Applied Physics A* **2003**, *77* (5), 623-626.
130. Li, H.-W.; Guan, Z.; Cheng, Y.; Lui, T.; Yang, Q.; Lee, C.-S.; Chen, S.; Tsang, S.-W., On the Study of Exciton Binding Energy with Direct Charge Generation in Photovoltaic Polymers. *Adv. Electron. Mater.* **2016**, *2* (11), 1600200.
131. Leblebici, S. Y.; Chen, T. L.; Olalde-Velasco, P.; Yang, W.; Ma, B., Reducing Exciton Binding Energy by Increasing Thin Film Permittivity: An Effective Approach to Enhance Exciton Separation Efficiency in Organic Solar Cells. *ACS Applied Materials & Interfaces* **2013**, *5* (20), 10105-10110.
132. Kraner, S.; Scholz, R.; Koerner, C.; Leo, K., Design Proposals for Organic Materials Exhibiting a Low Exciton Binding Energy. *J. Phys. Chem. C* **2015**, *119* (40), 22820-22825.
133. Menke, S. M.; Ran, N. A.; Bazan, G. C.; Friend, R. H., Understanding Energy Loss in Organic Solar Cells: Toward a New Efficiency Regime. *Joule* **2018**, *2* (1), 25-35.

134. Zhao, W.; Qian, D.; Zhang, S.; Li, S.; Inganäs, O.; Gao, F.; Hou, J., Fullerene-Free Polymer Solar Cells with over 11% Efficiency and Excellent Thermal Stability. *Adv. Mater.* **2016**, *28* (23), 4734-4739.
135. Chen, W.; Zhang, Q., Recent Progress in Non-Fullerene Small Molecule Acceptors in Organic Solar Cells (Oscs). *Journal of Materials Chemistry C* **2017**, *5* (6), 1275-1302.
136. Li, Y.; Liu, X.; Wu, F.-P.; Zhou, Y.; Jiang, Z.-Q.; Song, B.; Xia, Y.; Zhang, Z.-G.; Gao, F.; Inganäs, O.; Li, Y.; Liao, L.-S., Non-Fullerene Acceptor with Low Energy Loss and High External Quantum Efficiency: Towards High Performance Polymer Solar Cells. *J. Mater. Chem. A* **2016**, *4* (16), 5890-5897.
137. Nielsen, C. B.; Holliday, S.; Chen, H.-Y.; Cryer, S. J.; McCulloch, I., Non-Fullerene Electron Acceptors for Use in Organic Solar Cells. *Accounts of Chemical Research* **2015**, *48* (11), 2803-2812.
138. Yao, Z.; Liao, X.; Gao, K.; Lin, F.; Xu, X.; Shi, X.; Zuo, L.; Liu, F.; Chen, Y.; Jen, A. K. Y., Dithienopicenocarbazole-Based Acceptors for Efficient Organic Solar Cells with Optoelectronic Response over 1000 Nm and an Extremely Low Energy Loss. *J. Am. Chem. Soc.* **2018**, *140* (6), 2054-2057.
139. Baran, D.; Kirchartz, T.; Wheeler, S.; Dimitrov, S.; Abdelsamie, M.; Gorman, J.; Ashraf, R. S.; Holliday, S.; Wadsworth, A.; Gasparini, N.; Kaienburg, P.; Yan, H.; Amassian, A.; Brabec, C. J.; Durrant, J. R.; McCulloch, I., Reduced Voltage Losses Yield 10% Efficient Fullerene Free Organic Solar Cells with >1 V Open Circuit Voltages. *Energy Environ. Sci.* **2016**, *9* (12), 3783-3793.
140. He, B.; Yang, B.; Kolaczowski, M. A.; Anderson, C. A.; Klivansky, L. M.; Chen, T. L.; Brady, M. A.; Liu, Y., Molecular Engineering for Large Open-Circuit Voltage and Low Energy

Loss in around 10% Non-Fullerene Organic Photovoltaics. *ACS Energy Letters* **2018**, *3* (4), 1028-1035.

141. Wang, Y.; Qian, D.; Cui, Y.; Zhang, H.; Hou, J.; Vandewal, K.; Kirchartz, T.; Gao, F., Optical Gaps of Organic Solar Cells as a Reference for Comparing Voltage Losses. *Adv. Energy Mater.* **2018**, *8* (28), 1801352.

142. Liu, J.; Chen, S.; Qian, D.; Gautam, B.; Yang, G.; Zhao, J.; Bergqvist, J.; Zhang, F.; Ma, W.; Ade, H.; Inganäs, O.; Gundogdu, K.; Gao, F.; Yan, H., Fast Charge Separation in a Non-Fullerene Organic Solar Cell with a Small Driving Force. *Nat. Energy* **2016**, *1* (7), 16089.

143. Rand, B. P.; Burk, D. P.; Forrest, S. R., Offset Energies at Organic Semiconductor Heterojunctions and Their Influence on the Open-Circuit Voltage of Thin-Film Solar Cells. *Phys. Rev. B* **2007**, *75* (11), 115327.

144. Coffey, D. C.; Larson, B. W.; Hains, A. W.; Whitaker, J. B.; Kopidakis, N.; Boltalina, O. V.; Strauss, S. H.; Rumbles, G., An Optimal Driving Force for Converting Excitons into Free Carriers in Excitonic Solar Cells. *J. Phys. Chem. C* **2012**, *116* (16), 8916-8923.

145. Ward, A. J.; Ruseckas, A.; Kareem, M. M.; Ebenhoch, B.; Serrano, L. A.; Al-Eid, M.; Fitzpatrick, B.; Rotello, V. M.; Cooke, G.; Samuel, I. D. W., The Impact of Driving Force on Electron Transfer Rates in Photovoltaic Donor–Acceptor Blends. *Adv. Mater.* **2015**, *27* (15), 2496-2500.

146. Liu, X.; Li, Y.; Ding, K.; Forrest, S., Energy Loss in Organic Photovoltaics: Nonfullerene Versus Fullerene Acceptors. *Phys. Rev. Appl.* **2019**, *11* (2), 024060.

147. Linderl, T.; Zechel, T.; Brendel, M.; Moseguí González, D.; Müller-Buschbaum, P.; Pflaum, J.; Brütting, W., Energy Losses in Small-Molecule Organic Photovoltaics. *Adv. Energy Mater.* **2017**, *7* (16), 1700237.

148. Benduhn, J.; Tvingstedt, K.; Piersimoni, F.; Ullbrich, S.; Fan, Y.; Tropiano, M.; McGarry, K. A.; Zeika, O.; Riede, M. K.; Douglas, C. J.; Barlow, S.; Marder, S. R.; Neher, D.; Spoltore, D.; Vandewal, K., Intrinsic Non-Radiative Voltage Losses in Fullerene-Based Organic Solar Cells. *Nat. Energy* **2017**, *2* (6), 17053.
149. Azzouzi, M.; Yan, J.; Kirchartz, T.; Liu, K.; Wang, J.; Wu, H.; Nelson, J., Nonradiative Energy Losses in Bulk-Heterojunction Organic Photovoltaics. *Physical Review X* **2018**, *8* (3), 031055.
150. Marcus, R. A.; Sutin, N., Electron Transfers in Chemistry and Biology. *Biochimica et Biophysica Acta (BBA) - Reviews on Bioenergetics* **1985**, *811* (3), 265-322.
151. Bixon, M.; Jortner, J., Electron Transfer—from Isolated Molecules to Biomolecules. In *Advances in Chemical Physics*, 1999; pp 35-202.
152. Bäessler, H.; Köhler, A., “Hot or Cold”: How Do Charge Transfer States at the Donor–Acceptor Interface of an Organic Solar Cell Dissociate? *Phys. Chem. Chem. Phys.* **2015**, *17* (43), 28451-28462.
153. Vandewal, K.; Albrecht, S.; Hoke, E. T.; Graham, K. R.; Widmer, J.; Douglas, J. D.; Schubert, M.; Mateker, W. R.; Bloking, J. T.; Burkhard, G. F.; Sellinger, A.; Fréchet, J. M. J.; Amassian, A.; Riede, M. K.; McGehee, M. D.; Neher, D.; Salleo, A., Efficient Charge Generation by Relaxed Charge-Transfer States at Organic Interfaces. *Nat. Mater.* **2014**, *13* (1), 63-68.
154. Rau, U., Reciprocity Relation between Photovoltaic Quantum Efficiency and Electroluminescent Emission of Solar Cells. *Phys. Rev. B* **2007**, *76* (8), 085303.
155. Englman, R.; Jortner, J., The Energy Gap Law for Radiationless Transitions in Large Molecules. *Molecular Physics* **1970**, *18* (2), 145-164.

156. Alamoudi, M. A.; Khan, J. I.; Firdaus, Y.; Wang, K.; Andrienko, D.; Beaujuge, P. M.; Laquai, F., Impact of Nonfullerene Acceptor Core Structure on the Photophysics and Efficiency of Polymer Solar Cells. *ACS Energy Letters* **2018**, *3* (4), 802-811.
157. Borioni, J. L.; Puiatti, M.; Vera, D. M. A.; Pierini, A. B., In Search of the Best Dft Functional for Dealing with Organic Anionic Species. *Phys. Chem. Chem. Phys.* **2017**, *19* (13), 9189-9198.
158. Lin, Y. L.; Fusella, M. A.; Rand, B. P., The Impact of Local Morphology on Organic Donor/Acceptor Charge Transfer States. *Adv. Energy Mater.* **2018**, *8* (28), 1702816.
159. Guan, Z.; Li, H.-W.; Cheng, Y.; Yang, Q.; Lo, M.-F.; Ng, T.-W.; Tsang, S.-W.; Lee, C.-S., Charge-Transfer State Energy and Its Relationship with Open-Circuit Voltage in an Organic Photovoltaic Device. *J. Phys. Chem. C* **2016**, *120* (26), 14059-14068.
160. Liu, X.; Rand, B. P.; Forrest, S. R., Engineering Charge-Transfer States for Efficient, Low-Energy-Loss Organic Photovoltaics. *Trends in Chemistry* **2019**, *1* (9), 815-829.
161. Meyer, J.; Hamwi, S.; Kröger, M.; Kowalsky, W.; Riedl, T.; Kahn, A., Transition Metal Oxides for Organic Electronics: Energetics, Device Physics and Applications. *Adv. Mater.* **2012**, *24* (40), 5408-5427.
162. Kim, D. Y.; Subbiah, J.; Sarasqueta, G.; So, F.; Ding, H.; Irfan; Gao, Y., The Effect of Molybdenum Oxide Interlayer on Organic Photovoltaic Cells. *Appl. Phys. Lett.* **2009**, *95* (9), 093304.
163. Kröger, M.; Hamwi, S.; Meyer, J.; Riedl, T.; Kowalsky, W.; Kahn, A., Role of the Deep-Lying Electronic States of MoO₃ in the Enhancement of Hole-Injection in Organic Thin Films. *Appl. Phys. Lett.* **2009**, *95* (12), 123301.

164. Li, Y.; Sheriff, H. K. M.; Liu, X.; Wang, C.-K.; Ding, K.; Han, H.; Wong, K.-T.; Forrest, S. R., Vacuum-Deposited Biternary Organic Photovoltaics. *J. Am. Chem. Soc* **2019**, *141* (45), 18204-18210.
165. Oehzelt, M.; Koch, N.; Heimel, G., Organic Semiconductor Density of States Controls the Energy Level Alignment at Electrode Interfaces. *Nat. Commun.* **2014**, *5* (1), 4174.
166. Wang, C.; Irfan, I.; Liu, X.; Gao, Y., Role of Molybdenum Oxide for Organic Electronics: Surface Analytical Studies. *J. Vac. Sci. Technol. B* **2014**, *32* (4), 040801.
167. Wang, J.; Xu, L.; Lee, Y.-J.; De Anda Villa, M.; Malko, A. V.; Hsu, J. W. P., Effects of Contact-Induced Doping on the Behaviors of Organic Photovoltaic Devices. *Nano Lett.* **2015**, *15* (11), 7627-7632.
168. Limketkai, B. N.; Baldo, M. A., Charge Injection into Cathode-Doped Amorphous Organic Semiconductors. *Phys. Rev. B* **2005**, *71* (8), 085207.
169. Bäessler, H., Charge Transport in Disordered Organic Photoconductors a Monte Carlo Simulation Study. *Phys. Status Solidi B* **1993**, *175* (1), 15-56.
170. Yun, J.; Jang, W.; Lee, T.; Lee, Y.; Soon, A., Aligning the Band Structures of Polymorphic Molybdenum Oxides and Organic Emitters in Light-Emitting Diodes. *Phys. Rev. Appl.* **2017**, *7* (2), 024025.
171. Guo, Y.; Robertson, J., Origin of the High Work Function and High Conductivity of Moo₃. *Appl. Phys. Lett.* **2014**, *105* (22), 222110.
172. Inzani, K.; Grande, T.; Vullum-Bruer, F.; Selbach, S. M., A Van Der Waals Density Functional Study of Moo₃ and Its Oxygen Vacancies. *J. Phys. Chem. C* **2016**, *120* (16), 8959-8968.

173. Scanlon, D. O.; Watson, G. W.; Payne, D. J.; Atkinson, G. R.; Egdeell, R. G.; Law, D. S. L., Theoretical and Experimental Study of the Electronic Structures of MoO_3 and MoO_2 . *J. Phys. Chem. C* **2010**, *114* (10), 4636-4645.
174. Krishnakumar, S.; Menon, C. S., Electrical and Optical Properties of Molybdenum Trioxide Thin Films. *Bull. Mater. Sci.* **1993**, *16* (3), 187-191.
175. Deb, S. K.; Chopoorian, J. A., Optical Properties and Color-Center Formation in Thin Films of Molybdenum Trioxide. *J. Appl. Phys.* **1966**, *37* (13), 4818-4825.
176. Firlej, L.; Zahab, A.; Brocard, F.; Bernier, P., Electric Conductivity in C70 Thin Films. *Synth. Met.* **1995**, *70* (1), 1373-1374.
177. Ren, S. L.; Wang, K. A.; Zhou, P.; Wang, Y.; Rao, A. M.; Meier, M. S.; Selegue, J. P.; Eklund, P. C., Dielectric Function of Solid C70 Films. *Appl. Phys. Lett.* **1992**, *61* (2), 124-126.
178. Battaglia, C.; Yin, X.; Zheng, M.; Sharp, I. D.; Chen, T.; McDonnell, S.; Azcatl, A.; Carraro, C.; Ma, B.; Maboudian, R.; Wallace, R. M.; Javey, A., Hole Selective MoOx Contact for Silicon Solar Cells. *Nano Lett.* **2014**, *14* (2), 967-971.
179. Ding, H.; Lin, H.; Sadigh, B.; Zhou, F.; Ozoliņš, V.; Asta, M., Computational Investigation of Electron Small Polarons in A-MoO₃. *J. Phys. Chem. C* **2014**, *118* (29), 15565-15572.
180. Yang, J.-P.; Wang, W.-Q.; Cheng, L.-W.; Li, Y.-Q.; Tang, J.-X.; Kera, S.; Ueno, N.; Zeng, X.-h., Mechanism for Doping Induced P Type C60 using Thermally Evaporated Molybdenum Trioxide (MoO_3) as a Dopant. *J. Phys. Condens. Matter* **2016**, *28* (18), 185502.
181. Irfan; Zhang, M.; Ding, H.; Tang, C. W.; Gao, Y., Strong Interface P-Doping and Band Bending in C60 on MoOx. *Org. Electron.* **2011**, *12* (9), 1588-1593.
182. Yoo, J.; Jung, K.; Jeong, J.; Hyun, G.; Lee, H.; Yi, Y., Energy Level Alignment at C60/Dtdctb/Pedot:Pss Interfaces in Organic Photovoltaics. *Appl. Surf. Sci.* **2017**, *402*, 41-46.

183. Sotthewes, K.; van Bremen, R.; Dollekamp, E.; Boulogne, T.; Nowakowski, K.; Kas, D.; Zandvliet, H. J. W.; Bampoulis, P., Universal Fermi-Level Pinning in Transition-Metal Dichalcogenides. *J. Phys. Chem. C* **2019**, *123* (9), 5411-5420.
184. Greiner, M. T.; Helander, M. G.; Tang, W.-M.; Wang, Z.-B.; Qiu, J.; Lu, Z.-H., Universal Energy-Level Alignment of Molecules on Metal Oxides. *Nat. Mater.* **2011**, *11*, 76.
185. Tress, W., Interplay between Electrodes and Active Materials: The Open-Circuit Voltage and S-Shaped J-V Curves. In *Organic Solar Cells: Theory, Experiment, and Device Simulation*, Tress, W., Ed. Springer International Publishing: Cham, 2014; pp 315-357.
186. Ding, K.; Forrest, S. R., Reducing Energy Losses at the Organic--Anode-Buffer Interface of Organic Photovoltaics. *Phys. Rev. Appl.* **2020**, *13* (5), 054046.
187. Credgington, D.; Jamieson, F. C.; Walker, B.; Nguyen, T.-Q.; Durrant, J. R., Quantification of Geminate and Non-Geminate Recombination Losses within a Solution-Processed Small-Molecule Bulk Heterojunction Solar Cell. *Adv. Mater.* **2012**, *24* (16), 2135-2141.
188. Kirchartz, T.; Pieters, B. E.; Kirkpatrick, J.; Rau, U.; Nelson, J., Recombination Via Tail States in Polythiophene:Fullerene Solar Cells. *Phys. Rev. B* **2011**, *83* (11), 115209.
189. Clarke, T. M.; Ballantyne, A.; Shoaee, S.; Soon, Y. W.; Duffy, W.; Heeney, M.; McCulloch, I.; Nelson, J.; Durrant, J. R., Analysis of Charge Photogeneration as a Key Determinant of Photocurrent Density in Polymer: Fullerene Solar Cells. *Adv. Mater.* **2010**, *22* (46), 5287-5291.
190. Kyaw, A. K. K.; Wang, D. H.; Gupta, V.; Leong, W. L.; Ke, L.; Bazan, G. C.; Heeger, A. J., Intensity Dependence of Current–Voltage Characteristics and Recombination in High-Efficiency Solution-Processed Small-Molecule Solar Cells. *ACS Nano* **2013**, *7* (5), 4569-4577.

191. Cowan, S. R.; Street, R. A.; Cho, S.; Heeger, A. J., Transient Photoconductivity in Polymer Bulk Heterojunction Solar Cells: Competition between Sweep-out and Recombination. *Phys. Rev. B* **2011**, *83* (3), 035205.
192. Burlingame, Q.; Huang, X.; Liu, X.; Jeong, C.; Coburn, C.; Forrest, S. R., Intrinsically Stable Organic Solar Cells under High-Intensity Illumination. *Nature* **2019**, *573* (7774), 394-397.
193. Renshaw, C. K.; Zimmerman, J. D.; Lassiter, B. E.; Forrest, S. R., Photoconductivity in Donor-Acceptor Heterojunction Organic Photovoltaics. *Phys. Rev. B* **2012**, *86* (8), 085324.
194. Sundqvist, A.; Sandberg, O. J.; Nyman, M.; Smått, J.-H.; Österbacka, R., Origin of the S-Shaped Jv Curve and the Light-Soaking Issue in Inverted Organic Solar Cells. *Adv. Energy Mater.* **2016**, *6* (6), 1502265.
195. Peters, C. H.; Sachs-Quintana, I. T.; Mateker, W. R.; Heumueller, T.; Rivnay, J.; Noriega, R.; Beiley, Z. M.; Hoke, E. T.; Salleo, A.; McGehee, M. D., The Mechanism of Burn-in Loss in a High Efficiency Polymer Solar Cell. *Adv. Mater.* **2012**, *24* (5), 663-668.
196. Rivaton, A.; Tournebize, A.; Gaume, J.; Bussièrè, P.-O.; Gardette, J.-L.; Therias, S., Photostability of Organic Materials Used in Polymer Solar Cells. *Polymer International* **2014**, *63* (8), 1335-1345.
197. Ghasemi, M.; Hu, H.; Peng, Z.; Rech, J. J.; Angunawela, I.; Carpenter, J. H.; Stuard, S. J.; Wadsworth, A.; McCulloch, I.; You, W.; Ade, H., Delineation of Thermodynamic and Kinetic Factors That Control Stability in Non-Fullerene Organic Solar Cells. *Joule* **2019**, *3* (5), 1328-1348.
198. Miller, A.; Abrahams, E., Impurity Conduction at Low Concentrations. *Physical Review* **1960**, *120* (3), 745-755.
199. Jørgensen, M.; Norrman, K.; Krebs, F. C., Stability/Degradation of Polymer Solar Cells. *Sol. Energy Mater. Sol. Cells* **2008**, *92* (7), 686-714.

200. Ray, B.; Alam, M. A., A Compact Physical Model for Morphology Induced Intrinsic Degradation of Organic Bulk Heterojunction Solar Cell. *Appl. Phys. Lett.* **2011**, *99* (3), 033303.
201. Mateker, W. R.; McGehee, M. D., Progress in Understanding Degradation Mechanisms and Improving Stability in Organic Photovoltaics. *Adv. Mater.* **2017**, *29* (10), 1603940.
202. Reese, M. O.; Nardes, A. M.; Rupert, B. L.; Larsen, R. E.; Olson, D. C.; Lloyd, M. T.; Shaheen, S. E.; Ginley, D. S.; Rumbles, G.; Kopidakis, N., Photoinduced Degradation of Polymer and Polymer–Fullerene Active Layers: Experiment and Theory. *Adv. Func. Mater.* **2010**, *20* (20), 3476-3483.
203. Mateker, W. R.; Heumueller, T.; Cheacharoen, R.; Sachs-Quintana, I. T.; McGehee, M. D.; Warnan, J.; Beaujuge, P. M.; Liu, X.; Bazan, G. C., Molecular Packing and Arrangement Govern the Photo-Oxidative Stability of Organic Photovoltaic Materials. *Chem. Mater.* **2015**, *27* (18), 6345-6353.
204. Cros, S.; Firon, M.; Lenfant, S.; Trouslard, P.; Beck, L., Study of Thin Calcium Electrode Degradation by Ion Beam Analysis. *Nucl. Instrum. Methods Phys. Res. B* **2006**, *251* (1), 257-260.
205. So, F.; Kondakov, D., Degradation Mechanisms in Small-Molecule and Polymer Organic Light-Emitting Diodes. *Adv. Mater.* **2010**, *22* (34), 3762-3777.
206. Bovill, E.; Scarratt, N.; Griffin, J.; Yi, H.; Iraqi, A.; Buckley, A. R.; Kingsley, J. W.; Lidzey, D. G., The Role of the Hole-Extraction Layer in Determining the Operational Stability of a Polycarbazole:Fullerene Bulk-Heterojunction Photovoltaic Device. *Appl. Phys. Lett.* **2015**, *106* (7), 073301.
207. Rösch, R.; Tanenbaum, D. M.; Jørgensen, M.; Seeland, M.; Bärenklau, M.; Hermenau, M.; Voroshazi, E.; Lloyd, M. T.; Galagan, Y.; Zimmermann, B.; Würfel, U.; Hösel, M.; Dam, H. F.; Gevorgyan, S. A.; Kudret, S.; Maes, W.; Lutsen, L.; Vanderzande, D.; Andriessen, R.; Teran-

- Escobar, G.; Lira-Cantu, M.; Rivaton, A.; Uzunoglu, G. Y.; Germack, D.; Andreasen, B.; Madsen, M. V.; Norrman, K.; Hoppe, H.; Krebs, F. C., Investigation of the Degradation Mechanisms of a Variety of Organic Photovoltaic Devices by Combination of Imaging Techniques—the Isos-3 Inter-Laboratory Collaboration. *Energy Environ. Sci.* **2012**, *5* (4), 6521-6540.
208. Manor, A.; Katz, E. A.; Tromholt, T.; Krebs, F. C., Electrical and Photo-Induced Degradation of ZnO Layers in Organic Photovoltaics. *Adv. Energy Mater.* **2011**, *1* (5), 836-843.
209. Trost, S.; Becker, T.; Polywka, A.; Görrn, P.; Oszejca, M. F.; Luechinger, N. A.; Rogalla, D.; Weidner, M.; Reckers, P.; Mayer, T.; Riedl, T., Avoiding Photoinduced Shunts in Organic Solar Cells by the Use of Tin Oxide (SnO₂) as Electron Extraction Material Instead of ZnO. *Adv. Energy Mater.* **2016**, *6* (15), 1600347.
210. Park, S.; Son, H. J., Intrinsic Photo-Degradation and Mechanism of Polymer Solar Cells: The Crucial Role of Non-Fullerene Acceptors. *J. Mater. Chem. A* **2019**, *7* (45), 25830-25837.
211. Jiang, Y.; Sun, L.; Jiang, F.; Xie, C.; Hu, L.; Dong, X.; Qin, F.; Liu, T.; Hu, L.; Jiang, X.; Zhou, Y., Photocatalytic Effect of ZnO on the Stability of Nonfullerene Acceptors and Its Mitigation by SnO₂ for Nonfullerene Organic Solar Cells. *Mater. Horiz.* **2019**, *6* (7), 1438-1443.
212. Li, J.; Dong, Q.; Li, N.; Wang, L., Direct Evidence of Ion Diffusion for the Silver-Electrode-Induced Thermal Degradation of Inverted Perovskite Solar Cells. *Adv. Energy Mater.* **2017**, *7* (14), 1602922.
213. Rand, B. P.; Peumans, P.; Forrest, S. R., Long-Range Absorption Enhancement in Organic Tandem Thin-Film Solar Cells Containing Silver Nanoclusters. *J. Appl. Phys.* **2004**, *96* (12), 7519-7526.

214. Hexemer, A.; Bras, W.; Glossinger, J.; Schaible, E.; Gann, E.; Kirian, R.; MacDowell, A.; Church, M.; Rude, B.; Padmore, H., A Saxs/Waxs/Gisaxs Beamline with Multilayer Monochromator. *Journal of Physics: Conference Series* **2010**, *247*, 012007.
215. Gann, E.; Young, A. T.; Collins, B. A.; Yan, H.; Nasiatka, J.; Padmore, H. A.; Ade, H.; Hexemer, A.; Wang, C., Soft X-Ray Scattering Facility at the Advanced Light Source with Real-Time Data Processing and Analysis. *Review of Scientific Instruments* **2012**, *83* (4), 045110.
216. Ding, K.; Huang, X.; Li, Y.; Forrest, S. R., Photogeneration and the Bulk Quantum Efficiency of Organic Photovoltaics. *Energy Environ. Sci.* **2021**, *14* (3), 1584-1593.
217. Sajjad, M. T.; Ruseckas, A.; Jagadamma, L. K.; Zhang, Y.; Samuel, I. D. W., Long-Range Exciton Diffusion in Non-Fullerene Acceptors and Coarse Bulk Heterojunctions Enable Highly Efficient Organic Photovoltaics. *J. Mater. Chem. A* **2020**, *8* (31), 15687-15694.
218. Ferguson, A. J.; Kopidakis, N.; Shaheen, S. E.; Rumbles, G., Quenching of Excitons by Holes in Poly(3-Hexylthiophene) Films. *J. Phys. Chem. C* **2008**, *112* (26), 9865-9871.
219. Tzabari, L.; Zayats, V.; Tessler, N., Exciton Annihilation as Bimolecular Loss in Organic Solar Cells. *J. Appl. Phys.* **2013**, *114* (15), 154514.
220. Greenbank, W.; Djeddaoui, N.; Destouesse, E.; Lamminaho, J.; Prete, M.; Boukezzi, L.; Ebel, T.; Bessissa, L.; Rubahn, H.-G.; Turkovic, V.; Madsen, M., Degradation Behavior of Scalable Nonfullerene Organic Solar Cells Assessed by Outdoor and Indoor Isos Stability Protocols. *Energy Technol.* **2020**, *8* (12), 2000295.
221. Burlingame, Q.; Zanotti, G.; Ciammaruchi, L.; Katz, E. A.; Forrest, S. R., Outdoor Operation of Small-Molecule Organic Photovoltaics. *Org. Electron.* **2017**, *41*, 274-279.
222. Duan, L.; Uddin, A., Progress in Stability of Organic Solar Cells. *Adv. Sci.* **2020**, *7* (11), 1903259.

223. Duan, L.; Yi, H.; Zhang, Y.; Haque, F.; Xu, C.; Uddin, A., Comparative Study of Light- and Thermal-Induced Degradation for Both Fullerene and Non-Fullerene-Based Organic Solar Cells. *Sustain. Energy Fuels* **2019**, *3* (3), 723-735.
224. Oh, S.; Song, C. E.; Lee, T.; Cho, A.; Lee, H. K.; Lee, J.-C.; Moon, S.-J.; Lim, E.; Lee, S. K.; Shin, W. S., Enhanced Efficiency and Stability of Ptb7-Th-Based Multi-Non-Fullerene Solar Cells Enabled by the Working Mechanism of the Coexisting Alloy-Like Structure and Energy Transfer Model. *J. Mater. Chem. A* **2019**, *7* (38), 22044-22053.
225. Duan, L.; Guli, M.; Zhang, Y.; Yi, H.; Haque, F.; Uddin, A., The Air Effect in the Burn-in Thermal Degradation of Nonfullerene Organic Solar Cells. *Energy Technol.* **2020**, *8* (5), 1901401.
226. Cha, H.; Wu, J.; Wadsworth, A.; Nagitta, J.; Limbu, S.; Pont, S.; Li, Z.; Searle, J.; Wyatt, M. F.; Baran, D.; Kim, J.-S.; McCulloch, I.; Durrant, J. R., An Efficient, “Burn in” Free Organic Solar Cell Employing a Nonfullerene Electron Acceptor. *Adv. Mater.* **2017**, *29* (33), 1701156.
227. Jiang, K.; Wei, Q.; Lai, J. Y. L.; Peng, Z.; Kim, H. K.; Yuan, J.; Ye, L.; Ade, H.; Zou, Y.; Yan, H., Alkyl Chain Tuning of Small Molecule Acceptors for Efficient Organic Solar Cells. *Joule* **2019**, *3* (12), 3020-3033.
228. Wang, R.; Zhang, C.; Li, Q.; Zhang, Z.; Wang, X.; Xiao, M., Charge Separation from an Intra-Moiety Intermediate State in the High-Performance Pm6:Y6 Organic Photovoltaic Blend. *J. Am. Chem. Soc* **2020**, *142* (29), 12751-12759.
229. Fairley, N.; Fernandez, V.; Richard-Plouet, M.; Guillot-Deudon, C.; Walton, J.; Smith, E.; Flahaut, D.; Greiner, M.; Biesinger, M.; Tougaard, S.; Morgan, D.; Baltrusaitis, J., Systematic and Collaborative Approach to Problem Solving Using X-Ray Photoelectron Spectroscopy. *Appl. Surf. Sci. Adv.* **2021**, *5*, 100112.
230. Benson, S. W., Iii - Bond Energies. *Journal of Chemical Education* **1965**, *42* (9), 502.

231. Haynes, W. M., *Crc Handbook of Chemistry and Physics*. CRC Press: 2014.
232. Li, Y.; Huang, X.; Ding, K.; Sheriff, H. K. M.; Ye, L.; Liu, H.; Li, C.-Z.; Ade, H.; Forrest, S. R., Non-Fullerene Acceptor Organic Photovoltaics with Intrinsic Operational Lifetimes over 30 Years. *Nat. Commun.* **2021**, *12* (1), 5419.
233. Kim, J.; Hou, S.; Zhao, H.; Forrest, S. R., Nanoscale Mapping of Morphology of Organic Thin Films. *Nano Lett.* **2020**, *20* (11), 8290-8297.
234. Burlingame, Q.; Coburn, C.; Che, X.; Panda, A.; Qu, Y.; Forrest, S. R., Centimetre-Scale Electron Diffusion in Photoactive Organic Heterostructures. *Nature* **2018**, *554*, 77.
235. Cravino, A.; Schilinsky, P.; Brabec, C. J., Characterization of Organic Solar Cells: The Importance of Device Layout. *Adv. Func. Mater.* **2007**, *17* (18), 3906-3910.
236. Shrotriya, V.; Li, G.; Yao, Y.; Moriarty, T.; Emery, K.; Yang, Y., Accurate Measurement and Characterization of Organic Solar Cells. *Adv. Func. Mater.* **2006**, *16* (15), 2016-2023.
237. Shrotriya, V.; Li, G.; Yao, Y.; Chu, C.-W.; Yang, Y., Transition Metal Oxides as the Buffer Layer for Polymer Photovoltaic Cells. *Appl. Phys. Lett.* **2006**, *88* (7), 073508.
238. Qi, B.; Wang, J., Fill Factor in Organic Solar Cells. *Phys. Chem. Chem. Phys.* **2013**, *15* (23), 8972-8982.
239. Elumalai, N. K.; Uddin, A., Open Circuit Voltage of Organic Solar Cells: An in-Depth Review. *Energy Environ. Sci.* **2016**, *9* (2), 391-410.
240. Richards, T.; Bird, M.; Sirringhaus, H., A Quantitative Analytical Model for Static Dipolar Disorder Broadening of the Density of States at Organic Heterointerfaces. *The Journal of Chemical Physics* **2008**, *128* (23), 234905.
241. Dong, Y.; Cha, H.; Zhang, J.; Pastor, E.; Tuladhar, P. S.; McCulloch, I.; Durrant, J. R.; Bakulin, A. A., The Binding Energy and Dynamics of Charge-Transfer States in Organic

Photovoltaics with Low Driving Force for Charge Separation. *The Journal of Chemical Physics* **2019**, *150* (10), 104704.

242. Zhu, X.; Kahn, A., Electronic Structure and Dynamics at Organic Donor/Acceptor Interfaces. *MRS Bulletin* **2010**, *35* (6), 443-448.

243. Melianas, A.; Pranculis, V.; Xia, Y.; Felekidis, N.; Inganäs, O.; Gulbinas, V.; Kemerink, M., Photogenerated Carrier Mobility Significantly Exceeds Injected Carrier Mobility in Organic Solar Cells. *Adv. Energy Mater.* **2017**, *7* (9), 1602143.

244. Ray, B.; Alam, M. A., Random Vs Regularized Opv: Limits of Performance Gain of Organic Bulk Heterojunction Solar Cells by Morphology Engineering. *Sol. Energy Mater. Sol. Cells* **2012**, *99*, 204-212.

245. Yoshikawa, S.; Saeki, A.; Saito, M.; Osaka, I.; Seki, S., On the Role of Local Charge Carrier Mobility in the Charge Separation Mechanism of Organic Photovoltaics. *Phys. Chem. Chem. Phys.* **2015**, *17* (27), 17778-17784.

246. Huang, X.; Fan, D.; Forrest, S. R., Scalable Semitransparent Prototype Organic Photovoltaic Module with Minimal Resistance Loss. *Org. Electron.* **2021**, *97*, 106276.

247. Sheriff Jr., H. K. M.; Li, Y.; Qu, B.; Forrest, S. R., Aperiodic Optical Coatings for Neutral-Color Semi-Transparent Organic Photovoltaics. *Appl. Phys. Lett.* **2021**, *118* (3), 033302.

248. Emmott, C. J. M.; Röhr, J. A.; Campoy-Quiles, M.; Kirchartz, T.; Urbina, A.; Ekins-Daukes, N. J.; Nelson, J., Organic Photovoltaic Greenhouses: A Unique Application for Semi-Transparent Pv? *Energy Environ. Sci.* **2015**, *8* (4), 1317-1328.

249. Yin, Z.; Sun, S.; Salim, T.; Wu, S.; Huang, X.; He, Q.; Lam, Y. M.; Zhang, H., Organic Photovoltaic Devices Using Highly Flexible Reduced Graphene Oxide Films as Transparent Electrodes. *ACS Nano* **2010**, *4* (9), 5263-5268.

250. Chen, K.-S.; Salinas, J.-F.; Yip, H.-L.; Huo, L.; Hou, J.; Jen, A. K. Y., Semi-Transparent Polymer Solar Cells with 6% Pce, 25% Average Visible Transmittance and a Color Rendering Index Close to 100 for Power Generating Window Applications. *Energy Environ. Sci.* **2012**, *5* (11), 9551-9557.
251. Lucera, L.; Machui, F.; Kubis, P.; Schmidt, H. D.; Adams, J.; Strohm, S.; Ahmad, T.; Forberich, K.; Egelhaaf, H. J.; Brabec, C. J., Highly Efficient, Large Area, Roll Coated Flexible and Rigid Opv Modules with Geometric Fill Factors up to 98.5% Processed with Commercially Available Materials. *Energy Environ. Sci.* **2016**, *9* (1), 89-94.
252. Gevorgyan, S. A.; Madsen, M. V.; Dam, H. F.; Jørgensen, M.; Fell, C. J.; Anderson, K. F.; Duck, B. C.; Mescheloff, A.; Katz, E. A.; Elschner, A.; Roesch, R.; Hoppe, H.; Hermenau, M.; Riede, M.; Krebs, F. C., Interlaboratory Outdoor Stability Studies of Flexible Roll-to-Roll Coated Organic Photovoltaic Modules: Stability over 10,000h. *Sol. Energy Mater. Sol. Cells* **2013**, *116*, 187-196.
253. Galagan, Y.; J.M. Rubingh, J.-E.; Andriessen, R.; Fan, C.-C.; W.M. Blom, P.; C. Veenstra, S.; M. Kroon, J., Ito-Free Flexible Organic Solar Cells with Printed Current Collecting Grids. *Sol. Energy Mater. Sol. Cells* **2011**, *95* (5), 1339-1343.
254. Son, D.; Lee, J.; Qiao, S.; Ghaffari, R.; Kim, J.; Lee, J. E.; Song, C.; Kim, S. J.; Lee, D. J.; Jun, S. W.; Yang, S.; Park, M.; Shin, J.; Do, K.; Lee, M.; Kang, K.; Hwang, C. S.; Lu, N.; Hyeon, T.; Kim, D.-H., Multifunctional Wearable Devices for Diagnosis and Therapy of Movement Disorders. *Nature Nanotechnology* **2014**, *9* (5), 397-404.
255. Jinno, H.; Yokota, T.; Koizumi, M.; Yukita, W.; Saito, M.; Osaka, I.; Fukuda, K.; Someya, T., Self-Powered Ultraflexible Photonic Skin for Continuous Bio-Signal Detection Via Air-Operation-Stable Polymer Light-Emitting Diodes. *Nat. Commun.* **2021**, *12* (1), 2234.

256. Scholes, G. D.; Fleming, G. R.; Olaya-Castro, A.; van Grondelle, R., Lessons from Nature About Solar Light Harvesting. *Nature Chemistry* **2011**, *3* (10), 763-774.
257. Brédas, J.-L.; Sargent, E. H.; Scholes, G. D., Photovoltaic Concepts Inspired by Coherence Effects in Photosynthetic Systems. *Nat. Mater.* **2017**, *16* (1), 35-44.
258. Schachenmayer, J.; Genes, C.; Tignone, E.; Pupillo, G., Cavity-Enhanced Transport of Excitons. *Physical Review Letters* **2015**, *114* (19), 196403.
259. Myers, D. M.; Mukherjee, S.; Beaumariage, J.; Snoke, D. W.; Steger, M.; Pfeiffer, L. N.; West, K., Polariton-Enhanced Exciton Transport. *Phys. Rev. B* **2018**, *98* (23), 235302.
260. Saikin, S. K.; Shakirov, M. A.; Kreisbeck, C.; Peskin, U.; Proshin, Y. N.; Aspuru-Guzik, A., On the Long-Range Exciton Transport in Molecular Systems: The Application to H-Aggregated Heterotriangulene Chains. *J. Phys. Chem. C* **2017**, *121* (45), 24994-25002.
261. Saikin, S. K.; Eisfeld, A.; Valleau, S.; Aspuru-Guzik, A., Photonics Meets Excitonics: Natural and Artificial Molecular Aggregates. *Nanophotonics* **2013**, *2* (1), 21-38.
262. Feist, J.; Garcia-Vidal, F. J., Extraordinary Exciton Conductance Induced by Strong Coupling. *Physical Review Letters* **2015**, *114* (19), 196402.
263. Agranovich, V. M.; Litinskaia, M.; Lidzey, D. G., Cavity Polaritons in Microcavities Containing Disordered Organic Semiconductors. *Phys. Rev. B* **2003**, *67* (8), 085311.
264. Michetti, P.; La Rocca, G. C., Polariton States in Disordered Organic Microcavities. *Phys. Rev. B* **2005**, *71* (11), 115320.
265. Litinskaya, M., Propagation and Localization of Polaritons in Disordered Organic Microcavities. *Physics Letters A* **2008**, *372* (21), 3898-3903.

266. Lerario, G.; Ballarini, D.; Fieramosca, A.; Cannavale, A.; Genco, A.; Mangione, F.; Gambino, S.; Dominici, L.; De Giorgi, M.; Gigli, G.; Sanvitto, D., High-Speed Flow of Interacting Organic Polaritons. *Light: Science & Applications* **2017**, *6* (2), e16212-e16212.
267. Coles, D. M.; Michetti, P.; Clark, C.; Tsoi, W. C.; Adawi, A. M.; Kim, J.-S.; Lidzey, D. G., Vibrationally Assisted Polariton-Relaxation Processes in Strongly Coupled Organic-Semiconductor Microcavities. *Adv. Func. Mater.* **2011**, *21* (19), 3691-3696.
268. Yeh, P.; Yariv, A.; Hong, C.-S., Electromagnetic Propagation in Periodic Stratified Media. I. General Theory*. *J. Opt. Soc. Am.* **1977**, *67* (4), 423-438.
269. Ramos-Mendieta, F.; Halevi, P., Surface Electromagnetic Waves in Two-Dimensional Photonic Crystals: Effect of the Position of the Surface Plane. *Phys. Rev. B* **1999**, *59* (23), 15112-15120.
270. Liscidini, M.; Gerace, D.; Sanvitto, D.; Bajoni, D., Guided Bloch Surface Wave Polaritons. *Appl. Phys. Lett.* **2011**, *98* (12), 121118.
271. Barachati, F.; Fieramosca, A.; Hafezian, S.; Gu, J.; Chakraborty, B.; Ballarini, D.; Martinu, L.; Menon, V.; Sanvitto, D.; Kéna-Cohen, S., Interacting Polariton Fluids in a Monolayer of Tungsten Disulfide. *Nature Nanotechnology* **2018**, *13* (10), 906-909.
272. Hou, S.; Khatoniar, M.; Ding, K.; Qu, Y.; Menon, V. M.; Forrest, S. R. In *Exciton Polariton-Mediated Long-Range Excitation Energy Transport in Disordered Organic Semiconductors*, 2020 Conference on Lasers and Electro-Optics (CLEO), 10-15 May 2020; 2020; pp 1-2.
273. Aberra Guebrou, S.; Symonds, C.; Homeyer, E.; Plenet, J. C.; Gartstein, Y. N.; Agranovich, V. M.; Bellessa, J., Coherent Emission from a Disordered Organic Semiconductor

Induced by Strong Coupling with Surface Plasmons. *Physical Review Letters* **2012**, *108* (6), 066401.

274. Daskalakis, K. S.; Maier, S. A.; Kéna-Cohen, S., Spatial Coherence and Stability in a Disordered Organic Polariton Condensate. *Physical Review Letters* **2015**, *115* (3), 035301.